Focal Region Modelling and Characterisation of Paraboloidal Dish Solar Concentrators

Glen Johnston

October 1998

A thesis submitted for the degree of
Doctor of Philosophy
at the Australian National University

To Sandie,
Whose gentleness and patient support has helped me through the most difficult times
during the course of this project.

Declaration

This PhD thesis contains no material which has been accepted for the award of any other degree or diploma in any university. To the best of the author's knowledge and belief, no material previously published or written by another person has been included in this thesis, except where due reference is made in the text.

Glen Johnston

April 1998.

Acknowledgments

I have been very fortunate to have undertaken this course of research at the Australian National University, where I have been able to fulfil my career love of working with solar collectors, and at the same time work with some of the most insightful and creative people that Australia has to offer in this field.

My first thanks go to Professor Stephen Kaneff, for it was due to his encouragement and support that I decided to take up my studies at the ANU. He has also been a supportive and patient supervisor with the ups and downs of my research. This latter statement is also true of Dr. Ken Inall, whose reservoirs of experience and enthusiasm could not help but flow out of him and infect me whenever I had ideas to discuss with him.

I also consider myself lucky to have had Dr. Andrew Blakers as a Principle Supervisor, for his positive support and ready availability for anything I needed to discuss or ask his advice about. I have also gained a great deal of inspiration from his high standing and insightfulness as both an academic and a researcher.

This project was definitely a hands-on job, with few funds available to 'splash around' when it came to equipment or materials, and I am deeply indebted to the staff of the Energy Research Centre, ANUTECH, for their advice, ideas and many discussions that guided me through numerous uncertainties during the manufacture of various items required for the research. My thanks in particular to Bob Whelan for his wealth of experience and straight forward engineering ingenuity, and to Geoff Major and Warren Baker for their workshop savvy, warm friendship and unrestrained interest in my ideas and dreams. Ray Dicker also deserves mention in here somewhere, particularly for his sacrificial nature on those cold, late nights when I needed his help when photographing panels on the Big Dish, and Mark Dymond provided the essential, but friendly, switch on the back to get my feet back on the ground on the odd occasions when I could not see the forest for the trees. Good research runs well in a good environment, and these men provided that helpful commodity.

Numerous staff and academics at the Department of Engineering have helped me along in several ways and stages of my work , and I am grateful for the helpful environment the Department has provided. Outstanding among these has been Dr. Andres Cuevas, with whom I have shared as much friendship as academic guidance and support.

I am also heavily in debt to Associate Professor Mark Shortis, at the University of Melbourne, without whom my utilisation of the photogrammetric method would have been almost impossible. His lengthy and patient instructions and advice on the many subtleties of close-range photogrammetry again inspired me with the recognition that I was dealing with a true professional. I will be forever grateful for his participation that let me establish the definitive element in my research.

Together with all of these lights who have lent me guidance, I am pleased to offer my thanks to both my friends and colleagues, Dr. Keith Lovegrove and Dr. Andreas Luzzi. As well as endless discussions, sound advice and creative ideas, they have provided a friendship that has helped keep my perseverance going when at times it felt like giving up.

Abstract

The development of the 400 m^2 paraboloidal dish collector at the Australian National University has given the world its largest solar dish concentrator to date. Such large structures bring their own attendant problems when it comes to assessing their performance.

The project described in the following pages has investigated a new method of assessing the optical qualities of solar concentrators, with a view to predicting the focal region light distribution for these devices. The research has proceeded along five major avenues, with each providing support for, and using results from the other. These research paths consisted of:

1. Empirical measurements taken of the focal light distributions of the concentrators using videographic flux mapping;
2. A computer based ray trace modelling program developed for the purpose of creating predictions for the expected focal flux distributions;
3. The 3-dimensional coordinates of the reflective surfaces of the concentrators measured using the established technique of close-range photogrammetry;
4. Algorithms and procedures developed to process the measured surface information to extract the associated optical characteristics for the concentrators. Among these were:
   - a ray trace algorithm dubbed COMPREC that successfully predicts light distributions on a range of different receiver geometries placed in specified positions in the focal region of solar concentrators;
   - a surface manipulation program named TRIANGLEREORIENT that orients arrays of 3-dimensional surface coordinates into new orientations;
   - a surface fitting algorithm named GRADFITTER that calculates the best fitting bicubic B-spline interpolating surface to a set of measured data coordinates, and calculates surface normal information from this fitted surface;
   - an array of utility programs that can create concentrator surfaces having a range of different shapes and geometries.
5. Focal region light distributions predicted using the ray trace algorithm with the photogrammetrically measured and processed surface data as input, and the predicted and measured fluxes compared.

Preliminary investigations were undertaken using a 20 m^2 paraboloidal dish covered with approximately 2,300 flat mirror tiles, ranging in size from 5 cm to 10 cm in width and 10 cm in depth. Peak concentrations of some 900 suns were measured, and both ray trace simulations and photogrammetric measurements of the surface indicated that this dish has a surface slope error of 1.9 $\pm$ 0.1 milliradian. An average reflectivity of 0.74 was calculated for the dish at the time of the measurements.

For the case of the 400 m^2 dish, peak concentrations in the order of 1070 suns were recorded, and an average surface slope error of 6.5 milliradian was calculated for its reflective surfaces, again using ray trace predictions and photogrammetric characterisations of the reflective surfaces. Average dish reflectivity was both calculated and measured to be 0.72.

This project also reports on close range photogrammetry being utilised to characterise the optical surface of solar concentrators for the first time. This technique has been shown to provide both the coordinate accuracy (relative precisions up to 1:40,000)

required for the extraction of optical information, and the flexibility needed to measure surfaces of almost any size, shape or orientation. This work, together with its attendant analyses, constitutes the major contribution of this thesis to the field of solar device characterisation.

Contributions to the field

The current work was undertaken to contribute a new method to the field of solar collector analysis. The author considers that this has been achieved with a great deal of success. The technique of close-range photogrammetry has been studied and applied to the large area solar concentrator established at the Australian National University, and it has been found capable of measuring surface coordinates to precisions of better than 1:40,000. Together with the development of the necessary support tools of a computer based ray trace simulation program and a surface fitting program with which to extract optical information from the surface data, these techniques have formed a suite of analysis methods that have demonstrated their ability to predict focal region flux distributions in solar concentrators with a high degree of accuracy.

Specifically, these methods and contributions consist of:

- the application of close-range photogrammetry to measure the 3-dimensional surface coordinates of points on solar concentrator surfaces;
- a surface fitting algorithm named GRADFITTER that fits a bicubic spline surface to an array of measured surface coordinates, and extracts surface normal information from the surface coordinate data;
- a simplified method of analysis for extracting the equivalent standard deviation of a circular bivariate Gaussian distribution of surface slope errors from a frequency distribution of slope errors measured on a surface;

The author feels confident that a set of tools has been established with this work that will be productive in its application to a range of different solar concentrating devices, and to the development of further large area concentrators in the future.

The studies undertaken have led to a number of journal publications on the methods developed and the information gained from the investigations reported in the following thesis. They are listed as follows:

- "Photogrammetry: An Available Surface Characterisation Tool for Solar Concentrators, Part I: Measurements of Surfaces". Shortis, M.R. and Johnston, G.H.G. 1996. J. Sol. En. Eng. vol.118. No.3. pp.146-150.

- Johnston, G., Shortis, M. November 1997. "Photogrammetry: An Available Surface Characterization Tool for Solar Concentrators, Part II: Assessment of Surfaces." Journal of Solar Energy Engineering, Volume 119 - Number 4. pp.286-291.

- "Flux mapping the 400 m^2 'Big Dish' at the Australian National University." Johnston, G.H.G. 1995. J.Sol.En.Eng. vol.117. no.4. pp.290-293.

- "On the Analysis of Surface Error Distributions on Concentrating Solar Collectors." Johnston, G.H.G. 1995. J.Sol.En.Eng. vol.117, no.4. pp.294-296.

The following manuscript has been accepted for publication in the Solar Energy journal:

- "Focal Region Measurements of the 20 m^2 Tiled Dish at the Australian National University." Johnston, G.H.G. April 1998.

For the reader's reference, copies of the foregoing articles are found in Appendix 1.1 of this thesis.

The following manuscripts have also been accepted and presented at the nominated conferences:

- "Manufacturing Issues Versus Optical Performance of Spherical Reflecting Elements for Use With Dish Concentrators." Johnston, G.H.G; Lovegrove, K.; Luzzi, A. Australian and New Zealand Solar Energy Society (ANZSES) Solar '95 conference proceedings, Hobart, Tasmania. pp.395-403.

- "Focal Region Characterisation of Paraboloidal Dishes at the Australian National University." Johnston G.H.G. 1994. Proceedings of the 7th International Symposium on Solar Thermal Concentrating Technologies, Moscow, Russia. pp.760-775.

- "Focal Region Characterisation of Paraboloidal Dish Concentrators". Johnston, G.H.G. 1993. Australian and New Zealand Solar Energy Society (ANZSES) Solar '93 conference proceedings, Fremantle, Western Australia. vol.1. pp.57-62.

The author has also served as the Task III leader in the SolarPACES-Australia organisation, which involved information gathering, collation and presentation at two of the IEA SolarPACES meetings, held in Moscow (1994) and Villigen, Switzerland (1995). The author also presented information from an Australian perspective in the SolarPACES High Flux and Temperature Measurement Workshop, held in Köln, Germany in March, 1995.

Table of Contents

1. Introduction

1.1 Solar collector focal region measurement and prediction

Solar concentrators have been constructed and assessed for well over 100 years, and a large body of knowledge has been accumulated over a range of times and geographical locations. Knowledge of the distribution of light in the focal region is critical to the development of receiver designs for use with these concentrators, and for apportioning figures-of-merit for the quality and performance expected from them. The present study considers the reflective dish type concentrator, which forms one particular subset of what are known as 'point-focus concentrators' (amongst which are included point-focus lenses), and usually have associated with them the highest performance demands. These dishes ideally operate as 'imaging' concentrators, as distinct from the other type of reflective concentrator known as the 'non-imaging' concentrator, the most famous example of which is the Compound Parabolic Concentrator (Welford and Winston, 1979).

The performance sensitivity of dish concentrators arises due to both the very high concentration ratios and collected powers that can be achieved with them. 'Concentration ratio' has two common, but different, definitions (Stein and Diver, 1993):

(i) Optical concentration ratio (CR), defined as the ratio of the intensity (W m^{-2}) at any point in the focal region to the insolation (sunlight intensity) at the time of measurement. (Insolation when used for concentrators is taken as direct beam insolation and measured with a pyrheliometer having a full angular acceptance of approximately 5°.). Peak concentration ratio is the ratio of the peak intensity of a flux distribution to the insolation at the time of measurement.

(ii) Geometric concentration ratio (CR_g), defined as the ratio of the dish aperture area to the area of the focal region on a flat receiver surface, placed perpendicularly to the dish axis. As the focal spot is never a sharp-edged 'step-function' of intensity, focal region area in this case is sometimes assessed to a radial boundary from the centre of the focal spot that contains 90% of the total intercepted power. Sometimes, however, CR_g is expressed as the ratio of the collector aperture area to the receiver aperture area.

Both peak and geometric concentration ratio can be shown to be directly dependent on 5 parameters:

- angular width of the solar source
- rim angle of the concentrator
- dish aperture width
- surface quality of the reflecting surface (measured in milliradian deviation of the actual surface normal vector from the ideal normal vector)
- absolute reflectivity of the reflecting surface

The first three factors can be analysed using the principle of conservation of étendue, and is dealt with by Welford and Winston (1978). A basic description of this principle is instructive for understanding the operation of concentrators in general, and can be

comprehended by considering a simple 2-dimensional concentrator having input aperture width, a_1, and radiation source half-angle of θ_1, with an exit aperture of a_2 and exit half-angle of θ_2, as shown in Figure 1.1 below.

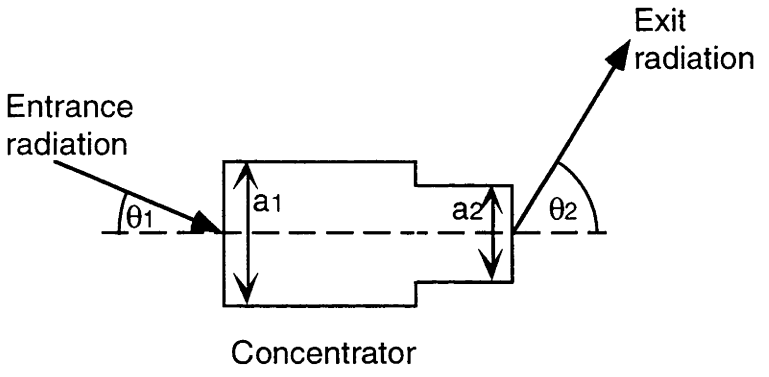

Figure 1.1. General description of entrance and exit radiation for a concentration system.

The principle of conservation of étendue states that, for ***paraxial rays*** (ie. rays close to the axis of the optical system)

$$a_1\theta_1 = a_2\theta_2 = \text{constant} \qquad \textbf{(1.1)}$$

When considering geometric concentration ratio for a point focus dish system, we have,

a_1 = entrance aperture of the dish,
θ_1 = solar half-angle (4.65 milliradian),
a_2 = the extent of the focal spot and
θ_2 = the angular extent of the radiation impinging at the focal spot.

However, these angles are often far from paraxial, and under these conditions it can be shown (Welford and Winston, 1978) that the theoretical geometric concentration ratio for a 3-dimensional concentrating system is given by

$$C_g = \left(\frac{n_2 \sin\theta_2}{n_1 \sin\theta_1} \right)^2 \qquad \textbf{(1.2)}$$

where n_1, n_2 are the refractive indices at the entrance and exit of the concentrator, respectively. The absolute maximum concentration will be achieved when θ_2=90°, ie. $\sin\theta_2$=1. At this point, the maximum concentration ratio will be simply

$$C_g = \left(\frac{n_2}{n_1 \sin\theta_1} \right)^2 \qquad \textbf{(1.3)}$$

These quantities of equation 1.2 are shown in Figure 1.2 for a dish concentrator.

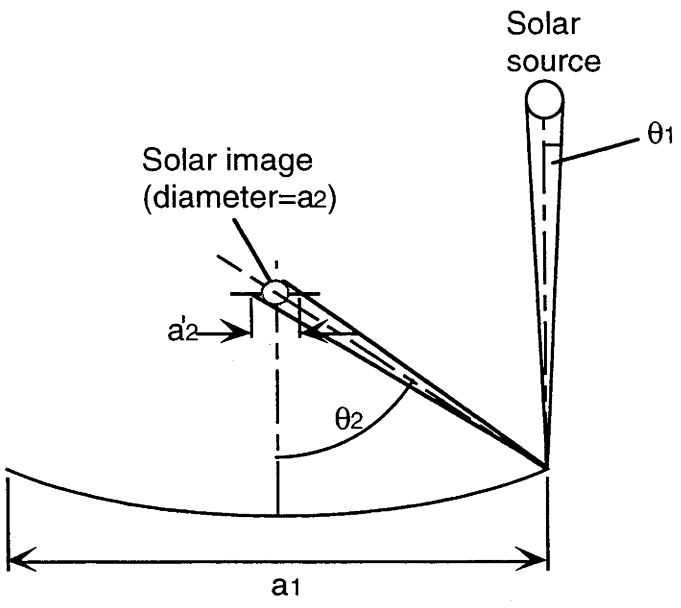

Figure 1.2. Parameters for conservation of étendue on a dish concentrator.

Figure 1.2 shows the sun's image reflected from the edge of the dish (which defines the maximal angular extent, θ_2), which shows θ_2 equals the rim-angle of the dish. The diameter of the sun's image appears as a circle in the focal region of diameter, a_2, but in reality the image is usually projected onto some receiver surface, such as a plane, and the image then intercepts a wider aperture, a'_2, having an elliptical area. This has the effect of reducing significantly the overall geometric concentration ratio. This 'smearing' of the focal spot into an ellipse increases with rim-angle, and is minimal for rays reflected near the vertex (origin) of the dish. As an example, taking the case of a 5 m diameter dish with a rim angle of 70°, the theoretical maximum geometric concentration ratio would be in the order of 40,800 suns. However, as noted by Welford and Winston, this ideal maximum is not achieved by parabolic concentrators, and Rabl (Dickinson and Cheremisinoff, 1980) points out that most concentrators fall short of the ideal by a factor of 2 to 4.

1.2 Overview of focal region measurement and prediction techniques

1.2.1 Focal region measurement techniques

Modern focal region measurement is largely undertaken using videographic flux mapping techniques, whereby a charge coupled device (CCD) video camera captures images of the focal flux projected onto a planar target. These electronic images are then analysed and presented digitally to extract information such as spatial extent, peak concentration and integrated power, etc. Sequences of images taken of focal regions on a target as it is traversed through a focal region can also be used to quantify the focal point of a concentrator. It is appropriate to note in this context that most practical solar concentrators are non-imaging devices, and as such will not produce a true 'focal point', but instead will produce a region having a minimum diameter, sometimes called the region of least confusion. However, it is common to refer to this region as the 'focal point', and this term will be used in the remainder of this monograph refer to the region of least confusion.

Amongst the earliest reports using this technique was a paper by King and Arvizu (1981) which reported the development of a Beam Characterisation System (BCS) for use at the Solar One central receiver plant, and later by Blackmon (1985), who reported that a videographic method was conceived, built and tested by McDonnell-Douglas Astronautics in 1974. Some Russian work (Azimov, et. al., 1986) was also reported, but did not appear to show the same level of development that was reported by Blackmon.

The HERMES system was developed by the Deutsche Forschungsanstalt für Luft und Raumfahrt (DLR, Germany) (Kleih, 1989) and used at the Plataforma Solar de Almeria (PSA) central receiver test facility at Almeria in Spain, and used similar operating principles to the BCS system used at Solar One. HIMAP (Kleih, 1990) was another smaller videographic flux measuring (or 'mapping') system developed by the DLR for use with the Schlaich Bergermann and Partner stretched membrane dishes.

Neumann (1994) discussed a videographic system developed at the DLR which utilises a rotating arm target that moves rapidly through a focal flux distribution. This method has advantages because no elaborate cooling system is required for the target (as it passes through the focal region in approximately 3 seconds), thus reducing a large component of the weight, cost and complexity of the system.

Other methods of measuring focal region light distributions have also been reported. These have included arrays of foil gauge radiometers scanned through the focal regions of concentrators, such as the JPL flux mapper (Starkey and Owen, 1981). These methods are able to measure absolute intensity directly, but require a substantial amount of hardware development and support. Somewhat related to this technique is one reported by Grilikhes (1968) whereby a fibre optic cable (light guide) was scanned through a flux distribution to collect light at well defined grid locations. The light intensity was then measured using a calibrated detector.

In the early 1980's researchers Thomas and Whelan (1981) described measurements attempted using photographic imaging of a full moon projected onto a flat target placed at the focal point of one of the ANU 20 m^2 tiled dishes. Experiments using lunar images were also reported by Grilikhes (1968) and Holmes (1982). Grilikhes' results showed some anomalies in the distribution of radiation which could not be correlated with any specific factors. Holmes' work used the lunar image to simply align heliostat facets and investigate the spatial extent of the focal radiant field. No flux density distributions were reported for this application.
The primary advantages of using a lunar image are that,

- it has a very similar angular width as the solar image, and
- the high heat fluxes associated with concentrated solar radiation, and which require sophisticated cooling and protection apparatus, are avoided.

The dominant disadvantages with lunar imaging are that,

- the moon does not display the same light distribution as the solar disk, and,
- the moon is only full for a few nights per month, and can be obscured by cloud during these brief availabilities.

Numerous calorimetric techniques have been developed (Diver, et. al., 1983; Moeller, et. al., 1980; Tugov and Gladilin, 1985), whereby the temperature rise in a cooling fluid passing through a sensor placed in the focal region is measured to determine the absorbed energy, usually using variable apertures in front of the sensor to assess the flux distribution at different radii from the centre of the distribution. This method is

somewhat limited in its resolution and the time required for a representative scan to be made of the field. It can require complicated position actuation and control mechanisms for placement in the high flux field.

Yamada and Noguchi (1976) reported the use of a digital pyrometer to measure the temperature distribution on a target placed in the focal region of a solar furnace.

Results have recently been reported (Yampolsky, 1995) for an apparently new type of concentrated flux density measurement device, described as a 'passable wire calorimeter'. This instrument uses resistance measurements of a crossed (64x64) array of wires placed in a focal region. Suitable computer data acquisition and post-processing extracts the spatial light intensity distribution across the wire array, assuming a radially symmetric distribution. Non-radially symmetric distributions can be assessed using grids rotated into a larger number of polar orientations in the field. The system is still experimental at the date of writing, and does not appear to offer any significant advantages over videographic imaging.

1.2.2 Focal region prediction techniques

Focal region prediction analysis has generally proceeded on two fronts:

1. Analytical, mathematical modelling, and ,
2. Numerical simulations, using digital computers.

Of course, the numerical simulations utilise a large amount of mathematical modelling, but the derived equations do not, in themselves, allow direct descriptions of the expected light distributions in a focal plane. Instead they must be used in iterative calculations to slowly 'assemble' a flux image.

The analytical methods have used many approaches (Jeter, 1986; Igel and Hughes, 1979; Antonova, et. al., 1986; Bammert, et. al., 1990; Pettit, et. al., 1983; Lipps and Walzel, 1978; Jones and Wang, 1995), with each method usually offering a perceived advantage over another when modelling particular situations or circumstances.

Numerical simulations have generally come under the generic term of ray trace modelling, of which the most popularly used codes are as follows:

1. HELIOS (Vittitoe, Biggs and Lighthill, 1977), an algorithm that uses cone optics concepts for heliostat field and central receiver modelling;
2. CIRCE (Romero, 1994), a derivative of HELIOS for modelling dish type concentrators;
3. MIRVAL (Leary and Hankins, 1979), a Monte Carlo type ray tracer for modelling heliostat fields and central receivers;
4. OPTDSH (Sanchez and Zarza, 1995), a Monte Carlo ray tracer for modelling circular dish concentrators.

All of the above codes are summarised in the useful compendium prepared by Sanchez and Zarza (1995).

1.2.3 Collector surface characterisation techniques

Several investigations of collector surface characterisations have been reported. Amongst the earliest was a laser scanning system designed to measure the surface quality of small reflective dish collectors, and given the name of the 'Leonov Aberrograph' (Tver'yanovich and Madaev, 1973). This involved dual scanning prisms which moved both radially and tangentially across the aperture of a collector, and recorded the position of a reflected laser beam on a photographic plate placed in the focal region of the dish. Another laser characterisation system for parabolic trough concentrators was reported (Butler and Pettit, 1977), and an investigation reported by Pettit (1976) examined the reflected beam profile from specular surfaces, with the aim of determining the slope error introduced by common reflective surfaces used in many solar collectors.

Bendt, Gaul and Rabl (1980) reported a novel method of determining the approximate surface slope error of a concentrator by misaligning the collector slightly away from the sun, and measuring the performance of the receiver under the misaligned conditions. The degree of misalignment was varied, and the relative changes in receiver output could be analysed to extract the probable surface slope error for the concentrator.

Another more recent and more sophisticated concentrator surface quality analyser which utilises a laser scanning/beam detection method is the Scanning Hartmann Optical Test (SHOT) system (Wendelin, Jorgensen and Wood, 1991). Here a laser and a pair of deflection mirrors are mounted near the radius of curvature (the 2f position) of the concentrator, and the beam is scanned across the concentrator surface. The point of intersection of the reflected beam with a planar target is detected and measured using a phase-locked quad-cell tracking unit. From the known direction of the laser beam and the subsequent coordinates of the reflected beam measured on the target, the surface normal information can be calculated, and the surface slope error deduced from this information. The technique is applicable to dish type collectors having f/D ratios (focal length divided by concentrator diameter) that are greater than 0.5.

Grossman (1994) has reported a method described as a '2f' optical performance system for measuring point focus (dish type) solar concentrator surface slope errors. It is a method applicable primarily to concentrators that have an f/D ratio of three or greater. The method utilises patterned and/or colored targets placed at the radius of curvature (or the '2f' position) of a parabolic concentrator, and a CCD camera placed at the same position viewing the reflector surface. The reflected patterns seen by the camera on the concentrator surface are analysed to calculate the surface slope errors that exist in different regions of the collector surface.

1.3 History of focal region measurement and prediction in Australia

The measurement and prediction of focal region flux distributions in solar concentrators has been pursued neither widely nor deeply in Australia. While this information is important in the performance specification of such concentrators, most previous work used mathematical modelling of the expected flux distributions as input data for receivers designed for placement in the focal region.

This situation has arisen primarily because of the relatively small number of high concentration solar collector projects that have been undertaken in this country. In fact, there have been only four research groups that have utilised or developed point-focus concentrators to date (1995):

1. The Solar Energy Research Centre (SERC) at the University of Queensland undertook some investigations using an Omnium-G-OG-7500S paraboloidal dish (Gray, 1993). Focal region flux measurements were performed on this system using a scanning arm mounted with 5 foil gauge radiometers that rotated through the desired region of the focal field, which was an adaptation of the JPL flux mapper Unfortunately SERC closed in 1985 and work with this concentrator ceased.

2. Researchers at the University of Melbourne undertook the Concentrating Receiver and Tracking Absorber (CRATA) project to develop a solar thermal energy conversion system (Charters and MacDonald, 1985). This project utilised a fixed spherical dish concentrator with a tracking cylindrical absorber. Some flux measurements were reported. However, this program was also terminated with no continuation elsewhere.

3. Solar Research Corporation (Melbourne, Victoria) has been pursuing a combined photovoltaic (PV)-thermal high concentration conversion system, with a proposal to frequency-split the incoming solar radiation, with wavelengths suitable for PV conversion being utilised to that end, and the remaining light being used for thermocatalytic conversion of water into hydrogen and oxygen. Their work is ongoing, and uses both a 1.77 m^2 concentrator and a 20 m^2 faceted concentrator (of the same design utilised at the White Cliffs solar power station installed by the Australian National University in the early 1980's). No focal flux measurements have been published from this group, although Lasich (1995) reports that while some rudimentary work has been undertaken in this field, most of their analytical work has been undertaken using a computer raytrace program developed in-house.

4. The most extensive and continuing work on dish concentration systems in Australia has been undertaken by the Energy Research Centre (ERC) at the Australian National University, Canberra. The White Cliffs project (Kaneff, 1991) is perhaps the most well known installation arising from these research and development efforts. This system consists of fourteen 20 m^2 paraboloidal dish concentrators, converting the solar radiation into thermal energy in a water-steam converter. The steam generated was used to power a 25 kW engine connected to an alternator for the production of electrical power. Results were reported by Bannister (1991) for mathematical modelling of the focal flux distribution for these dishes, but no experimental confirmation of these distributions was undertaken. A 400 m^2 'Big Dish' concentrator was then developed by the ERC under the direction of Professor S. Kaneff (Kaneff, 1993; Kaneff, 1994, Kaneff, 1997), with the concentrator going 'on sun' in May 1994 (Johnston, 1995a). Appendix 1.2 contains the specifications for this device.

From the small amount of published material on the focal region characterisations of most of the concentrators used by the above-mentioned groups, it was considered appropriate to undertake a research program in this area in an attempt to develop a state-of-the-art resource base that could provide expertise, tools and information for future performance assessments of Australian based solar concentrator developments.

1.4 Outline of the present work

This thesis details the algorithms and techniques developed to both measure and predict the focal flux distributions for both a 20 m^2 White Cliffs dish, and the 400 m^2 Big Dish at the Australian National University.

Three areas of development have been pursued during of the course of this PhD programme:

(i) Empirical measurement of the focal regions of the 20 m^2 and 400 m^2 dishes;

(ii) Development of appropriate computer ray-trace algorithms to model the expected flux distributions in the focal regions of these dishes;

(iii) Implementation of close-range photogrammetry to characterise the reflecting surfaces, such that predictive ray-trace modelling could be performed based on the shape of the actual concentrator contours.

These three research streams have been brought together to establish a suite of expertise, tools and information that the author believes can provide a basis for future developments and enhancements in this important field.

The thesis chapters and their content are laid out in the following sequence:

Chapter 1 (the present chapter) outlines the background to solar concentrator focal flux measurement and prediction, and describes previous work undertaken by other researchers in the field that bears some relationship to the studies undertaken in the present thesis;

Chapter 2 discusses the techniques employed and the measurements gained from the videographic flux measurements of the focal regions of the 20 m^2 and 400 m^2 dishes;

Chapter 3 describes the development of the ray trace algorithm COMPREC, and presents the results of performance tests undertaken in comparison with other ray tracing codes.

Chapter 4 reports the results of a comparison between the measured videographic flux images recorded in chapter 2, and predicted flux distributions calculated using COMPREC for simulated dishes having similar characteristics as the actual 20 m^2 and 400 m^2 dishes;

Chapter 5 introduces concepts and techniques used to apply close-range photogrammetry to the measurement of surface coordinates of the dish surfaces. Results of measurements and preliminary assessments of surface quality are also recorded here;

Chapter 6 presents more advanced methods of surface quality assessment using the photogrammetrically measured concentrator surface data. Surface normal assessment

and surface slope error measurement and analysis of the data presented in chapter 5 are also undertaken here;

Chapter 7 describes the results of ray trace predictions of the focal flux distributions of the 400 m^2 dish mirror surfaces using the analysed surface data obtained from the photogrammetric measurements and the surface normals calculated from this data using the results and methods described in chapters 5 and 6, respectively.

Chapter 8 provides an overview of, and conclusions for the results obtained in the study.

1.5 Research Environment

Most of the experimental work presented in this thesis was undertaken using the facilities of the Energy Research Centre, currently a division of ANUTECH at the Australian National University. All solar concentrator work was undertaken using both paraboloidal dish concentrators that were available in the Centre. Figure 1.3 shows the 20 m^2 dish.

Figure 1.3. 20 m^2 tiled dish at the Energy Research Centre, Australian National University.

This device has a nominal diameter of 5 m (actual diameter = 5.097 m), circular aperture concentrator, covered with approximately 2,300 flat, back-silvered 'green' glass mirror tiles. The tiles have an average dimension of 9 cm on a side (the sizes vary according to their radial position on the dish - tiles closer to the vertex have narrower widths, although their depths remain constant at 104 mm). Average (clean) mirror reflectivity is approximately 75%. The unit has a nominal focal length of 1.8 m, and was completed in 1982. Sun tracking is accomplished by alt-azimuth drives using closed-loop feedback control from a sun-sensor incorporating four photo diodes and a 'shadow stick'.

Figure 1.4 shows the 400 m^2 'Big Dish', completed in December 1993, and first placed 'on-sun' in May 1994.

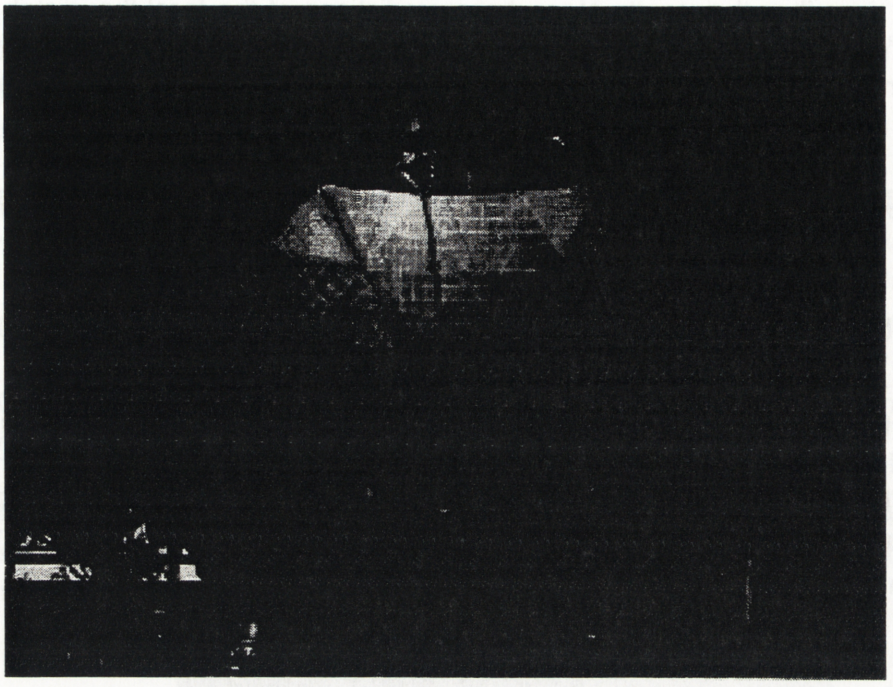

Figure 1.4. 400 m^2 'Big Dish' at the Energy Research Centre, Australian National University.

The 400 m^2 dish is a hexagonal aperture concentrator, having a nominal focal length of 13.1 m, and is comprised of 54 triangular mirror panels mounted on a space-frame sub-structure. The space-frame is constructed of tubular steel members bolted at their ends to steel nodes to form a self supporting array of tetrahedral units. The mirror panels are of a glass-foam-sheet metal sandwich construction, with the mirrors comprised of 30 cm or 60 cm square, back-silvered 2 mm thick 'green' glass tiles. The tiles have been elastically deformed to approximate the paraboloidal curvature required according to their position on the dish surface. Mounting of receivers and experimental apparatus in the focal region is accomplished by mounts provided on the end of a centrally mounted steel pole, supported by 8 steel guy wires attached to the perimeter of the dish. Sun tracking is accomplished by a hydraulically actuated alt-azimuth drive system using a computer based open loop control system.

Computing facilities at the School Computer Unit of the Research School of Physical Sciences and Engineering were utilised extensively for the characterisation studies, with the majority of programs written during the course of the research being compiled for DEC5000 machines running ULTRIX (a DEC version of UNIX). Numerical analysis programs such as MATLAB and Interactive Data Language (IDL) were also used within this environment.

2. Videographic Flux Mapping

2.1 Introduction

While section 1.2 described a number of techniques that have been used to measure focal region flux distributions, it was considered that videographic flux mapping offered the greatest utility and wealth of information above the other methods. The ready availability of CCD camera equipment and image processing facilities to the author also facilitated the choice of videographic imaging. This chapter describes the application of videographic flux mapping to the focal regions of the 20 m^2 and 400 m^2 dishes.

2.1.1 Investigations using the 20 m^2 tiled dish

A preliminary videographic technique was developed using the 20 m^2 (5 m diam.) tiled dish (described in §1.3). A flat, water cooled copper disk, 0.5 m in diameter was coated with a matt, high temperature resistant white paint. A foil gauge radiometer[1] was mounted in the centre of the disk, such that incident radiation fell on its active face. (The radiometer had been calibrated by HyCal Engineering just prior to the reported measurements. See Appendix 2.1) The water cooled target and radiometer assembly was mounted in the focal region, such that its position could be adjusted along the axis of the dish. Figure 2.1 and Figure 2.2 show the water cooled target with foil gauge radiometer, and the dish projecting a flux image onto the water-cooled target, respectively.

Figure 2.1. Water cooled target used for flux mapping mounted in place on the 20 m^2 dish. Foil gauge radiometer shown at the target centre.

[1]HiCal calorimeter. Model C-1312-A-300-072. HiCal Engineering, 9650 Telstar Ave., El Monte, California. CA 91731. USA. Calorimeter calibrated by HiCal in 1993.

Figure 2.2. Flux image projected onto water-cooled target at the focal point of the 20 m^2 tiled dish.

It was not possible to acquire a dedicated computer/frame grabber for the acquisition of video images directly from the camera during the course of the research. Instead, output from the camera was recorded on a Super VHS high-resolution video cassette recorder (VCR)[2], and the recorded images were later captured and digitised using a 7-bit frame grabber card installed in a Sun Sparc Station computer. Ideally, it would have been most desirable to have captured camera images directly to file through a frame grabber card utilising at least 8 bits of gray-scale digitisation. However, Neumann (1994) presents an analysis which indicates that using a 7 bit frame grabber and utilising a 50% dynamic range (ie. the peak measured intensity covers 50% of the maximum possible intensity recorded by the camera), then an uncertainty of approximately 4% in the overall integrated power under the measured flux distribution can be expected. It was considered that this level of precision was acceptable considering the limitation on equipment and funds that were available. In the following calculations using video image data, this uncertainty figure of 4% has been used, with an additional 1% allowed for the uncertainties introduced by the linearity corrections applied to the CCD array data (discussed in the next section). Figure 2.3 shows the schematic layout of the system used to flux map the focal region of the 20 m^2 dish.

[2]Panasonic Super VHS (PAL) video cassette recorder, model NV-FS100HQ.

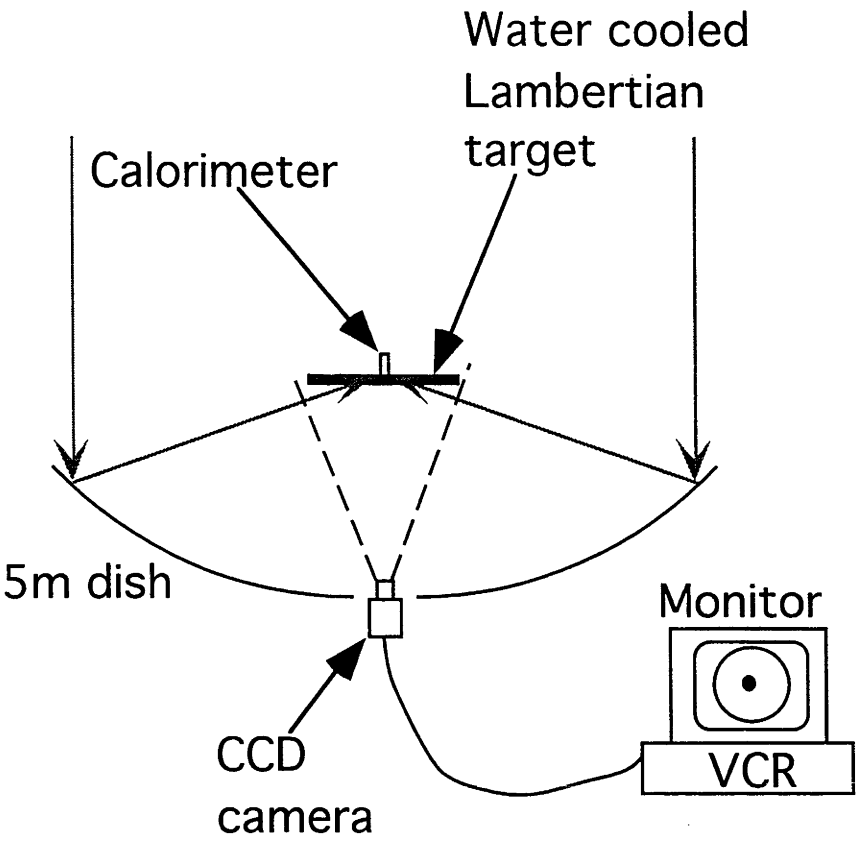

Figure 2.3. Equipment arrangement for measuring focal images for the 20 m^2 dish.

2.1.2 Camera calibration and linearisation

The linearity response of the CCD camera was measured using a set of calibrated neutral density filters placed in front of the camera while it was viewing an illuminated screen. This allowed the pixel response of the camera to be calibrated and used to correct measured images for CCD array non-linearities. Actual flux image correction involved fitting a 7th order polynomial to the inverse response curve as a function of neutral density filter transmissivity, and using this response curve to linearise the intensities measured by the camera. Appendix 2.2 describes the relationships used to effect both pixel linearisation and calibration.

The spatial linearity of the camera and lens system was also checked by capturing images of a screen having a 2x2 cm grid drawn on it, and measuring the position of the grids in the camera image. These measurements indicated that the camera and lens had an excellent spatial linearity response. Appendix 2.3 contains the results of these measurements.

2.1.3 20 m^2 dish flux image measurement

To avoid saturating the CCD camera with the bright focal spot images, three high density filters were placed in front of the camera lens to reduce the amount of reflected light passed to the camera. Absolute calibration of the flux images collected by the camera/filters/VCR/frame grabber system was accomplished by using the output signal

from the foil gauge radiometer together with the calibration/linearisation relationships (Appendix 2.2) to scale the digital images using the average of an annular ring of pixels immediately surrounding the image of the radiometer in the flux image. Intensities were also normalised to an insolation level of 1000 W m^{-2}.

2.1.4 20 m^2 dish flux image results

Figure 2.4 and Figure 2.5 show smoothed cross-sections through some flux distributions measured at a range of positions from the dish vertex. It should be noted that normally the image of the (black) radiometer in the centre of the target produces a 'drop-out' in the middle of the captured flux images. This radiometer image has been removed in the following figures by replacing the 'dark' values of the drop-out with a uniform value corresponding to the average of the pixel intensities adjacent to the radiometer image.

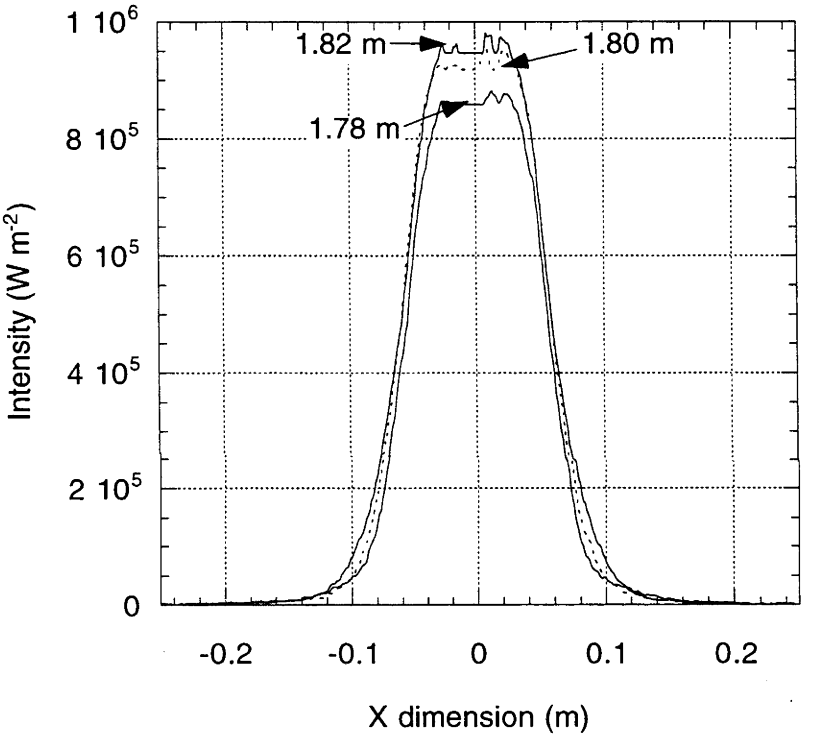

Figure 2.4. Smoothed flux cross-sections measured on the 0.5 m diameter water cooled target placed at 1.78 m, 1.80 m and 1.82 m from the vertex of the 20 m^2 dish (intensities normalised to 1000 W m^{-2} insolation).

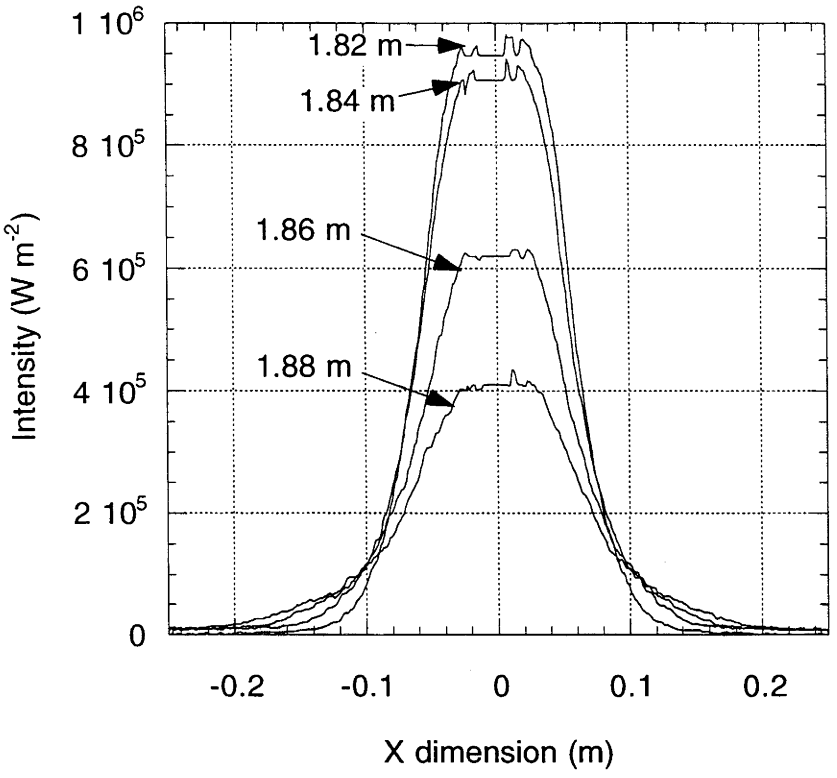

Figure 2.5. Smoothed flux cross-sections measured on the 0.5 m diameter water cooled target placed at 1.82 m, 1.84 m, 1.86 m and 1.88 m from the vertex of the 20 m^2 dish (intensities normalised to 1000 W m^{-2} insolation).

A range of parameters were also measured at the time of the flux measurements. These were:

1. Target cooling water input and output temperatures;
2. Target cooling water flow rate (using a container and stop watch method);
3. Direct beam insolation;

The target input/output temperatures and flow rate were used to calculate absorbed power on the target, while the direct beam insolation was used to scale the measured flux distribution to correspond to a normalised value of 1000 W m^{-2}.

Table 2.1 presents the results used for the calculation of integrated power, dish reflectivity and absorber reflectivity, obtained through numerical integration of the corrected CCD flux image and cold water calorimetry on the target placed 1.82 m from the dish vertex.

Table 2.1. Data calculated from videographic flux mapping and target calorimetry of the 20 m^2 dish taken with the target at 1.82 m from the dish vertex.

Parameter	Value	Uncertainty	Unit	Basis of uncertainty
Integrated Flux Power				
Insolation	920	45 (5%)	W m^{-2}	Note 1 (see list below)
Peak Radiometer Intensity	854	26 (3%)	kW m^{-2}	Note 2
Peak concentration	970	55	suns	Note 3
Intercepted dish aperture power	20.1	0.9 (5%)	kW	Note 4
Integrated power under flux distribution	14.8	1.1 (8%)	kW	Note 5
Estimated dish reflectivity	74	7 (9%)	%	Note 6
Target calorimetry				
Cooling water inlet temperature	24.1	0.1	°C	Note 7
Cooling water exit temperature	31.1	0.1	°C	Note 7
Water flow rate	86.2	0.8 (1%)	(g s^{-1})	Note 8
Absorbed target power	2.52	0.06 (2%)	kW	Note 9
Target reflectivity	83.0	8 (10%)	%	Note 10

Bases for uncertainty calculations

Note 1. 5% manufacturers error stated for pyrheliometer.
Note 2. 3% manufacturers error stated for radiometer.
Note 3. Propagation of errors (pyrheliometer error, radiometer error)
Note 4. Propagation of errors (pyrheliometer error, dish aperture error).
Note 5. Propagation of errors (digitisation error, radiometer error).
Note 6. Propagation of errors (Dish aperture power error, integrated flux power error). No measurements of actual dish reflectivity were taken at the time of flux measurements.
Note 7. Digital thermometer error.
Note 8. Propagation of errors (water mass, time period).
Note 9. Propagation of errors (temperature, mass flow rate, specific heat).
Note 10. Propagation of errors (absorbed target power error, integrated flux power).

One of the most succinct and revealing presentations of circular symmetric flux distribution data is to look at the percentage of total radiation that is contained within a specified radius from the centre of the distribution. Figure 2.6 and Figure 2.7 show the percent-power-in-radius (PIR), as a function of radius, for the flux distributions measured in Figure 2.4 and Figure 2.5. PIR is calculated as a percentage of the integrated power (14.7 kW) measured under the 1.82 m flux distribution. The 1.82 m position is used as a reference because it will contain the highest ratio of intercepted flux, as it has the narrowest distribution. Other focal positions may not have as high a intercepted power due to increased radiation spillage at the edges of the target.

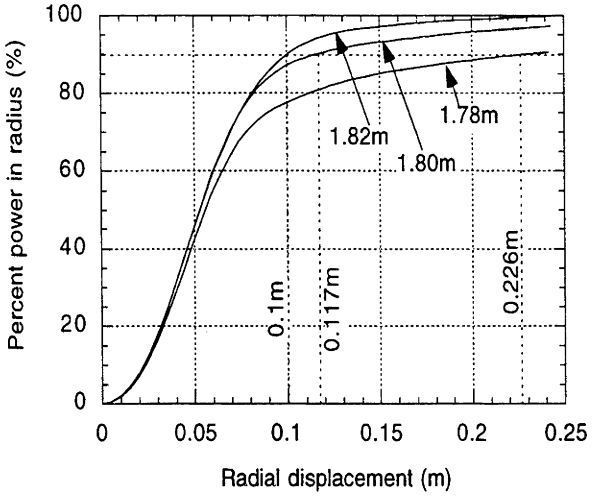

Figure 2.6. Percent power in radius (PIR) for flux distributions measured at 1.78 m, 1.80 m and 1.82 m from the 20 m^2 dish vertex. (Nominal dish focal length =1.81 m.)

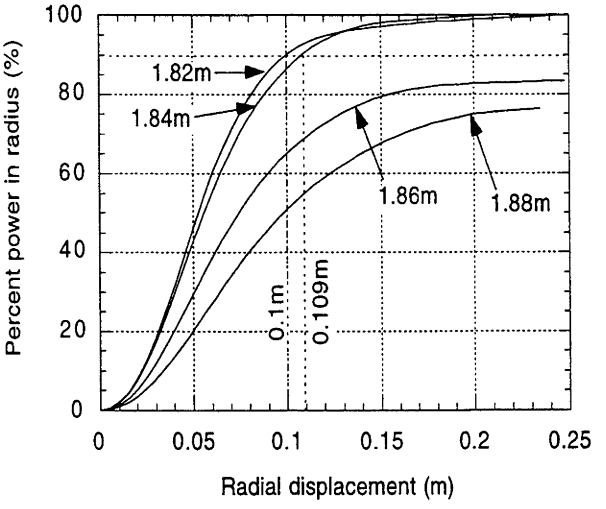

Figure 2.7. Percent power in radius (PIR) for flux distributions measured at 1.82 m, 1.84 m and 1.86 m and 1.88 m from the 20 m^2 dish vertex.

If it is desired to identify the flux distribution that has the 'tightest' distribution of power in the focal spot, then this can be seen immediately from the PIR plot having the steepest slope. From these plots the radius that contains 90% of the total target power can also be quickly determined, and is indicated on the appropriate curves in Figure 2.6 and Figure 2.7.

2.1.5 Discussion of 20 m^2 tiled dish results

A noticeable feature of Figure 2.4 to Figure 2.7 is the apparent non-uniform spacing between the flux curves as the target is moved through equally spaced (2 cm) positional increments. This is particularly noticeable in the difference between the 1.80 m to 1.82 m positions and the 1.82 m to 1.84 m position. This effect occurs because the actual focal point is at 1.812 m (calculated in section 5.4.1.3, Figure 5.6), which means that the 1.82 m position is closest to the actual focal point (and indeed shows the highest peak flux and narrowest spread), but the 1.80 m position is also quite close, and thus will show a close approximation to the 1.82 m flux. The 1.84 m position is actually quite removed from the focal point, and shows a significant degradation due to this fact. The rapidity of change in the flux distributions with changes of only several millimetre in the target position derives from the large rim angle (70°) of the dish. Such large rim angles

create highly localised focal spots, due to the high convergence angles of the reflected beams from the edge of the dish.

It is apparent from Figure 2.4 and Figure 2.5 that the distributions at 1.80 m and 1.82 m appear to be somewhat 'flat topped', even though this effect is somewhat accentuated by the replacement of the radiometer image in the centre of these distributions with a uniform intensity value. This effect is indeed confirmed by the ray trace modelling presented in chapter 4. However, the removal of the radiometer image in the flux images further away from these positions gives the tops of these distributions a flatter appearance than they have in reality. This anomaly arises because of the relatively large area occupied by the radiometer compared to the area of the central region of the flux distributions.

Total integrated power values from the videographic images have uncertainties in the order of 10%. Considering the techniques used to capture and process the flux images, this figure rates well, particularly in comparison with similar figures quoted by other researchers (Seitz, 1995; Monterreal, 1995).

The peak concentration ratio of 970 suns (read directly from Figure 2.4) is calculated as a ratio of the intensity measured by the target radiometer to the insolation measured by the pyrheliometer. This figure will be dependent on the dish reflectivity. Concentration ratio will decrease linearly with reflectivity.

The estimated dish reflectivity of (74 $\pm$ 7)% is calculated as a ratio of the integrated power under the videographic flux distribution to the collected power in the dish aperture. The absolute accuracy of this figure will depend on both the uncertainties in the measured parameters, as well as the proportion of flux intercepted by the target. If the target does not intercept the significant majority of radiation arriving at the focal point, then this ratio will be a measure of the target interception factor and dish reflectivity, and not that of the dish reflectivity alone. Visual inspection of the distributions of radiation shown in Figure 2.4 and Figure 2.5 appears to confirm the impression that the target indeed intercepts the vast majority of incident radiation. Unfortunately, no mirror reflectivity measurements were taken at the time of the flux measurements.

The cold water calorimetry calculations for the target indicate that only approximately 17% of the incident radiation on the target is absorbed, with the rest presumably reflected away. This indicates that the white matt paint used to coat the target has a reflectivity of approximately 83% (calculated as a ratio of the absorbed target power (2.52 kW) to the integrated flux image power (14.8 kW).

2.2 Investigations using the 400 m^2 dish

The technique used to measure the flux distributions on the 400 m^2 dish was conceptually the same as that used with the 20 m^2 dish. However, due to time restrictions imposed by the operating schedule of the 400 m^2 dish, only one day was allocated for the collection of flux images. This imposed severe limitations on the experimental flexibility that could be employed while collecting flux images, and on the ability to recheck or redo measurements if the initial results proved anomalous.

2.2.1 400 m^2 dish experimental arrangement

A new water cooled target was fabricated, and the CCD camera was mounted in a specially made water cooled jacket, to protect it from the higher (back radiation) intensities that exist near the 'Big Dish' focal region. The water cooled target was an aluminium sandwich structure, 1.2 m square, 0.025 m thick, with 20 mm channels welded and riveted internally to provide a structured pathway for the cooling water to pass through the device. The target surface facing the focal flux was painted with the same matt-white, high temperature paint that was applied to the 0.5 m diameter target used with the 20 m^2 dish. The radiometer was mounted in the centre of the target for flux calibration. Figure 2.8 and Figure 2.9 show the internal construction of the target and the water cooled target mounted on the central tower and special 'quadripod' support legs used to mount objects in the focal region of the 400 m^2 dish, respectively. Figure 2.10 shows the target in the focal position of the 400 m^2 dish.

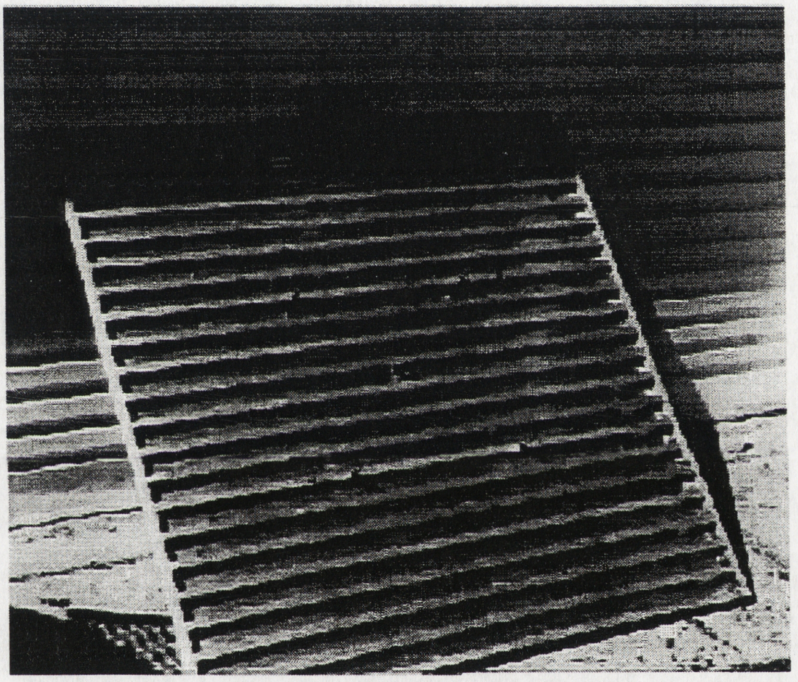

Figure 2.8. Internal construction of aluminium water-cooled target used for flux mapping the Big Dish.

Figure 2.9. Aluminium water-cooled target mounted on quadripod support for placement in the focal region of the Big Dish. The apparent 'dappled' appearance of the target surface shows the bare aluminium surface before painting with the matt white surface paint.

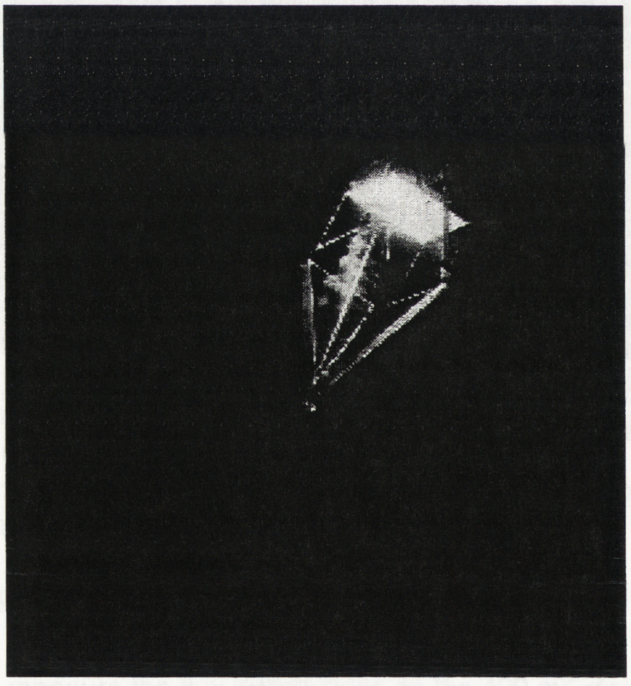

Figure 2.10. Flux image projected onto the water cooled target at the focal point of the 400 m^2 dish.

Figure 2.11 shows a schematic layout of the equipment used with the 400 m^2 dish flux map experiment.

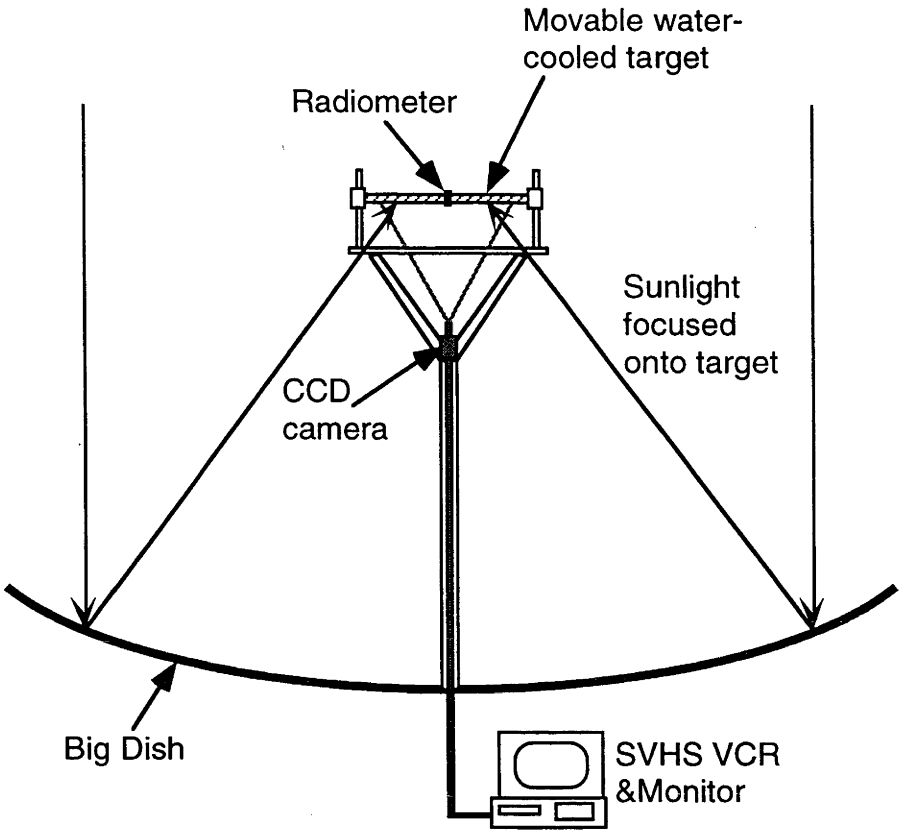

Figure 2.11. Equipment layout used for flux mapping the 400 m^2 dish.

Water flow through the target at the time of flux capture was measured using the 'container and stop-watch' technique. Output signals from the inlet and outlet target water temperatures (measured using thermocouples) were recorded continuously, as were the radiometer and tracking pyrheliometer output signals.

The target position was controlled by an electric motor and gearbox which pulled/released four guy-wires mounted through pulleys at the corners of the target. This allowed movement along the four corner guide posts that also supported the target. Absolute target position was established by painting a sequence of black and white bands, each 10 cm long, on one of the guide posts. The position of the target guide ring on the guide post could be assessed visually by comparing its relative position to the black and white bands. Figure 2.12 shows this arrangement.

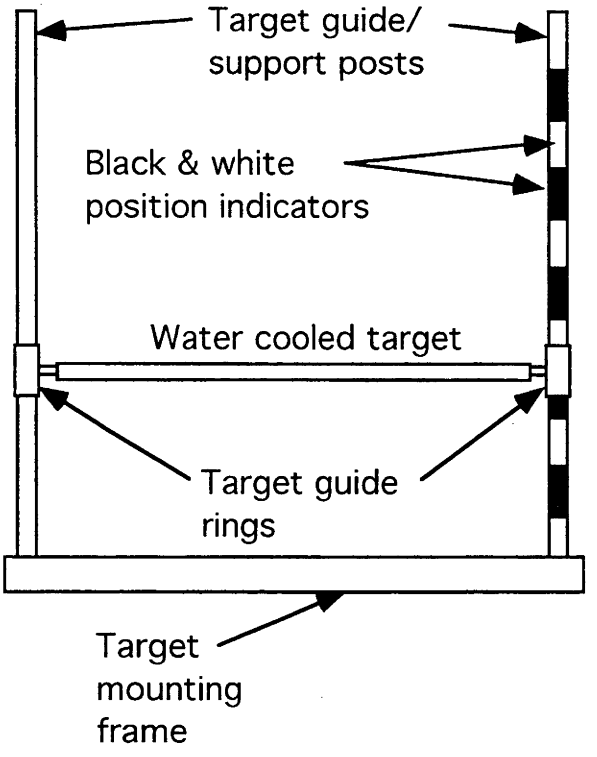

Figure 2.12. Position detection method for the 1.2 m water cooled target.

2.2.2 Difficulties encountered with 400 m^2 dish measurements

The position indicators allowed fairly accurate observation of the target position (± 5 mm) under workshop test conditions. However, under on-sun viewing conditions, the excessive brightness of the focal spot on the target (even when viewed through a high density filter) made observation of the black and white position indicators difficult. This introduced an uncertainty in the target position of approximately 30 to 40 mm. While this was considered to be an unsatisfactory level of accuracy, time restrictions did not allow for the development of a new position sensing system.

Checking the mounting position for the target support frame after the measurements were completed indicated a misplacement of the target frame by 40 mm. This meant that positioning the target at the nominal positions of 12.7, 12.8, 12.9, 13.0, 13.1, 13.2, 13.3 and 13.4 m actually placed the target at positions 40 mm below these values, that is, at 12.66, 12.76, 12.86, 12.96, 13.06 13.16, 13.26 and 13.36 m. (This misplacement was found to be advantageously offset through later photogrammetric assessments of the 400 m^2 focal length to be 13.075 m (section 5.4.3.3). This meant that the actual positions of the target were now only 15 mm below the focal point.) Due to an oversight during collection of flux images, the nominal 13.3 m (actual 13.26 m) target position was omitted, and images for this position do not appear in the flux distributions presented in the next section.

Some 5 minutes after pointing the dish 'on sun', it was noticed that the three high density filters in front of CCD camera had cracked, due to high temperature gradients induced in the filters by high levels of back radiation reflected from the water-cooled target. Camera body temperature showed no adverse heating due to this event, but the captured flux images display characteristic light leakages through the cracked filters. Fortunately, the

cracks passed through one side of the images, and not through the centres. This allowed some recovery of information by reprocessing the images at a later stage. It was clear that the use of absorption filters for light reduction under such high power levels was not a practical exercise, and that glass substrate metal reflective filters would have been much more desirable. Unfortunately, such filters were unavailable at the time of the tests, and measurements had to continue using the cracked filters.

2.2.3 Flux image results

Figure 2.13 shows an image of the flux distribution measured at the 13.1 m focal position. Figure 2.14 shows a surface plot of the light intensities shown in Figure 2.13. Both images show the high light levels beside the main flux distribution arising from the cracked filters.

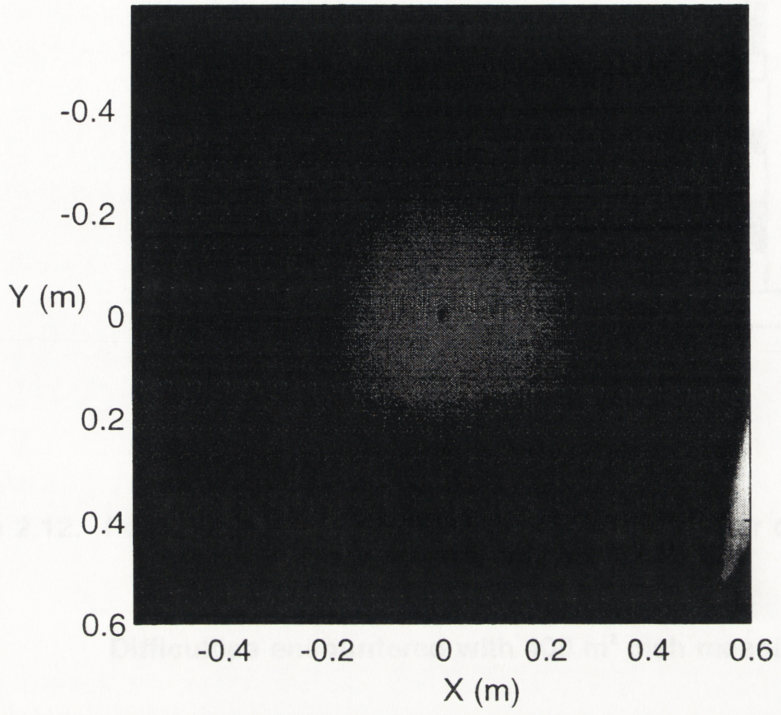

Figure 2.13. Light distribution in the focal region at 13.1 m from the vertex of the 400 m^2 dish.

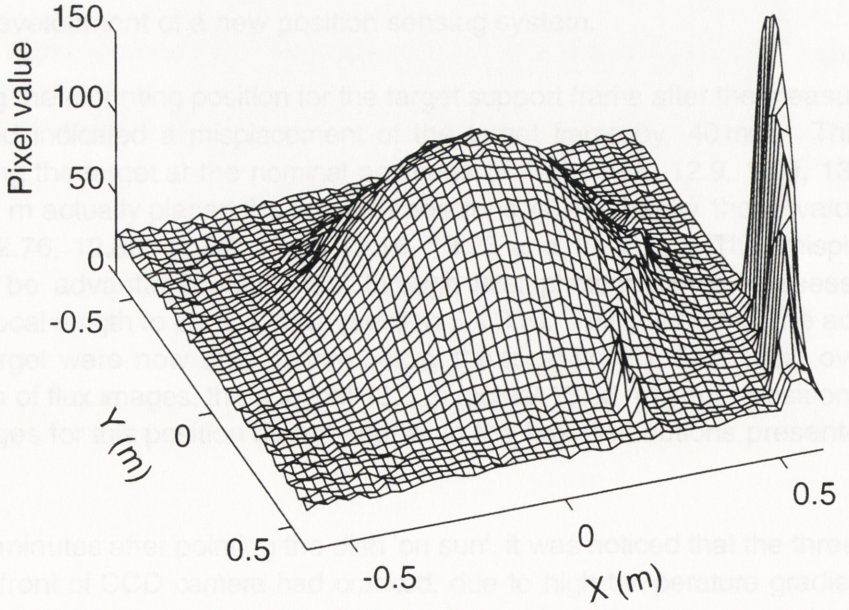

Figure 2.14. Surface plot of the light distribution shown in Figure 2.13.

The captured flux images were processed to remove the image of the black radiometer in the centre of the target, and to correct for camera non-linearity. The images were scaled and calibrated according to the readings taken from the foil gauge radiometer mounted in the target, and intensities were normalised to an insolation level of 1000 W m^{-2}. To allow realistic integrated power calculations to be performed, use was made of the strong circular symmetry apparent in the majority of the flux distributions, and the left half of the image was duplicated and 'flipped' into the position of the right half. This created an image that was free from the spurious light signals arising from the cracked lens filters.

Figure 2.15 and Figure 2.16 show (smoothed) cross sections through these flux density distributions measured videographically for the 400 m^2 dish.

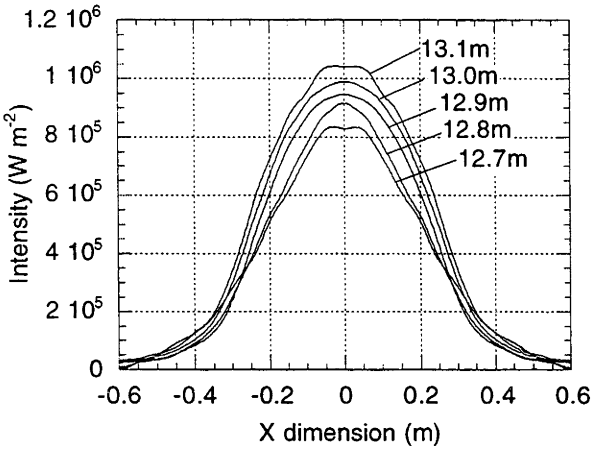

Figure 2.15. Flux distribution cross sections measured at nominal positions of 12.7 m, 12.8 m, 12.9 m, 13.0 m and 13.1 m from the 400 m^2 dish vertex. (Nominal dish focal length = 13.1 m.)

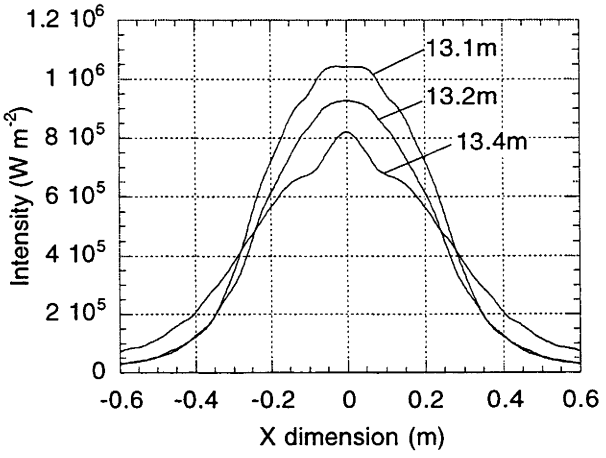

Figure 2.16. Flux distribution cross sections measured at nominal positions of 13.1 m, 13.2 m and 13.4 m from the 400 m^2 dish vertex.

Figure 2.17 and Figure 2.18 show the percent power in radius (PIR) plots for the flux distributions shown in Figure 2.15 and Figure 2.16, respectively. PIR is calculated as a percentage of the integrated power measured under the 13.1 m flux distribution.

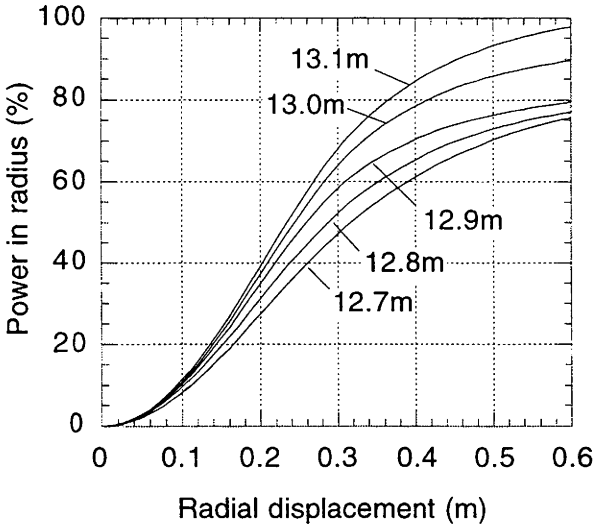

Figure 2.17. Percent power in radius (PIR) for flux distributions measured at nominal positions of 12.7 m, 12.8 m 12.9 m, 13.0 m and 13.1 m from the 400 m^2 dish vertex. (Nominal dish focal length = 13.1 m.)

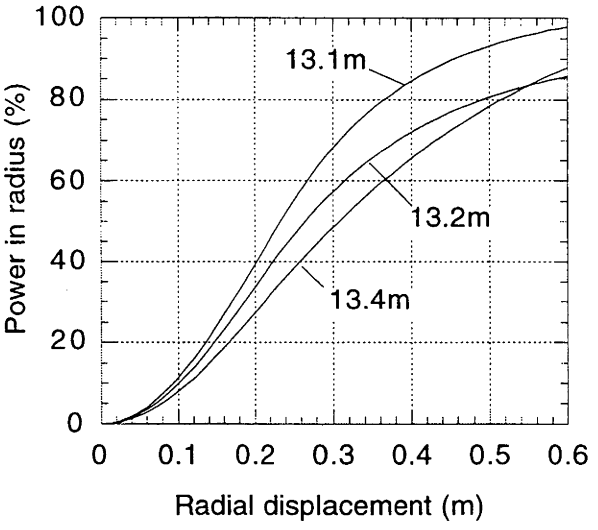

Figure 2.18. Percent power in radius (PIR) for flux distributions measured at nominal positions of 13.1 m, 13.2 m and 13.4 m from the 400 m^2 dish vertex.

Table 2.2 presents the results used for the calculation of integrated power, dish reflectivity and absorber reflectivity, obtained through numerical integration of the corrected CCD flux image and cold water calorimetry on the target placed 13.1 m from the dish vertex.

Table 2.2. Data calculated from videographic flux mapping and target calorimetry of the 400 m^2 dish, taken with the target 13.1 m from the dish vertex.

Parameter	Value	Uncertainty	Unit
Integrated Flux Power			
Insolation	870	43 (5%)	W m^{-2}
Peak radiometer Intensity	905	27 (3%)	kW m^{-2}
Peak concentration	1040	60 (6%)	suns
Intercepted dish aperture power	344	17 (5%)	kW
Integrated power under flux distribution	241	19 (8%)	kW
Dish reflectivity	70	7 (10%)	%
Target calorimetry			
Cooling water inlet temperature	16.0	0.1	°C
Cooling water exit temperature	39.2	0.1	°C
Water flow rate	491	(1%)	(g s^{-1})
Absorbed target power	47.7	1.0 (2%)	kW
Target reflectivity	80.3	1.4 (8%)	%

2.2.4 Discussion of 400 m^2 Dish Results

Review of Figure 2.15 and Figure 2.16 show that the distributions display an approximately Gaussian form. Figure 2.17 and Figure 2.18 reveal consistent PIR curves, except for the 13.4 m position, where the skirts of the distribution appear to contain more power than that shown in the 13.2 m distribution. This apparent anomaly also appears in the flux cross section for the distribution, shown in Figure 2.16, where the tails of the distribution show noticeably higher values than either the 13.1 m or 13.2 m distributions. It was considered that this deviation was most likely due to a target positioning error, and further analysis of the data associated with this image was not undertaken.

Reference to

Table 2.2 indicates that the peak concentration is 1070 suns, which will vary with dish reflectivity. The reflectivity appears to be in the order of 70% (assuming that the target intercepts a significant majority of the focal region radiation at 13.1 m from the dish vertex). An independent measurement of mirror reflectivity was carried out on the dish surface at the time of the flux measurements. 18 points were chosen randomly across the dish surface and a pyrheliometer was used to measure the insolation and then the reflected intensity at each point. For the reflected intensity measurements, the pyrheliometer was mounted less than 5 cm from the mirror surface, in order to minimise the concentrating effect of the curved mirror surfaces. Figure 2.19 shows the reflectivity versus data point index from these measurements.

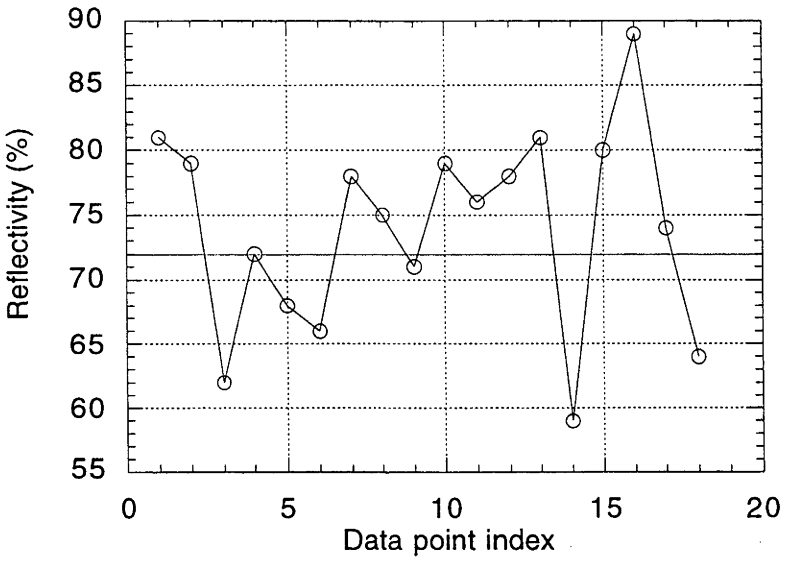

Figure 2.19. Reflectivity versus data point index for 18 readings taken across the surface of the 400 m² dish.

The data in the foregoing figure show a high degree of variation. This was due to the fact that the dish had not been cleaned for several days before the readings were taken, and some regions showed a higher degree of dust deposition than others. These readings showed an average dish reflectivity of 72% with a standard deviation of 7%. These figures support the reflectivity value calculated from the flux measurements.

2.3 Discussion of flux map results

The foregoing results and analyses of the videographic flux measurements for the 400 m² dish provide the experimental data and framework against which the ray trace modelling and photogrammetric surface analysis can be compared in the following chapters. The key results for both dishes are contained in Table 2.1 and

Table 2.2, with Figure 2.4 and Figure 2.15 providing visual descriptions of the most important focal flux distributions for the 20 m^2 and 400 m^2 dishes, respectively.

Dominant sources of error in the videographic flux mapping process arose from the limited (7 bit) intensity resolution of the video framegrabber used to digitise the flux images, as well as the uncertainty in the positioning of the flux target used to measure the 400 m^2 dish flux distributions. Some error was also introduced in the removal of spurious light signals contained in the 400 m^2 flux images (due to the light leakages in the images from the cracked filters used with the CCD camera), although the apparent symmetry of the images mandates that this error should be small.

3. Computer Ray Trace Modelling

3.1 Introduction

The previous chapter described the results of videographic measurements of the focal region flux distributions for the 20 m^2 and the 400 m^2 dishes. The present chapter presents the development and features of a computer based ray trace algorithm that is used to numerically simulate focal flux distributions for concentrators having a range of input specifications. The following chapter compares the empirical measurements of chapter 2 with simulated fluxes predicted using the ray trace code described in the present chapter.

3.1.1 Ray trace requirements and existing programs

A number of ray trace codes have been written by various researchers. Each program has usually been developed for specific applications, such as focal region modelling for heliostat/central receiver systems, point focus dishes, secondary concentration devices or parabolic trough systems. Sanchez and Zarza (1995) provide an excellent compendium of commonly available programs in use for a range of different solar thermal modelling needs, including ray tracing. It is not the purpose of the current project to provide a critique of each of these algorithms. However, in the first year of the author's investigations, such a compendium was unavailable, and knowledge of available ray trace codes was gained from reading the literature, with further 'leads' being gained through personal communication with the respective authors/researchers.

Parameters in the author's research environment mandated that a ray trace algorithm should be able to:

1. Model point focus dish solar concentrator configurations having both circular (20 m^2 dish) and hexagonal (400 m^2 dish) apertures;
2. Model reflective surfaces composed of 2300 small, flat mirror tiles (20 m^2 dish), as well as elastically curved mirror surfaces (400 m^2 dish) and arbitrarily defined numerical surfaces (such as photogrammetrically characterised surfaces);
3. Model primary flux on different receiver geometries and orientations placed at specified coordinates in the focal region;
4. Model reflecting surface slope errors;
5. Model dish pointing errors;
6. Model different sunshapes;

Other criteria can be assessed, but the above were considered to be of primary interest considering the concentrators available to the author. A ray trace code dubbed PSF (acronym for Primary Solar Flux) had been developed previously at the ANU (Bannister, 1991) to model the flux distributions expected at the focal point of the 20 m^2 tiled dish, and this was investigated for its suitability according to the above criteria. It was found to only allow modelling of the unique architecture of the 20 m^2 dish, did not allow for the incorporation of surface slope errors, and could not model dish pointing errors and different sunshapes. Its output was utilised in the present study to compare with the

output of the ray trace code that was later developed by the author under identical input conditions, as a preliminary reference, but beyond this it was not utilised.

It became apparent that CIRCE2 (Romero, 1994) and OPTDSH (Wendelin, 1991), two established and well respected codes, might be able to provide the type of modelling required by the above criteria. However, it required many months before either of these programs could be delivered to the author, and it was considered advantageous to develop a ray trace program within the ANU environment, and such a project was begun. The algorithm was dubbed 'COMPREC', an acronym for COMPound RECeiver, as it was designed to model receivers composed of a number of different geometries. Overall, the program satisfies the majority of the criteria described above, although it was decided that modelling receivers having different tilt angles/orientations was not a necessary requirement for the types of simulations envisaged for the project.

As CIRCE2 and OPTDSH became available, it became clear that they could not accommodate the requirements dictated by the 2300 flat mirror tiles on the 20 m^2 dish. Thus COMPREC became the primary modelling tool used for simulating and investigating theoretical focal flux distributions in the ANU dishes. CIRCE2, however, was used as a standard with which to compare and check COMPREC's output under identical input conditions for simple reflecting surfaces.

3.2 COMPREC development - design philosophy

The method of ray tracing chosen used straightforward geometrical optical principles. Essentially, an array of incoming sun vectors is defined, and a point on the concentrator surface is chosen. The sun vectors are scanned from the chosen point, and reflection rays calculated for each. Intersection points for the reflected rays on the defined receiver surface(s) are calculated, and determinations made as to which rays are within the specified boundaries, and which of the (possibly multiply defined) receiver hit points is closest to the surface point (this test allows for shading of one receiver surface by another). Receiver hits are cast into one of the 50 by 50 grid 'bins' defined across each receiver surface, such that a count of 1 is added to the respective bin each time a hit is encountered. In this way a cumulative array of hit points is built up across the receiver surfaces. A new concentrator surface point is chosen after scanning all the sun vectors, and the above process repeated. When all sun vectors and concentrator surface points have been examined, the binned counts on the receiver surfaces are converted to absolute intensity values, and each receiver surface saved to a file. The files can then be read and displayed using a commercial analysis and display program (for example, Interactive Data Language (IDL)[3], MATLAB[4], etc.).

Figure 3.1 shows the program flow chart that describes the overall operating structure of COMPREC.

---

[3]Interactive Data Language (IDL). Research Systems Inc. 777 29th St. Suite 302, Boulder, Colorado. CO 80303. USA.

[4]Matlab. The MathWorks, Inc. 24 Prime Way, Natick, Massachusetts. 01760. USA.

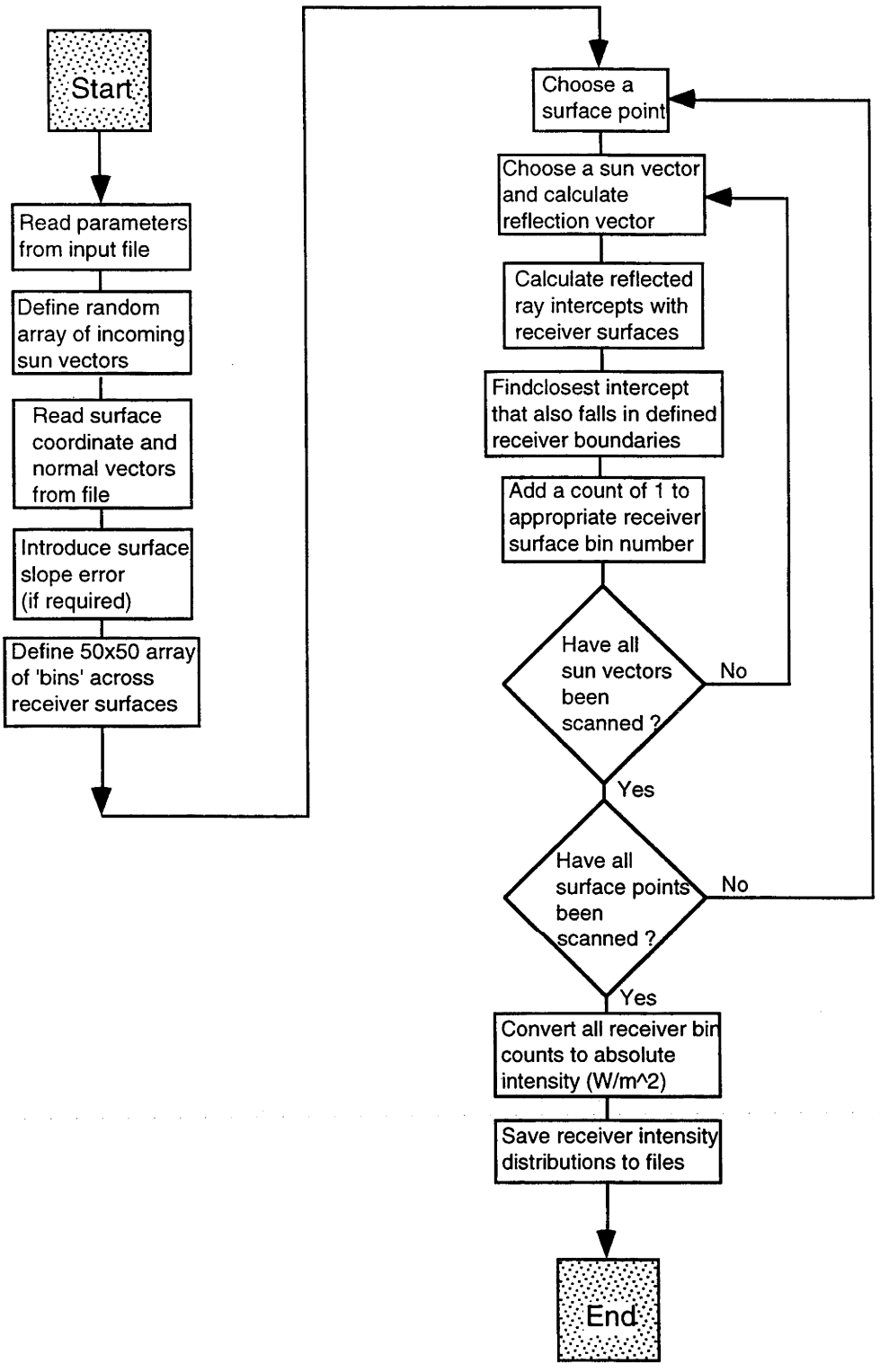

Figure 3.1. Flow chart describing the program structure developed for ray tracing code COMPREC.

One of the important objectives which was required of COMPREC was that it should be able to read in surface coordinates from a file in a predefined format. This allows the input of surface coordinates that have been defined or generated from real surface data. In this way, empirically measured surfaces can be modelled and ray traced to determine the focal flux distributions that will arise from them. The format chosen was that of an interleaved series of alternating surface point position vectors and their associated normal vectors, as shown in Figure 3.2 below.

Surface Point 1	.X
	.Y
	.Z
Surface Normal 1	.X
	.Y
	.Z
Surface Point 2	.X
	.Y
	.Z
Surface Normal 2	.X
	.Y
	.Z
etc.	

Figure 3.2. Data format of points and normals stored in dish surface definition file.

Implementation of COMPREC involved defining a number of parameters. These included definition of the 'sun-shape' used to model solar intensity, creation of the reflective surfaces used to model the concentrators, calculating the useful intersections of the reflection vectors with the defined receiver surfaces (accounting for shading of one receiver surface by another), and saving the resulting receiver surface intensity arrays to files. These developments are described in the following sections.

3.2.1 Definition of sunshape

The description of sunshape involves some uncertainty, due to the varying nature of the sun's image seen through different atmospheric conditions. Schubnell (1992) describes this effect, and its influence on the focal image in imaging solar concentrators, and points out that sunshape also varies according to wavelength. However, this wavelength dependence is small, and was not introduced into the sunshape model used in COMPREC. Variation in solar intensity across the sun's disk, also known as 'limb darkening', is a noticeable effect, and can be accentuated by atmospheric scatter. Figure 3.3 shows a cross-section across a typical solar disk, taken at 22:46 UT from Holloman AFB, New Mexico, USA on December 21, 1995 (Solar Environment Centre, 1995).

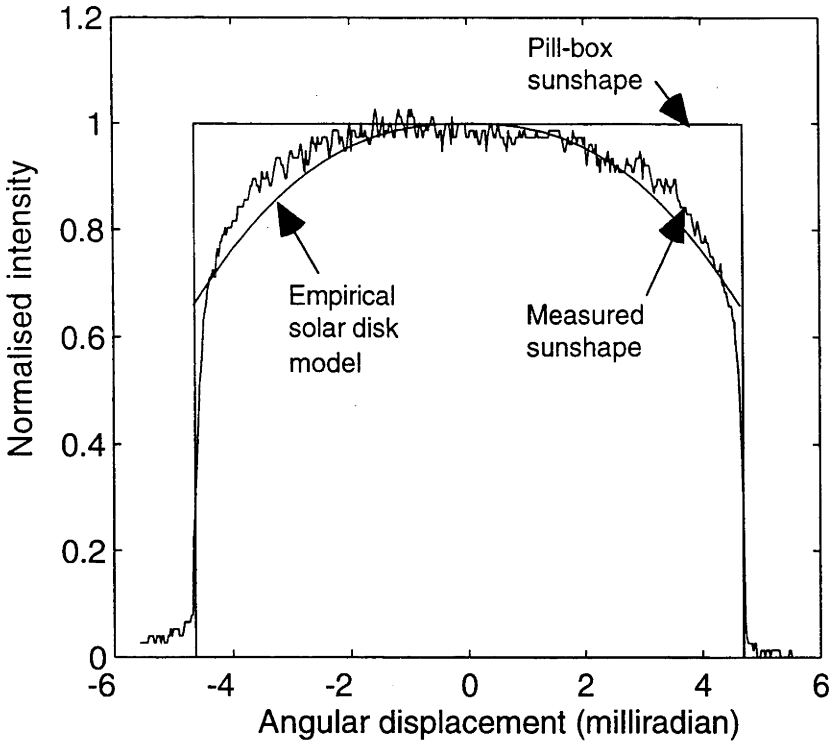

Figure 3.3. Pill box sunshape together with an empirical solar disk model and an actual solar image taken on December 21, 1995 at Holloman AFB, New Mexico at 22:46 UT.

Researchers have often modelled the sun as having a 'pill-box' (ie. uniform) intensity distribution, with an angular half width (subtended from the earth) of 4.65 milliradian (Bammert, et. al., 1990). Figure 3.3 also shows a 'pill-box' sunshape, together with one (Jefferies, 1985) of a number of possible empirical models that have been used by different groups. Jones and Wang (1995) indicate that their modelling showed that approximately 3% difference results between using a pill-box sunshape, an empirical solar disk model and a Gaussian sunshape model. Although COMPREC was constructed with the capacity to model different sunshapes, in practice a 'pill-box' shape was used to minimise execution times and because the difference in focal region flux distribution was comparatively small.

The sun's disk was modelled as a random array of vectors having a definable half-angular extent (usually the nominal value of 4.65×10^{-3} radian was used). Figure 3.4 shows a typical array of 10,000 sunpoints defined across the sun's disk. A random array of sun vectors was used because it was found that a regular grid of points sometimes created a 'spatial beating' effect across the tops of some distributions at focus. This had the appearance of sharp ripples, especially near the central regions, and arose due to interference effects between the spatial frequency used to define the sun grid, and the frequency of the grid used to define the receiver surface.

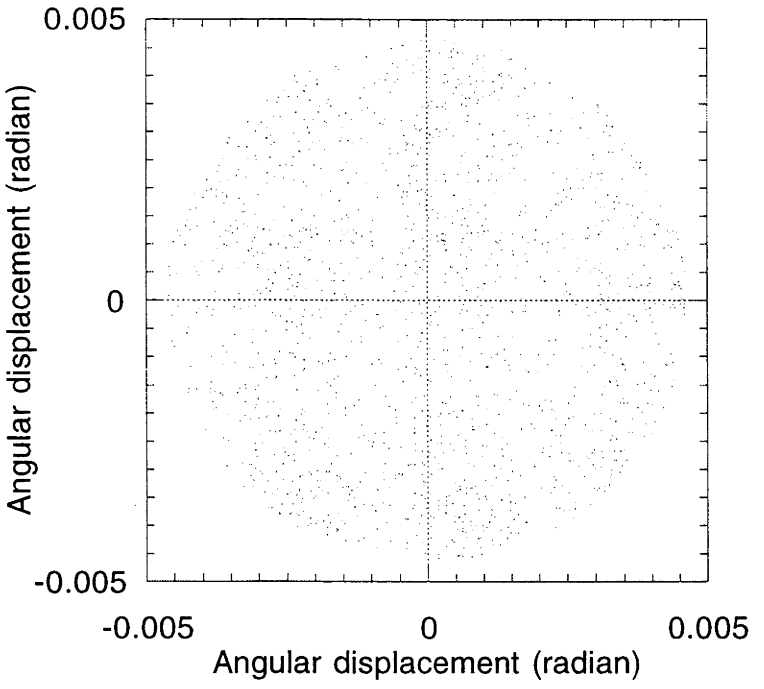

Figure 3.4. Example of a random distribution of 10,000 data points defining the sun's surface used by COMPREC.

3.2.2 Modelling surface slope, specularity and tracking errors.

Romero (1994) has an excellent discussion of the distribution of errors on the surfaces of concentrators. His descriptions point out that most randomly distributed errors conform to a bivariate Gaussian distribution, of the form,

$$P = \frac{1}{2\pi\sigma_x\sigma_y}\left(e^{-\frac{x^2}{2\sigma_x^2}} + e^{-\frac{y^2}{2\sigma_y^2}}\right) \qquad \textbf{(3.4)}$$

where,

P = probability of the normal vector deviating to the (projected plane) coordinates (x,y)

σ_x, σ_y = the standard deviations in the x and y directions for the given error distribution

This defines an elliptical distribution. However, a large number of distributions fall within a circular distribution, where $\sigma_x = \sigma_y$ and the probability distribution simplifies to,

$$P = \frac{1}{2\pi\sigma^2}\left(e^{-\frac{\left(x^2+y^2\right)}{2\sigma^2}}\right) = \frac{1}{2\pi\sigma^2}\left(e^{-\frac{\left(r^2\right)}{2\sigma^2}}\right) \qquad \textbf{(3.5)}$$

where,

σ = the circular standard deviation

r = the radial coordinate from the distribution centre

Jones and Wang (1995) note that this single error (σ) (usually quantified in milliradian) actually reflects a combination of three primary errors that influence the spread of radiation in a focal region. These are,

(i) Surface slope error, σ_{slope}. 'Ripples' and imperfections in the concentrator mirror surfaces due to manufacturing/fabrication are described as slope error;

(ii) Specularity error, σ_{spec}. Aberrations in the glass and reflective surfaces with dimensions approaching that of the wavelength of light create a diffusion in the light reflected from mirror surfaces, and is referred to as specularity error, or sometimes just 'specularity';

(iii) Tracking error, σ_{track}. This term applies to tracking solar concentrators, and arises due to imperfections in the tracking mechanism of the collector. If the collector is not pointing directly at the sun, then the focal spot will shift by an angular amount equal to twice the tracking error. This will also cause a slight asymmetry in the distribution of focal radiation.

As the distribution of these errors will generally follow Poisson statistics (which become Gaussian distributions for large sample sets), the equivalent error, σ_{eq}, can be found through a simple quadratic combination of the 3 errors:

$$\sigma_{eq} = \sqrt{\sigma^2_{slope} + \sigma^2_{spec} + \sigma^2_{track}} \qquad (3.1)$$

It should be noted that the tracking error will influence the time integrated distribution of focal radiation, but that it will not influence the instantaneous spread of flux at any given time in the same way as σ_{spec} and σ_{slope} do. The short term effect of tracking error will be to create an asymmetry in a flux distribution, whereas the slope and specularity errors will spread the flux symmetrically (assuming there are no systematic distortions in the concentrator surface) at all times. In the current thesis, the terms 'surface slope error', or 'slope error', will be used to refer to the combination of the above error terms, ie. equivalent error, σ_{eq}.

3.2.3 Reflector Surface Generation

Generation of reflector surfaces for use by COMPREC is performed by auxiliary programmes DISHFITTER, TILEFITTER and HEXFITTER.

3.2.3.1 DISHFITTER

DISHFITTER defines a circular dish reflector having a continuous surface, having 100% reflectivity and zero slope error. Slope error (if required) is introduced in COMPREC.

The reflector type (paraboloidal, spherical or polynomially defined), diameter, focal length and the number of (odd) grid points desired in the x and y directions are entered. An output file name is also entered, and the resulting array of surface points and normals are stored using real (4 byte) binary data type in the alternating interleaved sequence of points and normals defined above (Figure 3.2).

3.2.3.2 TILEFITTER

TILEFITTER defines a circular dish having an array of square tiles arranged in annular rings upon a paraboloidal substrate, and was designed to create models of the surface of the 20 m^2 tiled dish. A grid of data points is applied to each tile, and tiles of a specified dimension are placed around the dish surface on paraboloidal coordinates until the required surface is covered. Due to the requirement that gridpoints across each tile have the same surface normal, surface slope error is not introduced in COMPREC (as this would introduce a slope error on each individual surface normal), but instead is calculated in TILEFITTER and applied to the appropriate tile normals.

Dish diameter, focal length, tile dimensions, surface slope error on the tiles and numbers of x,y gridpoints per tile are input, and the resulting array of interleaved surface points and normals are saved in a user specified file.

3.2.3.3 HEXFITTER

HEXFITTER takes a circular array of dish data points and normals, and extracts those points that fall within the boundaries of a hexagon having the same diagonal lengths as the circular dish diameter.

3.2.4 Modelling actual target reflectivity properties.

Consideration was given to the fact that COMPREC was designed to produce flux predictions that would be compared with actual videographically measured flux distributions. Accurate comparisons would have to account for any peculiarities in the target reflectivity, particularly involving any non-Lambertian qualities that it may have. Investigations were undertaken to assess the 'Lambertian-ness' of the matt white paint that was used to coat the actual target surfaces. Appendix 3.1 contains the results of these measurements. They show that the paint is not ideally Lambertian in its reflectance properties, but instead shows a linear decrease in reflectance with viewing angle from the normal. This functional relationship was incorporated into COMPREC and tests performed to assess the influence that this phenomenon would have on the flux predictions. Figure 3.5 shows the superposition of two predicted fluxes from COMPREC, with and without the non-Lambertian reflectivity function.

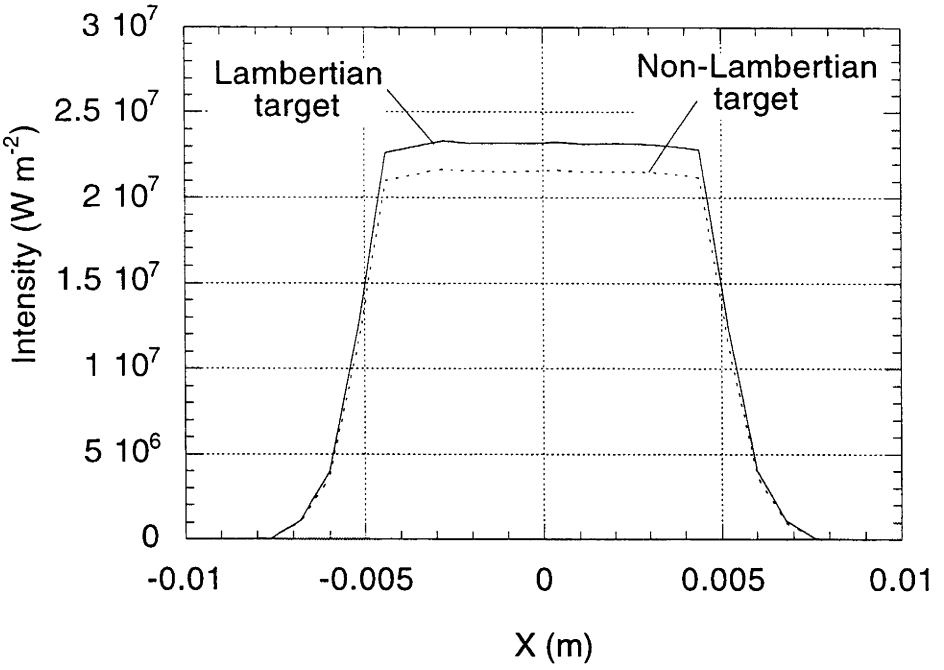

Figure 3.5. Superposition of flux plots from COMPREC using Lambertian and non-Lambertian target reflectivities.

It appears that the non-Lambertian surface produces an image intensity that is lower than that expected from a Lambertian surface. However, Figure 3.6 shows that when the flux plots are scaled to have the same peak intensity, they are identical.

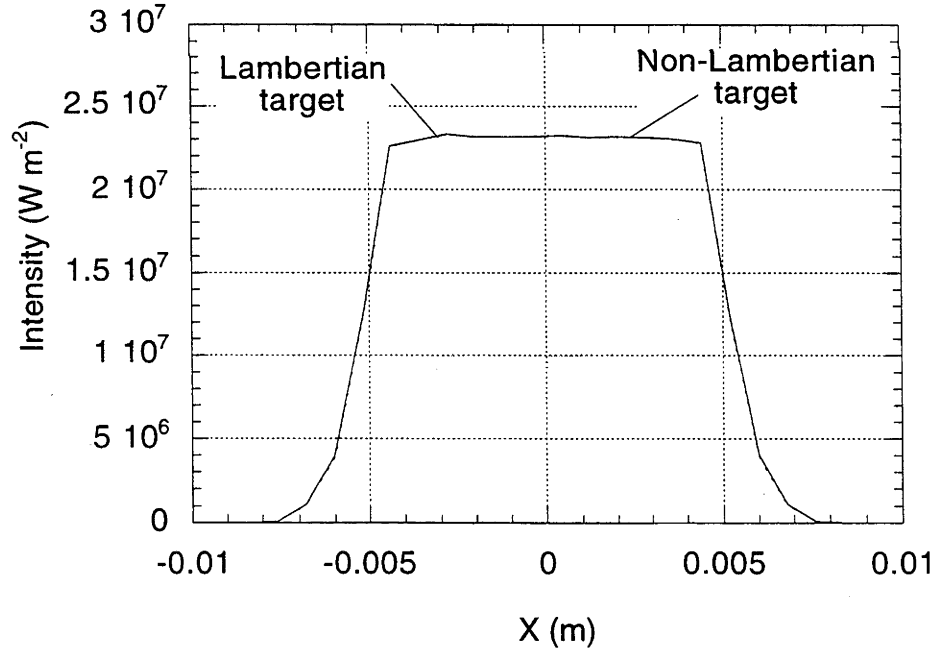

Figure 3.6. Superposition of fluxes from COMPREC with Lambertian and non-Lambertian target reflectivities linearly scaled to have the same peak flux.

Figure 3.6 indicates that the non-Lambertian nature of the reflecting surface only serves to linearly scale the amplitude of the flux distribution, and does not appear to non-linearly scale its width. In this case, incorporation of the non-Lambertian reflectivity function into ray trace models was unnecessary, as any measured flux distribution was linearly

scaled by the absolute value of the foil gauge radiometer used to calibrate the flux images, and this fact calibrated the distribution to be independent of the linear scaling effect of the non-Lambertian reflectivity of the target surface. This simple solution would probably not have been available if the paint reflectivity function was a noticeably non-linear function of viewing angle.

3.2.5 Calculation of receiver intersection points

Calculation of the receiver intersection points involves a straightforward analysis of a vector intersection with a defined mathematical surface, and the relevant mathematical analyses for these calculations are contained in Appendix 3.2.

3.2.6 COMPREC input and output files and formats

COMPREC gains its input by reading a predefined input file called 'RecDishIn.dat'. Appendix 3.3 contains a sample 'RecDishIn.dat' input file. Use of the file is explained in the appendix.

Output flux images are saved as a 50x50 array of data points in a binary data format, with each number representing the light intensity at the specified point on the grid. The array must be called into a separate data analysis and display package, such as IDL (Interactive Data Language) or MATLAB (MATrix LABoratory), to observe and analyse the flux distribution. Dimensional scaling of the data field must be performed by reference to the target dimensions originally stored and used in 'RecDishIn.dat'.

3.3 COMPREC output

3.3.1 Initial Testing

COMPREC output was tested against an analytical calculation of flux distribution proposed by Jeter (1986). Figure 3.7 shows the superposition of flux images calculated by Jeter's analysis (1986) (dotted lines) and those calculated by COMPREC under identical input conditions.

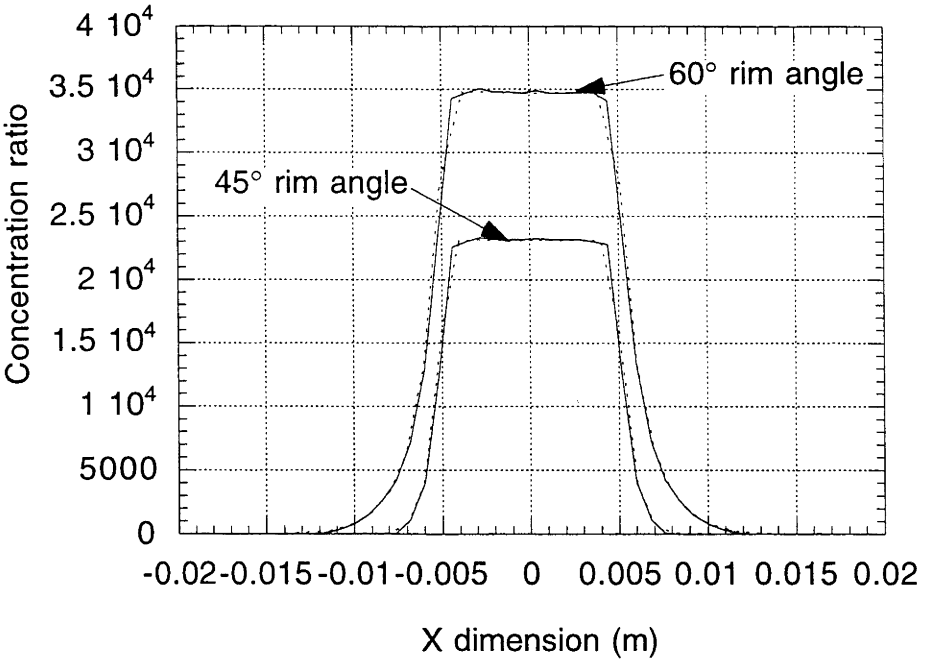

Figure 3.7. Superposition of COMPREC fluxes (solid lines) and analytical fluxes (dotted lines) (Jeter, 1986) for 1 m focal length dishes having rim angles of 45° and 60° respectively. Pill box sunshape used for both models.

Flux distributions calculated by CIRCE2 using identical input conditions (25 m diameter circular dish, 13.1 m focal point, 4.65 milliradian half-angle, pill-box sunshape, 1.2 m diameter circular target placed at the focal point) was also used for comparing the performance of COMPREC. Figure 3.8 shows the superposition of flux distributions calculated by CIRCE2 and COMPREC.

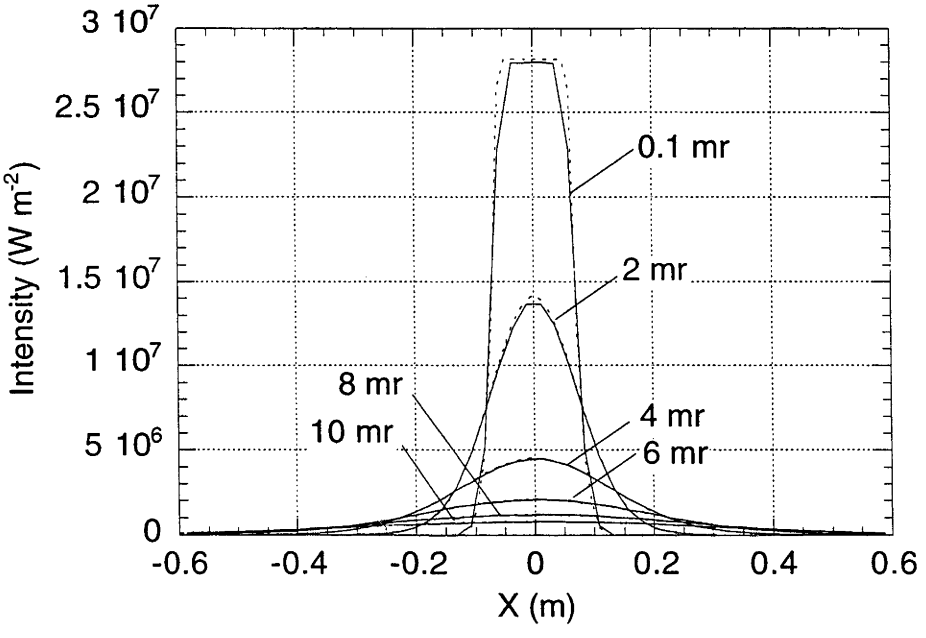

Figure 3.8. Superposition of CIRCE (dotted lines) and COMPREC (solid lines) fluxes under identical input conditions for surface slope errors ranging from 0.1 milliradian (the smallest value allowed in CIRCE) to 10 milliradian, in 2 milliradian increments.

Figure 3.8 shows that COMPREC compares very favourably with CIRCE2, and lends further confidence to the reliability and accuracy of COMPREC. The only noticeable deviation between the output of the two programs occurs in the 0.1 milliradian distribution, where a slight disparity appears near the edges of the central peak. This constitutes less than 1% deviation between the distributions, and is not regarded as a difference requiring correction in either program.

Comparisons with the PSF (Primary Solar Flux) algorithm were also undertaken. Figure 3.9 shows the superposition of the fluxes predicted by COMPREC and PSF for a 0.5 m diameter target placed at the 1.81 m focal point of a modelled dish.

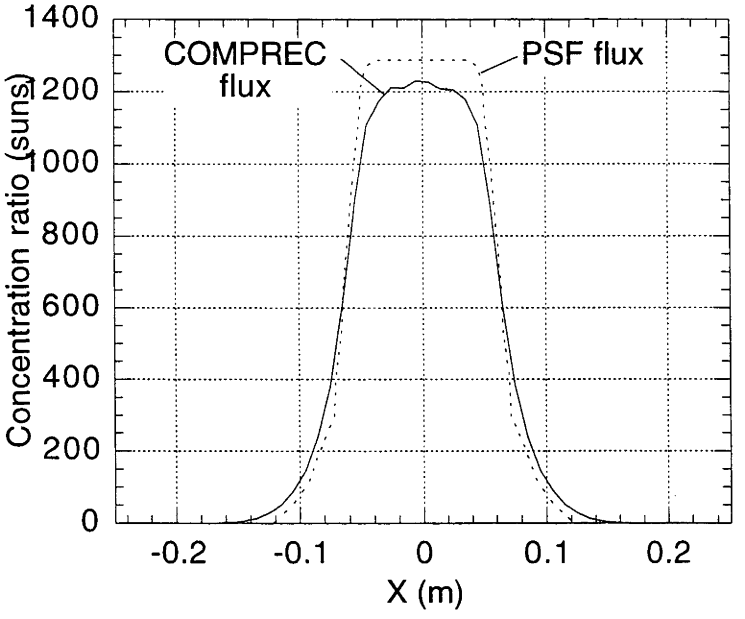

Figure 3.9. Superposition of predicted fluxes from COMPREC and PSF for a 0.5 m diameter target placed at the 1.81 m focal point of a modelled 20 m^2 tiled dish.

Figure 3.9 shows that PSF predicts a flux with sharper, slightly narrower shoulders than that predicted by COMPREC. It was considered that this difference may have been due to different tile geometries being defined between the two programs. The program TILEFITTER (developed to model the 20 m^2 dish for COMPREC) incorporated the feature of the actual dish that the mirror tiles had different tangential widths (while constant radial depths) between the different annular tile rings placed on the dish surface. It was surmised that PSF used a constant tile depth **and** width. Investigations with COMPREC using a 20 m^2 dish modelled with uniformly square mirror tiles 0.1 m on a side showed flux predictions that matched the PSF predictions, which appeared to indicate that PSF used uniformly square tiles in it dish surface models. This was thus considered to be a further limitation with PSF.

3.3.2 Modelling the 20 m^2 tiled dish.

Figure 3.10 shows a surface flux plot of the flux distribution expected at the 1.81 m focal point of the 20 m^2 tiled dish at the ANU, while Figure 3.11 shows a cross section through

this distribution. The reflecting surface was modelled as 2,262 flat mirror tiles having varying widths[5], laid on perfectly paraboloidal coordinates with zero surface slope error.

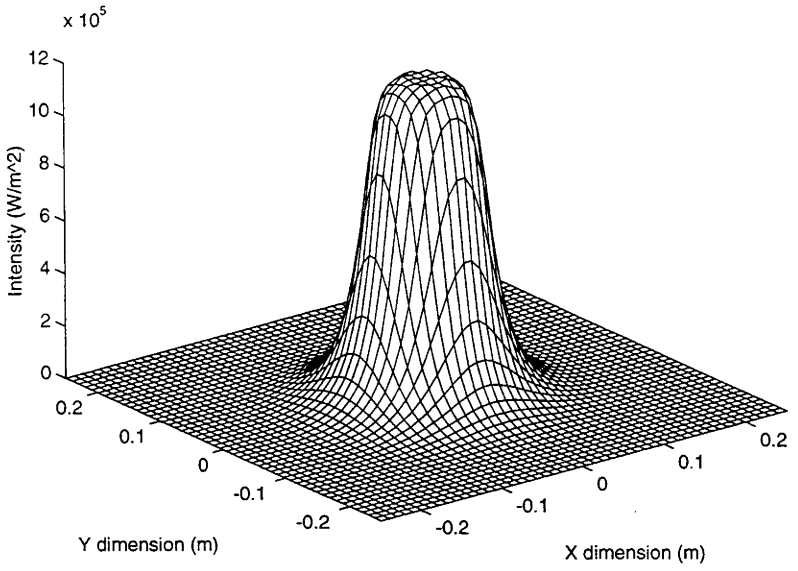

Figure 3.10. Flux distribution expected at the 1.81 m focal point of the 20 m^2 tiled dish, assuming zero surface slope error.

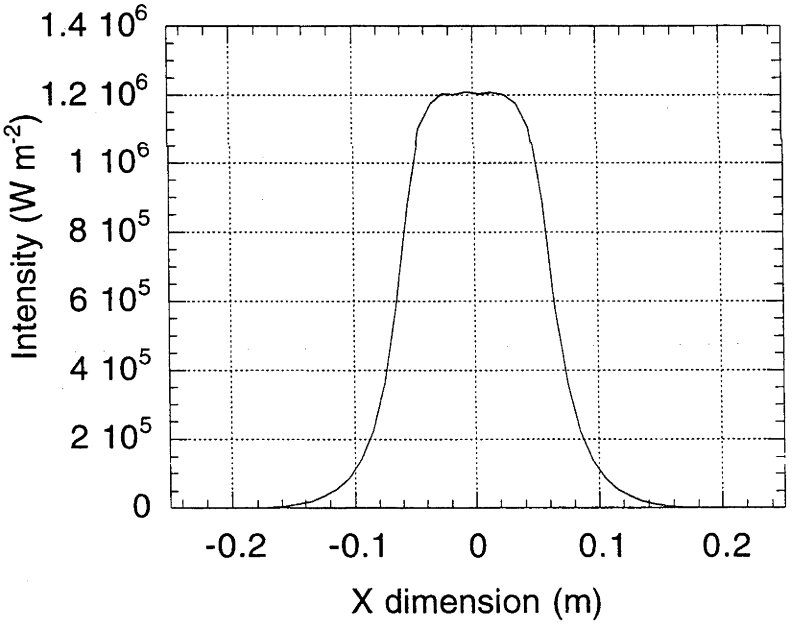

Figure 3.11. Cross section through the flux distribution shown in Figure 3.10.

For comparison, Figure 3.12 shows the flux distribution expected for an ideal paraboloidal dish having a 20 m^2 aperture area, 1.81 m focal length and zero slope error. Figure 3.12 also shows the flux distributions expected for both Kuiper's (solid line) and a pillbox (dotted line) sunshape.

[5] Tile widths varied from 45 mm to 100 mm, depending on the radial position on the dish surface. Tile depth was constant at 105 mm.

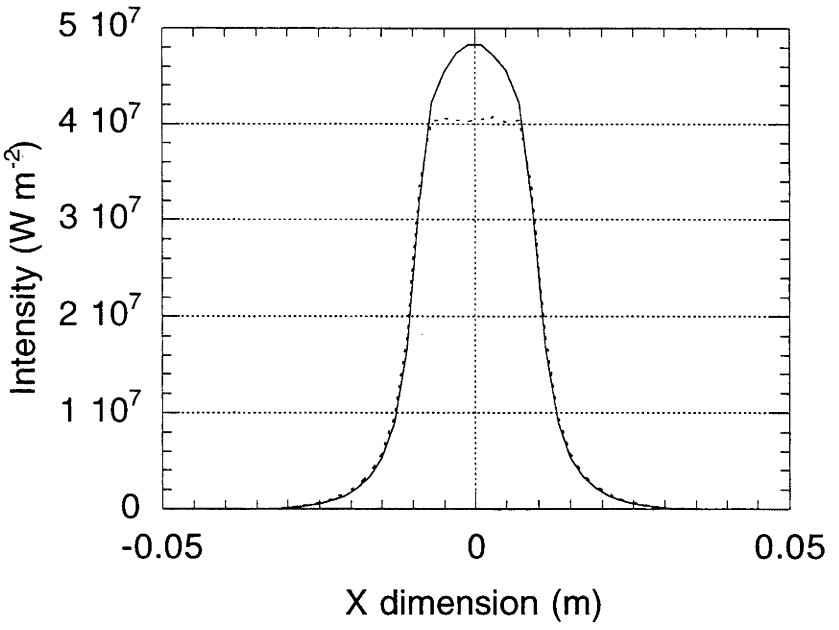

Figure 3.12. Focal flux distribution expected for an ideal (smooth) paraboloidal dish having the same dimensions as the 20 m^2 tiled dish. Solid line uses Kuiper's sunshape (Figure 3.3); dotted line uses a pillbox sunshape. Note difference from Figure 3.11 in both ordinate and abscissa scales.

Figure 3.11 indicates that a much broader, flat-topped distribution can be expected at the focal point of the 20 m^2 tiled dish than for the ideal paraboloidal concentrator (note the difference in target dimensions between Figure 3.11 and Figure 3.12). This observation conforms with intuition, as it is expected that the nature of the 10 cm flat mirror tiles will create a much greater spread of radiation in the focal region than if the dish was an ideal continuous surface. This feature also accounts for the fact that the influence of sunshape is negligible when predicting flux distributions for the 20 m^2 tiled dish. Figure 3.13 shows that two distributions are virtually identical when modelled with Kuiper's sunshape and a pillbox sunshape.

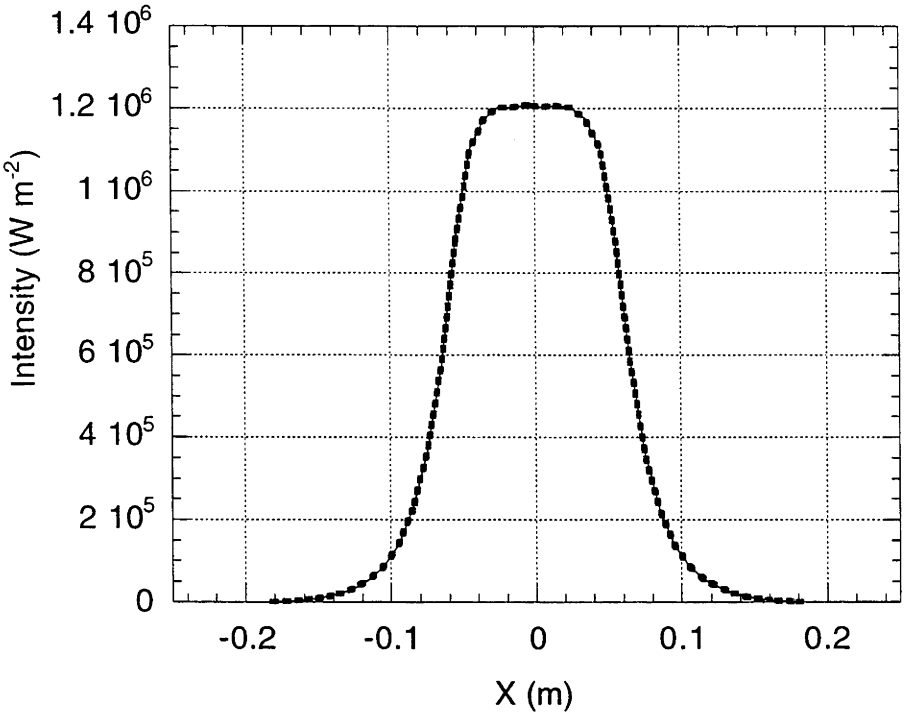

Figure 3.13. Superposition of two flux distributions at the focal point of the 20 m^2 tiled dish using pillbox (dotted line) and Kuiper's distribution (solid line) sunshapes.

Figure 3.13 indicates that no advantage is gained using a non-pillbox sunshape for modelling studies for the tiled dish. All simulations performed in this case thus used a pillbox sunshape for computational expediency.

3.3.3 Modelling the 400 m^2 dish having a continuous, paraboloidal surface.

Without prior knowledge of the surface slope errors existent on a dish having a continuous surface, it is impossible to provide realistic predictions of the flux distribution that could be expected in its focal region. Figure 3.14 shows a family of flux distributions predicted by COMPREC for surface slope errors ranging from 0.0 to 10.0 milliradian on the surface of a 400 m^2 hexagonal dish, analogous to the dish at the ANU.

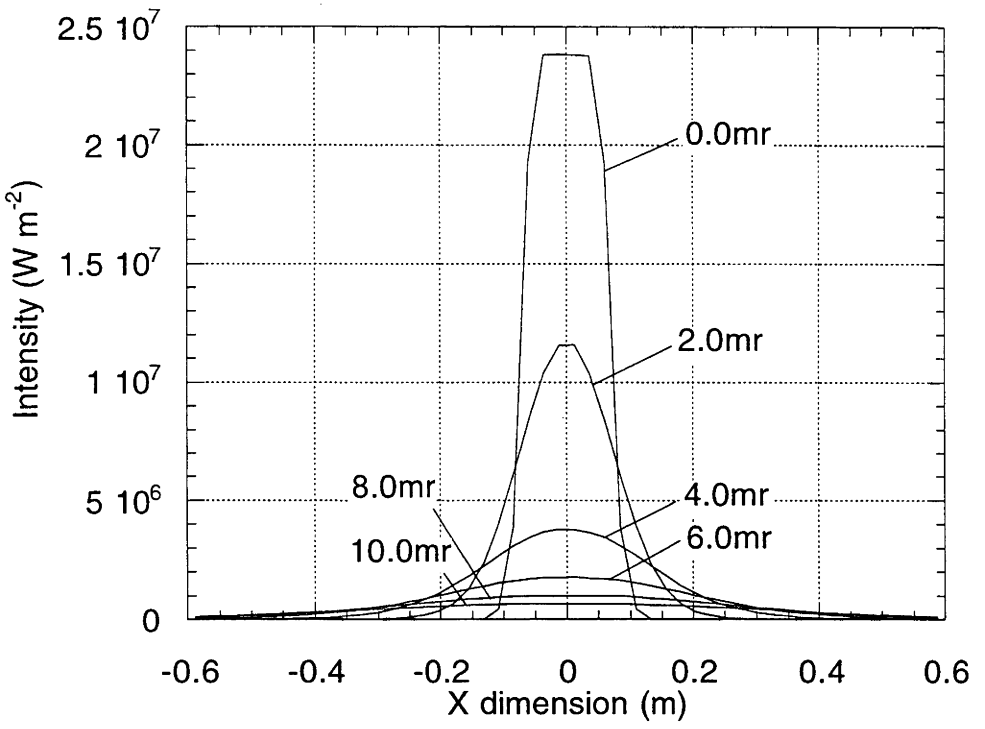

Figure 3.14. Superposition of predicted flux distributions at the 13.1 m focal point of a 400 m^2 hexagonal aperture dish having 0.0 mr to 10.0 mr of surface slope error, in 2 milliradian increments. (Insolation=1000 W m^{-2}; mirror reflectivity=100%.)

Further modelling of the focal flux of the 400 m^2 dish is undertaken in chapter 4, where comparison with measured focal fluxes allows an approximate model for the dish surface slope error to be formulated.

The distributions shown in Figure 3.14 were produced using a pill-box sunshape. While the sunshape was an insignificant influence for the 20 m^2 tiled dish flux distributions, this will not necessarily be the case for concentrators having higher surface accuracies. Modelling runs were performed for concentrators having different slope errors and using different sunshapes. It was found that the effect of sunshape only appeared to become significant for concentrators having average surface slope errors less than 2 milliradian. As the dishes modelled in the current study had slope errors greater than this figure, it was considered safe to continue using a pill-box sunshape for all computer ray-trace modelling.

3.4 Discussion of ray trace code

The results presented in this chapter establish the viability of the COMPREC ray trace code to undertake simulations according to the criteria laid down in section 3.1. While the algorithm satisfies the required functional characteristics, it has shown that it is a CPU and memory 'hungry' program. Maximum memory allocation for the program utilises some 12 megabytes of random access memory, and using a high performance DEC 5000 Alpha work station requires 8 to 12 hours of processing time to calculate a flux distribution for the 20 m^2 dish. Admittedly, the nature of the 20 m^2 tiled dish surface places heavy demands on the processing, as each of the 2262 mirror tiles must have an array of data points defined across it (usually an 8x8 grid), which defines a total data set of more than 144,000 points. If each one of these points processes 2000 sun points (the array defining the solar disk), then a total of 29 million sets of calculations must be performed. The situation is relaxed considerably for a smoothly continuous reflector surface (such as modelling the 400 m^2 dish), as many fewer data points (5,000 to 10,000) were found sufficient to accurately model the focal flux distributions. This allowed simulations to be performed in under an hour in most cases. If the number of sun points are reduced to, say, 200, this processing time is cut even further to just a few minutes, with usually quite adequate focal fluxes being produced.

However, the most realistic test of COMPREC must be to simulate measured fluxes from real concentrators, and this is undertaken in the following chapter.

4. Comparisons of Measured and Predicted Flux Distributions

4.1 Introduction

The foregoing chapter described the capabilities of the ray trace program COMPREC to simulate focal region flux distributions for reflective solar concentrators. This chapter will present the results of comparisons between the measured distributions of chapter 2 and simulated distributions developed using COMPREC and a set of input parameters that approximate the physical characteristics of the real concentrators. This stage serves to further establish the viability of COMPREC as a predictive tool, which can be used in later investigations to reliably predict focal region light distributions from surface data measured on the concentrators.

4.2 Measured and predicted fluxes for the 20 m^2 tiled dish

As an example of the comparison between the measured and predicted distributions for the 20 m^2 dish, Figure 4.1 shows the superposition of the optimum flux measured (at 1.82 m) in Figure 2.4 with the predicted flux (COMPREC) described in Figure 3.11, using a surface slope error of 0.0 milliradian. In order to compare the relative spread of the distributions, the predicted flux has been scaled by a factor of 0.79, such that it has the same peak intensity as the measured distribution in Figure 2.4.

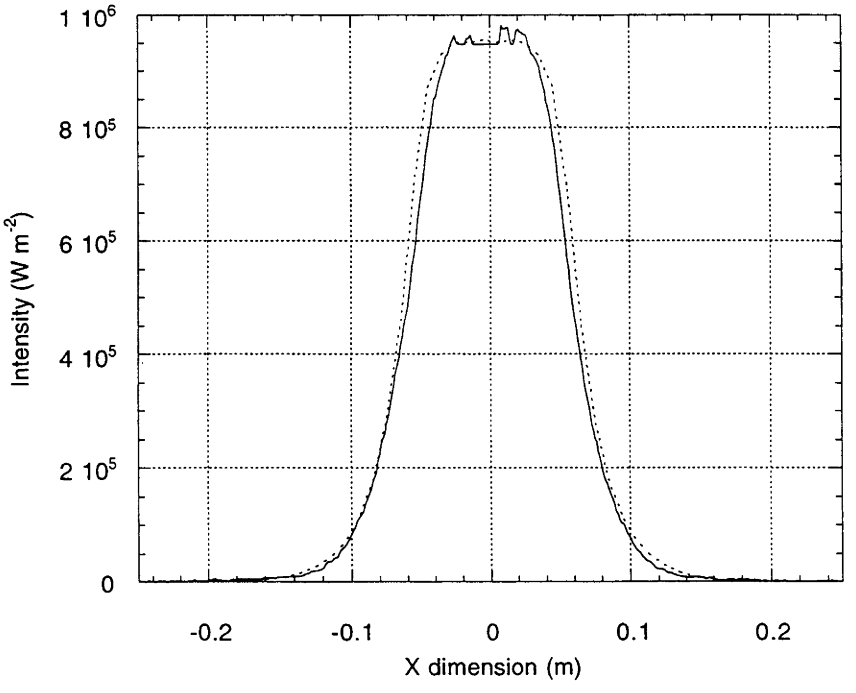

Figure 4.1. Measured (solid line) and predicted (dotted line) distributions at 1.82 m from the dish vertex using zero surface slope error in the predicted distribution.

Figure 4.1 shows that the measured distribution exhibits a narrower extent than that predicted by the ray trace model, and is most noticeable near the peak of the distributions. Figure 4.2, Figure 4.3 and Figure 4.4 show the superposition of measured and predicted flux distributions for slope errors of 1.0, 2.0 and 3.0 milliradian, respectively.

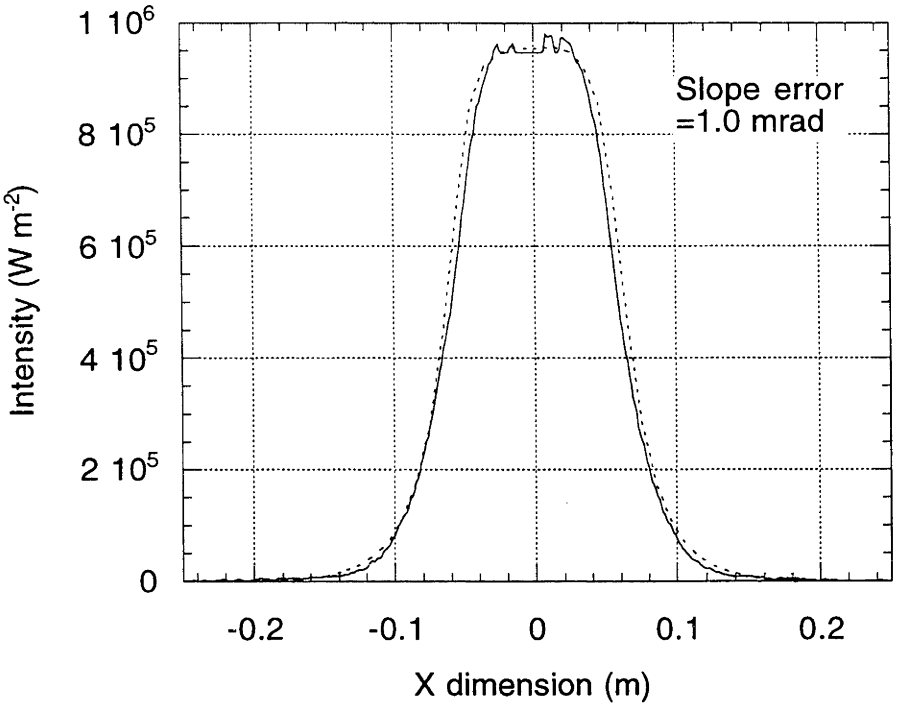

Figure 4.2. Superposition of measured (solid line) and predicted distributions, surface slope error = 1.0 milliradian.

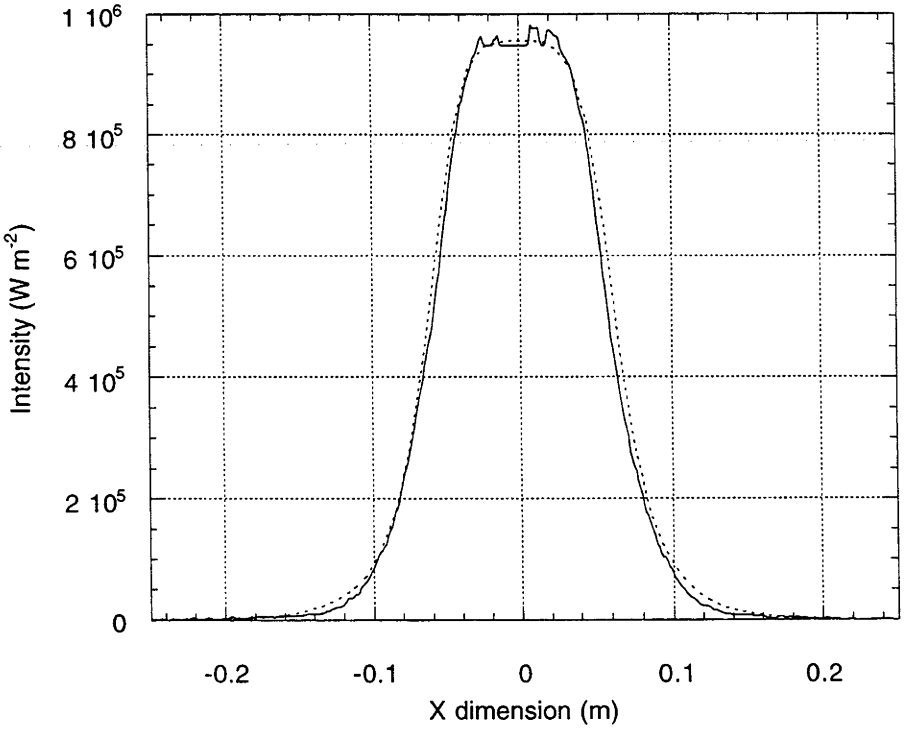

Figure 4.3. Superposition of measured (solid line) and predicted distributions, surface slope error = 2.0 milliradian.

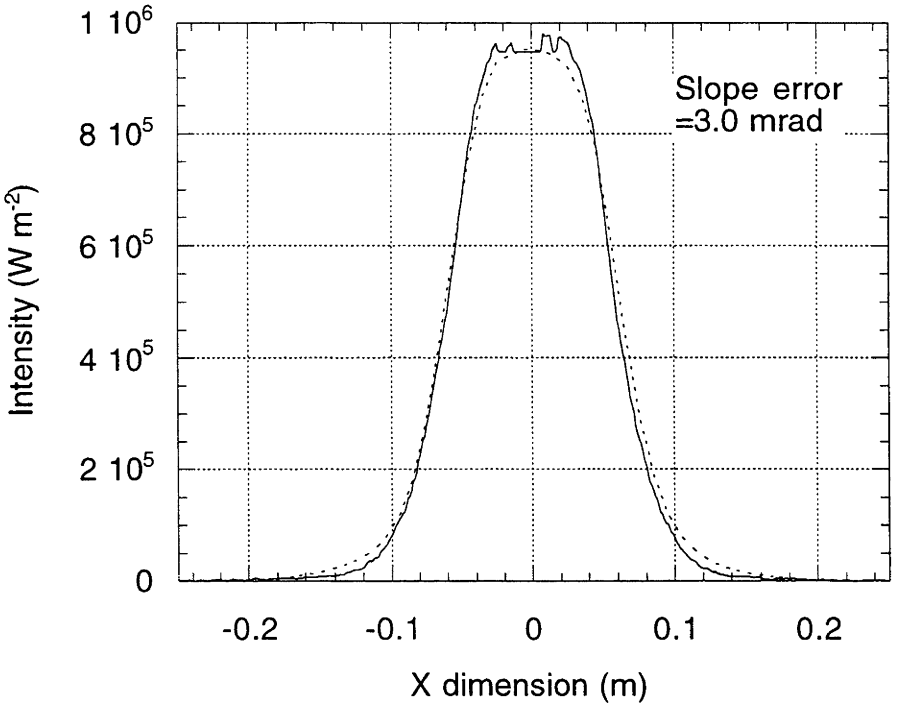

Figure 4.4. Superposition of measured (solid line) and predicted distributions, surface slope error = 3.0 milliradian.

Figure 4.1 and Figure 4.2 show that 0.0 and 1.0 mrad of slope error produce predicted flux distributions that are too broad around the central regions of the distribution. Figure 4.3 indicates that 2.0 mrad of surface slope error produces a predicted distribution that is a close approximation to the measured distribution. The predicted distribution using 3.0 mrad of slope error shown in Figure 4.4 exhibits excessive rounding in the shoulders of the central area of the distribution, and appears to be a poorer approximation than the comparison shown in Figure 4.3 (2.0 mrad of surface slope error).

Later photogrammetric characterisation of the surface of the 20 m^2 dish (see section 6.6) indicated that approximately 1.8 milliradian of surface slope error existed on the dish. This appears to be supported by the close approximations evident in Figure 4.3, and these comparisons formed the basis for choosing a surface slope error of 2.0 milliradian for all further ray trace modelling using the dish.

It should be noted that the measured and predicted flux comparisons of Figure 4.1 to Figure 4.4 show equal peak intensities, in order to compare the relative spatial spread of the measured and predicted distributions. However, this is not the most accurate comparison, due to the slight differences between the flux 'volumes' (that is, integrated power) under the measured and predicted distributions. The more correct measure of comparison should be when the predicted distribution is scaled to contain the same integrated power as the measured distribution. Figure 4.5 shows the superposition of measured and predicted fluxes for the 20 m^2 dish such that both contain the same integrated power. The scaling factor used to achieve this normalisation was calculated to be 0.72, which is also a direct indication of the average dish reflectivity.

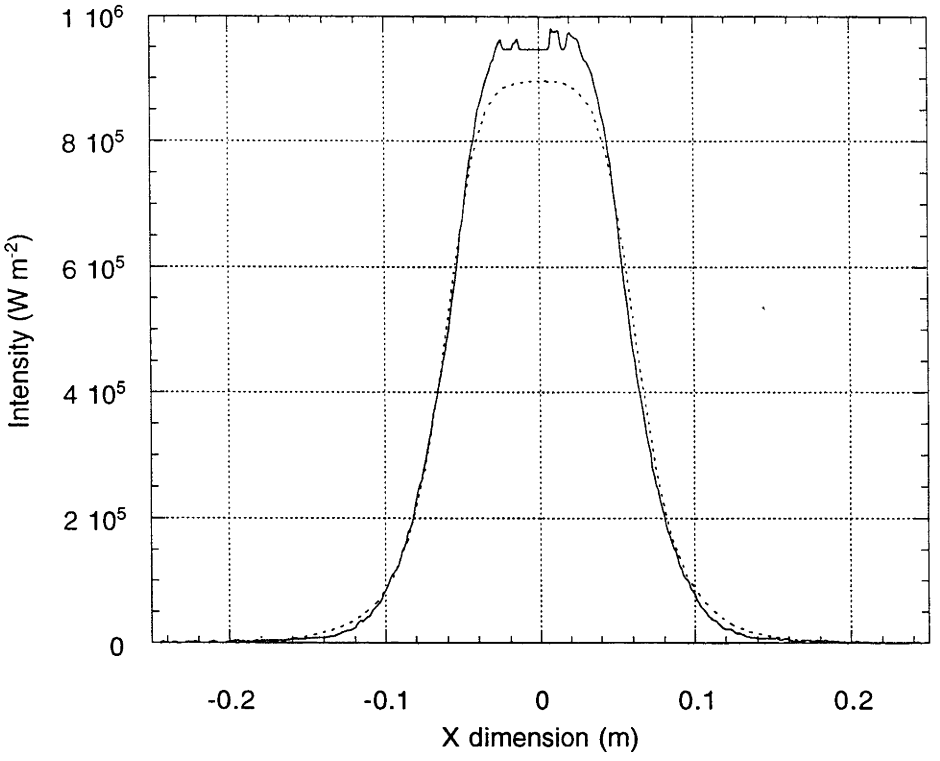

Figure 4.5. Superposition of measured and predicted fluxes having equal integrated powers. Surface slope error = 2.0 milliradian. Scaling factor = reflectivity = 0.72.

Figure 4.5 shows the predicted peak flux decreases by approximately 8% from the measured value to produce a distribution that contains the same integrated power as the measured distribution. It can be noted that the noticeable decrease in intensity shown in the peak region of the distribution is compensated by the apparently smaller increase in the 'shoulders' and 'tails' of the distribution. This lower intensity in the tails will represent the same energy displaced from the peak areas, by virtue of the fact that the tails cover a significantly larger area than the peak.

Appendix 4.1 contains the complete set of measured flux images superposed with the respective ray trace predictions at the measured positions of 1.78 m to 1.88 m from the 20 m^2 dish vertex. A surface slope error of 2.0 milliradian, and an average dish reflectivity of 0.72 has been used in all plots.

4.3 Measured and predicted fluxes for the 400 m^2 dish

Figure 4.6 shows the measured distribution at the nominal 13.1 m focal point of the 400 m^2 dish (normalised to 1000 W m^{-2} insolation) superimposed upon the predicted distributions (COMPREC) for the dish having a range of slope errors from 5.5 mrad to 7.0 mrad. All predicted distributions shown in Figure 4.6 have been scaled to contain the same integrated power as the measured distribution. (Actual model used dish focal length=13.075 m, target position=13.06 m, according to discussion in section 2.2.2 and section 5.4.3.3.)

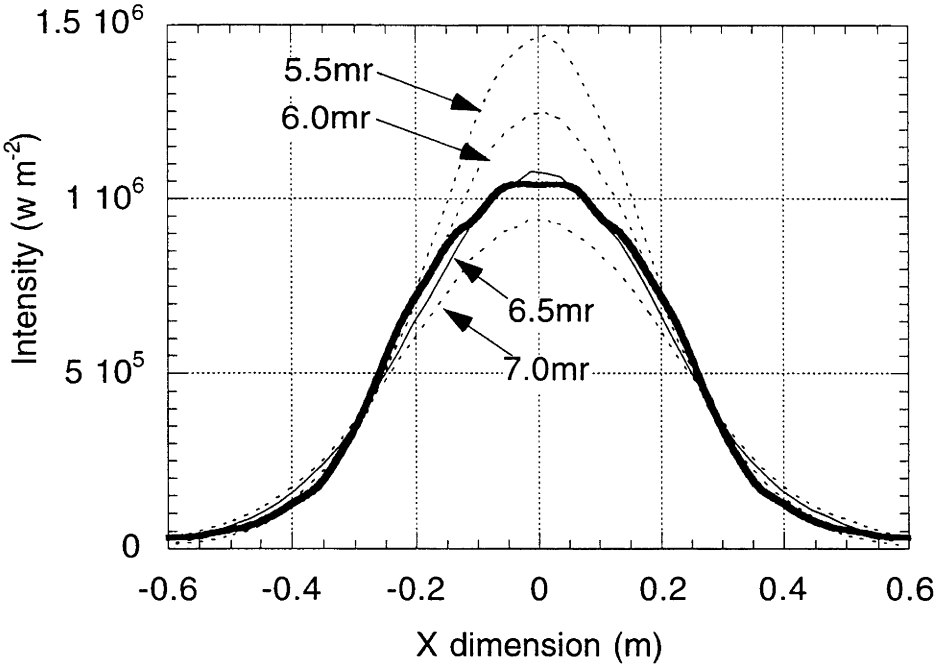

Figure 4.6. Superposition of measured (solid, heavy line) and predicted (dotted and solid light lines) flux distributions for a target position of 13.06 m from the vertex of the 400 m^2 dish. Predicted distributions use surface slope errors of 5.5, 6.0, 6.5 and 7.0 milliradian, with the closest fit (6.5 mrad) shown as a light solid line.

As shown in Figure 4.6, the closest fitting predicted distribution occurs for a dish surface slope error of 6.5 milliradian. The scaling factor required to normalise the integrated power under this distribution is 0.70. Calculation of the intercepted power under the predicted distribution indicates that greater than 98% of the reflected energy is intercepted by the 1.2 m target. Assuming this fact will also be true of the measured distribution, then the scaling factor of 0.70 between the predicted and measured distribution will also be a direct measure of the average dish reflectivity. This figure is supported by the measured average reflectivity (0.72) reported in section 2.2.4 (Figure 2.19). Using these measurements (0.72 dish reflectivity, and 6.5 milliradian surface slope error) allows the model to be extended to predict flux distributions at other focal region positions. Figure 4.7 and Figure 4.8 show the predicted flux distributions at nominal positions of 12.8, 12.9, 13.0, 13.1, 13.2, 13.3 and 13.4 m from the dish vertex.

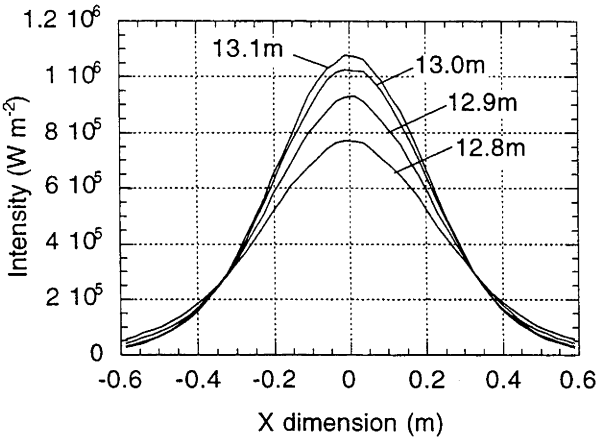

Figure 4.7. Predicted fluxes at indicated target positions less than the nominal focal length of a 400 m² hexagonal dish. Reflectivity=0.72, slope error=6.5 mrad.

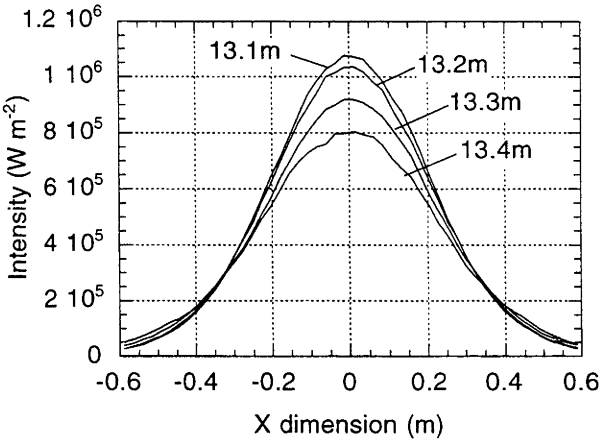

Figure 4.8. Predicted fluxes at indicated target positions greater than the nominal focal length of a 400 m² hexagonal dish. Reflectivity=0.72, slope error=6.5 mrad.

Figure 4.9 to Figure 4.14 show the measured and predicted distributions for the target positions at 12.76, 12.86, 12.96, 13.06, 13.16 and 13.36 m (note that the 13.3 m position was not measured (section 2.2.2)).

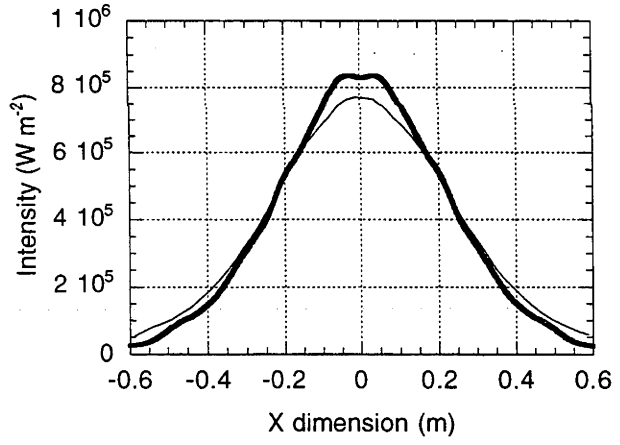

Figure 4.9. Predicted (light line) and measured (heavy line) fluxes at 12.76 m.

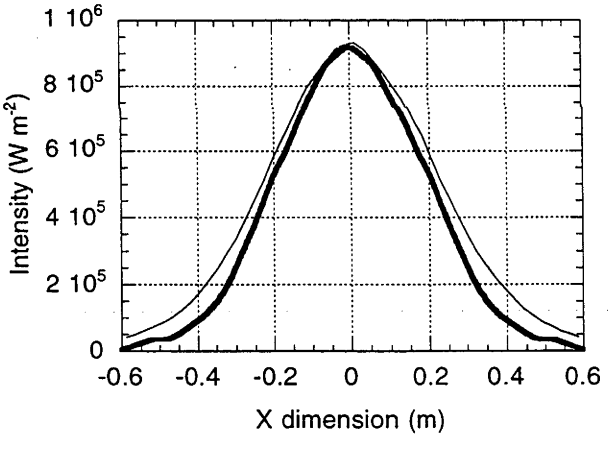

Figure 4.10. Predicted (light line) and measured (heavy line) fluxes at 12.86 m.

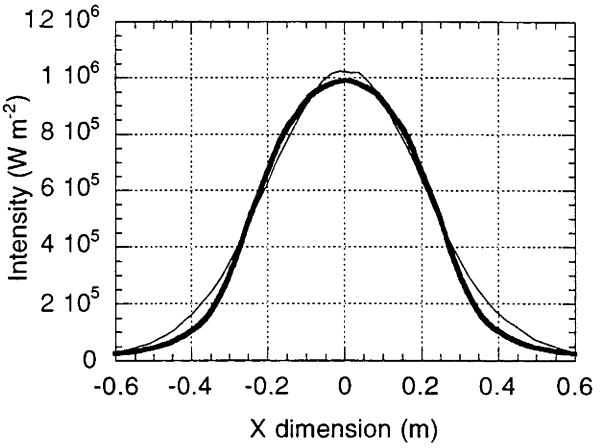

Figure 4.11. Predicted (light line) and measured (heavy line) fluxes at 12.96 m.

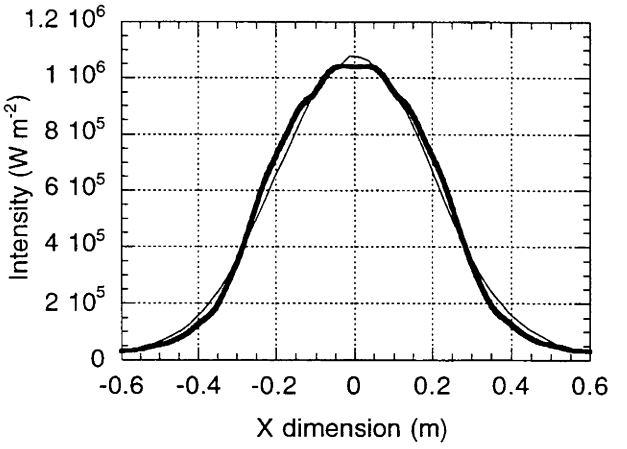

Figure 4.12. Predicted (light line) and measured (heavy line) fluxes at 13.06 m.

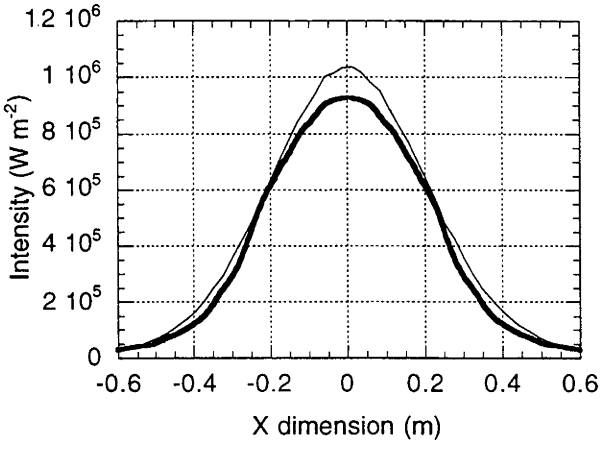

Figure 4.13. Predicted (light line) and measured (heavy line) fluxes at 13.16 m.

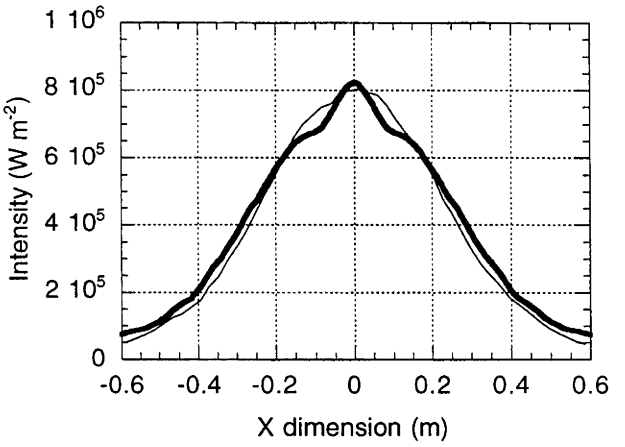

Figure 4.14. Predicted (light line) and measured (heavy line) fluxes at 13.36 m.

4.4 Discussion of flux comparisons

Reference to the superposed images for the predicted and measured flux distributions for the 20 m^2 dish show high levels of conformance between the two data sets. Appendix 4.1 shows that some disparities appear between the measured and predicted distributions at different focal positions in regions near the skirts of the distributions. However, these differences constitute a worst-case relative error of 5% to 8% in most cases, and is considered to be within the bounds of measurement error for the system. No other straight forward explanations are apparent for the discrepancies. As the flux target is moved to more distant positions (1.86 and 1.88 m) from the focal point, it becomes apparent that the narrow detail of the distribution peak's becomes overshadowed by the size of the foil gauge radiometer. (The radiometer image region has been modified in the flux images to remove the 'drop-out' due to the radiometer, and instead replaced by a constant flux value, which explains the truncated nature of the distributions at the 1.86 and 1.88 m.) The predicted distributions indicate that the measured distributions should have slightly higher and more rounded peaks than those captured in the videographic images.

A similar degree of similarity between the measured and predicted distributions for the 400 m^2 dish is evident. A noticeable deviation appears in the 12.86 m flux distribution (Figure 4.10), where the predicted flux is consistently higher over the whole flux field. This effect indicates that the predicted flux will have a greater integrated power than the measured distribution. A similar effect is evident at the 13.2 m target position (Figure 4.13). The most likely source of the apparent deviations comes from the comparatively large uncertainty (±0.04 m) in the target positions for the measured distributions.

The results presented in this chapter establish a reliable standard between the ray trace program COMPREC and the measured fluxes for both the 20 m^2 and 400 m^2 dishes. It shows that successful models can be constructed for both the tiled and continuous surface reflectors, which in turn forms the basis for extending the predictive aspects of the program to characterised surfaces that have a numerical surface description, as will be measured in the next chapter.

5. Photogrammetric Measurements of Concentrator Surfaces

5.1 Introduction

The foregoing chapters have outlined the results of both videographic measurements of focal flux distributions and numerical prediction of these distributions using mathematical models. While the models have been able to show a satisfactory degree of correlation with the measured distributions, it was the aim of the present study to develop a method whereby focal flux distributions could be reliably predicted for an actual concentrator, without relying on empirical focal flux measurements for confirmation. Clearly, the development of such a system would itself have to rely on such empirical comparisons to assess its validity, but if its reliability can be shown, then it would be possible to expect a mature system to allow prediction of light intensity distributions on any receiver placed in any position or orientation in the focal region of the concentrator without the need for actual focal flux measurements. Such a method would rely on assessing the optical characteristics of the concentrator, and then using these optical parameters as input to a ray tracing algorithm to allow prediction of the focal flux based on the measured surface data. To this end, investigations were undertaken to review different methods of concentrator optical surface measurement.

Initial investigations looked at traditional astronomical reflecting telescope mirror testing methods, (Malacara, 1978) but it soon became apparent that these techniques were applicable to optical surfaces that had a far higher quality (surface precisions to within several wavelengths of light) than that produced for solar concentrator applications.

Several solar concentrator testing methods were examined, among them the SHOT technique (Wendelin, 1991), which is an adaptation of the principles employed in the Hartmann test used for astronomical telescope testing, and the '2f' testing method (Grossman, 1994). However, these technologies were found to be more suitable for small to medium size (~15 m diameter) concentrators, and would require significant and costly adaptations when applied to concentrators the size of the 400 m^2 dish (maximum diameter=24.8 m, focal length=13.1 m). The funding available for the present project prohibited much contemplation of investigations that would require significant financial resources.

The author investigated an adaptation of the SHOT method which used a scanning laser beam and a novel beam detection method (Appendix 5.1), but calculations indicated that the method would suffer from inferior precision capabilities, and the project was abandoned. Information acquired at a much later date revealed however, that some image processing algorithms used for object centroid identification in CCD camera images could provide a much higher level of accuracy than that expected in the early investigations into the technique. While this knowledge came too late in the current project for consideration, this information could form the basis of renewed investigations into the method in the future.

Moiré fringe effect techniques and laser interferometry (Sainov, 1993; Kowarschik et al, 1993; Nadeborn et al, 1993; Jarvis, 1983; Harthong and Sahli, 1992) have also been

investigated for surface contour measurement, and provide interesting insights into current endeavours in surface remote sensing (although to the author's knowledge have not been implemented for large scale solar collector analysis).

These methods are mostly applicable to smaller scale collectors (< 10 m maximum dimension) and it can be difficult to ensure that both optimum and reliable precisions are achieved in the results. They are also usually system specific, in that they are constructed to assess one particular collector size or geometry, and must be modified and/or reconstructed to assess new collector designs or shapes.

Discussions with a number of industry representatives raised the prospect of using close-range photogrammetry to measure the surface coordinates of the dish, and to then extract appropriate optical information from these surface measurements. This method was investigated and showed particular promise due to its ability to measure objects of almost any size or orientation with a high degree of precision (Frazer, 1992). It was considered that if this method proved viable, then it could form an avenue of introduction for a new technique in the field of solar concentrator optical assessment. Inspiration to investigate this technique at minimal cost was also engendered through the availability of a photogrammetric processing system available at the University of Canberra, an institution in close proximity to the author.

Photogrammetry has a long history, and is discussed briefly by Shortis and Johnston (1995). Further information on the topic is available in Slama (1980). Advances in computer processing power and digital techniques over the last two decades has led to a high level of sophistication in photogrammetric analyses, with the particular field of close-range, or analytical, photogrammetry developing rapidly as an applied technique in both research and industry.

5.2 Photogrammetric Method

Photogrammetry uses the principles of stereovision reconstruction to measure the 3-dimensional coordinates of objects in space. Essentially, the requirements for photogrammetric surface measurements are:

(i) Unique points ('targets') must exist on a surface which can be commonly identified in different photographs taken of the surface. This usually requires the placement of retroreflective targets to a surface (although Maas (1994) reports interesting results using 'structured light', which utilises projected light patterns onto a surface for target creation and identification). Photographs are taken using a flash, and the retroreflecting targets selectively reflect light back to the camera, such that they become unique highlights against a dark background. Indirectly, this requirement of uniqueness also indicates the need for target stability between photographs.

(ii) A series of (at least two) photographs must be taken of the surface from different positions (or 'stations'), with optimum convergence angles of 90°, or more, between stations. Measured coordinate accuracy usually improves according to the square root of the number of photographs taken of the object (Shortis and Johnston, 1996).

(iii) A reference coordinate system must be established with which to identify the approximate camera station coordinates with respect to the measured object, as well as

coordinates on the object itself. The usual reference system chosen in this project was the aperture plane of the reflector surface being measured.

(iv) Accurate coordinates of at least three targets on the object's surface (referred to as 'control points'). These points were usually three points chosen to also define the coordinate reference plane described in (iii) above.

(v) An accurate measure of 'image space coordinates' (ie. coordinates on the photographs) of the target images.

(vi) Software with which to process the measured image space coordinates to extract the 3-dimensional object space coordinates. The present project utilised the CRAMPA suite of programs (Shortis, 1993). This software utilises a least-squares adjustment of camera station coordinates, lens calibration parameters and control point specifications to provide projections (with precision estimates) of the most probable coordinates of the measured targets.

Two photogrammetric methods were employed in the characterisation of the measured surfaces. The first used film-based photogrammetry, while the second employed digital photogrammetry.

5.2.1 Film-based photogrammetry

The film-based method was used in the early investigations of the project to measure:

(i) the 20 m^2 tiled dish,
(ii) one 30x30 cm mirror tile (used as part of the 400 m^2 dish surface),
(iii) one of the first inner mirror panels of the 400 m^2 dish, and
(iv) an array of selected data points across the entire surface 400 m^2 dish.

The film-based technique used photography taken with a Hasselblad semi-metric camera fitted with a Reseau plate for fiducial mark identification and film flattening. (A Reseau plate is a glass plate fitted to the film plane of the camera that has 27 fine crosses deposited across the surface of the plate in a regular grid pattern. These provide 'fiducial marks' that are used in later photogrammetric measurements of the photographs to allow for estimations of film distortion, and calculation of certain internal camera geometry parameters.) The 90° camera roll between stations was used for calculation of lens calibration parameters (performed by the photogrammetric software), and to minimise what is known as 'projective coupling' that can occur between these calculated lens parameters (Shortis and Johnston, 1996). A high resolution[6] black and white film was used to record the photographic images.

The photographs were developed and the target images on each photograph were viewed and digitised using an analytical stereo-plotter[7]. This is a time consuming process and very prone to suffering from human errors such as poor target observation and/or target misidentification. (This latter problem is particularly serious, as the targets must be digitised in exactly the same sequences in all photographs, and any reversal or

[6] Kodak TechPan film

omission of targets in the sequence will prohibit finding a solution in the photogrammetric software analysis applied later.) This procedure provides what are called 'machine' or 'image-space' coordinates of the targets. These coordinates are then processed using photogrammetric software (Shortis, 1993) to calculate what is called a 'bundle adjustment' of the digitised data. This process employs a multivariable least squares adjustment of numerous parameters in the object, image and camera coordinate spaces to calculate the most probable x, y and z object coordinates of the target points, with precision estimates for each point. Automatic adjustment of camera station position and camera lens calibration parameters is undertaken during the processing, such that only initial estimates of these parameters are required to give the software a reasonable starting point for its iterative solutions.

5.2.2 Digital photogrammetry

The digital technique was employed exclusively in the later stages of the program to measure:

(i) seven triangular mirror panels on the surface of the 400 m^2 dish, and
(ii) seven 60x60 cm mirror tiles (one from each of the seven panels described in (i) above.

Digital photogrammetry uses a still digital camera that captures an image of the measured surface in a digital electronic form (which is then usually translated into a TIFF type image file). Targets are disks of retro-reflective adhesive film[8] placed on the surface to be measured. These retro-reflective targets selectively reflect incident light back to its source. An electronic flash is mounted on the digital camera, such that at the moment of exposure the flash discharges and illuminates the targets. Light reflects back from the targets and the camera exposure is set such that it captures the image as an array of bright points on a dark background. Figure 5.1 shows the digital image of a triangular mirror panel with retro-reflecting targets attached (panel and mirror tile boundaries have been highlighted for clarity) .

[7] ADAM MPS-2 (Micro Photogrammetric System). ADAM Technology Inc. Unit 3/375 Enterprise Unit Complex, Technology Park, Bentley, Western Australia, Australia, 6102.
[8] 3M 'ScotchLite' material.

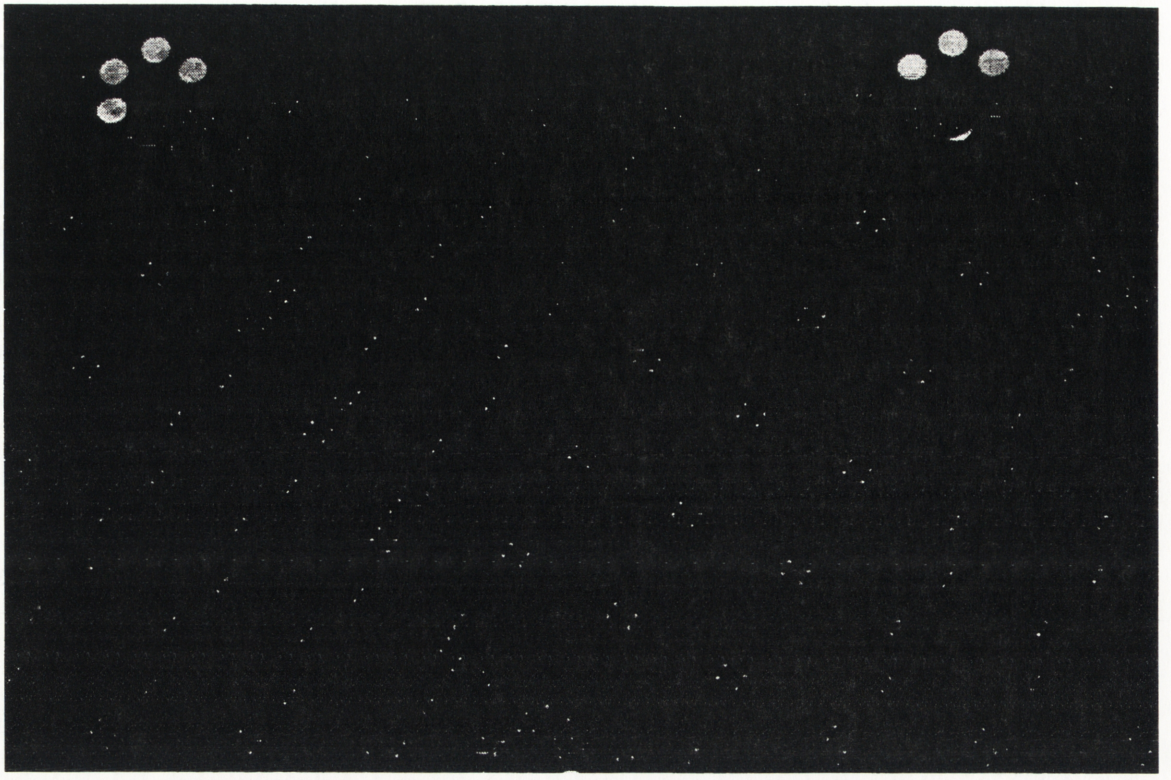

Figure 5.1. Digital image of triangular mirror panel and tiles with attached retro-reflecting targets. Panel and tile boundaries have been artificially highlighted for clarity.

This digital image can then be downloaded into a computer and the image displayed on a screen. Using appropriate software[9], the target images are identified and their image coordinates calculated. This then provides the required image coordinate data required for processing with the photogrammetric bundle adjustment software described above.

Appendix 5.2 describes the procedures and software used to perform a photogrammetric analysis of the captured digital images.

5.3 Measurement philosophy

The overall aim of photogrammetric surface measurement was to:

(i) assess the quality of concentrator reflecting surfaces, and
(ii) predict the focal region flux distribution for sunlight reflected off the measured surfaces.

Issue (i) can be assessed by orienting the measured surface to have the same coordinate orientation as an ideal dish (usually alignment of z-axes) and then simply subtracting measured z-coordinates from their ideal counterparts. Issue (ii) requires a more complex analysis to extract surface normal information from the numerical surface coordinates.

[9] DISKVIEW. Associate Professor Mark Shortis. Department of Geomatics, University of Melbourne, Melbourne, Australia.

As the photogrammetric technique was examined and experimented with, it became apparent that the greatest limitations were imposed by the time required to 'target up' the surfaces to be measured, and the subsequent digitisation and processing of the image coordinates of the targets. This then implied a trade-off between achieving improved surface accuracy through high target densities, and the processing time required for these target densities.

However, it also became apparent that using even modest target densities would make the time required to measure the surface of the entire 400 m^2 dish prohibitive. It was decided at an early stage that a more realistic philosophy of measurement would be to measure representative parts of the dish, and then to duplicate these around a set of key coordinates defined on the dish surface to enable a 'pseudo reconstruction' of the entire reflecting surface. To this end it was decided to:

(i) measure one representative mirror tile from each of the nine representative panel types on the dish surface;
(ii) measure the coordinates of the vertices of all mirror tiles on each of the nine panel types;
(iii) measure the coordinates of the vertices of all mirror panels across the surface of the 400 m^2 dish.

The mirror tiles would then be duplicated and placed across the panel surfaces according to the vertices measured on the panels. These mirror covered panels would then be duplicated and placed in turn across the panel vertices measured across the surface of the 400 m^2 dish.

Using this schema, it was apparent that the mirror tiles become the fundamental 'working unit' upon which the measurement of surface normal information needs to be applied. Once the tile surface coordinates and their associated normal vectors have been calculated, they need only be duplicated to the appropriate positions on the mirror panels, and then the relevant panels (covered with tiles and surface normals) can be duplicated across the surface of the entire 400 m^2 dish.

It is recognised that this approximation technique introduces a number of limitations on the realism of the surface representation that can be achieved. Specifically, the orientation of the tiles across a panel surface will be accurately represented, but the variation arising from each individual tile will be lost, as only one tile type is being placed at the coordinates of all the tiles on the panel surface. Similarly, the orientation of all the mirror panels will be represented accurately, but the variations arising from the characteristics of each individual mirror panel will be lost.

Figure 5.2 shows the schema adopted for identifying panels and tiles on the 400 m^2 dish surface.

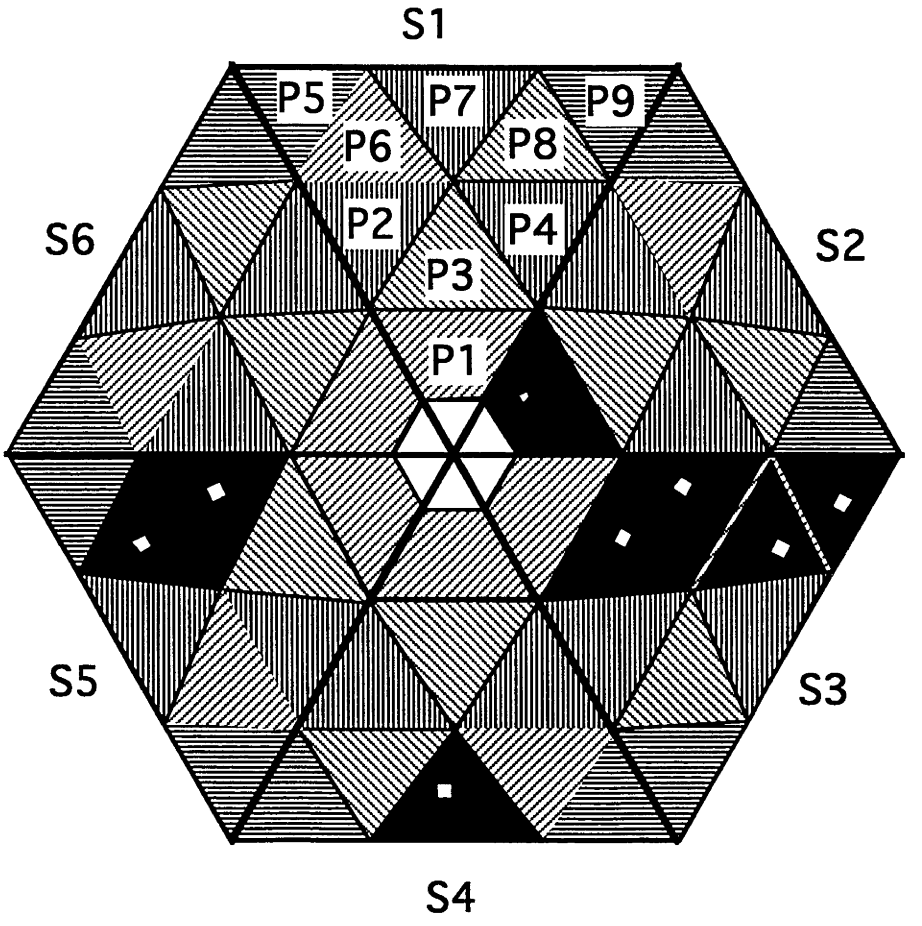

Figure 5.2. Classification schema used to identify panels and tiles on the surface of the 400 m^2 dish.

The figure above shows the hexagonal aperture of the dish divided into six sectors (S1 to S6), with nine panel types evident in each sector (P1 to P9, shown cross-hatched for clarity). Using this nomenclature, panels are referred to by their sector and panel position, such that the 2nd panel on sector 3, would be referred to as 's3p2', etc. The solid black panels in Figure 5.2 indicate those panels that were chosen for photogrammetric measurement. As only one tile (shown as small white rectangles in Figure 5.2) was measured on each panel type, these tiles are simply referred to by appending a 't' to the panel label, such that the mirror tile measured on panel s3p2 would be referred to as 's3p2t'.

It will be seen from Figure 5.2 that only eight panel types are identified as having been measured photogrammetrically. Unfortunately the ninth panel type was unable to be measured due to an oversight which resulted in the omission of photography of the panel. It was decided to duplicate the measured surface of the 5th panel type (as it corresponds most closely with the ninth panel position) into the ninth panel orientation to provide the full complement of panels for the dish surface in later analysis.

Experience was gained in the early stages of the photogrammetric method by studies conducted using the 20 m^2 tiled dish. The following section will describe the results of these investigations using this dish, which will also outline several of the experimental principles that were developed and used for characterising the surface of the 400 m^2 dish.

5.4 Surface Measurement

Four sets of surfaces were measured. These were:

(i) The 20 m^2 dish surface (320 targets).

(ii) One 30x30 cm (36 targets) and seven 60x60 cm mirrors tiles (171 targets) from the mirror panels on the 400 m^2 dish (eight tiles in total).

(iv) The vertices of all mirror tiles across eight mirror panels from the 400 m^2 dish

(iii) The coordinates of the panel vertices across the entire 400 m^2 dish..

The methodology and preliminary photogrammetric results for each of surface sets will be presented in turn.

5.4.1 Assessment of the 20 m^2 tiled dish surface

5.4.1.1 Methodology for the 20 m^2 tiled dish

Due to the large number of tiles (2262) on this dish, it was obviously impractical to place targets on the surface of every tile. It was decided to place targets at the corner junction of approximately every 6th tile, and every second annular ring of tiles. The corner junction provides the point of closest contact to the underlying fibreglass dish substrate, and the chosen arrangement of targets produced an array of 320 target points. Figure 5.3 shows the layout (in the x-y plane) of the target placements on the 20 m^2 tiled dish, with an inset shown of the labelled target image used for all the film-based photogrammetric assessments.

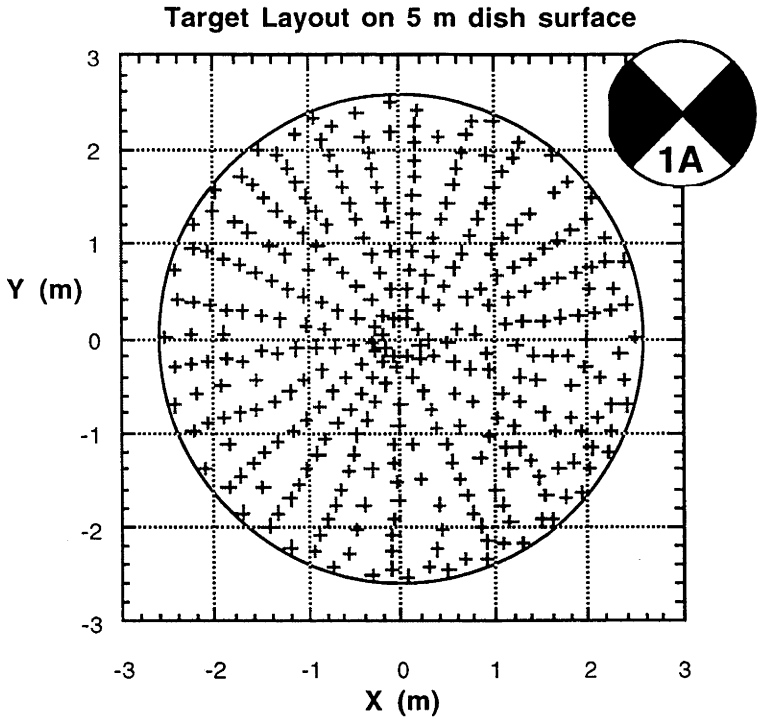

Figure 5.3. Layout of 320 targets across the surface of the 20 m^2 tiled dish. Inset at upper right shows a target image of the type used on the dish.

Four photographs were taken of the dish from four different stations with 90° of camera 'roll' between stations (that is, the camera was rotated 90° about an axis parallel to the lens axis), as shown in Figure 5.4 below.

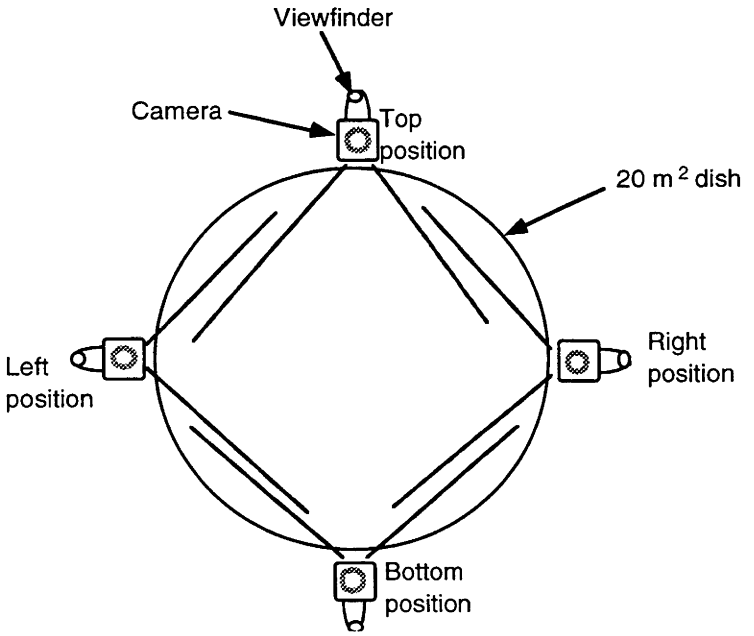

Figure 5.4. Camera station layout around the 20 m^2 dish.

The distances between three (approximately) equally spaced targets around the periphery of the dish were measured and used to create both 'control points' (that is,

target points whose coordinates were accurately known), and a reference plane and coordinate system against which all other parameters would be measured. The photographs of the dish were developed, and the target images were viewed and digitised using an analytical stereoplotter. Photogrammetric processing[10] was undertaken on the digitised target image positions (called 'image coordinates') and the 3-dimensional object coordinates of the targets were calculated. Image space precision was calculated to be 7.7 μm (that is, the precision of the measured target coordinates on the photographs), which gave an average object space precision of 0.9 mm (this is the rms error expected in the actual coordinates calculated for the dish surface). The overall relative network precision was 1:7000 (this is the ratio of the largest dimension of the object to the rms object space precision).

As the photogrammetric calculations can produce coordinate data that are not aligned in the desired orientation, an algorithm named TRIANGLEREORIENT was written to take an array of surface data points and reorient them into a specified position and orientation defined by three reference coordinates. TRIANGLEREORIENT was also developed for later use when duplicating and aligning mirror tiles and panels onto the 400 m^2 dish surface.

5.4.1.2 Characterisation of the 20 m^2 dish

Figure 5.5 shows the photogrammetrically measured surface calculated for the 20 m^2 tiled dish, after reorientation by TRIANGLEREORIENT to align the dish with a regular coordinate system (that is, dish vertex at the origin, with the dish axis aligned with the z-axis).

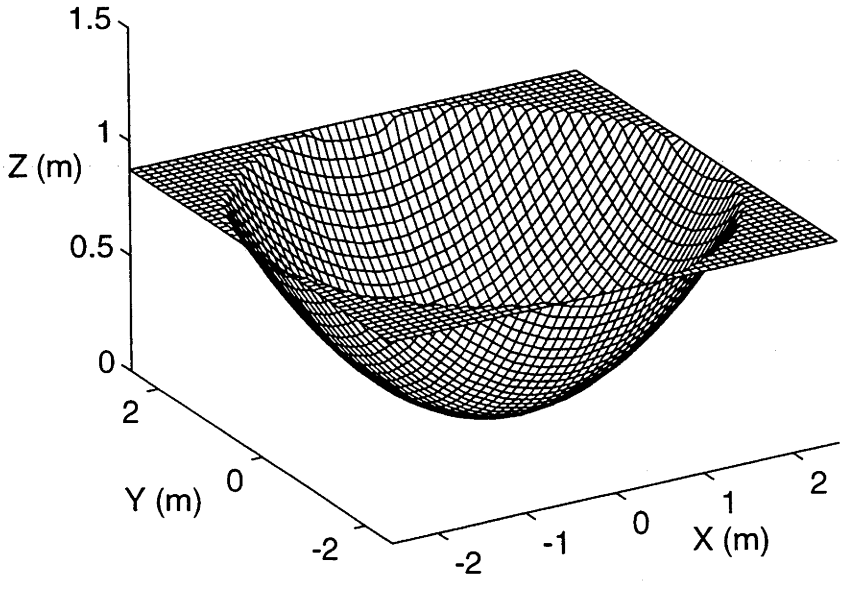

Figure 5.5. Photogrammetrically measured surface of the 20 m^2 dish.

[10] CRAMPA suite of programs. Associate Professor Mark Shortis. Department of Geomatics, University of Melbourne, Melbourne, Australia.

5.4.1.3 Z-coordinate deviation assessment

While Figure 5.5 appears to show a regular paraboloid, more accurate assessment of its conformance to the ideal paraboloidal shape can be undertaken by calculating the deviation of the measured z-coordinates from the ideal shape. Definition of the ideal shape, however, requires a description of the closest fitting paraboloid to the measured data. This can be found by taking a least squares fit to the data coordinates to calculate the focal point of the measured surface data. As the ideal paraboloid is defined by,

$$z = \frac{x^2 + y^2}{4f} \qquad \textbf{(5.1)}$$

where f is the focal length of the paraboloid, it can be seen that plotting the z-coordinates versus $\left(x^2 + y^2\right)/4$ (that is, $r^2/4$) should yield a straight line with a slope,

$$m = \frac{1}{f} \qquad \textbf{(5.2)}$$

and an intercept equal to whatever z-axis offset may exist in the data set. Thus,

$$f = \frac{1}{m} \qquad \textbf{(5.3)}$$

Figure 5.6 shows the plot of z versus $\left(x^2 + y^2\right)/4$ for the 20 m^2 dish data.

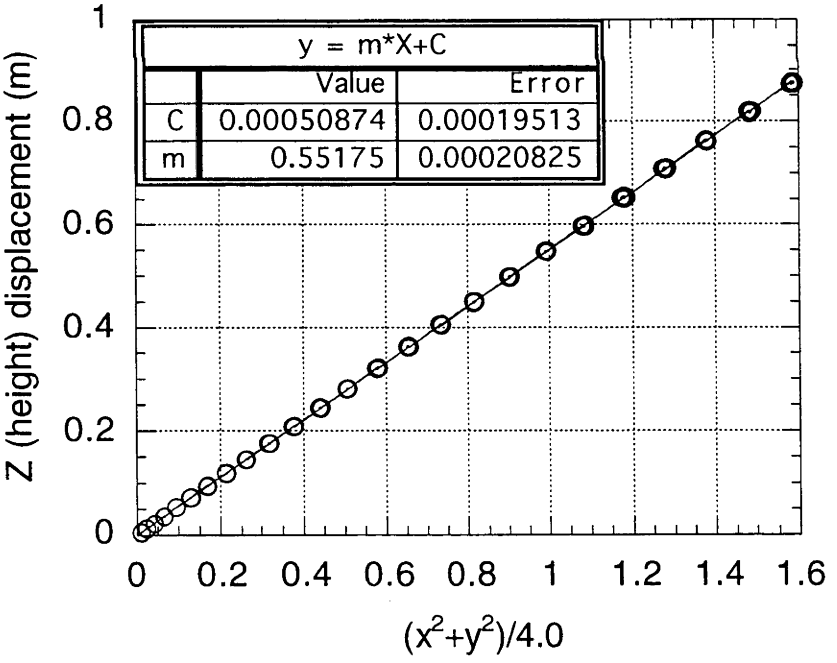

Figure 5.6. Plot of z versus $(x^2+y^2)/4$ for the 20 m^2 dish surface.

The slope of 0.55175 m^{-1} in Figure 5.6 shows the dish to have a focal length of 1.8124±0.0007 m. This value can be used to create an ideal paraboloid against which to compare the measured data surface. Deviations were calculated by subtracting the ideal from the measured z-coordinates, that is,

$$DZ = Z_{measured} - Z_{ideal} \qquad (5.4)$$

It is thus seen that negative deviations indicate that the measured surface falls below the ideal at that point, while positive deviations show the measured surface to be higher than the ideal.

Figure 5.7 shows a surface plot of the z-coordinate differences between the measured data and an ideal paraboloid having a focal length of 1.8124 m.

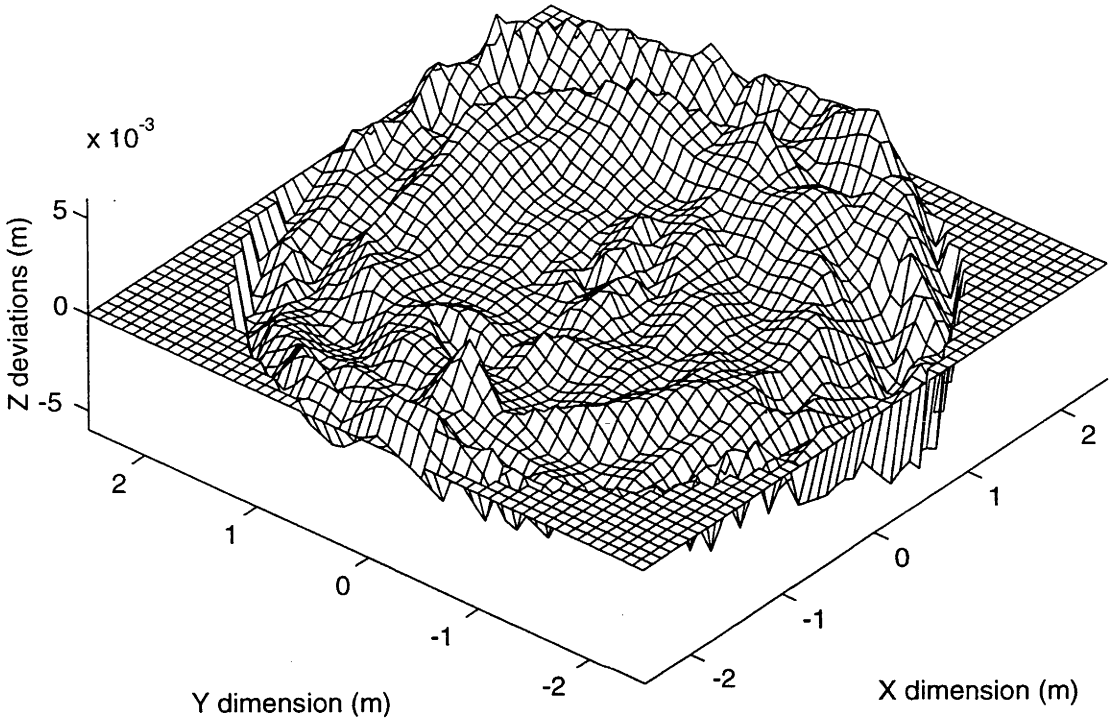

Figure 5.7. Spatial distribution of the z-coordinate deviations between the measured data points on the surface of the 20 m² tiled dish and an ideal paraboloid having a focal length of 1.8124 m.

Figure 5.7 shows maximum deviations in the order of ±5~6 mm. A frequency distribution of these deviations provides a statistical estimate of the error in the measured dish coordinates. Figure 5.8 displays the statistical spread of errors.

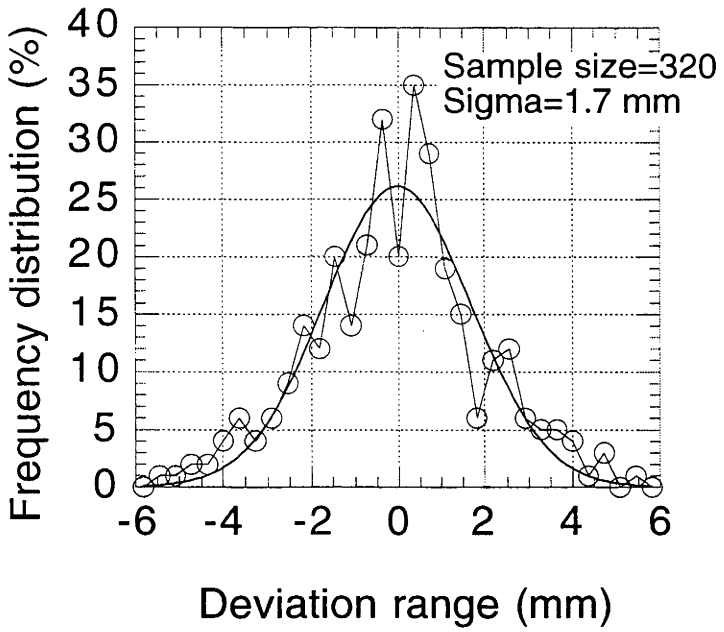

Figure 5.8. Frequency distribution of the z-coordinate deviations shown in Figure 5.7. Fitted Gaussian distribution shown as a smooth curve through the data points.

Figure 5.8 shows that the spread of errors follows an approximately Gaussian distribution, with a mean of zero and a standard deviation of 1.7 mm.

5.4.2 Assessment of mirror panel vertices across the 400 m^2 dish surface.

5.4.2.1 Methodology for the 400 m^2 dish

Measurement of the mirror panels across the surface of the 400 m^2 dish surface was achieved by placing targets at identical positions near the vertex of each of the 54 mirror panels on the dish surface. Figure 5.9 shows the target layout that was used.

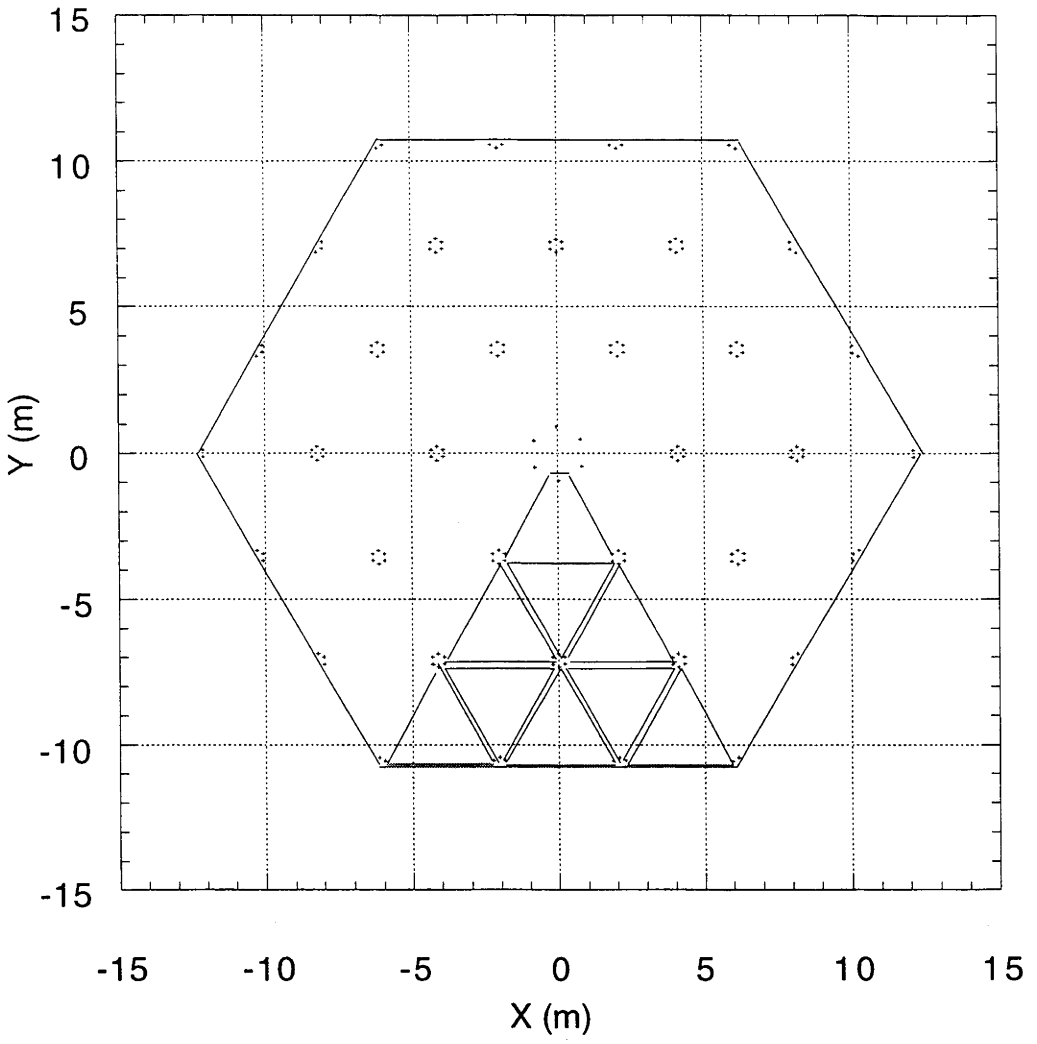

Figure 5.9. Target layout (small crosses) across the triangular mirror panels on the 400 m^2 dish surface. Dish boundaries and one sector of panels have been highlighted for clarity.

Figure 5.10 shows a plan of the camera stations (labelled A, B, C, D, E and F) that were used to photograph the surface of the dish.

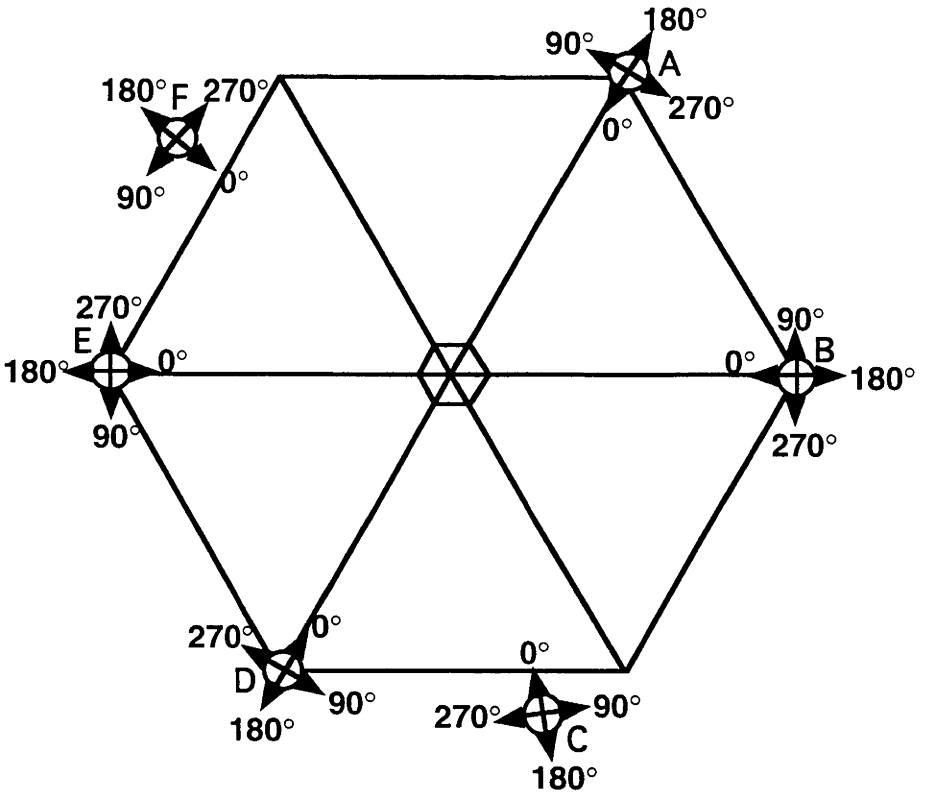

Figure 5.10. Camera station layout around the 400 m² dish.

As the 400 m² dish had no actuation at the time of the measurements, it was fixed in its rest position, with its axis pointing vertically upwards. A viewing distance of approximately 30 m from the dish vertex was required to enable a full image of the dish to be captured in the camera's field of view. To establish this photographic geometry, a large crane (40 m maximum boom extension) was hired to allow photography to be undertaken from the required height above the dish.

Consultations with Shortis (1993a) indicated that six camera stations, with at least two photographs taken from each station having 90° camera roll between photographs, would provide a suitable network to achieve an overall object space precision of 1:25,000, or an approximate measurement resolution of ± 1 mm on the dish surface. This figure was chosen, as a coordinate precision of ± 1 mm between panel vertices spaced approximately 4 m apart would allow a surface slope error precision of approximately 0.25 milliradian to be achieved.

As shown in Figure 5.10, four photographs were taken from each station, with 90° camera roll between shots, providing a total of 24 photographs.. As film based photography was used for this exercise, with subsequent target image digitisation conducted manually using an analytical stereo plotter, it was decided to only use 12 photographs of the 24 that were taken of the dish, in order to minimise the time taken to process the results. As photogrammetric processing software was not available to the author at the time of these measurements, a commercial organisation[11] was employed to process the data files of digitised image coordinates. Image coordinate uncertainties of 1.5 μm were observed from the photogrammetric bundle adjustment, which produced an average object space (target coordinate) precision of 1.3 mm.

[11] Broken Hill Pty. Ltd. Engineering Division, Wollongong, NSW, Australia.

5.4.2.2 Results of the photogrammetric surface characterisation of the 400 m^2 dish

Figure 5.11 shows a surface plot of the reconstructed data coordinates from the photogrammetric characterisation of the mirror panel vertex targets across the surface of the 400 m^2 dish. The dish has been reoriented using TRIANGLE REORIENT such that the dish axis is aligned with the z-axis of a regular coordinate system.

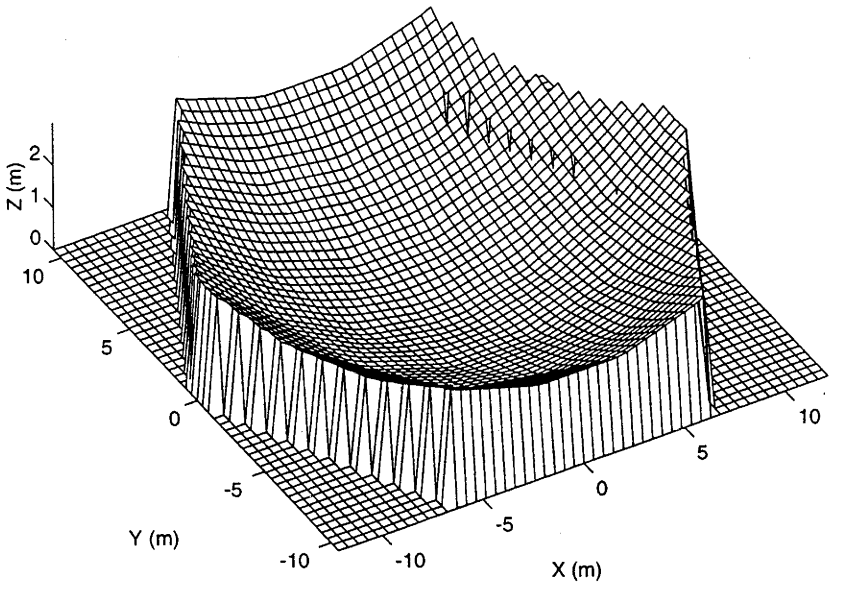

Figure 5.11. Surface plot of the photogrammetric characterisation of the 400 m^2 dish surface. (Vertical lines on the far side of the dish surface are plotting anomalies, and are not part of the surface data.)

5.4.2.3 Z-coordinate deviations of the panel vertices

Later analysis of the complete set of mirror panels duplicated and oriented into their correct orientations on the dish surface, showed an over-all focal length of 13.075 ± 0.008 m. This value was used to construct an ideal paraboloidal surface with which to compare the measured data points, and allowed a z-coordinate deviation plot (calculated by subtracting the ideal from the measured z-coordinates) to be constructed. Figure 5.12 shows a surface plot of the spatial distribution of the z-coordinate deviations.

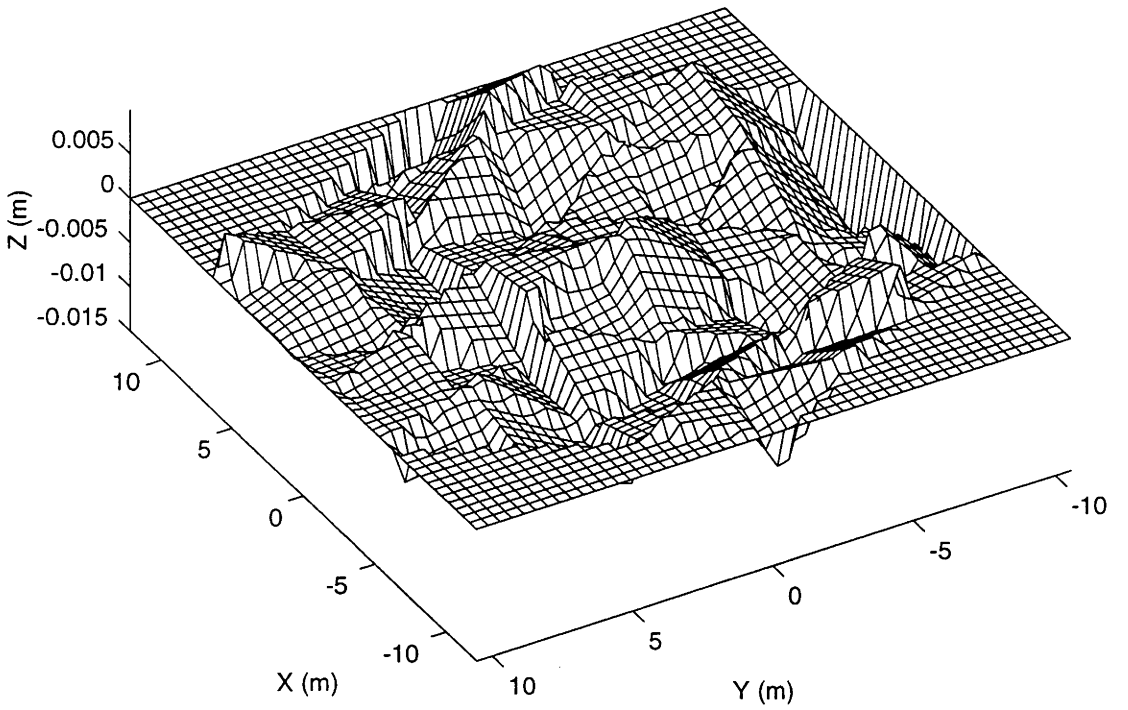

Figure 5.12. Spatial distribution of the z-coordinate deviations of the panel vertices across the surface of the 400 m^2 dish.

The deviations of the individual triangular panels can be clearly seen in Figure 5.12. It is interesting to note that this information could be used directly to adjust the orientations of the mirror panels to take up a more ideal orientation on the dish surface.

Figure 5.13 shows a frequency distribution of z-coordinate deviations for the panel vertices.

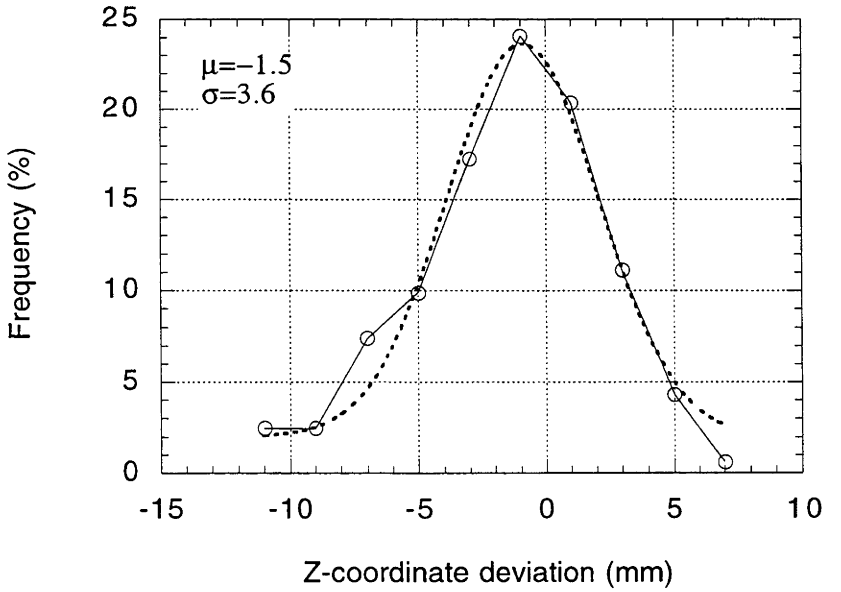

Figure 5.13. Frequency distribution of z-coordinate deviations for the panel vertices of the 400 m^2 dish.

As can be seen in Figure 5.13, the distribution of errors is approximately Gaussian, with a mean of -1.5 mm and a standard deviation of 3.6 mm. Note that the mean and standard deviation are calculated using the standard statistical formulas applied to the measured data set, and are not those calculated from the best-fit Gaussian curve shown in Figure 5.13. The best fit values show a mean of -0.88 mm and a standard deviation of 4.5 mm. These apparent differences are most likely due to the deviation of the actual frequency distribution from an ideal Gaussian form.

As it is the variation between panels (rather than the average offset, represented by the mean) that contributes to the overall surface slope error of the mirror panels (but is by no means the only contributor to the overall surface slope error), the standard deviation can be used to estimate the slope error expected from the panel coordinate deviations. The average distance of 3.9 m between vertex targets predicts that a variation of ± 3.6 mm in the z-dimension will introduce a slope error of 0.9 milliradian. The negative sign of the mean indicates that on average the panel vertex coordinates are slightly lower than their ideal positions.

5.4.3 Assessment of panel surfaces on the 400 m^2 dish

5.4.3.1 Methodology for the 400 m^2 dish mirror panels

Photogrammetric assessment of the mirror panels on the surface of the 400 m^2 dish was conducted over two separate time periods, with approximately 2 years elapsing between the periods. The first assessment used film-based photogrammetry (as described in section 5.2.1 above) on one of the six inner panels of the dish (s2p1), as well as one of the 30x30 cm mirror tiles on its surface (s2p1t). The second assessment utilised the newer and more advantageous technique of digital photogrammetry (section 5.2.2), applied to seven mirror panels, as well as one 60x60 cm mirror tile on each of these surfaces. These panels were s3p2, s3p3, s5p4, s3p5, s3p6, s4p7 and s5p8, with associated tiles from each panel.

Alignment targets were placed in identical positions near the corners of each tile across both the 30 cm tiles on s2p1 (measured using film-based photogrammetry), and the 60 cm tiles on the seven panel types that were measured using digital photogrammetry, such that the representative tiles that were measured (section 5.4.4) could be easily duplicated and oriented into the other tile positions across the entire panel surfaces.

Figure 5.14 and Figure 5.15 show the schematic layout of the tile corner alignment targets across the s2p1 and s3p2 mirror panel.

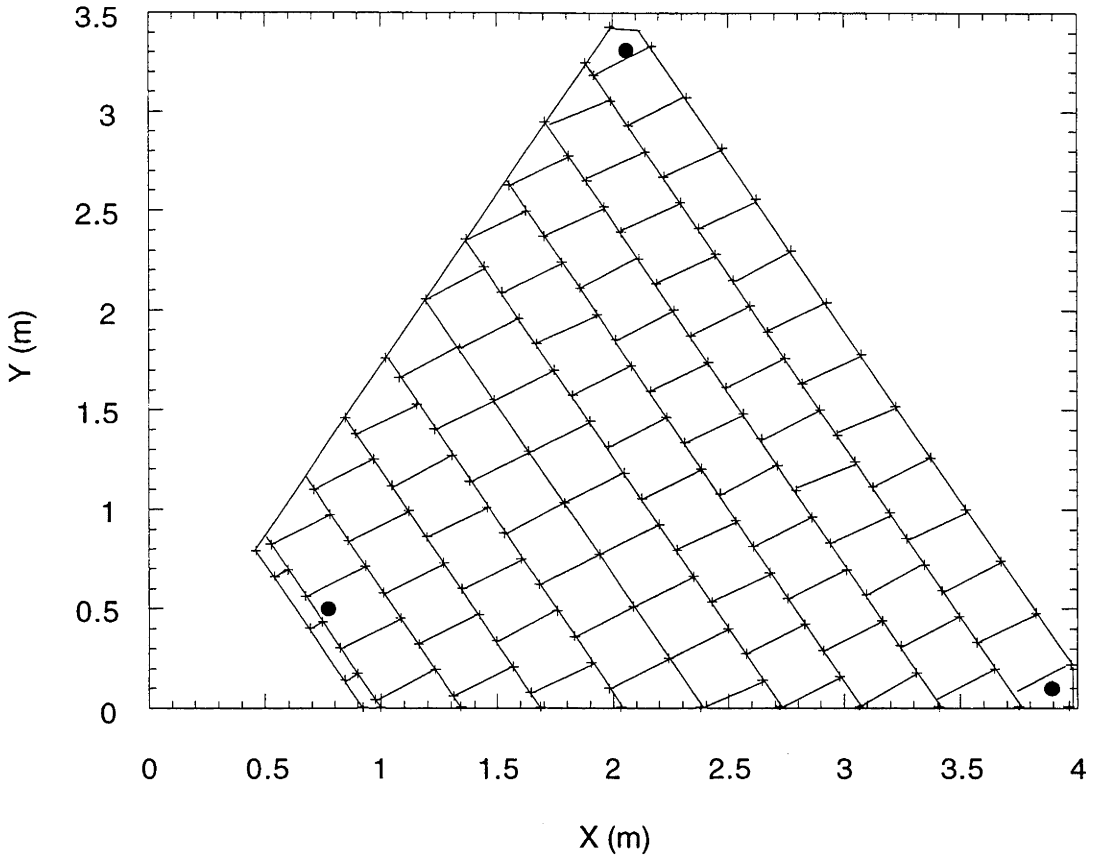

Figure 5.14. Target layout on s2p1 panel (covered with 30 cm tiles). Note (artificially enlarged) alignment targets near vertices of the panel.

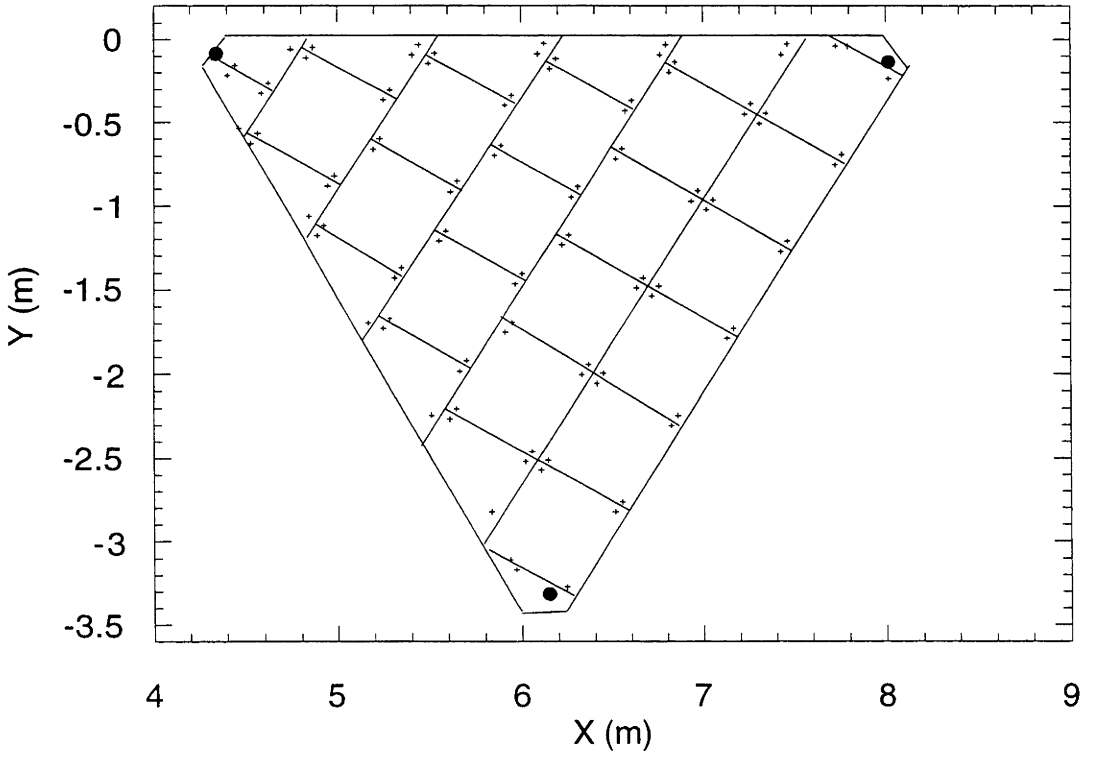

Figure 5.15. Target layout on s3p2 panel (covered with 60 cm tiles). Note (artificially enlarged) alignment targets near vertices of the panel.

Figure 5.14 and Figure 5.15 also show the alignment targets placed near the vertices of the panels (the targets have been slightly enlarged for clarity). These were placed in identical positions on each triangular mirror panel on the dish surface, and were later used to duplicate and orient the panels into their appropriate positions across the dish (measured in section 5.4.2).

The digital images of the targeted panels were processed and photogrammetric bundle adjustments performed on the data sets. Table 5.1 summarises the precision estimates that were calculated during the photogrammetric analysis of the mirror panel surfaces.

Table 5.1 Summary of photogrammetric precision estimates for measurements of the 400 m^2 dish mirror panels.

Panel name	Image coordinate uncertainty (μm)	Object space uncertainty (mm)	Overall network precision**
s2p1*	1.5	0.4	1:13,000
s3p2	0.35	0.1	1:40,000
s3p3	0.35	0.1	1:40,000
s5p4	0.4	0.11	1:40,000
s3p5	0.28	0.08	1:40,000
s3p6	0.5	0.12	1:40,000
s4p7	0.32	0.1	1:40,000
s5p8	0.3	0.09	1:40,000

*Processed using film-based photogrammetry

**The ratio of the largest dimension of the object to the rms object space precision.

5.4.3.2 Characterisation of the mirror panel surfaces

Figure 5.16 shows the surface mesh plot of the s2p1 panel from the photogrammetric data. The figure shows the panel adjusted into an ideal paraboloidal orientation, with its three alignment vertices aligned with ideal paraboloidal coordinates.

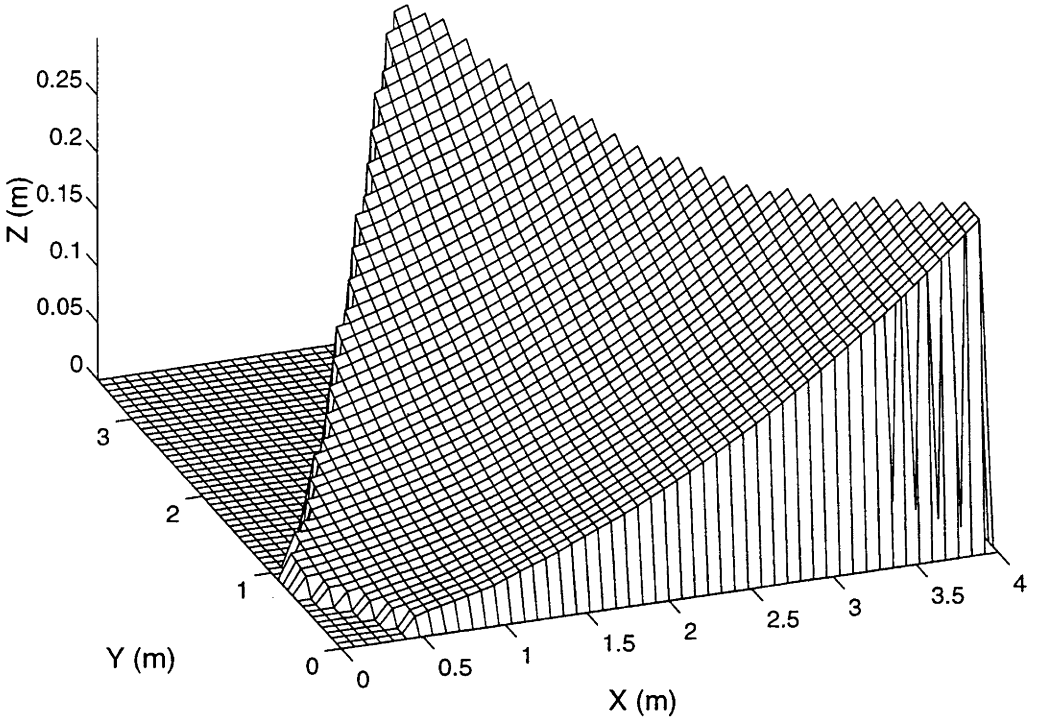

Figure 5.16. Surface plot of measured tile corner target points on panel s2p1 (covered with 30 cm tiles). Surface interpolated to a 50x50 grid.

5.4.3.3 Z-coordinate deviation assessments

As it is the panel surfaces that determine the final alignment of the mirror tiles, it was considered appropriate to duplicate and orient the relevant mirror panels into their respective positions (determined by the vertex coordinates measured in section 5.4.2.2) on the 400 m^2 dish surface, in order to gain an overall focal length determination for the dish. This created a data surface containing more than 5200 points. Figure 5.17 shows the z-versus $(x^2+y^2)/4$ plot for this surface.

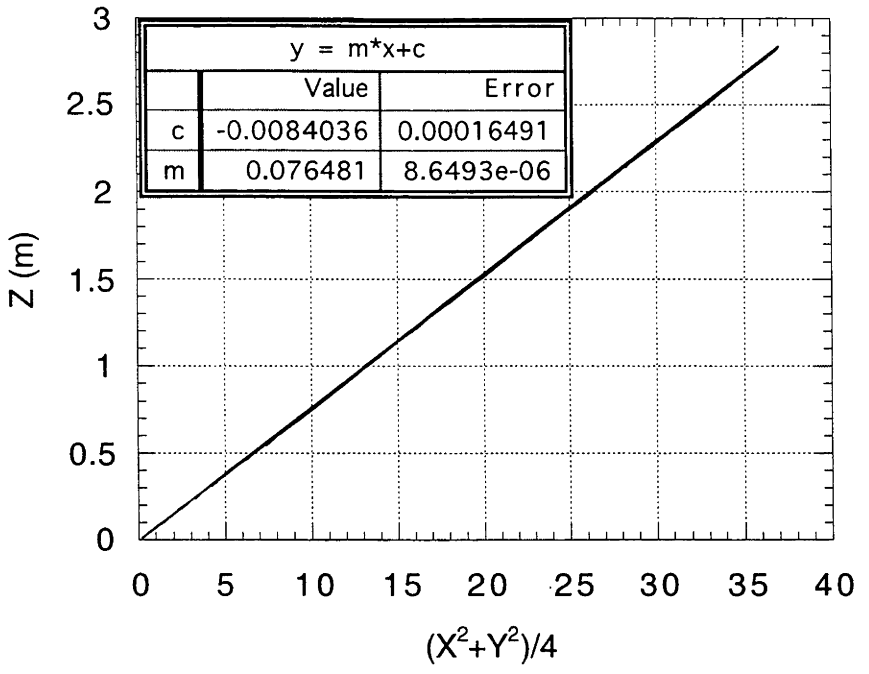

Figure 5.17. z versus $(x^2+y^2)/4$ for the data surface created from the duplication and orientation of panels across the entire surface of the 400 m^2 dish

Figure 5.17 shows a slope of 0.076481 m^{-1}, which in turn predicts a focal length of 13.075 ± 0.002 m for the dish. Using this value to construct an ideal paraboloid with which to compare the measured data, allows a z-coordinate deviation plot to be constructed for every data point across the panel surface. Plots of the measured coordinates subtracted from the ideal coordinates were constructed. Figure 5.18 shows the spatial distribution of surface deviations across the s2p1 panel aligned to an ideal paraboloidal orientation using a dish of focal length 13.075 m.

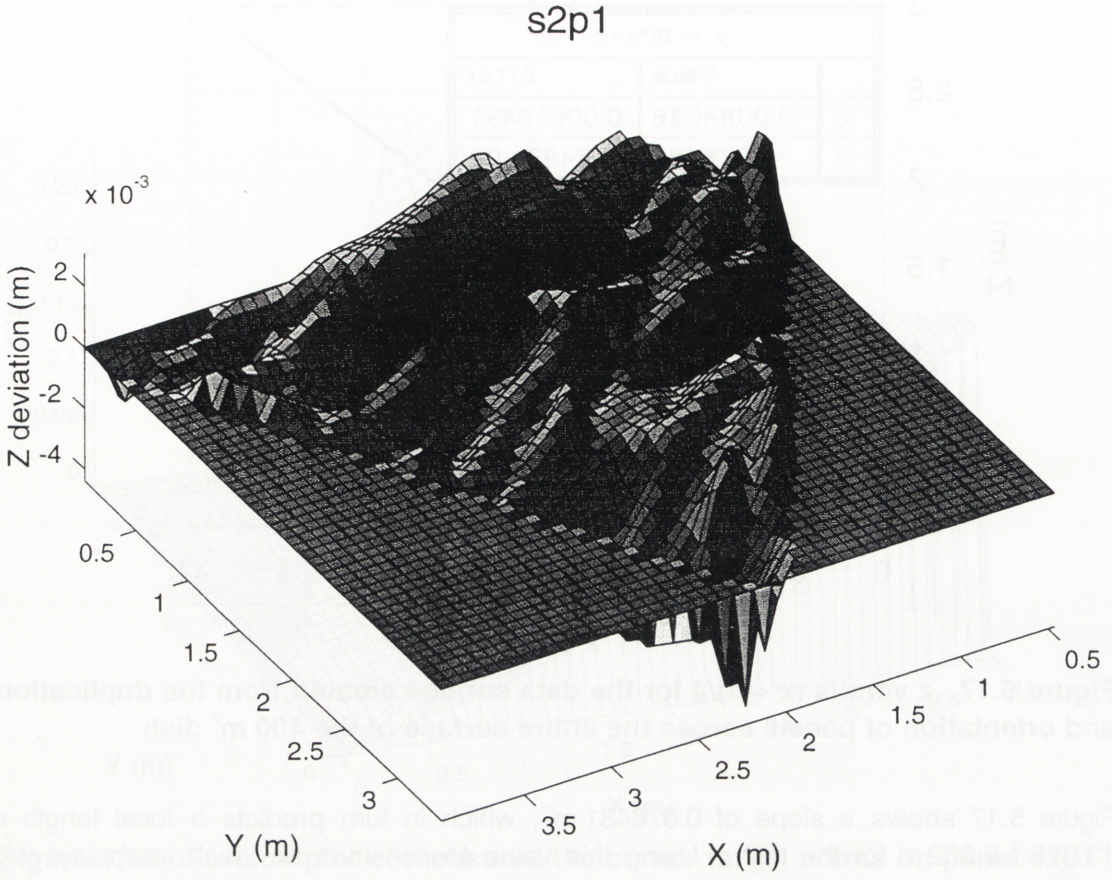

Figure 5.18. Spatial distribution of z-coordinate deviations across the s2p1 mirror panel (aligned to an ideal paraboloidal orientation).

Figure 5.19 shows the frequency distribution of the z-coordinate deviations of Figure 5.18.

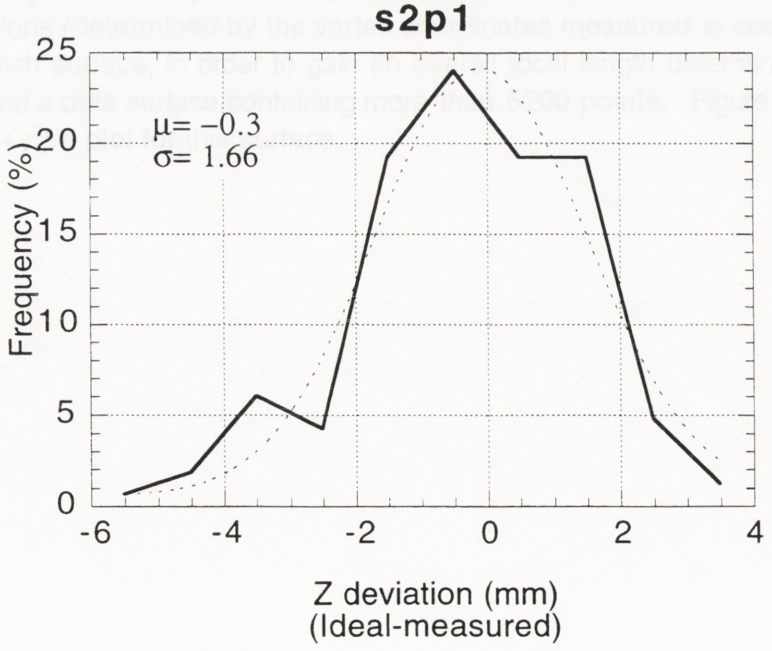

Figure 5.19. Frequency distribution of z-coordinate deviations across the s2p1 mirror panel. Dotted line shows the best-fit Gaussian distribution to the data.

Figure 5.19 shows that the s2p1 panel has an overall negative z-coordinate deviation (mean=-0.3 mm), which indicates that the panel is slightly less concave than its corresponding ideal paraboloidal surface. Appendix 5.3 contains spatial distribution plots and z-coordinate deviation frequency distributions for the seven remaining panels.

Table 5.2 summarises the z-coordinate deviations for the measured panels, aligned with an ideal paraboloidal orientation.

Table 5.2. Summary of mean and standard deviations for the triangular mirror panels, aligned with an ideal paraboloidal orientation.

Surface	Mean deviations (mm)	Standard deviation of deviations (mm)
s2p1	-0.3	1.66
s3p2	8.1	4.7
s3p3	7.1	3.8
s5p4	4.3	4.0
s3p6	4.5	3.0
s4p7	8.2	4.1
s5p8	5.2	3.2

5.4.4 Assessment of the mirror tile surfaces on the 400 m^2 dish.

5.4.4.1 Methodology for the 400 m^2 dish mirror tiles

The mirror tiles on the surface of the 400 m^2 dish consist mostly of 60x60 cm tiles and some 30x30 cm tiles that had been elastically deformed to hold an approximately paraboloidal shape while mounted on the triangular panels, characterised in section 5.4.3 above.

The tiles were visually inspected, and nearly all tiles displayed 'ripples' in their surfaces, which were an obvious deviation from the smoothly varying paraboloidal curve. However, the ripples themselves were also continuous in nature, and showed no sharp discontinuities or rapid inflections.

The 30 cm tile chosen for measurement was one of approximately 80 on the s2p1 panel, and showed features in common with a number of other tiles, with an apparent trough and slight peak in both dimensions. A 6x6 array of targets were chosen for placement across this tile, as it appeared that this target sampling density quite adequately covered the apparent frequency of ripples on the tile surface. An alignment template was used to place the four corner targets in identical positions on all tiles across the panel to allow for later duplication and alignment of the measured tile onto the other tile positions on the panel.

Shannon's sampling theorem was used as an approximate guide for target point density selection, such that the spatial frequency of the sample points was roughly twice the frequency of the surface deviations apparent in the tile. Using a 6x6 array on a 30 cm

tile gave a sampling frequency of approximately 20 m^{-1}, which in turn allowed measurement of spatial frequencies of up to 10 m^{-1}. The observable ripple frequencies on the tiles were calculated to be approximately 2 to 3 m^{-1}, and it was thus considered that the chosen sampling density would be adequate to model the variations observed on the tiles.

The target density was increased slightly for the 60 cm tiles, with an approximate array of 13x13 targets being used, 171 target points in total. Targets used on the 60 cm tiles were 5 mm in diameter, with four 20 mm diameter targets placed at the corners, with an identical orientation and spacing on each tile. These latter, larger targets were placed in identical corner positions on every tile across the seven panel types that were measured using digital photogrammetry, and served as alignment indices for placement of the measured tiles onto the respective positions of the remaining tiles on the mirror panels during later processing.

Figure 5.20 and Figure 5.21 show the layout of targets placed across the surfaces of the 30 cm tile (s2p1t) and one of the 60 cm tiles (s3p2t).

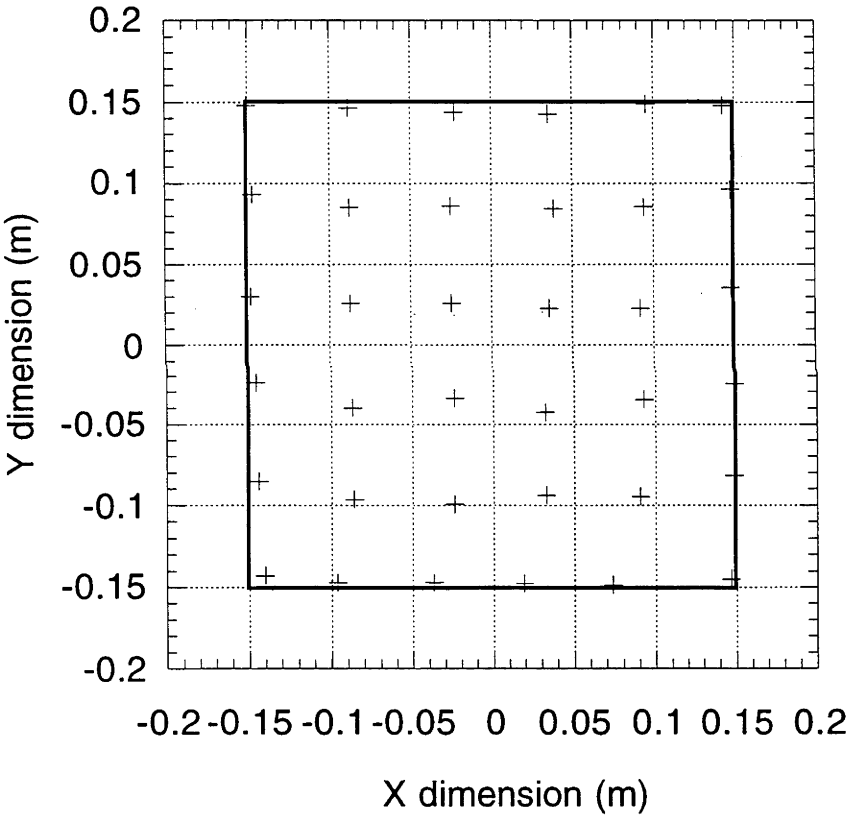

Figure 5.20. Target layout on the 30x30 cm mirror tile (s2p1t). Crosses mark the placement of targets, while the solid line marks the boundary of the mirror tile.

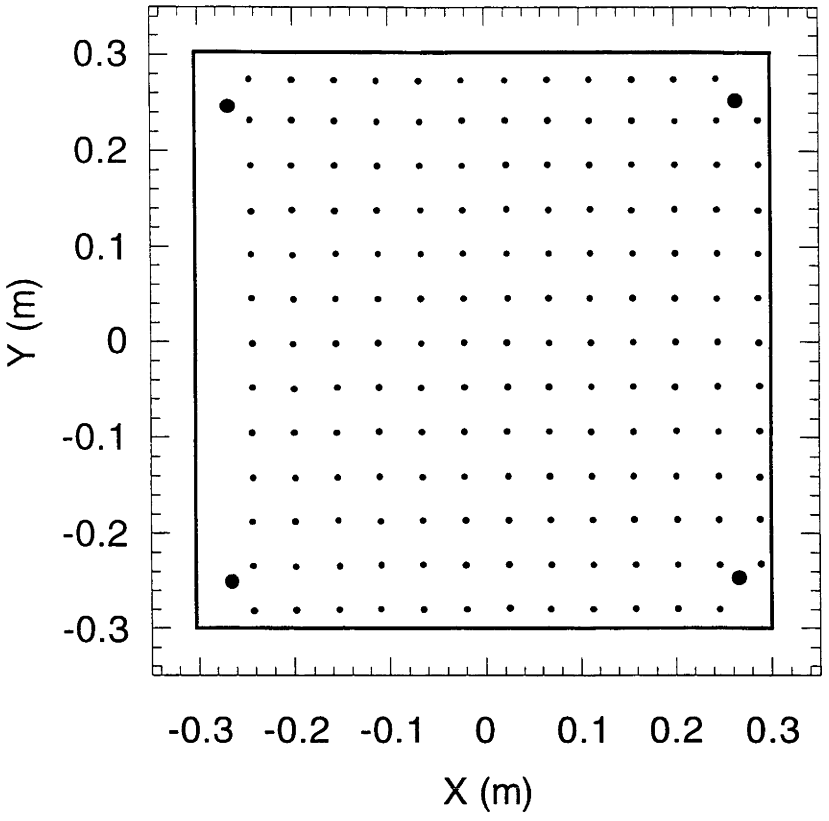

Figure 5.21. Target layout on a 60x60 cm mirror tile (s3p2t), showing large, corner alignment targets. Solid line shows the tile boundary.

The photogrammetric software available to the author at the time of the measurements could only process a maximum of 12 photographs. This mandated using a camera station layout for the mirror tiles whereby three photos from four camera stations were taken, with 90° camera roll between photos. The camera roll sequence was staggered between stations such that an equal number of photos having all roll positions (0°, 90° ,180° and 270°) was achieved. Figure 5.22 shows a typical camera station layout around a tile.

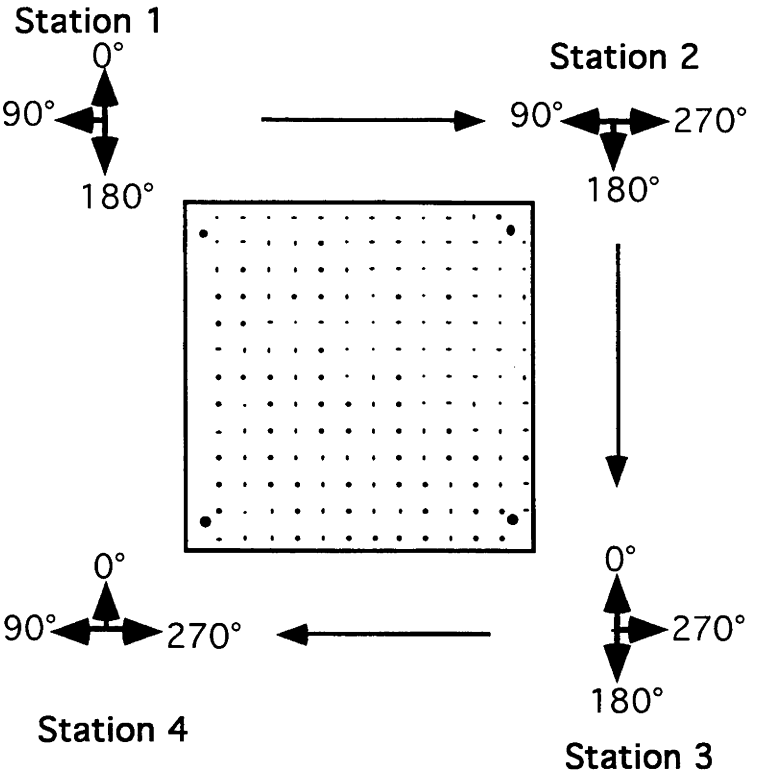

Figure 5.22. Camera station layout around a mirror tile, showing staggered camera roll between stations.

The images of the tile surfaces were processed and analysed using the photogrammetric bundle adjustment software. Table 5.3 summarises the coordinate precision estimates resulting from the photogrammetric analysis of the mirror tiles.

Table 5.3. Summary of photogrammetric precision estimates for measurements of the 400 m^2 dish mirror tiles.

Tile name	Image coordinate uncertainty (μm)	Object space uncertainty (mm)	Overall network precision
s2p1t (30 cm)*	4.14	0.04	1:7,500
s3p2t (60 cm)	0.32	0.02	1:25,000
s3p3t (60 cm)	0.32	0.02	1:25,000
s5p4t (60 cm)	0.32	0.02	1:25,000
s3p5t (60 cm)	0.32	0.02	1:25,000
s3p6t (60 cm)	0.32	0.02	1:25,000
s4p7t (60 cm)	0.32	0.02	1:25,000
s5p8t (60 cm)	0.32	0.02	1:25,000

*Processed using film-based photogrammetry

5.4.4.2 Results of the photogrammetric assessment

Figure 5.23 and Figure 5.24 show the photogrammetrically determined surfaces for the s2p1t and s3p2t mirror tiles shown in Figure 5.21 and Figure 5.22, centrally aligned about the z-axis, and with three of their vertices touching the x-y plane.

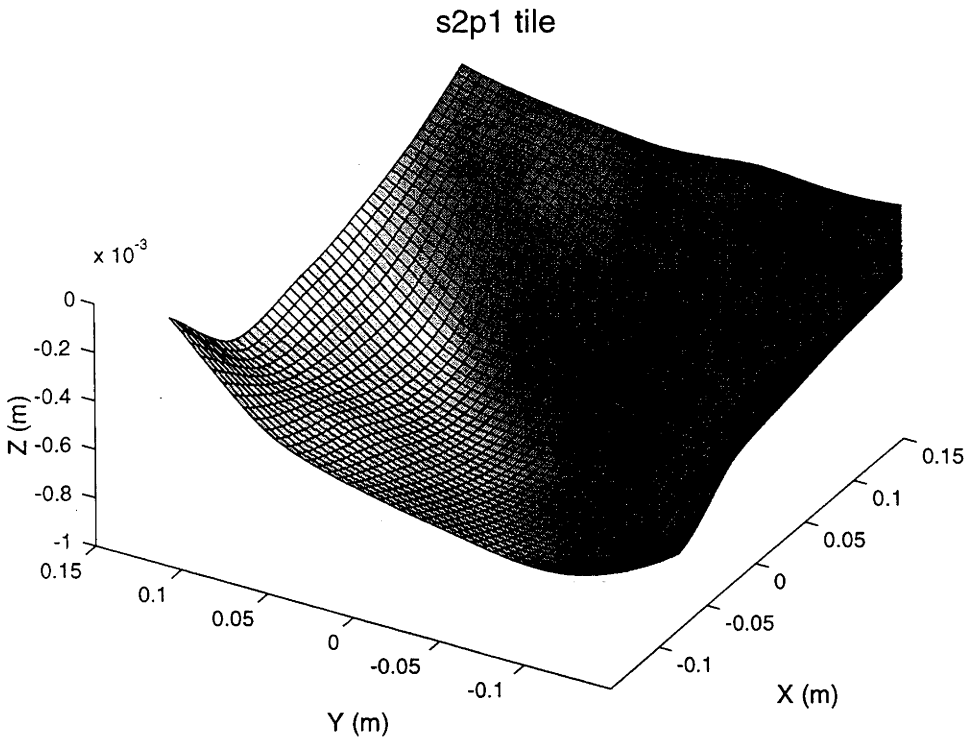

Figure 5.23. Surface plot of the s2p1t 30x30 cm tile shown in Figure 5.20 (interpolated to a 50x50 grid).

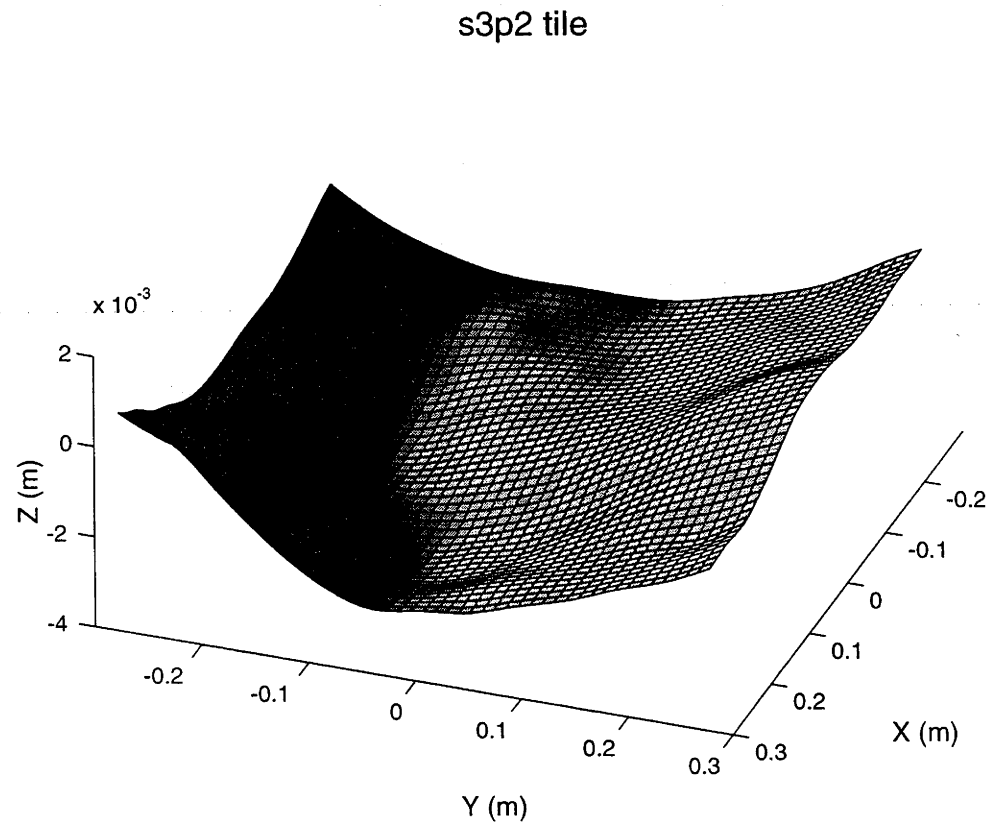

Figure 5.24. Surface plot of s3p2t 60x60 cm tile shown in Figure 5.21 (interpolated to a 50x50 grid).

5.4.4.3 Z-coordinate deviation assessments

Comparison of the measured tiles with an ideal paraboloid required reorienting the tiles to take up an ideal paraboloidal orientation. This was accomplished by calculating the ideal coordinates of three vertices of the tiles for a paraboloid having a focal length of 13.075 m (calculated in section 5.4.3.3), and using TRIANGLE REORIENT to translate and rotate the tiles into their appropriate paraboloidal orientations.

Figure 5.25 shows the plot of z-coordinate versus $\left(x^2 + y^2\right)/4$ for all the measured mirror tiles.

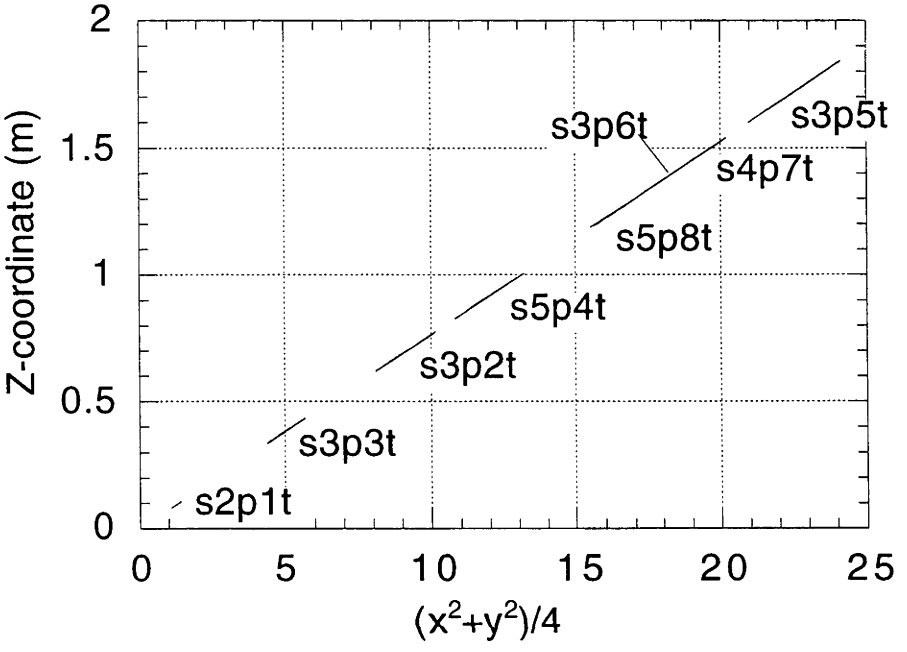

Figure 5.25. Plot of z-coordinate versus $(x^2+y^2)/4$ for the measured mirror tiles on paraboloidal orientations.

Table 5.4 (below) lists the focal lengths calculated from Figure 5.25. However, it was considered that the deviations of the tiles should be calculated against an ideal paraboloid having the average focal length of 13.075 m, and not against the individual focal lengths of each tile. Z-coordinate subtractions between the measured and ideal coordinates were thus performed using the same procedure described in previous sections. Figure 5.26 and Figure 5.27 show the spatial distribution of these z-coordinate deviations for the s2p1t and s3p2t tiles.

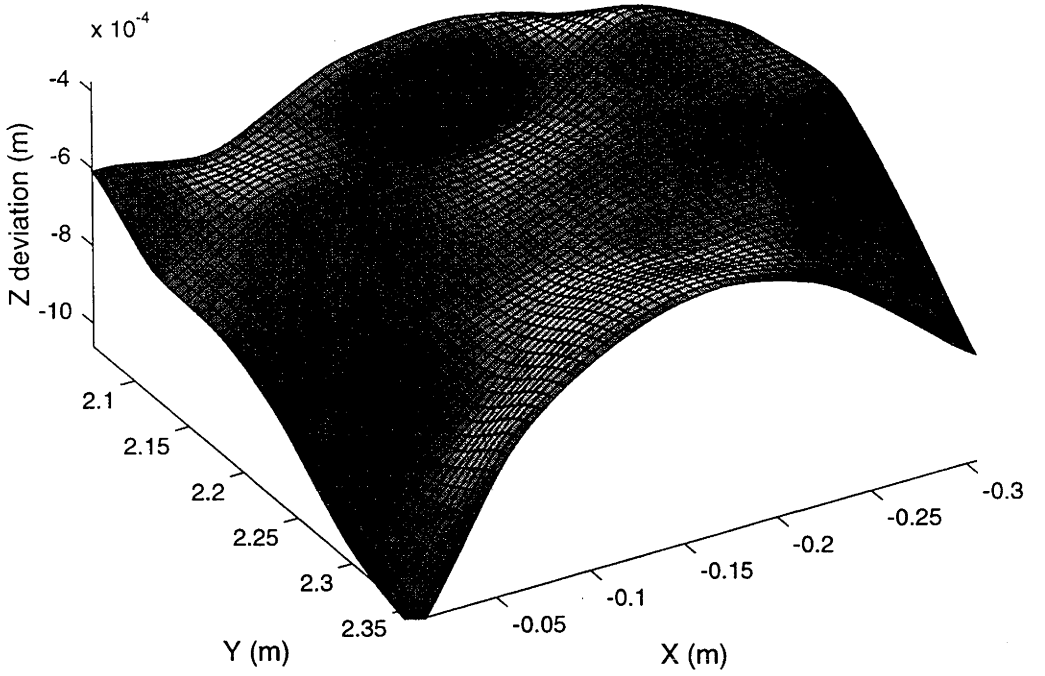

Figure 5.26. Surface deviation plot for the s2p1t (30 cm) mirror tile.

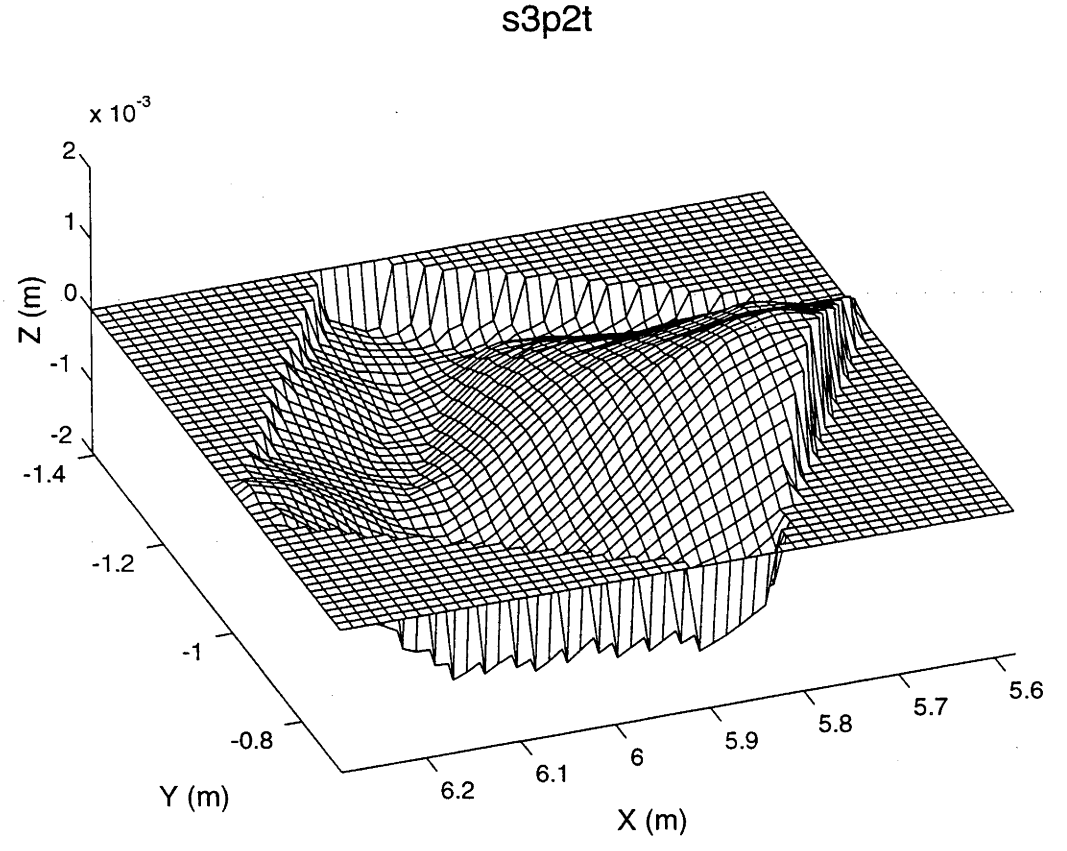

Figure 5.27. Surface deviation plot for the s3p2t (60 cm) mirror tile.

A statistical frequency distribution of z-coordinate deviations was performed for the tiles. Figure 5.28 and Figure 5.29 show the frequency distribution of errors for the s2p1t and s3p2t tiles.

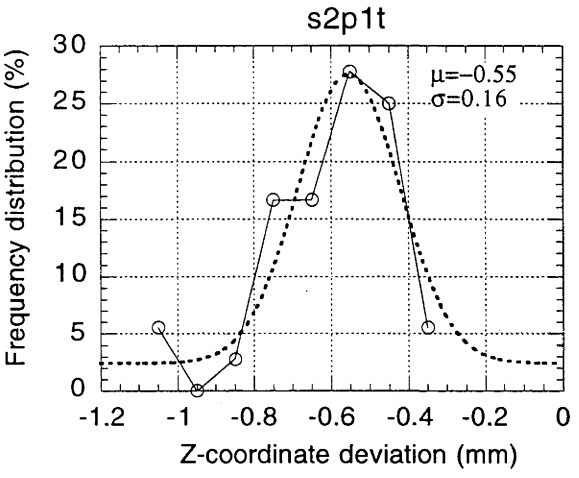

Figure 5.28. Frequency distribution of z-coordinate deviations for s2p1t. Dotted curve shows best-fit Gaussian distribution of errors. σ has been calculated for the whole data set, and is not the SD of the fitted curve.

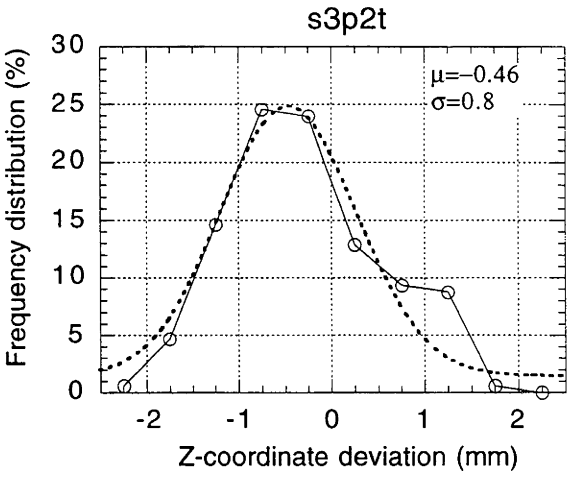

Figure 5.29. Frequency distribution of z-coordinate deviations for s3p2t. Dotted curve shows best-fit Gaussian distribution of errors. σ has been calculated for the whole data set, and is not the SD of the fitted curve.

Appendix 5.4 contains z-deviation surface plots and frequency distributions for the remaining mirror tiles.

Table 5.4 summarises the results of the focal length and standard deviation of z-coordinate errors calculations.

Table 5.4. Calculated focal lengths and standard deviation of z-coordinate deviations for the measured tiles.

Surface	Focal length (m)	Mean deviations (mm)	Standard deviation of z-coordinate deviations (mm)
s2p1t 30 cm tile	13.14 ± 0.04	-0.6	0.16
s3p2t 60 cm tile	13.26 ± 0.02	-0.3	0.8
s3p3t 60 cm tile	13.37 ± 0.03	0.5	1.0
s5p4t 60 cm tile	13.04 ± 0.02	0.8	0.8
s3p5t 60 cm tile	13.156 ± 0.007	-0.3	0.5
s3p6t 60 cm tile	13.106 ± 0.006	-0.1	0.3
s4p7t 60 cm tile	13.168 ± 0.009	0.2	0.6
s5p8t 60 cm tile	13.22 ± 0.02	0.7	0.9

5.5 Discussion of photogrammetric measurements

Digital photogrammetry offers an effective surface characterisation technique, with the end result allowing accurate surface slope measurements to be performed on

concentrator surfaces, and ray tracing preformed on this data to predict the focal region characteristics of concentrators. Its advantages include:

- An ability to measure a wide range of objects, having almost any size (from 'planets to pinheads') and orientation;
- It is a 'non-contact' measurement technique, although this feature can be compromised in some close range applications (such as the present case) where identifiable targets are required on the object surface. In this situation, contact must be made with the surface to attach the targets, but the photography and subsequent photogrammetric processing do not require contact with the surface;
- High coordinate accuracies are achievable, with increased accuracies attainable through the collection of more photographs from different stations around the object. Accuracy improvement increases according to the square root of the number of photographs processed. The present studies produced overall relative network precisions ranging from approximately 1:7,000 to almost 1:30,000. These figures are average values for the three coordinates measured. Generally it is found that the z-(depth)-coordinate shows approximately 50% higher coordinate error than the x and y coordinates, although this effect depends on the degree of angular convergence between the camera stations, with angles of 90° or greater between stations being optimum;
- It is a portable technology, requiring only a camera and flash unit, and a computer for later image processing;
- It is a comparatively low cost measurement technology, with current high resolution digital cameras available for AUD15,000 to AUD20,000, with photogrammetric processing software available for approximately AUD10,000. Coupled with a high performance computer for numerical processing, costing approximately AUD3,500, shows that a measurement system could be established for approximately AUD30,000 to AUD35,000. When it is considered that this provides a very general 3-dimensional measurement technological (as noted in the points above) that can be used to measure structures and surfaces (reflective and non-reflective) with a high degree of accuracy, it represents a very attractive option where numerous objects require measurements;
- Extremely precise camera station positions and lens calibration parameters are not mandatory, with only approximate (±20%) initial estimates for these parameters being required to start the iterative least-squares solution going when performing the photogrammetric 'bundle adjustment' processing. At least three coordinate points ('control points') on the object surface must be known with a reasonable degree of accuracy, to allow suitable 'real world' scaling of the final output coordinates to be performed.

Primary disadvantages with the method include:

- The process of 'targeting up' the surface to be measured can be a very time consuming and laborious process, and can compromise the possible advantage that photogrammetry offers of being a non-contact measurement system. However, some alternative methods using structured light projection systems have been investigated (Maas, 1992), which could offer a method of simply projecting an array of 'light dots' onto the surface to be measured, and taking photographs of the projected light array. This completely eliminates the need for the application of surface targets, but does introduce the drawback that highly reflective surfaces (such as mirrors) would not show the light dots on their surface in a measurable sense. These surfaces could most likely be sprayed with a light, easily washed-off water-based paint to provide

an opaque surface onto which the structured light patterns could be projected and seen;

- A significant amount of operator training is required to both use and interpret the large range of parameters that must be monitored and controlled in both the photographic and bundle adjustment processing stages. This is particularly true of the CRAMPA suite of programs, that are direct outgrowths of academic research software. Other packages may be available that are more user friendly, but these were unable to be assessed because of their high cost and/or lack of availability to the author's research environment.

The results presented in this chapter show some of the measurements and characterisations that can be achieved using close range photogrammetry. In this particular application involving paraboloidal surfaces, analysis of z-coordinate deviations allows quantitative figures to be assembled that show the approximate conformance of the measured surfaces with the ideal shape, as well as providing spatial visualisation of the distribution of the deviations across the surfaces. It also allows an estimation to be made of the most probable focal length expected for the surfaces.

However, further analysis is required to extract surface normal information from the measured data coordinates. This will allow both a quantification of the optical quality of the surfaces, and the generation of surface normals which can be used to produce ray trace predictions of the focal flux distributions that can be expected for sunlight reflected from the reflective surfaces. The development of these more advanced analysis tools is the subject of the next chapter.

6. Quality Assessment of Photogrammetric Surfaces

6.1 Introduction

Chapter 5 introduced the technique of photogrammetry to measure the reflecting surfaces of the paraboloidal concentrators at the ANU. While preliminary assessments of the conformance of the surfaces with an ideal paraboloidal shape were undertaken through the examination of z-coordinate deviations, these calculations do not provide a definitive measure of the optical qualities of a reflective surface, and , as such, cannot provide an indication of the expected focal region performance of the concentrator.

The primary requirement that enables an optical assessment to be undertaken is that a surface must be known in a form for which surface normal data can be calculated. (Some researchers (Grossman, 1994; Wendelin, 1991) also refer to the surface normal as 'surface slope' information, and the two will be used interchangeably in the subsequent discussion.) For analytic surfaces this represents no difficulty, as the normal is found simply by taking the gradient of the surface equation (actually, for concave concentrator reflecting surfaces, the negative of the gradient must be used, as the positive gradient is calculated for the convex side of the surface). Surfaces which have been defined by a discrete array of numerical surface coordinates, however, present a situation of some complexity, as there is no straightforward method(s) of extracting surface normal information from the coordinate array. Numerical methods become the only avenue of approach to such problems. Crude estimations can be made by creating a triangulation network (typically DeLaunay triangulation) (Renka, 1996b), and using a method of 'nearest neighbour' estimation of surface normal, by taking a set of surrounding data points close to a point of interest, constructing a sequence of triangles around the point, and by taking the cross product of two sides of each of the triangles, an array of surface normals can be calculated around the point, as shown in Figure 6.1.

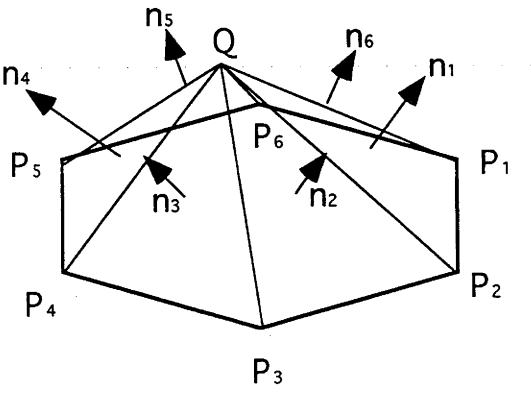

Figure 6.1. Array of surface normals, n_i, calculated around a point, Q, from triangles created between Q and its neighbours, P_i.

An "average" surface normal can be calculated at the point, Q, by taking the average of the x,y and z coordinates of all the surface normal components around the point. However, this represents a very rough approximation to the normal and is not useful for accurate calculations.

A process of fitting an analytic surface to the array of surface coordinates offers a more realistic approximation to the surfaces measured in the present analysis (the reflecting surfaces were clearly smoothly varying functions). Numerous algorithms and methods have been developed to fit analytic surfaces to numerical data, and it is not the aim of the present study to undertake an exhaustive review of all the nuances and characteristics of the different techniques. It was found that a number of algorithms are available which have a wide respectability and use in the numerical data fitting literature, and these algorithms were identified and tested for their applicability to the types of surfaces measured in this project.

6.2 Assessment of available algorithms

Assessing the surface fitting accuracy of the range of different types of surface fitting algorithms available requires a standard reference against which to compare the fitted results. Goshtasby and O'Neill (1993) suggest a number of surfaces for comparison. These surfaces represent fairly arbitrary devices, however, and it was considered more appropriate to use model surfaces that provided a closer approximation to the surfaces under test.

Clearly, as the measured surfaces were intended to be close approximations to a paraboloidal shape, this surface offers itself as the initial reference against which a fitting algorithm should be tested. If a fitted surface to an array of paraboloidal data coordinates does not produce a close approximation to the surface normals expected for the surface, then it will probably not fulfil the requirements expected of it when the surface contains perturbations from the ideal shape.

Assessment of the quality of fit was judged by the magnitude of the average surface slope error between the ideal surface and the fitted surface. Surface slope error was measured as the average magnitude of the deviation vectors between the ideal surface normal vector and the calculated normal from the fitting function. Figure 6.2 illustrates this concept.

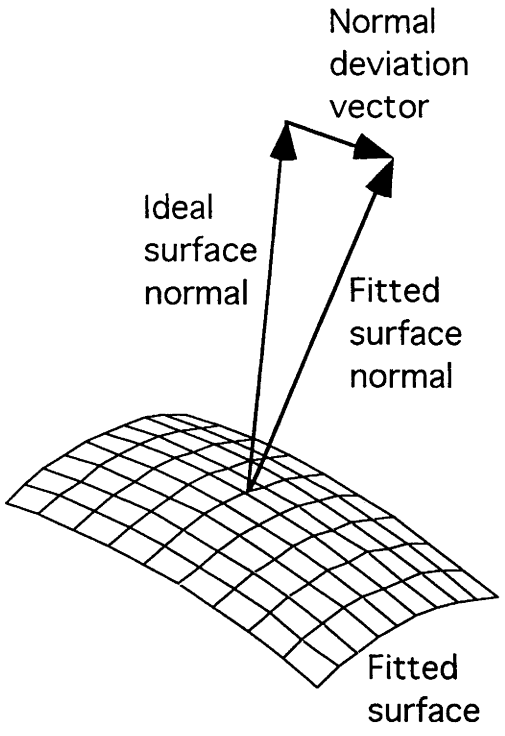

Figure 6.2. Illustration of the concept of normal deviation vector. The mean magnitude of an array of normal deviation vectors is used as a measure of surface slope error.

Assessment of fitting accuracy also requires a realistic accuracy criterion against which to measure the performance of a fitting routine. This criterion will clearly be dependent on the regime of errors that are expected to be encountered on the measured surfaces. For example, it is apparent that if reflecting surfaces suitable for astronomical telescope use were being assessed, then a measurement system and fitting routines would have to be capable of sensing surface slope errors in the order of nano- to pico radian. Solar concentrators do not have such high accuracy requirements, and reference to published results for some the highest quality solar concentrators in existence give suitable bounds on the accuracy requirements for this type of work. Stein and Diver (1993) indicates that stretched membrane dishes present some of the highest quality reflecting surfaces (for example, the Sclaich-Bergermann & Partner dishes) currently in existence, and these generally show surface slope errors of between 1.8 and 2.5 milliradian. It was considered that a fitting accuracy equal to 10% of these high quality concentrator slope errors would provide a realistic upper bound within which to work. Taking a good quality concentrator to have a surface slope error of 2.0 milliradian, places a bound of 0.2 milliradian on the required accuracy criterion. This value is used in subsequent assessments as the nominal bound of accuracy against which fitting routines should be judged.

Other features of the measured data also dictated some specific requirements of a fitting algorithm. Placement of targets on a surface did not always conform to a regular grid, and the boundary aperture of many measured surfaces did not have a square or rectangular perimeter (for example, the circular aperture of the 20 m^2 dish, and the triangular apertures of the mirror panels on the 400 m^2 dish). These characteristics meant that several algorithms were discarded from further examination, as they required the input data sets to conform to regularly gridded, rectangular boundary schema.

After review of a number of algorithms, it was decided to pursue further testing with three programs. These were:

1. BVIP (Bi-Variate Interpolation Polynomial) offered by the Naval Surface Weapons Centre (NSWC, 1992);

2. SRFPACK (together with TRIPACK), (Renka, 1996a and 1996b);

3. SURFIT (Dierckx, 1993).

A preliminary test surface was defined based on the 20 m^2 dish (that is, diameter = 5 m, focal length = 1.81 m), and the x,y coordinates of the target positions on this dish (see Figure 5.3)were used to calculate an ideal set of associated z-coordinates. For two of the fitting routine tests (BVIP and SURFIT), surface normals were calculated by interpolating two orthogonal elementary vectors (length = 10^{-8} m) from the point of interest into the fitted surface, and taking the cross product of the vectors to calculate the surface normal vector at that point. SRFPACK calculated first order derivatives directly within the routine, and these values were used to calculate surface normal vectors.

6.2.1 BVIP

BVIP attempts to fit a quadratic polynomial surface to local sets of data points around a chosen point of interest. The 'local' or 'global' influence of the data field can be adjusted by specifying the numbers of nearest neighbours to the point of interest that are used by the algorithm to calculate the fitting surface. Figure 6.3 shows a plot of average surface slope error versus number of nearest neighbours calculated using BVIP.

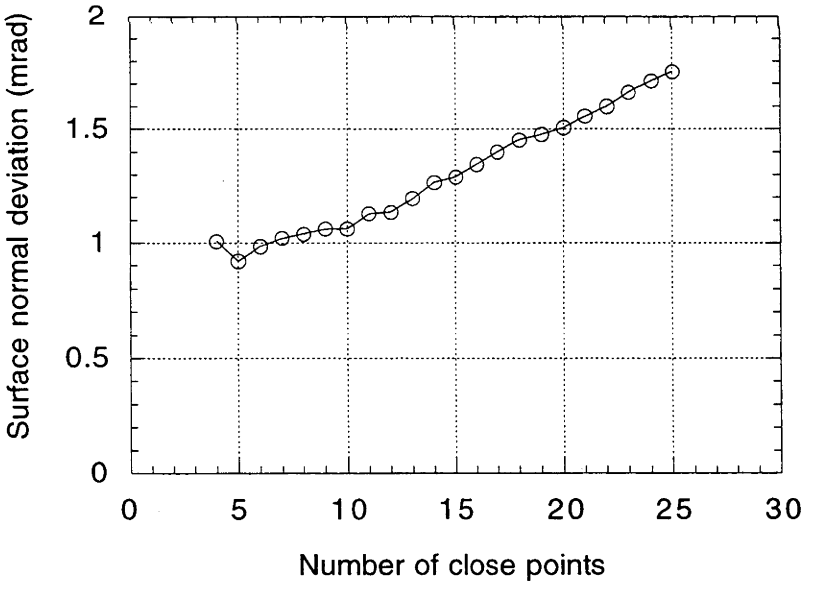

Figure 6.3. Surface normal deviations (slope error) versus number of nearest neighbours using BVIP.

It can be seen that at best, BVIP only approximates an ideal surface to within approximately 0.9 milliradian.

6.2.2 SRFPACK

SRFPACK uses a Hermite interpolatory tension spline that calculates surface derivatives (normals) directly and has two modes of assessment. One uses a local fitting function, while the other calculates a surface fit based on the total (global) data field and which uses automatic adjustment of a tension factor to accommodate local variations in the data field. Both modes were assessed. Support software was written to facilitate interfacing with the SRFPACK and TRIPACK routines (TRIPACK is a triangulation package intended for use with SRFPACK). Application of the routines to the test surface returned average surface slope errors of 1×10^{-4} milliradian for the local fitting mode, while the global mode returned slope errors of 6 to 8 milliradian. The large difference between these two modes was a cause of some concern, and communication with Renka (1996c) did not produce any further indications as to why the global fitting mode displayed such large surface slope errors.

6.2.3 SURFIT

The SURFIT routine (Dierckx, 1993) was implemented through the use of the NAG libraries E02DDF and E02DEF (NAG, 1994). This algorithm uses B-spline representations of the surface fitting function, which incorporates automatic knot placement in the data surface according to the tension set by a smoothing factor, S. (See Dierckx (1993) for a discussion of spline curve and surface fitting in general, and B-splines in particular. A complete description of the SURFIT package is also found there.) E02DDF calculates the B-spline fitting coefficients for the surface data, while E02DEF evaluates the spline function at any specified interpolation point. Interface software was written to access the routines in the NAG library, and assessments made using the test surface returned average surface slope errors of 2×10^{-5} milliradian. This was clearly the closest approximation to the test surface of the three routines.

6.3 Evaluation of fitting accuracy

6.3.1 Assessment of an optimal fitting routine

The model paraboloidal surface was useful in preliminary assessments of the suitability of the various surface fitting codes, but was not a realistic representation of the actual surfaces measured photogrammetrically. Review of the 20 m^2 dish and the 400 m^2 dish mirror tile surfaces and their apparent deviation from the desired paraboloidal shape, showed that surface fitting accuracy must also be tested over a range of test surfaces that included non-paraboloidal ripples and perturbations. Although not immediately obvious, it also became apparent that the test ripples should not be curves defined by quadratic or cubic functions, as the fitting routines intrinsically used these types of approximating equations (eg. bicubic splines and B-splines) and would return unrealistically good fits for curves of this type. It was thus decided to construct test surfaces consisting of the basic paraboloidal shape, with superimposed two-dimensional sinusoidal ripples imposed on the surface. The spatial amplitude and frequency of these sinusoids could be varied in order to assess the performance of the fitting functions under varying conditions. These test surfaces were generated using the following basic form:

$$z = \frac{x^2 + y^2}{4a} + A\left(\sin(\omega x) + \sin(\omega y)\right)$$

where,

a = the focal length of the test paraboloid,
A = the amplitude of the bi-sinusoidal ripples,
ω = the spatial angular frequency (radian m^{-1}) of the bi-sinusoidal ripples

Note that in later analysis spatial frequency (f, m^{-1}) is used instead of spatial angular frequency (ω, radian m^{-1}). ω is related to f by the usual relationship,

$$\omega = 2\pi f$$

Figure 6.4 shows a mesh plot of such a paraboloidal surface with superimposed bi-sinusoidal ripples.

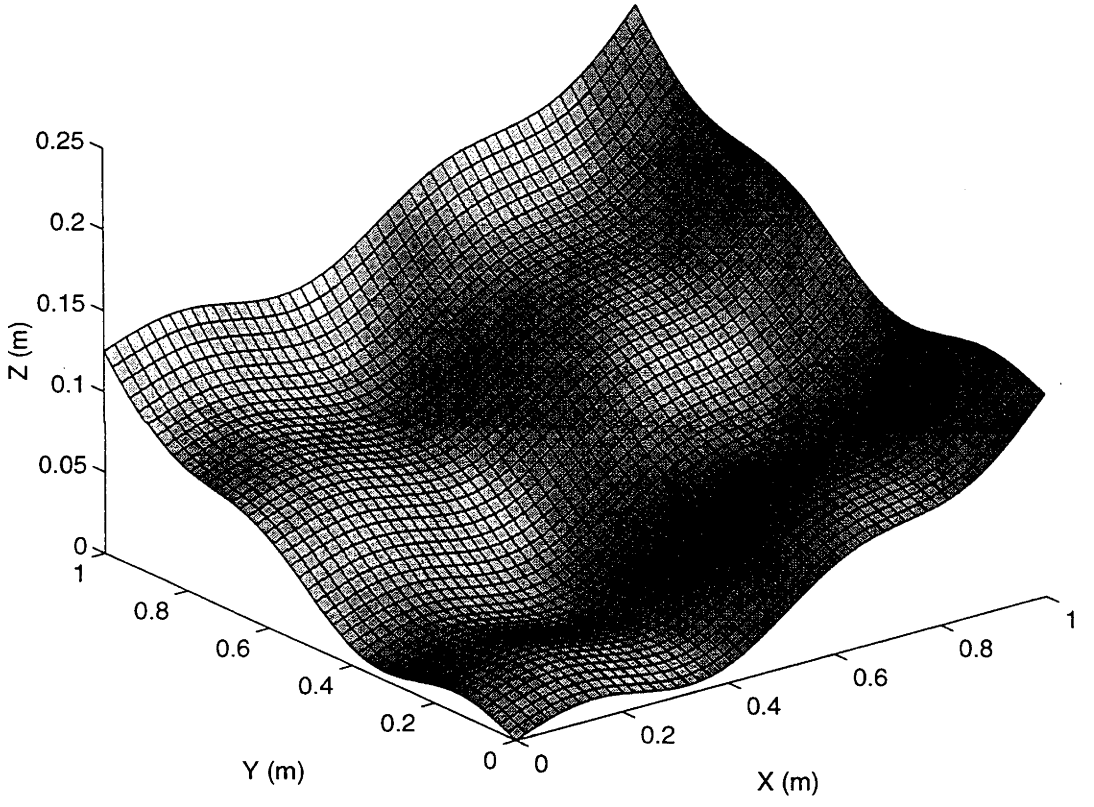

Figure 6.4. Example of a paraboloidal surface with superimposed bi-sinusoidal ripples.

It was decided to change the test surface from the 20 m^2 dish target layout to the 60 cm mirror tile target layout for the 'rippled paraboloid' tests, as it was this type of surface upon which the majority of surface assessment would be performed. Average surface slope error was recorded for a range of ripple amplitudes and spatial frequencies for both the SURFIT and SRFPACK-local routines, where surface slope error in this case is defined as the deviation of the fitted surface normal from the ideal normal of the rippled paraboloidal surface, rather than deviation from the paraboloidal surface only. Figure 6.5 and Figure 6.6 show the results of these tests for SURFIT and SRFPACK-local, respectively.

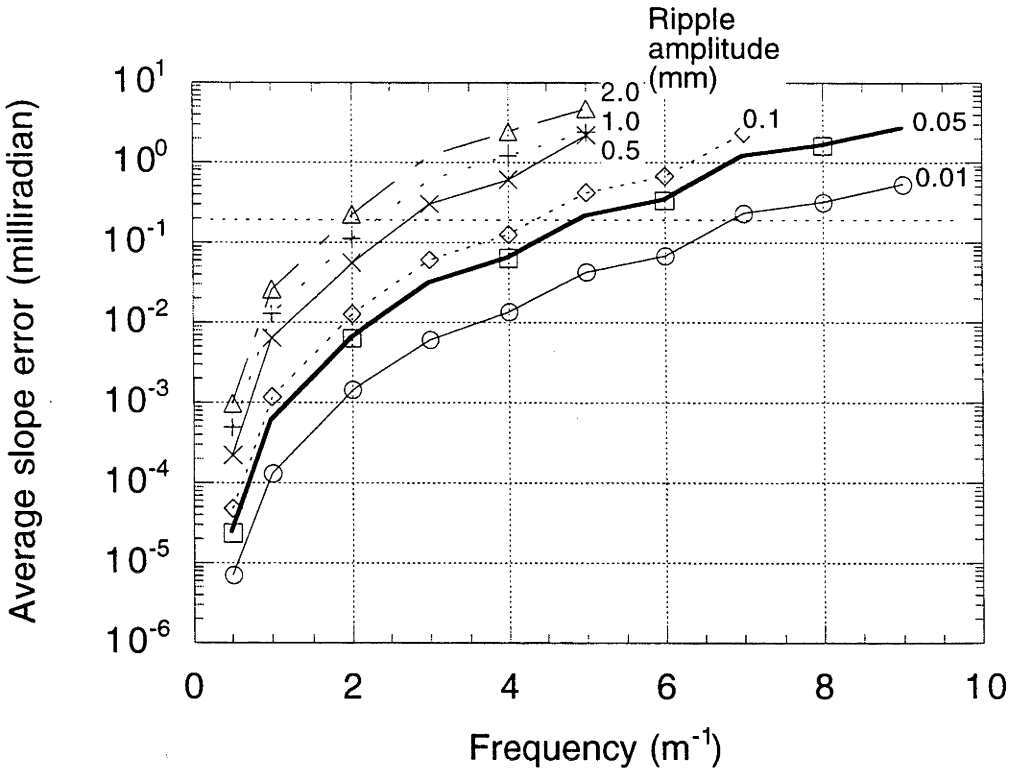

Figure 6.5. Average slope error versus spatial frequency for a range of sinusoidal ripple amplitudes using the SURFIT (E02DDF and E02DEF) routine.

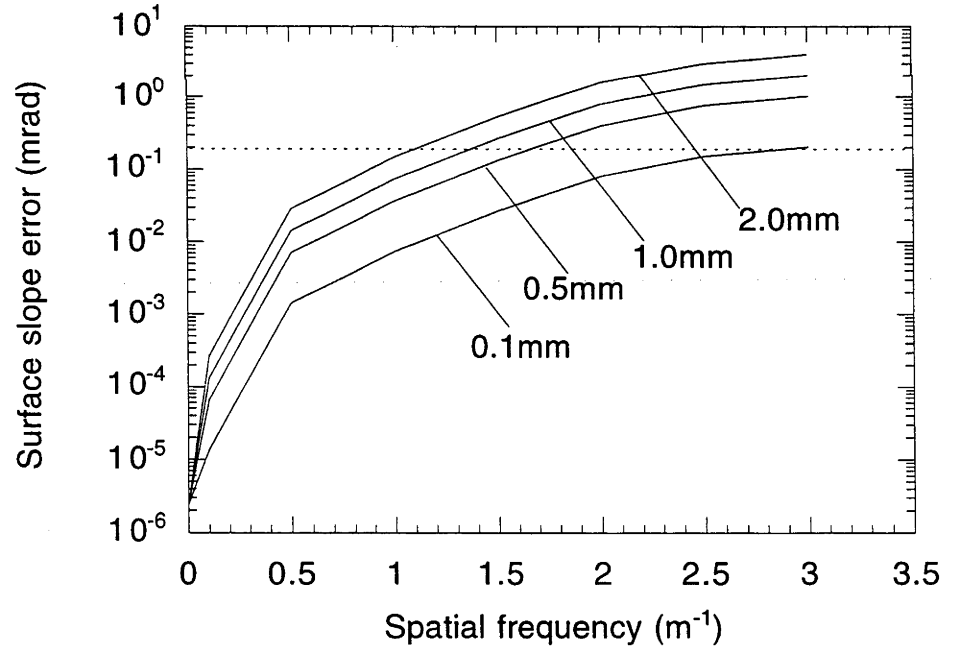

Figure 6.6. Average slope error versus spatial frequency for a range of sinusoidal ripple amplitudes (mm) using the SRFPACK-local routine.

Examination of Figure 6.5 and Figure 6.6 show that for the same spatial frequency, the SURFIT routine consistently produces lower average surface slope errors than the SRFPACK-local routine. This indicates that the SURFIT routine is able to more closely follow the introduced ripples than the SRFPACK-local routine. It was decided that the

SURFIT (E02DDF, E02DEF) routine should be used for the assessment of surface slope errors on the measured reflector surfaces.

Figure 6.5 shows a dotted line drawn at the 0.2 milliradian level of surface slope error. It can be seen that to maintain this level of fitting accuracy requires surface ripples having ±2.0 mm amplitude to have a spatial frequency of 2.0 m^{-1} or less. Similarly, ripples having amplitudes of ±1.0 and ±0.5 mm can have spatial frequencies up to 2.5 and 3.0 m^{-1}, respectively to maintain this level of fitting accuracy.

This criteria for slope error fitting accuracy can be refined further through a Fourier transform analysis of the measured surfaces. Figure 6.7 shows a plot of the frequency component amplitudes versus x and y-dimension frequencies for the s3p2t mirror tile z-coordinate deviations (the z-coordinate deviations were processed instead of the complete tile surface in order to remove the interference due to components that belonged to the paraboloidal surface).

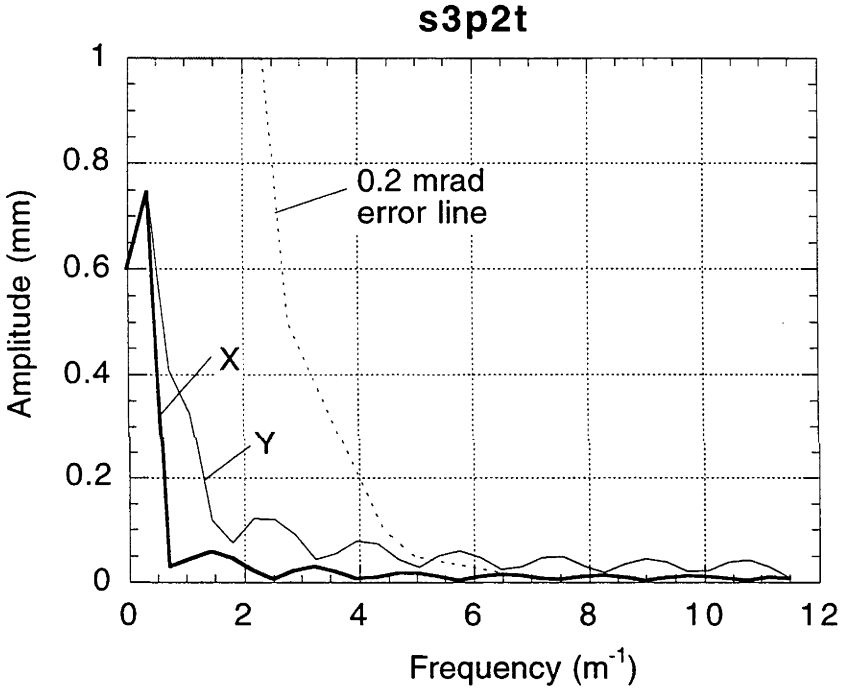

Figure 6.7. Plot of x and y dimension frequency amplitudes versus frequency for the s3p2t mirror tile z-coordinate deviations. Dotted line shows the 0.2 milliradian slope error cut-off function, derived from Figure 6.5.

Fourier spectral curves for the remaining mirror tile z-coordinate deviations are contained in Appendix 6.1. As noted in this appendix, the fast Fourier transform (FFT) produces a spectral 'surface', but as the dominant components always appeared along the x and y axes of the surface plots, it was these components that have been plotted in the accompanying figures.

Figure 6.7 also shows the 0.2 milliradian slope error cut-off function. This curve is derived from Figure 6.5, where the points on the ripple amplitude curves corresponding to 0.2 milliradian surface slope error were recorded and plotted against their corresponding spatial frequencies. This curve defines the point, for a ripple having a given amplitude, where the uncertainty in the calculated surface slope error would exceed 0.2 milliradian. This means that the points where this curve cuts through the

Fourier spectral curves in Figure 6.7, indicates that the uncertainty in the surface slope error for these frequencies will equal or exceed 0.2 milliradian. It can be seen that the error cut-off curve passes through the Fourier spectra at frequencies of approximately 5.5 m^{-1}, and that the greater proportion of the frequency components represented in the surface will be modelled with accuracies significantly better than 0.2 milliradian. Conversely, it appears that the EO2DDF/EO2DEF routines can model the components at higher frequencies with an accuracy less than 0.2 milliradian.

Integrating the 'volume' contained under the FFT spectral surfaces for frequencies that exceed the intersection points of the 0.2 milliradian slope error cut-off curve with the spectral curves (ie. frequencies greater than approximately 5.5 m^{-1}) shows that the relative contribution of these components to the overall slope error uncertainty is approximately 20%. While significant, this represents a minor contribution to the overall surface slope error uncertainty and appears to indicate that GRADFITTER will model at least 80% of the surface with an accuracy better than 0.2 milliradian.

6.3.2 Assessment of closeness of fit

One of the strengths, but accompanying liabilities, with the SURFIT routine is that it utilises a manually adjustable smoothing factor, S, which must be varied to obtain the closest fit to the data surface. If S is too large, then the surface is smoothed excessively, and small local variations are lost. If S is too small then the B-spline fitting surface can introduce spurious oscillations into the fit. The tension factor can be likened to the tension applied to a rug or blanket that lies over an irregular surface. If the tension is high (large S), then the rug is pulled taut over the surface, and does not show much detail of the underlying features. If the tension factor is too loose, then the rug will accommodate the underlying features, but can also include ripples and warps that are not part of the data surface. Figure 6.8 shows a bilinear interpolation of the s3p3t surface deviations (from an ideal paraboloid). A bilinear interpolation method simply calculates the z-coordinate of an interpolation point by linear interpolation on a plane between the three nearest measured data points to the interpolation point. Figure 6.9 to Figure 6.11 show the three cases for bicubic B-spline fits applied to the surface having too much tension (features excessively smoothed), too little tension (excessive rippling between data points) and the optimal tension (close conformance to original data set).

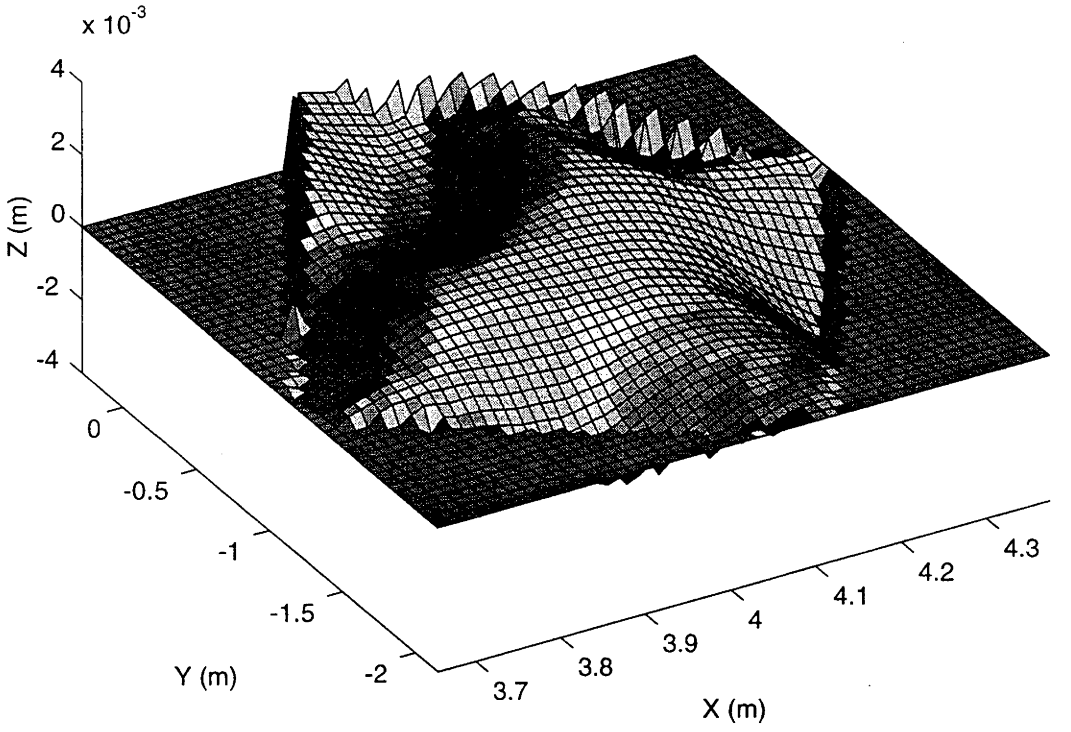

Figure 6.8. Bilinear interpolation of the s3p3t tile surface deviation from an ideal paraboloid, interpolated to a 50x50 grid.

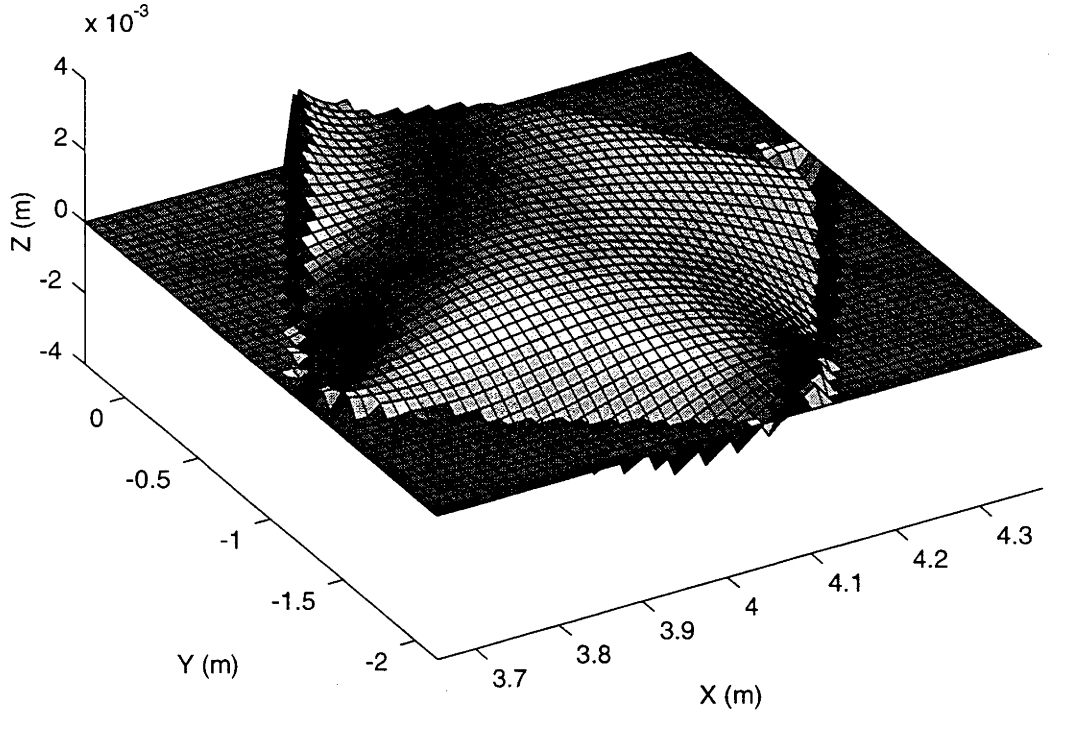

Figure 6.9. Bicubic B-spline fit to the s3p3t deviations using a large smoothing factor (S=1.0), causing excessive smoothing of the data.

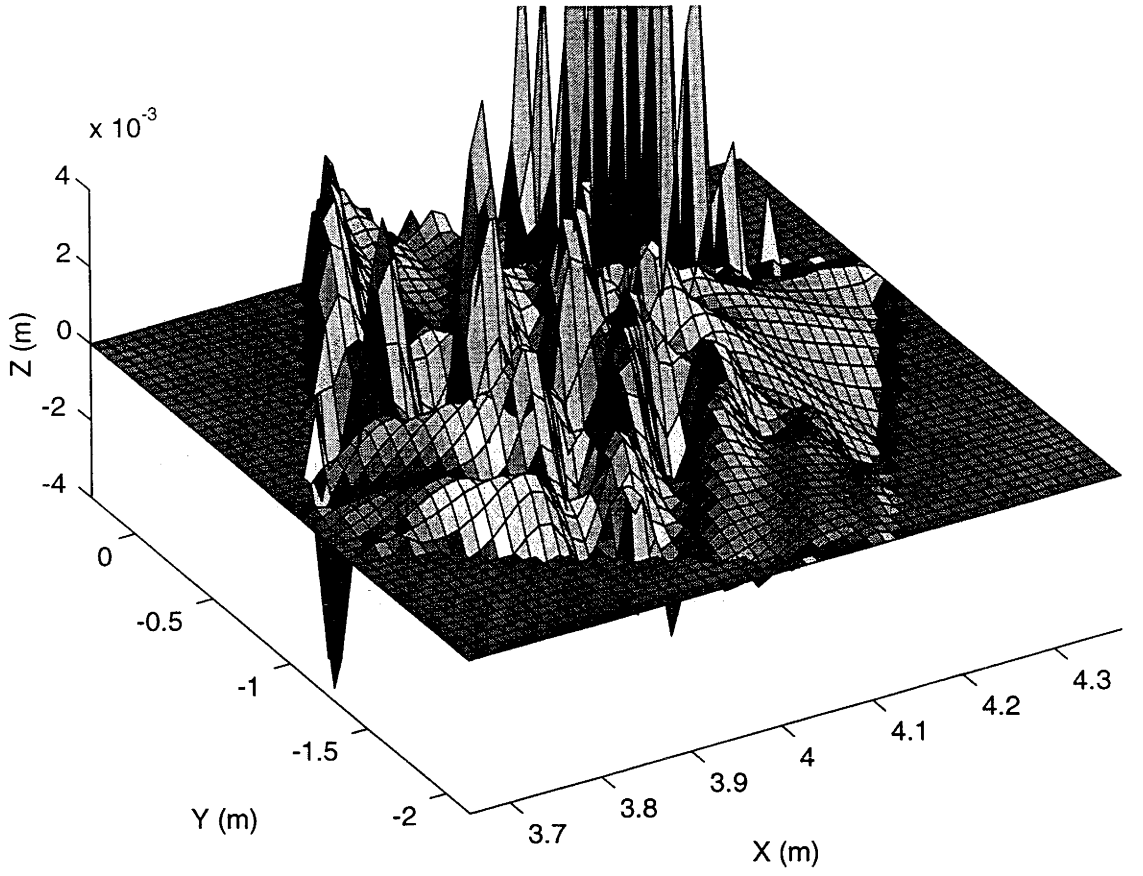

Figure 6.10. Bicubic B-spline fit to the s3p3t deviations using a small smoothing factor ($S=1.3 \times 10^{-13}$), causing excessive rippling between data points.

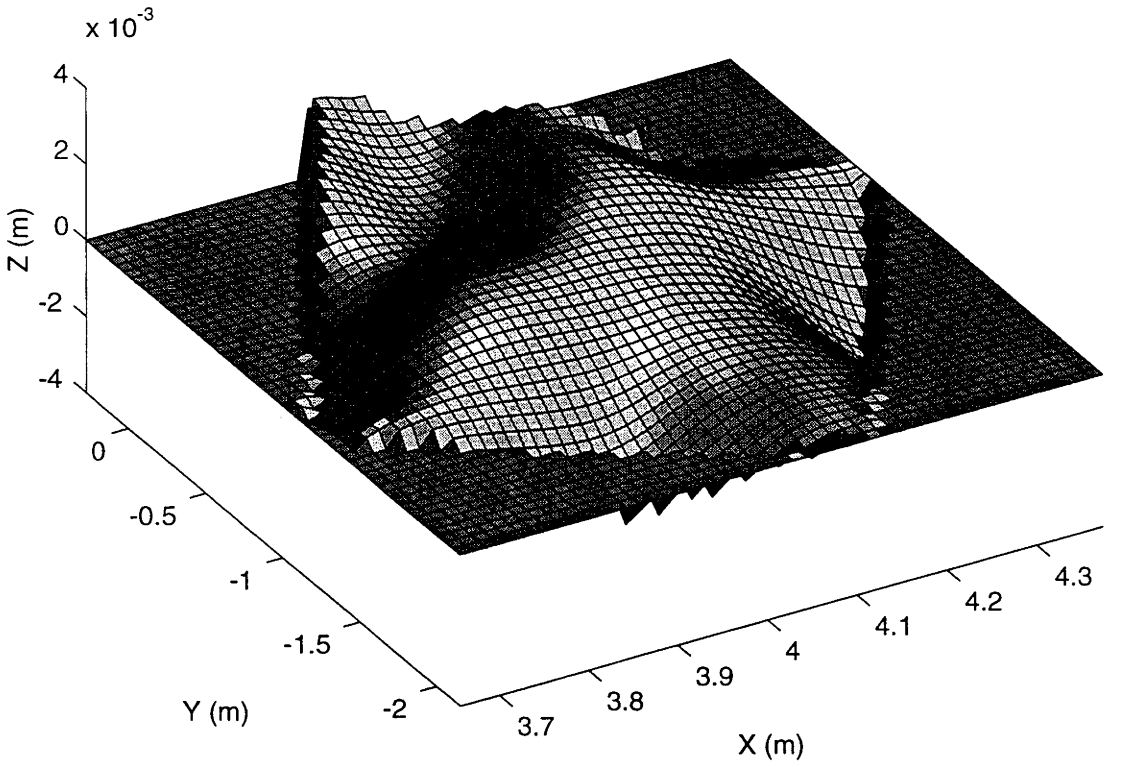

Figure 6.11. Bicubic B-spline fit to the s3p3t deviations using an optimal smoothing factor (S=9.2 x 10^{-9}), producing a close fit between the measured and fitted surfaces.

Figure 6.12 shows the subtraction between the bilinearly fitted surface of Figure 6.8 and the spline fitted surface of Figure 6.11.

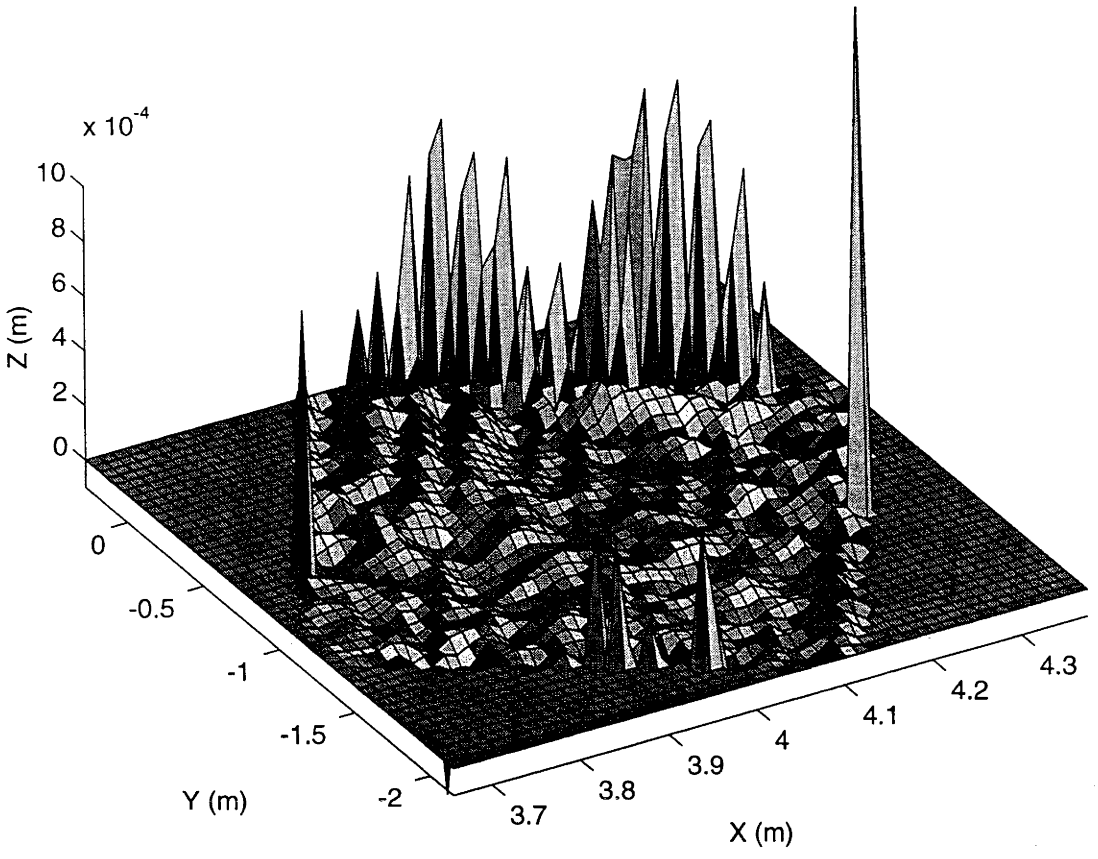

Figure 6.12. Subtraction between the bilinearly fitted surface of Figure 6.8 and the optimal spline fitted surface of Figure 6.11.

The large deviations apparent at certain points on the boundaries of the plot are typical excursions that can occur at edges or discontinuities for numerical data fits, and constitute only 1% of the data points on the surface. The rms deviation shown in Figure 6.12 is 26 μm (excluding the aberrant edge values).

Figure 6.9 and Figure 6.10 raise the issue of what constitutes an 'optimal' fit to a data surface, and highlight the 'liability' associated with having a manually adjusted smoothing factor. It becomes apparent that the bicubic spline fit could be made to do 'anything' depending on the choice of the smoothing factor. It was decided to use the bilinear data fit as a reference surface with which to compare the bicubic spline fits, as this represents a robust surface fit that neither excessively smooths nor oscillates between the data points. A program named GRADFITTER was written that used the E02DDF and E02DEF routines, but which also allowed calculation of sets of interpolating data points such that deviations of the spline surface points between the measured data points could be assessed. Contemplation of Figure 6.9 and Figure 6.10 indicates that the spline surface deviation from a bilinear fit should be comparatively high for both an excessively smoothed and excessively rippled spline fit. A close to optimal fit should be obtained when the smoothing factor has been adjusted until the interpolated deviations are a minimum. Figure 6.13 and Figure 6.14 illustrate this concept using two dimensional data.

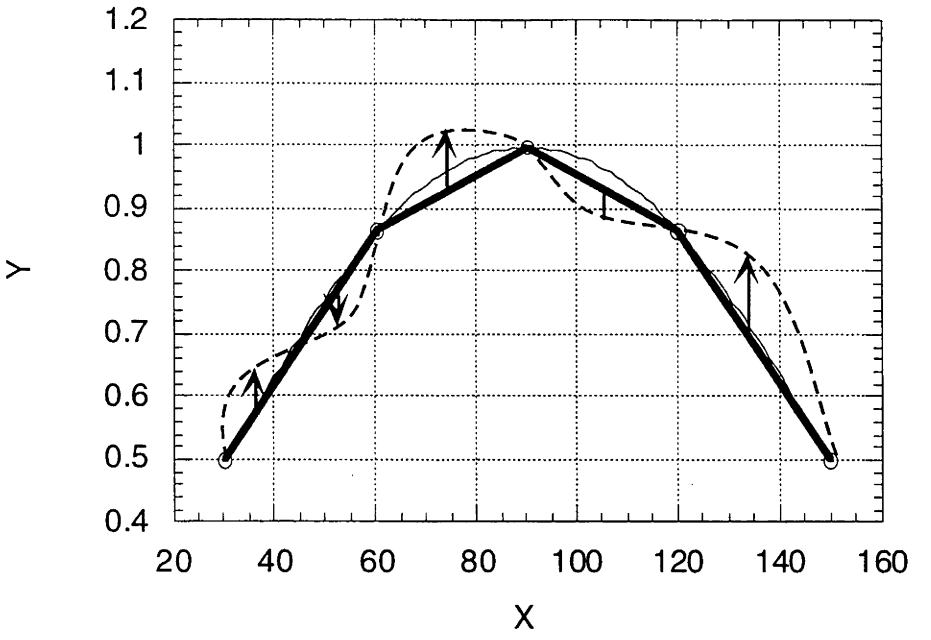

Figure 6.13. Excessive deviations (arrows) between an oscillating spline fit (dashed line) and a linear interpolation (heavy straight lines) of a data set. Optimal fit shown as a light continuous line.

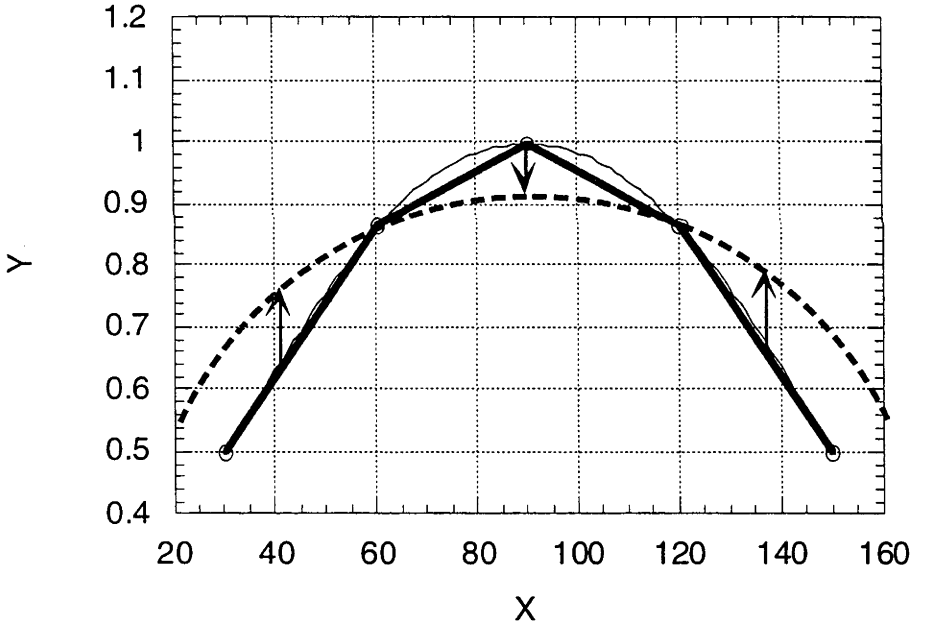

Figure 6.14. Excessive deviations (arrows) between an over-smooth spline fit (dashed line) and a linear interpolation (heavy straight lines) of a data set. Optimal fit shown as a light continuous line.

It was decided to implement the interpolating data points between the measured data coordinates on the three-dimensional surfaces by creating triangulated panels between the measured data points and then divide each triangle into a 5x5 grid, as shown in Figure 6.15.

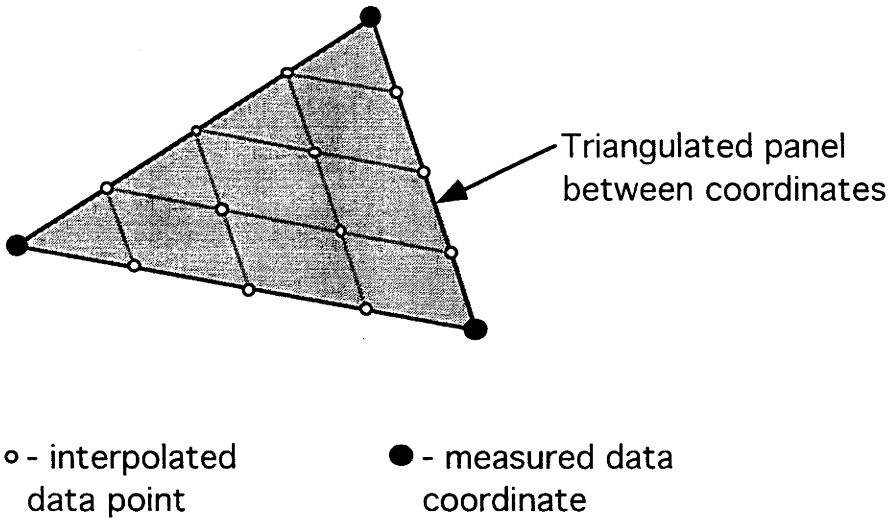

Figure 6.15. Layout of interpolating data points on triangulated panel between measured surface coordinates.

This subdivision gave an extra 12 interpolation points on the triangular panels between the measured data points. Both bilinear and bicubic spline values at the interpolating points were calculated for a given fit, and the rms difference between the z-coordinates of the fits was used as a measure of the closeness-of-fit between the bicubic spline and bilinear fits.

This approach to finding the optimal fit to a data set was assessed by applying the interpolation scheme described above to the bi-sinusoidal test surfaces. Spatial amplitudes and frequencies were chosen, and the variations in rms z-coordinate fitting error (referred to simply as fitting error), together with the change in surface slope error, were plotted as functions of the smoothing factor, S. Over numerous tests a trend became apparent where often both the fitting error and the slope error would decrease and plateau with S, until a point was reached where the fitted surface started rippling rapidly, and both the fitting and surface slope errors increased noticeably. This became a signal point to indicate that the optimal fit should be selected using the smoothing factor that occurred just prior to the rapid change in the fitting and slope errors. Figure 6.16 shows examples of this type of behaviour for two different bisinusoidal ripple amplitudes and frequencies.

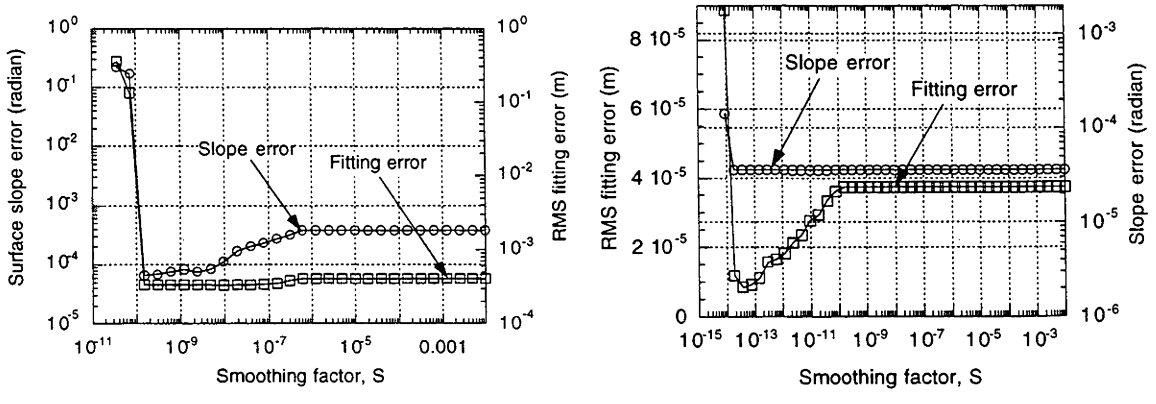

Figure 6.16. Examples of the variation in fitting error and surface slope error with smoothing factor, S, for bicubic spline fits to bisinusoidally rippled surfaces. Note the points where both curves increase rapidly with decreasing S-value.

However, there were instances where this behaviour did not occur, and both the slope and fitting errors either decreased to a relatively constant value and did not display any sharp increases in either values with decreasing S, or they decreased to a point, then both started rising slowly again after reaching a minimum. Figure 6.17 shows an example of this type of behaviour.

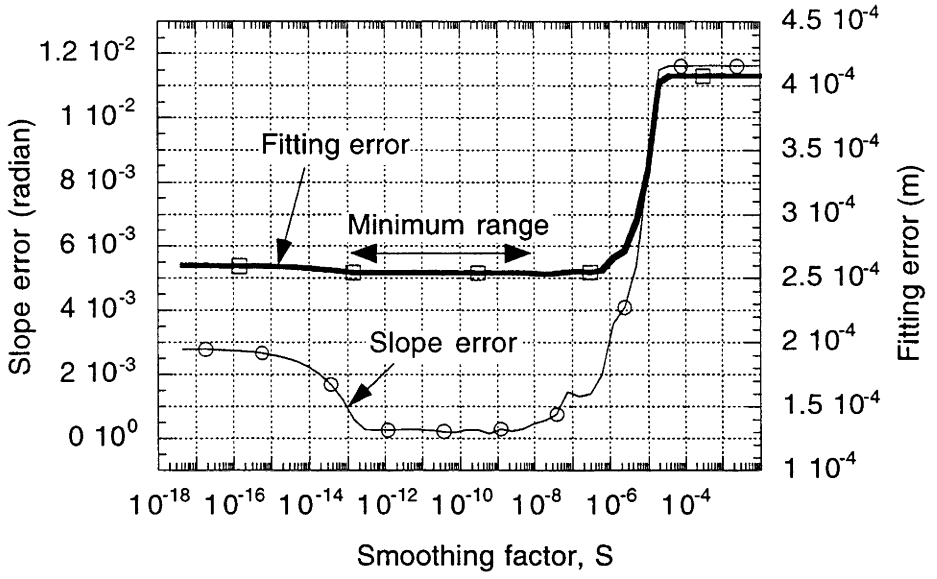

Figure 6.17. Examples of changes in fitting and slope errors versus smoothing factor, without rapid variations in the values with decreasing S. Note that different scales are used for each abscissa.

It can be seen that the fitting error generally displays a slower variation with S than the slope error, and these small changes must be observed closely to detect the points of minimum deviation. However, when it was apparent that a slowly varying situation existed, such as displayed in Figure 6.17, it was found sufficient to choose an S-value that fell in the midpoint of the minimum range of the fitting error (shown in Figure 6.17).

In all of these cases it became clear that choosing the minimum point of the fitting error gave a reliable guide to the closeness of fit between the bicubic spline surface and the underlying data surface. This method was used to select an appropriate smoothing factor for use with the measured photogrammetric surfaces.

However, there were two instances where the change in the fitting error did not immediately coincide with the change in the surface slope error. Figure 6.18 shows an example of one of these events.

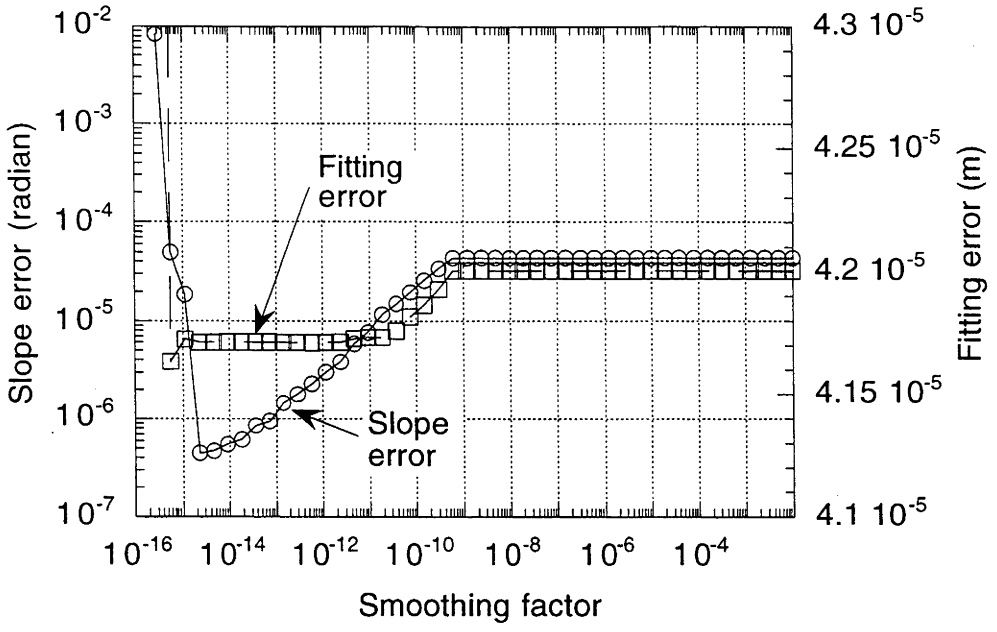

Figure 6.18. Examples of changes in fitting and slope errors versus smoothing factor, showing where the changes in fitting error do not coincide with the slope error. Note that different scales are used for each abscissa.

No apparent cause was identifiable for this effect, and it constitutes an area that requires further analysis. Unfortunately, time restrictions prevented the author from fully resolving this discrepancy, and it is envisaged that this will form a source of further research in future work. However, it was not considered to be a cause of major concern, due to its rarity of occurrence, and it was decided to process the photogrammetric surfaces using the minimisation of fitting error method to determine the optimal fit conditions.

6.4 Surface normal assessment of surfaces

GRADFITTER was used to calculate the surface normals across the 20 m^2 dish surface and the eight mirror tile types that were measured on the surface of the 400 m^2 dish. Figure 6.19 and Figure 6.20 are example plots showing the spatial distribution of surface slope errors that were calculated for the 20 m^2 dish surface and the s3p2t mirror tile.

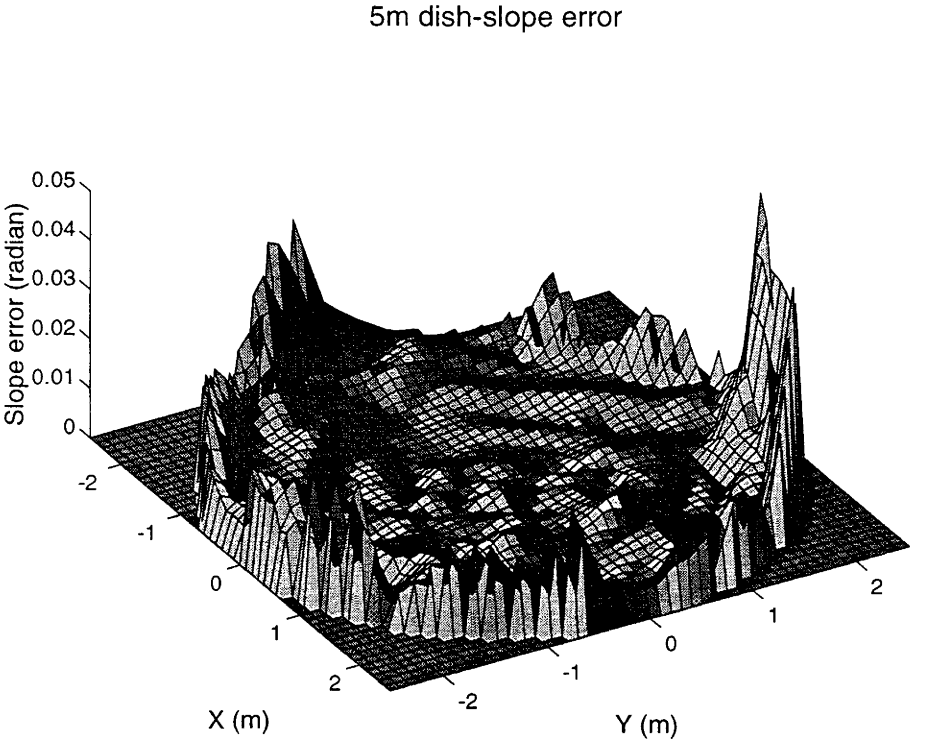

Figure 6.19. Spatial distribution of surface slope errors across the surface of the 20 m^2 tiled dish.

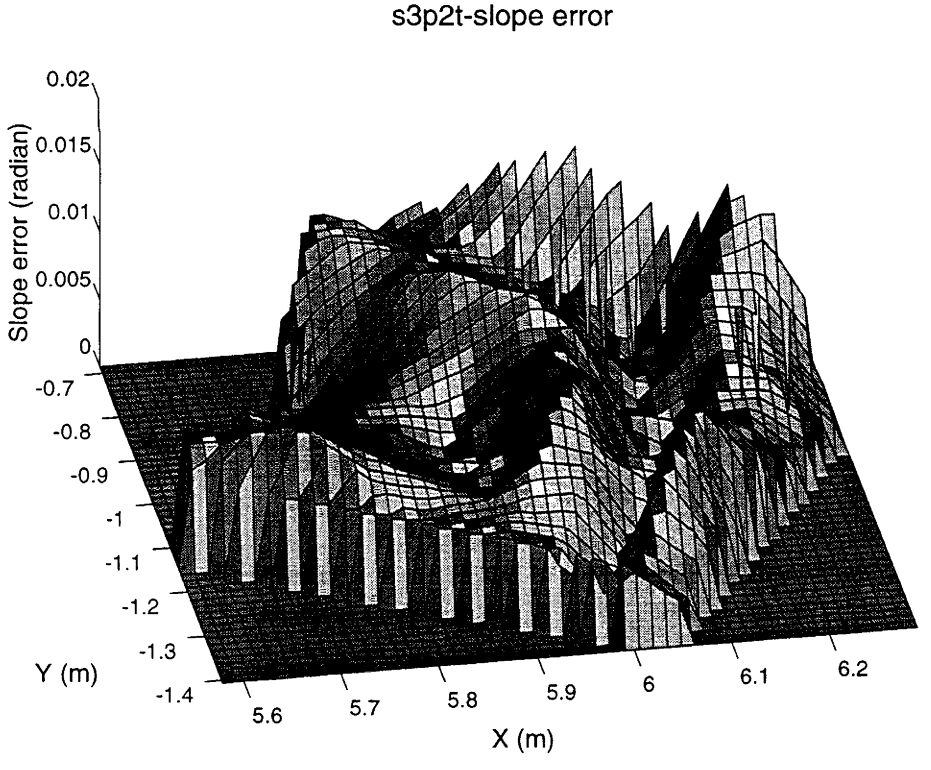

Figure 6.20. Distribution of surface slope errors across the s3p2t (60 cm) mirror tile.

Appendix 6.2 contains slope error surface plots for the remaining mirror tiles.

Review of the surface slope error distributions does not appear to show any systematic or regular type of distribution across the measured surfaces. However, Romero (1994) indicates that a bi-variate Gaussian distribution of surface slope errors can be used to successfully model many reflector surfaces. This has the general form,

$$P = \frac{1}{2\pi\sqrt{\sigma_x \sigma_y}} e^{-\left(\frac{x^2}{2\sigma_x^2}+\frac{y^2}{2\sigma_y^2}\right)} \qquad \textbf{(6.1)}$$

where,

P = probability density distribution
= standard deviation in the x-dimension
σ_y = standard deviation in the y-dimension

Figure 6.21 shows a graphic description of this distribution.

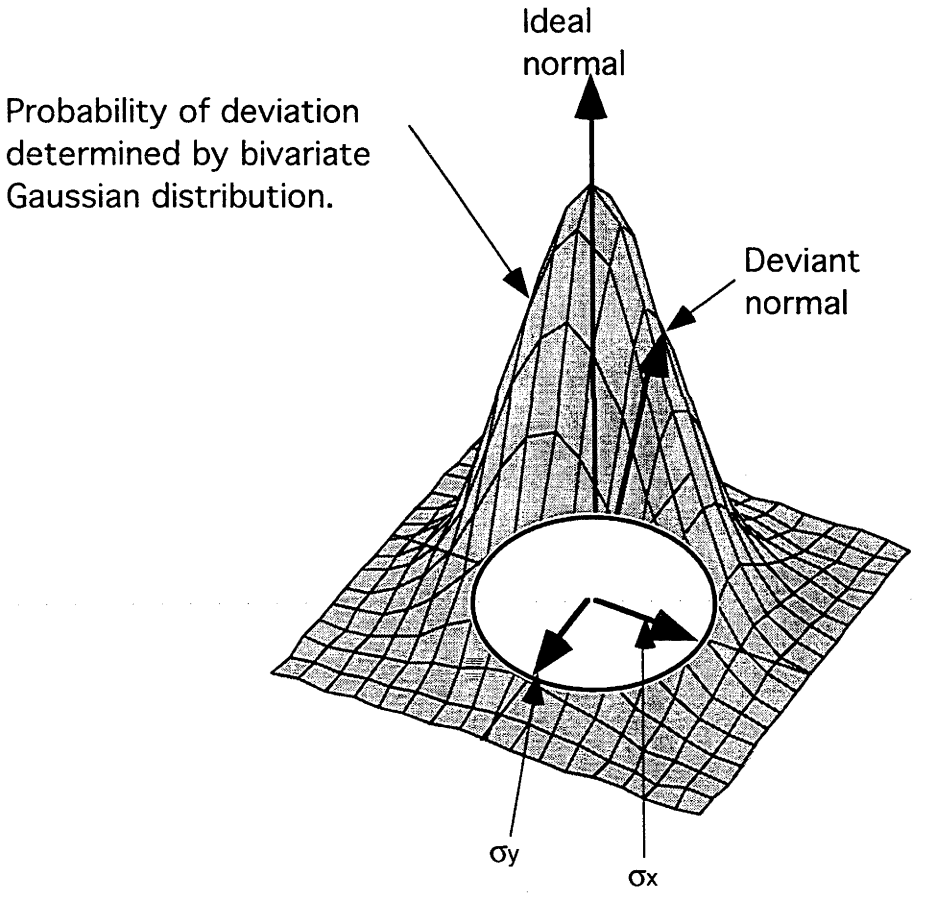

Figure 6.21. Illustration of the bivariate Gaussian probability distribution (or 'envelope'), defining the likely deviations expected for actual surface normals on measured surfaces.

Generally, this is classed as elliptical error distribution function, as the case where $\sigma_x \neq \sigma_y$ will produce an error distribution having an elliptic projection on the x-y plane. The case where $\sigma_x = \sigma_y$ leads to a circular error distribution function, characterised by a single standard deviation, σ, and the probability density function simplifies to,

$$P = \frac{1}{2\pi\sigma} e^{-\frac{x^2}{2\sigma^2}} \qquad (6.2)$$

This simple model can be used as an initial standard of comparison with the measured distribution of surface slope errors. However, the circular error distribution implies that the surface normal deviation becomes defined by the radial (θ) component of the deviant vector, and is independent of the tangential component (ϕ), as illustrated in Figure 6.22, below:

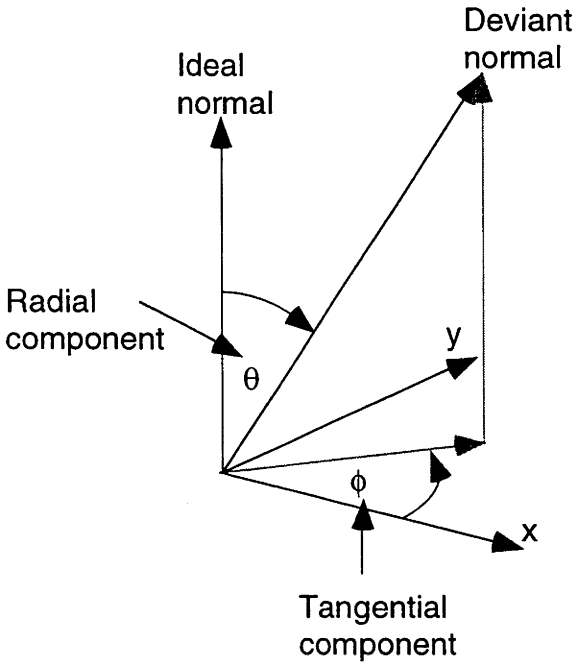

Figure 6.22. Illustration of the radial and tangential components (spherical coordinates) of a deviant normal vector.

This then translates the bivariate probability distribution into one defined by a univariate parameter - that is, the radial component, θ.

6.5 Calculation of bi-variate standard deviation from univariate data.

Calculation of the standard deviation of a circular bi-variate Gaussian probability distribution from an array of univariate radial (θ) deviations requires transforming the probability distribution equation into a univariate form. Equation 3.2 defines a probability per unit area in the x-y plane. Translating from two-dimensional (x,y) coordinates to one-dimensional radial (r) coordinates (Johnston, 1995b), such that the probability per unit area as a function of radius from the most probable direction is calculated, produces a Rayleigh distribution of the form,

$$P = \frac{r}{\sigma^2}\left(e^{-\frac{(r^2)}{2\sigma^2}} \right) \qquad (6.3)$$

This describes a skewed distribution of the form shown in Figure 6.23.

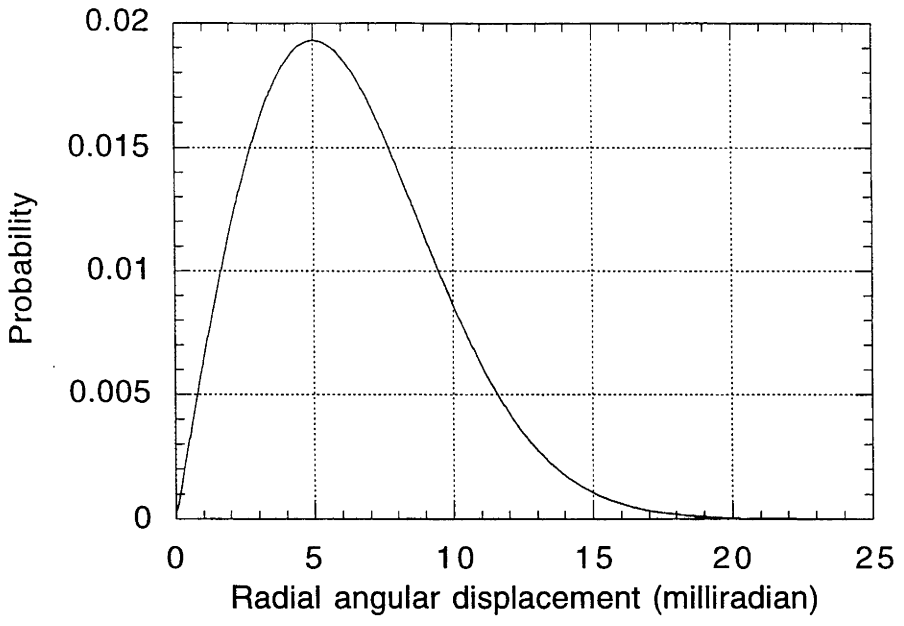

Figure 6.23. Rayleigh distribution describing the probability distribution of radial deviations of normal vectors from their ideal direction. σ = 5 milliradian.

It is noteworthy, and easily shown (Johnston, 1995b) that the mode of the Rayleigh distribution is defined by the standard deviation, σ, of the bi-variate Gaussian distribution of errors.

This model can be used to assess the distribution of surface slope errors for the measured surfaces.

6.6 Surface normal assessment of measured surfaces

Figure 6.24 shows the frequency distribution of surface slope errors calculated for the 20 m^2 dish.

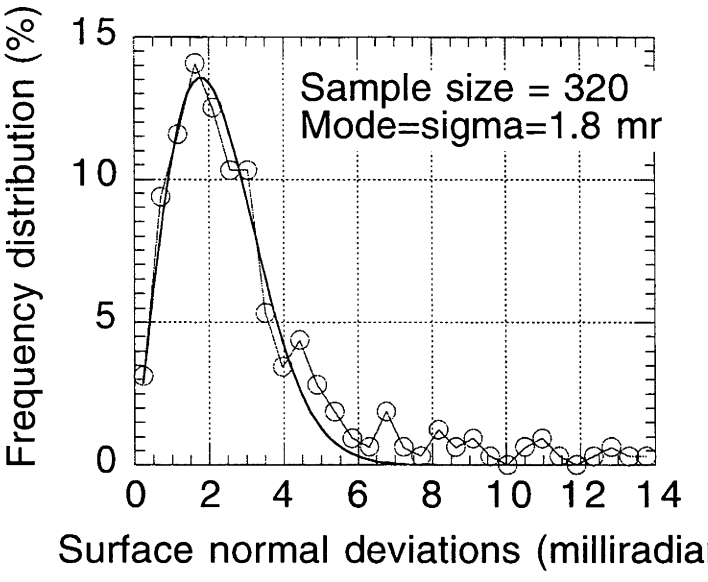

Figure 6.24. Frequency distribution of surface slope errors for the 20 m^2 dish. Smooth curve shows the best fit Rayleigh distribution. Mode indicates the approximate standard deviation of a corresponding bi-variate Gaussian distribution of surface slope errors.

The distribution of measured data shows a close approximation to the fitted Rayleigh distribution, although the tail of the measured distribution shows a slightly greater density of high-value slope errors than those predicted by the Rayleigh distribution. Such a correspondence appears to support the concept that the distribution of surface slope errors of the 20 m^2 dish follows an approximately bi-variate Gaussian probability density distribution. The indicated standard deviation of 1.8 milliradian in Figure 6.24 also supports the modelled value of 2.0 milliradian used in section 4.2 (Figure 4.3) to simulate the measured flux distribution for the dish.

Figure 6.25 shows the frequency distribution of surface slope errors for the s3p2t (30 cm) mirror tile measured on the 400 m^2 surface, with the superposed best-fit Rayleigh distribution to the data.

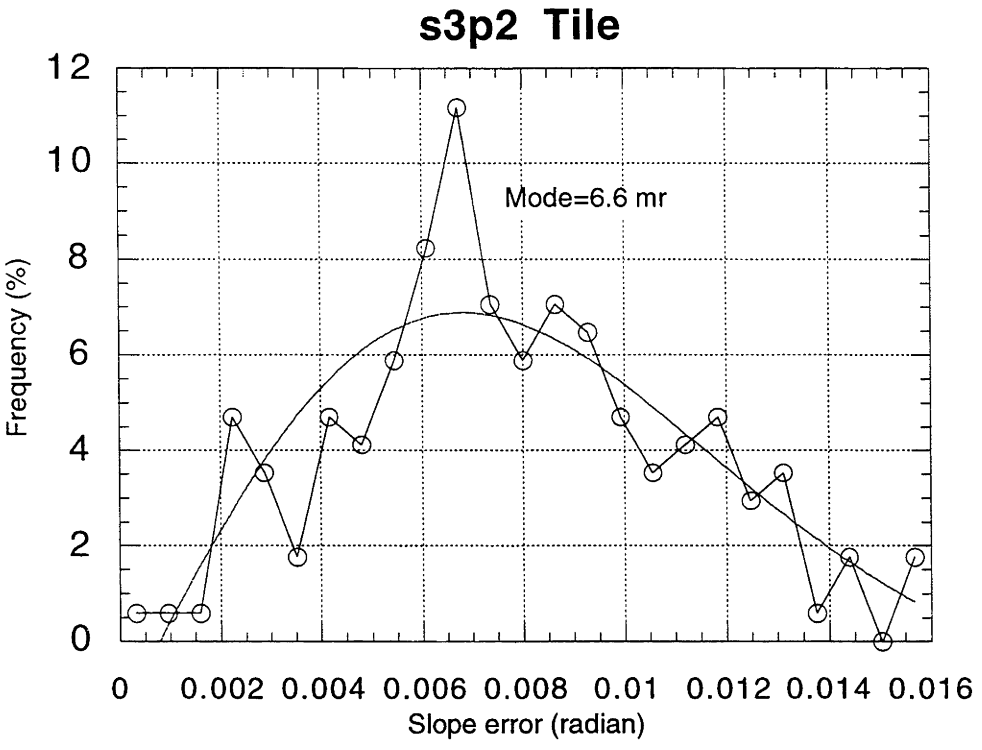

Figure 6.25. Frequency distribution of surface slope errors for the s3p2t mirror tile. The indicated mode is calculated from the best-fit curve to the data set.

It can be seen that Figure 6.25 shows a more 'jagged' distribution than the ideal Rayleigh distribution (smooth line), which makes it more difficult to identify its overall shape. However, as the fitted curve shows, the distribution is not inconsistent with a bi-variate Gaussian distribution of the surface slope errors.

Appendix 6.3 contains the frequency distribution plots for the remaining seven mirror tiles. It can be seen that the surface slope errors for all of these surfaces show a high degree of conformance to a Rayleigh distribution.

However, it should be borne in mind that such a model only provides a convenient method for classifying the distribution of surface slope errors. The real strength of surface normal assessment is the calculation of actual surface normals at defined points on the surface, which then allows ray tracing to be performed on the surface and focal fluxes predicted. As such, it is not absolutely essential that the measured surface normals conform to either a bi-variate Gaussian, or any other distribution, as it is the knowledge of the actual normals rather than their approximate distribution that is of greatest significance to the overall goal of predicting the focal flux distribution.

This does not preclude the fact that conformance with expected models does provide a useful indicator of the optical quality of a surface, and allows for quick assessments of the expected performance of a reflector.

For the case of the 400 m^2 dish, there are clearly many combinations of surfaces that could be assessed for overall surface slope error. As shown in appendix 6.3, slope errors due to the mirror tiles alone can be calculated. Surface fits (using GRADFITTER) can also be performed on the tile vertex coordinates on the measured mirror panels (see Figure 5.14 and Figure 5.15), and surface slope errors calculated for these surfaces. Figure 6.26 shows the frequency distribution of slope errors calculated for the s2p1 mirror

panel (that is, without any tiles on its surface), oriented to assume the measured vertex coordinates at its respective position on the dish surface.

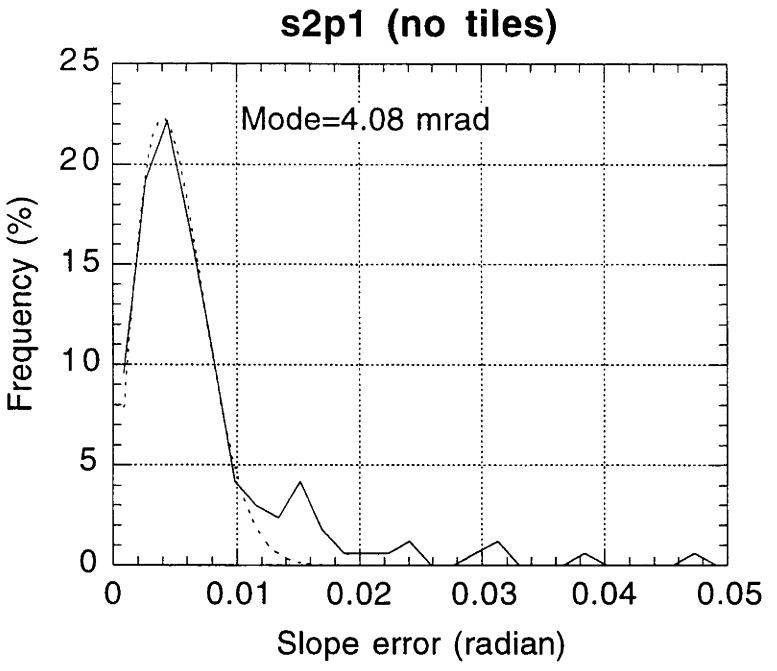

Figure 6.26. Frequency distribution of surface slope errors across the s2p1 mirror panel, using the tile vertex coordinates only (ie. mirror tiles have not been placed on the panel surface). The dotted curve shows the best-fit Rayleigh distribution to the data, with the mode calculated from this best-fit curve.

Appendix 6.4 contains the frequency distribution plots for the remaining measured mirror panels. However, review of Figure 5.14 and Figure 5.15 indicates that the data points at the mirror tile vertices do not constitute a regularly gridded data surface, and represent a comparatively low sampling frequency. These facts will not allow a reliable surface fit to be made for the panel surfaces, and it is expected that the relatively high slope errors indicated in appendix 6.4 are due to this effect.

Duplicating the mirror tiles (and normals) across their respective mirror panels provides indications of the surface slope error due to the individual mirror panels covered with tiles. Figure 6.27 shows the frequency distribution that arises for the s1p1 mirror panel covered with s2p1t mirror tiles. (The tiles were oriented using TRIANGLEREORIENT to assume the individual coordinates measured for the tile vertices on the panel, while the panel had been reoriented to assume the measured vertex coordinates on the dish surface.)

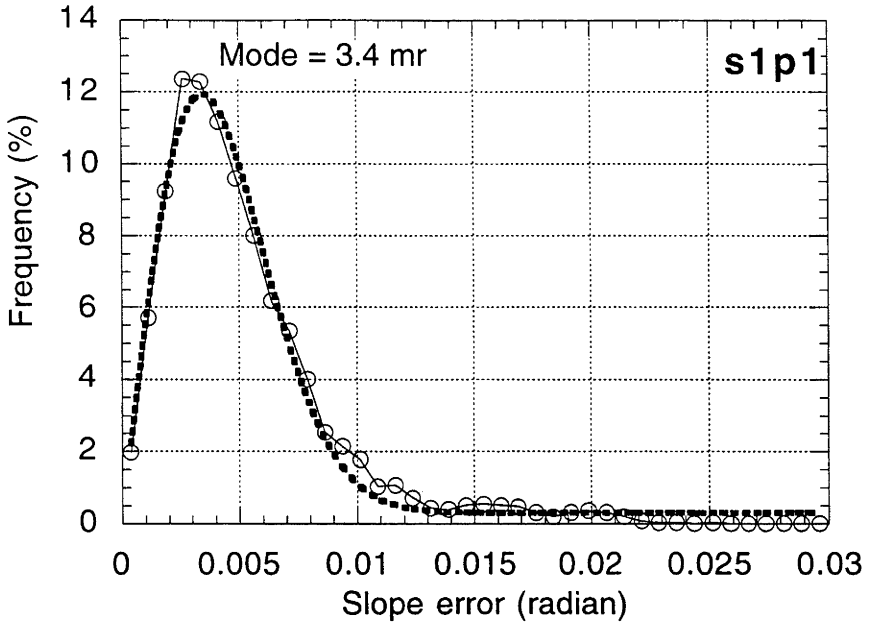

Figure 6.27. Frequency distribution of surface slope errors for s2p1t mirror tiles duplicated across the surface of the s1p1 mirror panel. The dotted curve shows the best-fit Rayleigh distribution to the data, with the mode calculated from this best-fit curve.

Appendix 6.5 contains the frequency distributions for the remaining panel types covered with their respective mirror tiles. Reference to the frequency distributions in the appendix shows that the errors introduced by placing the tiles onto the measured vertex coordinates on the panels (and then the panels oriented into the respective panel positions on the dish surface) produces very different error distributions from those existing on the tiles themselves. Table 6.1 summarises the standard deviation of surface slope errors for the tiles and the respective panels covered with tiles, and oriented into their measured positions on the dish surface for one dish sector (sector 1).

Table 6.1. Summary of surface slope error standard deviations for tiles and tile covered panels on sector 1 of the 400 m^2 dish.

Panel type	Tile slope error (mrad)	Panel + tiles slope error (mrad)	Quadratic difference
p1	1.6	3.4	3
p2	6.6	10.1	7.6
p3	7.8	8.7	3.9
p4	5.7	8.8	6.7
p5	4.7	7.4	5.7
p6	3.2	5.1	4.0
p7	4.7	6.1	3.9
p8	3.9	6.4	5.1
p9	4.7**	6.8**	4.9**

*As these errors are standard deviations, they will normally be combined as a sum of squares. The 'quadratic difference' column is thus calculated as $\sqrt{(col3)^2 - (col2)^2}$

** Slope error from s3p5 and s3p5t used for panel type 9 calculations.

The table indicates that the standard deviation of surface slope error increases for all panel/tile composites above that existing for the tile itself, which is intuitively what one would expect. As a generalisation it appears that the mirror panels contain anything from 3 to 8 milliradian of surface slope error, which is the same order of magnitude as that which exists on the tiles, although it is seen that the panel errors are often slightly larger than those contributed by the tiles.

Taking all of the surface slope errors for all panels and tiles on sector 1 of the 400 m^2 dish and calculating the frequency distribution of errors for this ensemble provides an overall indication of the surface quality of the dish. Figure 6.28 shows the frequency distribution of the combined mirror panels and tiles on sector 1 of the 400 m^2 dish.

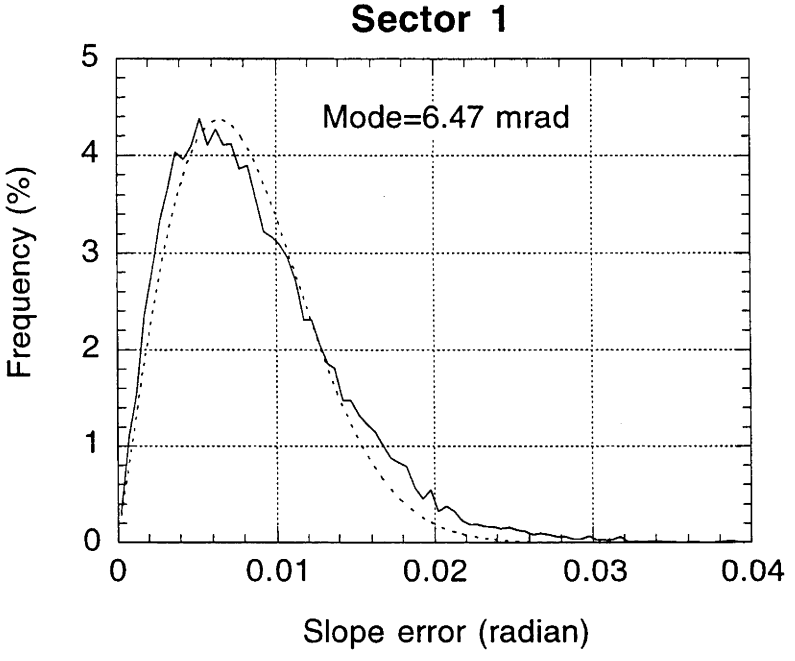

Figure 6.28. Frequency distribution of surface slope errors across nine panels covered with mirror tiles on sector 1 of the 400 m^2 dish.

Appendix 6.6 contains the slope error frequency distributions for the remaining five 400 m^2 dish sectors, while Table 6.2 summarises the slope error standard deviations that are calculated from these plots.

Table 6.2. Summary of surface slope error standard deviations for the six sectors of the 400 m^2 dish.

Sector #	1	2	3	4	5	6
Slope error (radian)	6.47	6.63	6.41	6.70	6.45	6.44

An overall dish slope error can be calculated by combining all six sectors of the 400 m^2 dish and making a frequency distribution plot of the ensuing data points (a total of more than 178,000 points). Figure 6.29 shows the resulting frequency distribution for this complete ensemble of surfaces.

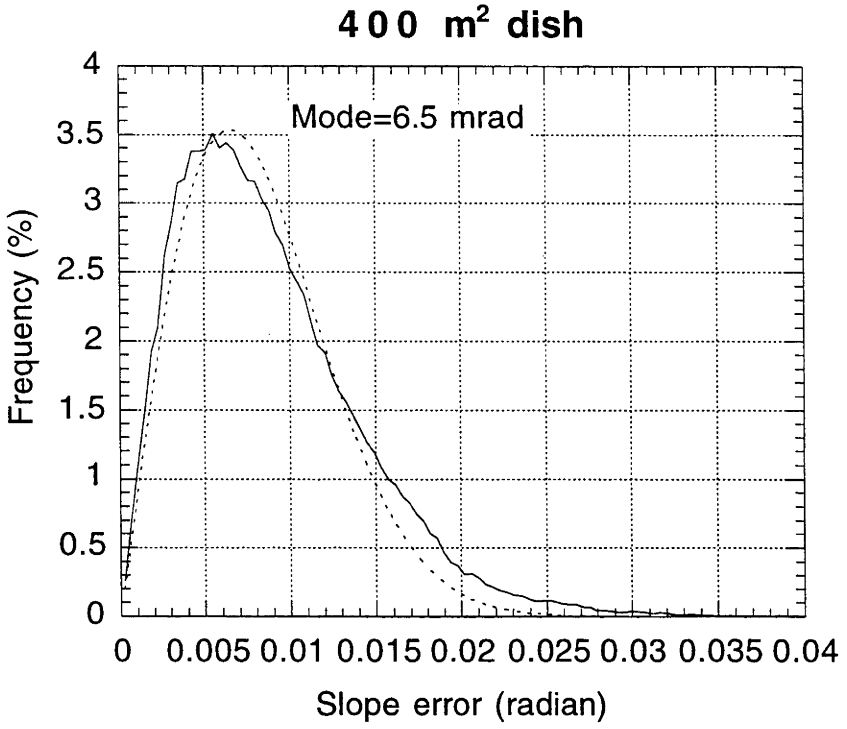

Figure 6.29. Frequency distribution of surface slope errors for the entire ensemble of tiles and panels across the 400 m² dish surface. The dotted curve shows the best-fit Rayleigh distribution to the data, with the mode calculated from this best-fit curve.

As indicated in Figure 6.29, the distribution shows a mode occurring at approximately 6.5 milliradian, which defines the standard deviation of the corresponding bi-variate Gaussian distribution of errors for the dish. This demonstrates a close comparison with the figure of 6.5 milliradian determined by comparing the measured flux distribution with a ray trace predicted flux in section 4.3 (Figure 4.12). However, it is apparent that the measured distributions of slope errors shown in the figures for the dish sectors in Appendix 6.6, and for the entire dish surface in Figure 6.29, do not conform exactly to an ideal Rayleigh (and, in turn, bi-variate Gaussian) distribution of errors. It can be seen in all of the aforementioned graphs, that the modes of the measured distributions occur at slightly reduced slope errors than the best-fit curve, while the right-hand tails of the measured distributions display a slightly increased probability above those predicted by the best-fit curve.

6.7 Discussion of slope error assessments

This chapter has described the development of the surface fitting routine GRADFITTER, which uses a bicubic B-spline algorithm to fit a smooth surface to photogrammetrically measured surface coordinates. The accuracy of surface normals calculated for the fitted surface will be determined by the sampling frequency of the target points placed on the surface relative to the fundamental frequencies present in the surface perturbations. Section 6.3 describes the analysis undertaken to assess the accuracy of fit according to surface slope errors modelled on artificially rippled paraboloidal surfaces. These calculations appear to show that the sampling frequencies chosen (approximately 22 m^{-1}) for the mirror tiles should enable GRADFITTER to model and measure surface slope error on the tiles to a precision of 0.2 milliradian. However, the method of

assessment using a fast Fourier transform (FFT) of the surfaces also indicates that there may be some regions on the tiles where the calculated slope errors may have errors exceeding this value. The author considers that this constitutes a field deserving further analysis that was unable to be completed during the course of the present project.

Examination of the surface slope error frequency distribution plots of the 400 m^2 dish sectors, and the complete dish, shows that the spread of the distributions show close similarities to the ideal Rayleigh distributions expected for slope errors that are determined by a circular bivariate Gaussian distribution of errors. However, as noted in section 6.6, the fit is not perfect, and systematic deviations from the best-fit Rayleigh distribution are apparent in all of the sector and dish error frequency distribution plots. This information can lead us to expect that focal flux distributions predicted for these surfaces will not conform to those expected from surfaces having bivariate Gaussian distributions of surface slope errors. However, it should be re-emphasised that finding the actual slope error distribution model that best describes the measured slope errors is not essential to the utilisation of the calculated surface normals for ray tracing purposes. This fact highlights an attractive feature of direct surface normal calculation from a measured surface data.

The following chapter takes the surface normal information that has been developed in the present chapter and presents the ray trace predicted focal fluxes for the 400 m^2 dish using COMPREC.

7. Ray Trace Predictions From Photogrammetrically Measured Surfaces

7.1 Introduction

The previous chapter discussed the development and analysis of the surface normal properties of the photogrammetrically measured surfaces presented in chapter 5. While characterisation of a reflecting surface by a single number, namely the standard deviation of a bivariate Gaussian distribution of surface slope errors, is a convenient and succinct way of indicating a surface's probable optical performance, it may not necessarily provide an accurate description of the peculiarities of a given reflector. The object of the present study is to investigate the accuracy of using calculated surface normals directly in a ray trace program, to predict the likely flux distribution that will occur in the focal region of a given concentrator, and to compare this model with the results achieved from both videographic flux mapping and ray trace predictions using a simple bivariate Gaussian distribution of surface slope errors.

These ray trace models and comparisons were undertaken using the surface data generated in the foregoing chapters, and will be presented in the following sections.

7.2 Ray trace models using the panels and sectors of the 400 m^2 dish.

The power of the individual photogrammetric measurements of the various components of the dish surface now becomes available, in that flux predictions for the various parts of the reflector can be produced as required. For example, Figure 7.1 shows a surface mesh plot of the ray trace predicted flux arising from the s1p1 mirror panel (with mirror tiles) on a 1.2 m square target at the nominal 13.1 m focal point (model target placed at 13.06 m - see section 2.2.2) of the 400 m^2 dish, while Figure 7.2 shows the corresponding flux image that would appear on the target surface.

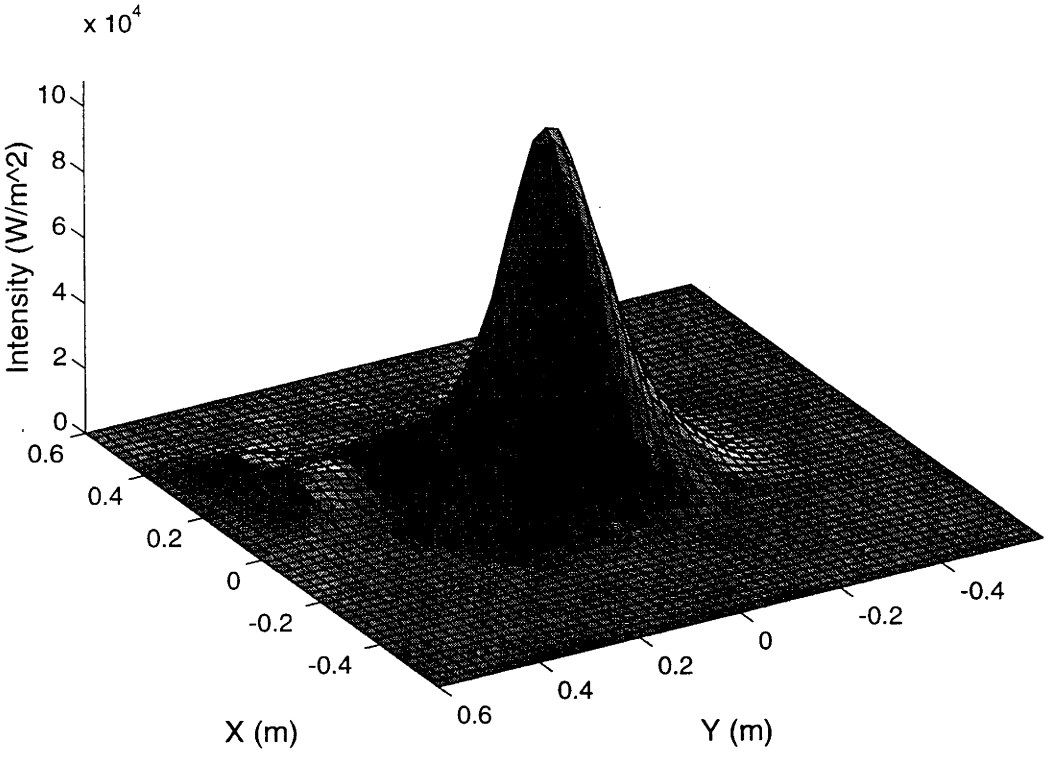

Figure 7.1. Surface mesh plot of the predicted flux calculated for the s1p1 mirror panel, arising from analysis of photogrammetric measurements of the panel surfaces.

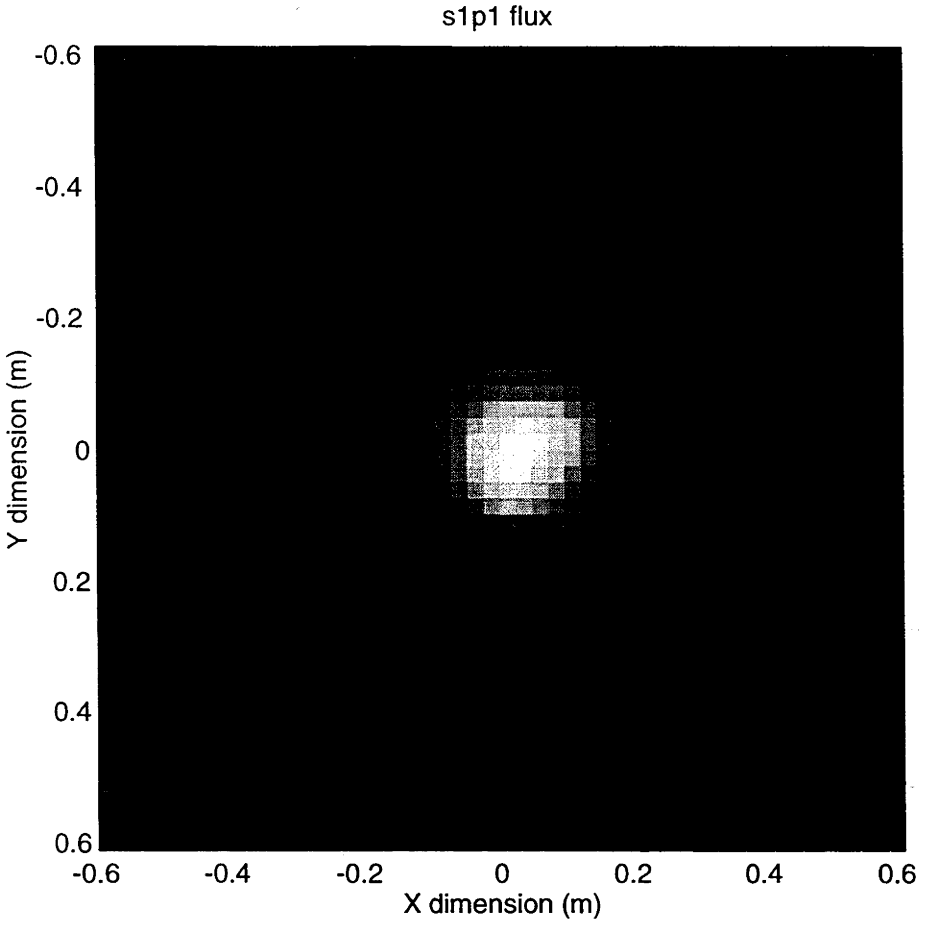

Figure 7.2. Flux image of the distribution shown in Figure 7.1.

Appendix 7.1 contains the predicted flux images for the remaining mirror panels on sector 1 of the 400 m^2 dish. If desired, flux distributions arising from each mirror tile positioned on each panel surface could be calculated. Review of the predicted fluxes shown in Appendix 7.1 shows that the spread of the distributions correlates with the calculated surface slope errors (Table 6.1, section 6.6) for the panels, with the s1p1 panel having the lowest surface slope errors, and also the narrowest distribution with the highest peak flux. Such results conform with intuitive expectations. The remaining panels show poorer surface slope errors and corresponding increases in the spread of the distributions, accompanied by appropriate decreases in their peak fluxes.

Figure 7.3 shows the predicted flux distribution arising from the photogrammetric assessment of the complete 400 m^2 dish surface, while Figure 7.4 shows the gray-scale image of this distribution.

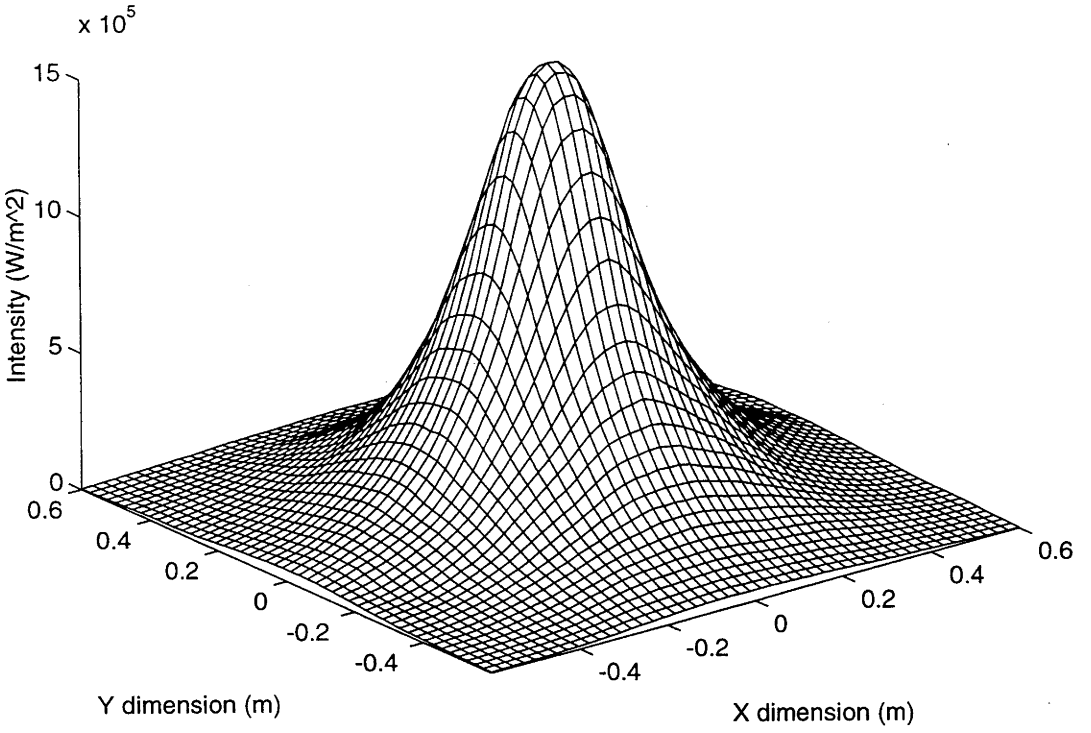

Figure 7.3. Flux distribution predicted for the 400 m^2 dish calculated from photogrammetric measurements of the dish surface.

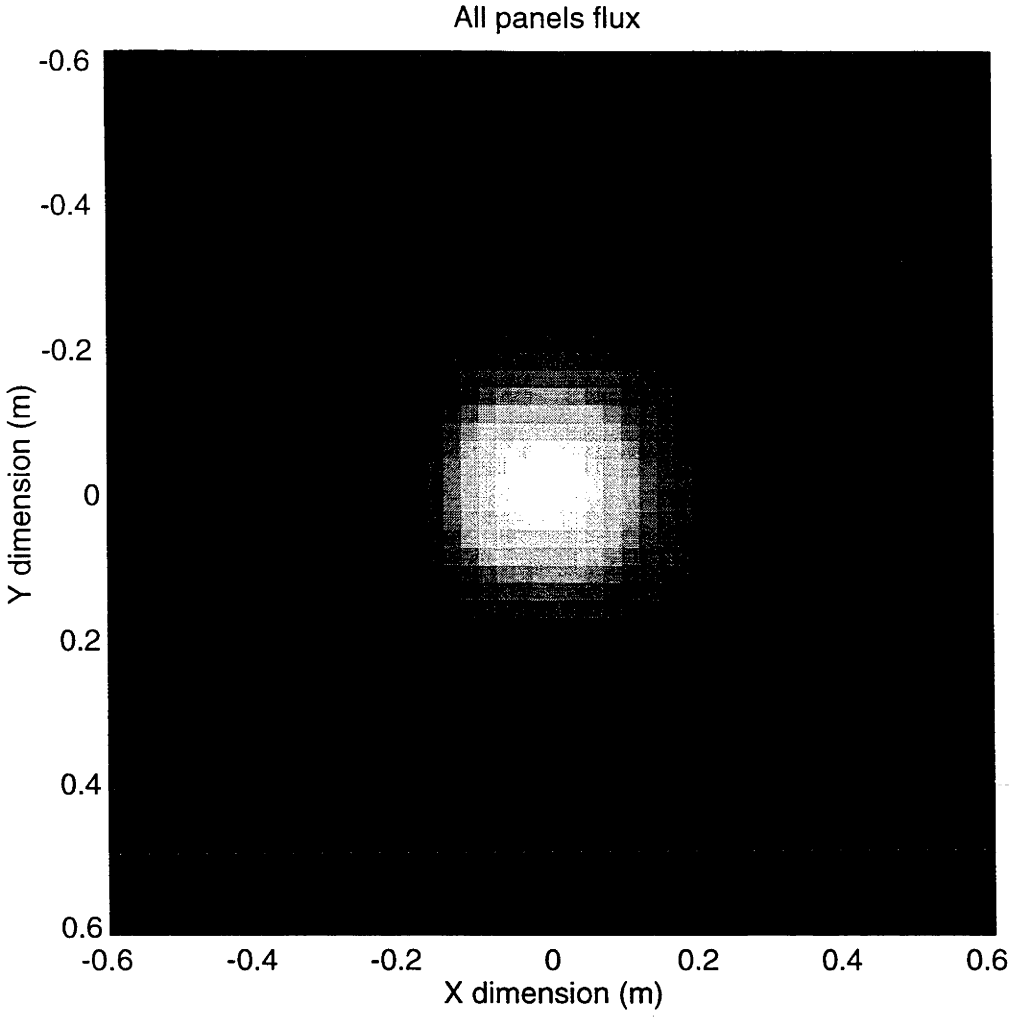

Figure 7.4. Flux image of the distribution shown in Figure 7.3.

7.3 Comparisons with measured and modelled distributions

The overall goal of the photogrammetric measurement process is to predict fluxes that can be compared with the measured distributions. Figure 7.5 shows superposed cross-sections of the photogrammetrically predicted flux (Figure 7.3), the videographically measured flux (Figure 2.15) and the optimal simulated flux (Figure 4.12), using a slope error of 6.5 milliradian). The photogrammetrically predicted and simulated fluxes have been scaled to contain the same integrated power as that contained in the measured distribution.

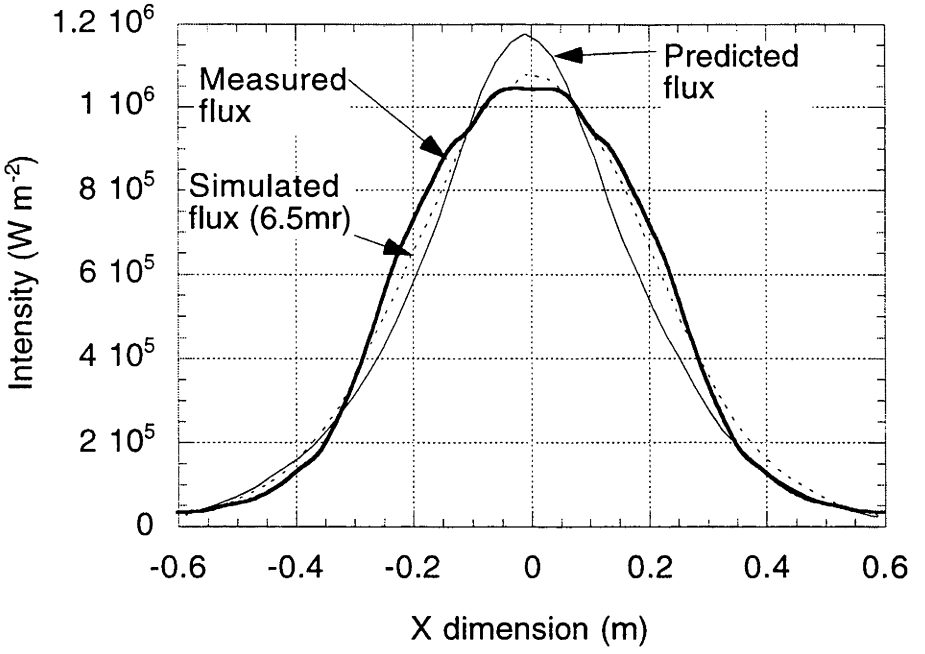

Figure 7.5. Superposition of measured (heavy line), photogrammetrically predicted (light line) and simulated (dashed line) fluxes at the 13.1 m focal point of the 400 m^2 dish. All distributions have equal integrated power.

The percent-power-within-radius plots for the three distributions plotted in Figure 7.5 are shown in Figure 7.6. The percent power in radius has been calculated as a proportion of the total integrated power intercepted by the 1.2 m square target. The curves do not reach 100% because the percentage is calculated as a function of radius, which extends to the boundaries of the square target, but misses the small quantities of power incident on the corners of the target.

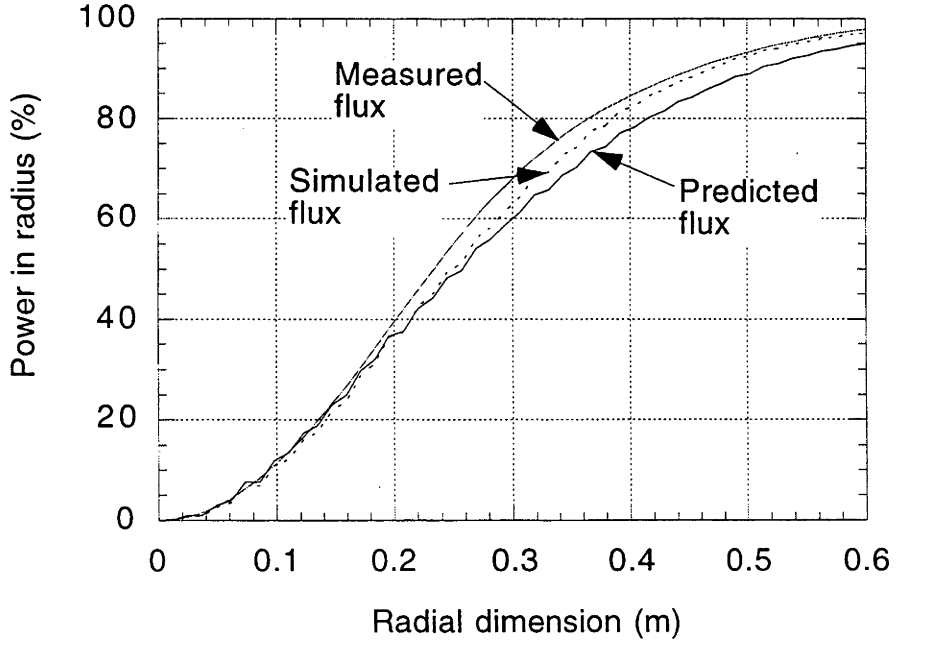

Figure 7.6. Percent-power-within-radius (PIR) plots for the measured, photogrammetrically predicted and simulated flux distributions shown in Figure 7.5.

7.4 Discussion

The results presented in this chapter constitute the key performance tests of the photogrammetric measurement system, and the associated surface processing techniques.

Review of Figure 7.5 and Figure 7.6 indicate that the photogrammetrically predicted flux produces a worst-case deviation of approximately 10% in the calculation of power at a radius of 0.35 m from the distribution centre, with a similar deviation in the calculation of the peak intensity of the distribution. The simulated flux, based on a 6.5 milliradian circular bivariate Gaussian distribution of surface slope errors, shows a slightly better correlation with the measured distribution, with a 5% deviation in the worst-case power-within-radius prediction (at 0.35 m from the distribution centre), and approximately 2% deviation in the simulated peak flux.

These results are discussed further in the following chapter, where the quality of the predicted distribution, and possible sources of error, are examined.

8. Project overview and conclusions

8.1 Goals achieved

This project has sought to both measure and predict the focal region characteristics of solar concentrators, with particular emphasis on point-focus dish collectors at the Australian National University. The research program has been undertaken on the following five distinct fronts:

- Empirical measurements were taken of the focal light distributions of the concentrators using videographic flux mapping;
- A computer based ray trace modelling program was developed for the purpose of creating predictions for the expected focal flux distributions;
- The 3-dimensional coordinates of the reflective surfaces of the concentrators were measured using the established technique of close-range photogrammetry;
- Algorithms and procedures were developed to process the measured surface information to extract the associated optical characteristics for the concentrators;
- Focal region light distributions were predicted using the ray trace algorithm with the photogrammetrically measured and processed surface data as input, and the predicted and measured fluxes compared.

All of the above fields have been pursued successfully, with results from each endeavour forming stepping stones that were used by the other parts to form a consistent and self-supporting assessment system. These features were most evident in the following relationships:

- Measured and predicted flux distributions for the 20 m^2 dish showed highest agreement when a surface slope error of 2.0 milliradian was used to predict the focal flux with the ray trace code. This observation lent confidence to the ray trace code that it was a reliable tool for use with later work.
- The figure of 2.0 milliradian surface slope error for this dish was corroborated by later photogrammetric measurements, which predicted that the dish surface should have approximately 1.8 milliradian of surface slope error;
- Similar comparisons between the measured and predicted flux distributions for the 400 m^2 dish showed the closest correlation when a surface slope error of 6.5 milliradian was used by the ray trace code. Subsequent photogrammetric measurements of the dish surface again corroborated this figure by predicting that the dish should have an overall surface slope error of 6.5 milliradian.
- The linear scaling factor of 74% required to reduce the ray trace predicted flux distribution for the 400 m^2 dish to have the same integrated power as the measured flux distribution, was a direct indication of the average reflectivity of the dish surface. Direct measurement of the reflectivity of the dish at the time of the flux measurements showed an average reflectivity of 72%. This fact again corroborated the reliability of the ray trace code to accurately predict the focal flux distributions of the concentrators.
- The focal flux predicted for the 400 m^2 dish, which directly utilised the photogrammetrically measured and processed surface data, showed a close approximation to the measured flux distribution. This observation formed the final 'touch stone' in the process of validating the reliability and accuracy of photogrammetrically measured surface information.

8.2 Contributions to the field

This thesis makes the following important contributions to the field of solar collector measurement:

1. The application of close-range photogrammetry to the measurement of large area solar concentrators is the first reported instance of this work in the literature to the author's knowledge.

2. Analysis techniques and algorithms have been developed that allow optical (surface normal) information to be extracted from the measured surface data, and for focal region light distributions to be predicted from this information.

3. A simplified assessment technique has been developed for estimating the standard deviation of surface slope error from a distribution of surface slope errors across a concentrator surface.

8.3 Observations on results

8.3.1 Flux prediction from photogrammetric surface data

One of the key comparisons of the project was the superposition of the measured flux distribution with the predicted distribution using photogrammetrically determined surface data for the 400 m^2 dish (Figure 7.5). While the two distributions show a close similarity in their spatial extents, deviations between the shoulders of the distributions, and their peak intensities deserve comment. It can be seen that the measured distribution shows shoulders that are convex, while the predicted distribution shows concave shoulders, and a peak flux that is almost 10% higher than the measured flux. There can be several explanations for these discrepancies:

1. The surface fitting algorithms that were developed to calculate surface normal information may not have been able to resolve the normals with a sufficient degree of accuracy to properly represent the curvatures present in the mirror tile surfaces;
2. Insufficient surfaces may have been measured to allow a full representation of the dominant characteristics of the dish surface. This effect could arise from the process adopted in this project of measuring only one mirror tile, and one panel type, from each of eight different panel types;
3. The process of duplicating these measured mirror tiles across each of their respective panels, and then duplicating each panel (covered with duplicated tiles) into each of the respective positions on the 400 m^2 dish surface may produce a surface that is not sufficiently representative of the actual dish surface;
4. The reflective surfaces of the dish may have changed and degraded over the 2 year period between the events of measuring the flux distributions (May 1994) and the subsequent photogrammetric measurements of the dish mirror surfaces (April 1996). Thus the predicted distribution may be deviant from the measured distribution because it is derived from a surface that has changed from that which existed at the time of the measured distribution.
5. The surface of the dish may change as it changes its elevation. As the dish was lying with its axis vertical for the photogrammetric assessment of the mirror panel

vertices, and then the axis moved to a horizontal position for the photogrammetric measurements of the individual panels. Finally the dish elevation was approximately 20° when the videographic flux images were taken. These changes in orientation could influence the shape of the flux images.

With regard to point 1, while insufficient fitting accuracy may be partly responsible for the observed differences between the measured and predicted distributions, the author considers it unlikely to be a major cause of the effect. This is because the focal region distribution is a montage of approximately 3,000 (comparatively small) focal spots from the mirror tiles on the dish surface. A moment's reflection (no pun intended) reveals that almost any focal distribution could be created by canting or aiming the focussing mirror tiles to various regions of the target plane, and as such it is the orientation of the tiles that will have the greater influence on the overall focal region distribution, rather than the flux distribution arising from any one tile. As such, the level of surface fitting accuracy to the tile surfaces will probably not have a great enough influence to produce the observed deviations.

Points 2 and 3 may be very real contributors to the differences between the predicted and measured distributions. This possibility could only be proven by measuring more surfaces and including them in the overall analysis. Time limitations prevented further investigation of this option.

Point 4 is a possible cause that could only be assessed by measuring the focal flux distribution a second time, nearer to the time when the later set of photogrammetric measurements were made. This was not possible due to the cost and time required to disassemble and remove the receiver hardware that was installed immediately after the initial flux mapping was completed.

8.3.2 Surface fitting and accuracy assessments

The development of the surface fitting algorithm GRADFITTER raised two issues that the author considers to be the source of some uncertainty in the calculation of surface normal information from the photogrammetrically measured surface coordinate data. These are:

1. uncertainties in choosing the optimum smoothing factor that should be used in the fitting algorithm, that both avoids excessively smoothing the data or introducing subtle, rapid fluctuations that may also misrepresent the actual surface, and,
2. uncertainties in the actual accuracy when calculating the average surface normals for a surface.

Point 1 was addressed adequately in the present study, with both numerical and visual demonstrations of the closeness of fit that was achievable using the method of minimisation of the deviations between the fitted bicubic spline surface and a linearly interpolated surface fit to the data. However, some inconsistencies on two occasions when modelling the artificial (bisinusoidal ripple) data surfaces seemed to indicate that there could be some situations where the point of minimum deviation between the bicubic spline and bilinear surface fits was not actually the point of minimum surface slope error. While this occurrence was comparatively rare, it did raise questions about the optimum surface fitting criteria used in the fitting process.

With regard to point 1, it was able to be demonstrated that the surface slope fitting error would most likely be 0.2 milliradian or better. However, comparisons made between the spatial frequencies apparent in the surface from a Fourier transformation of the data, and the slope errors that appeared to be associated with some of these frequencies from analysing artificially created model surfaces, appeared to indicate that there could be some regions of the measured tile surfaces where the level of 0.2 milliradian surface normal fitting accuracy may have been exceeded. The author considers that, while the analysis presented in this study is sufficient to allow a high degree of trust in the fitted surface accuracy, the methods of uncertainty determination require further refinement. It is considered that more work is required in assessing the validity of taking surface slope errors associated with an artificial surface having a single frequency component and comparing this error with the frequency components that are part of a composite of frequencies that constitute an actual surface.

8.4 Recommendations for future research

The author considers that quite a deal more work should be undertaken to address the two issues mentioned above, with regards to the optimisation of the surface fitting criteria and the process of surface fitting error determination. Other fitting models can be examined and tested, such as using higher order B-spline fitting algorithms, or approximating the surfaces using an iteratively refined sum of Gaussian fitting functions (Goshtasby and O'Neill, 1993).

The author has recently received an upgraded version of the CRAMPA suite of programs for performing photogrammetric bundle adjustments using up to 2000 data points and 50 photographs. This is a major improvement over the current software, which will only handle 250 data points and 12 photographs. This new software will allow further work to be undertaken in the assessment of surfaces at much higher sampling point densities, and the effects of these higher sample frequencies will be analysed and documented.

The method of photogrammetric measurement of surface information for solar concentrators has a high potential for offering a universal type of assessment system, as photogrammetry can be applied to almost any surface having a wide range of sizes and/or shapes, whether specular or non-specular. Future studies are planned to assess such diverse devices as satellite dishes (to determine the possible opportunities for using these as solar concentrators when covered with a reflective surface), and linear troughs.

One clear advantage offered by the photogrammetric system is that molds used in the fabrication and production of reflective surfaces for solar concentrators can be assessed before any reflectors are manufactured from them. This has the potential to greatly reduce development time for solar concentrators. Assessments can also be undertaken to quantify the degree of mismatch that occurs between a mold surface and the surface of the reflector that is created from it. This process would require additional studies to measure and understand the changes that occur between a mold and the manufactured item, to allow projections to be made about the expected quality of the reflector surface when manufactured from a mold using a specific fabrication technique.

Other work is also planned using photogrammetry to measure the degree of gravitational sag that occurs across the surface of the 400 m^2 dish as it assumes different elevations. Such a study could provide insights into the possible changes in the focal flux distribution as the dish changes it horizontal orientation.

References

Antonova, R.N.; Tarnizhevskii, B.V.; Aliev, S.A. 1986. Determination of Energy Density on the Thermal Receiver of a Facet Concentrator. Geliotekhnika. Vol.22. No.4. p48–52.

Azimov, S.A.; Belen'kii, Y.A.; Pirmatov, I.I. 1986. A Focal Spot Analyser Based on a TV Camera. Geliotekhnika. Vol.22. No.2. p.16-21.

Bammert K.; Hegazy A.; Lange H. 1990. Determination of the Distribution of Incident Solar Radiation in Cavity Receivers with Approximately Real Parabolic Dish Collectors. J. Sol. En. Eng. Vol. 112, Pergamon Press p.112-243.

Bannister, P. 1991. An Experimental and Analytical Assessment of a Steam Rankine Solar Thermal System. PhD thesis. Australian National University, Canberra, ACT. Australia. 0200. p.26, 27.

Blackmon, J.B. 1985. Development and Performance of Digital Image Radiometer for Heliostat Evaluation at Solar One. J. Sol. En. Eng. Vol.107, Pergamon Press p.315-321.

Butler, B.L. and Petit, R.B. 1977. Optical Evaluation Techniques for Reflecting Solar Concentrators. Optics Applied to Solar Energy Conversion. SPIE. Vol.114. pp.43-49.

Charters, W.W.S. and MacDonald, R.W.G. 1985. Solar Steam Generation. Report to NERDDP, Project #607. May 1985. Dept. Of Mechanical and Manufacturing Engineering, University of Melbourne, Parkville, Victoria, Australia. 3052.

Dickinson, W.C. and Cheremisinoff, P.N.. 1980. Solar Energy Technology Handbook. Part A, Engineering Fundamentals. P.259.. Marcel Dekker, New York.

Dierckx, P. 1993. Curve and Surface Fitting with Splines. Oxford University Press. pp.249-280.

Diver, R.B.; Carlson, D.E.E.; MacDonald, F.J.; Fletcher, E.A. 1983. New High Temperature Solar Research Furnace. J. Sol. En. Eng. Vol. 105. pp.288-293.

Fraser, C. S., 1992. Photogrammetric Measurement to One Part in a Million. Photogrammetric Engineering and Remote Sensing, Vol. 58, No. 3, pp. 305-310.

Goshtasby, A. and O'Neill, W.D. 1993. Surface Fitting to Scattered Data by a Sum of Gaussians. Computer Aided Geometric Design. vol.10. pp.143-156.

Gray, E. 1993. Griffith University, Department of Physics, Brisbane, Queensland, Australia. Private communication.

Grilikhes, V.A. 1968. Experimental Investigation of the Distribution of Irradiance in the Near-Focal Region of a Paraboloidal Concentrator. Geliotekhnika. Vol.4. No.4. p.31-36.

Grossman, J.W. 1994. Development of a 2f Optical Performance Measurement System. Presented at a Joint Solar Engineering Conference, American Society of Mechanical Engineers (ASME).

Harthong, J. and Sahli, H. 1992. Theory of Moiré Sensing by Means of Contour Functions. Applied Optics. vol.31. no.10. pp.1436-1443.

Holmes, J.T. 1982 "Heliostat Operation at the Central Receiver Test Facility, 1978-1980." J. Sol. En. Eng. v.104. pp.133-138.

Igel, E.A., Hughes, R.L. 1979. Optical Analysis of Solar Facility Heliostats. Solar Energy. Vol.22. pp.283-295. Pergamon Press.

Jarvis, R.A. 1983. A Perspective on Range Finding Techniques for Computer Vision. IEEE Transactions on Pattern Analysis and Machine Intelligence. vol.PAMI-5, no.2. pp.122-139.

Jefferies, K.S. 1985. "Optical Analysis of Parabolic Dish Concentrators for Solar Dynamic Power Systems in Space". NASA Technical Memorandum 87080.

Jeter, S.M. 1986. The Distribution of Concentrated Solar Radiation in Paraboloidal Collectors. J. Sol. En. Eng. Vol. 108, Pergamon Press p.219-225.

Johnston, G.H.G. 1995a. Flux mapping the 400 m^2 'Big Dish' at the Australian National University. J.Sol.En.Eng. vol.117. no.4. pp.290-296.

Johnston, G.H.G. 1995b. On the Analysis of Surface Error Distributions on Concentrating Solar Collectors. J.Sol.En.Eng. vol.117, no.4. pp.294-296.

Johnston, G.H.G. 1996. A Compendium of Computer Algorithms Used for Ray Tracing and Surface Characterisation of Solar Concentrators. Department of Engineering, Australian National University, Canberra, Australia.

Jones, P.D. and Wang, L. 1995. Concentration Distributions in Cylindrical Receiver/Paraboloidal Dish Concentrator Systems. Solar Energy. vol.54. no.2. pp.115-123.

Kaneff, S. 1991. The White Cliffs Project: Overview for the period 1979 - 1989. ISBN 0-7305-6954-3, Office of Energy, NSW, Australia.

Kaneff, S. 1993. Paraboloidal Dishes of 400 m^2 and Larger. Proc. International Solar Energy SOciety (ISES), Solar WOrld Congress, Budapest 23-27 August, Vol. Solar Thermal, p.6.

Kaneff, S. 1994. Big Dishes for Concentrating Photovoltaics, Solar Thermal and Other Applications. Proc. 6th Sde Boqer Symposium on Solar Electricity Production, 27-29 November. Keynote Paper, Ben-Gurion University of the Negev. Pp.14-29.

Kaneff, S. 1997. A 400 m^2 Aperture 'Power Dish'. Proc. 35th Annual Conference of the Australian and New Zealand Solar Energy Society (ANZSES) Solar '97. Ed. T. Lee, Canberra, December 1-3, Paper 90.

King, D.L. and Arvizu, D.E. 1981. Heliostat Characterisation of the Central Receiver Test Facility. J.Sol.En.Eng. vol.103. pp.82-88.

Kleih, J. 1989. Qualification of Concentrating Mirror Systems with the HERMES Measurement System and the HELIOS Simulation Program. Technical Report ESA-TT-1213, Deutsche Forschungsanstalt für Luft-und Raumfahrt (DLR-European Space Agency). Report available from Abteilung Wissenschaftliches Berichtswesen der DLR, PO. Box 90 60 58, 500 Köln 90, Germany.

Kleih, J. 1990. Dish-Stirling Test Facility. 5th Symposium on Solar High Temperature Technologies, August 27-31, 1990. Davos, Switzerland.

Kowarschik, R., Kühmstedt, P., and Schreiber,. W. 1993. 3-Coordinate Measurements with Structured Light. 2nd International Workshop on Automatic Processing of Fringe Patterns. Akademie Verlag Physical Research Series, Berlin. pp.204-208.

Lasich, J. 1995. Solar Research Corporation, 6 Luton Lane, Hawthorn, Victoria, Australia. Private communication.

Leary, P.L. and Hankins, J.D. 1979. User's Guide for MIRVAL - A Computer Code for Comparing Designs of Heliostat-Receiver Optics for Central Receiver Solar Power Plants. Sandia National Laboratories report. SAN77-8280, Livermore, CA USA.

Lipps, F.W. and Walzel, M.D. 1978. An Analytic Evaluation of the Flux Density Due to Sunlight Reflected from a Flat Mirror Having a Polygonal Boundary. Solar Energy. vol.21. pp.113-121.

Maas, H.G. 1992. Robust Automatic Surface Reconstruction with Structured Light. XVII ISPRS Congress, Washington, DC. Published in the International Archives of Photogrammetry and Remote Sensing, vol. 29.

Malacara, D. 1978. Optical Shop Testing. John Wiley & Sons. New York.

Moeller, C.E.; Brumleve, T.D.; Grosskreutz, C.; Seamon, L.O. 1980. Central Receiver Test Facility Albuquerque, New Mexico. Solar Energy. Vol.25. pp.291-302. Pergamon Press.

Monterreal, R. 1995. Basic Problems on Flux Measurement in Solar Power Plants Derived From Measurement Procedure/Error Analysis at PSA. . High Flux and Temperature Measurement Workshop March 2-3, 1995, Köln, Germany. SolarPACES Technical Report No.III-2/95, pp.107-109.

Nadeborn, W., Andrä, P., and Osten, W. 1993. Model Based Identification of System Parameters in Optical Shape Measurement. 2nd International Workshop on Automatic Processing of Fringe Patterns. Akademie Verlag Physical Research Series, Berlin. pp.215-221.

NAG. 1994. Numerical Algorithms Group manual. Jordan Hill, OX2 8DR, Oxford, UK. Email: infodesk@nag.co.uk

Neumann. 1994. Flußdictemessung von konzentrierter Solarstrahlung mit Videokameras. 9th Internationales Sonneforum, 1994. pp. 67-77.

NSWC. 1992. Numerical Algorithms Library Manual. Naval Surface Warfare Centre, Dahlgren, Virginia, USA. pp.437-440.

Pettit, R.B., Vittitoe, C.N. and Biggs, F. 1983. Simplified Calculational Procedure for Determining the Amount of Intercepted Sunlight in an Imaging Solar Concentrator. J.Sol.En.Eng. vol.105. pp.101-107.

Renka, R.J. 1996a. Algorithm 752: SRFPACK: Software for Scattered Data Fitting with a Constrained Surface Under Tension. ACM Transactions on Mathematical Software , vol.22, no.1. pp-9-17.

Renka, R.J. 1996b. Algorithm 751: TRIPACK: A Constrained Two-Dimensional DeLaunay Triangulation Package. ACM Transactions on Mathematical Software , vol.22, no.1. pp.1-8.

Renka, R.J. 1996c. Private communication.

Romero, V. 1994. CIRCE2/DEKGEN2: A software package for facilitated optical analysis of 3D distributed solar energy concentrators. Sandia report. SAND91-2238.UC-236. Sandia National Laboratories, US Dept. of Energy.

Sainov, V. 1993. Accuracy and Dynamic Range in Shape Measurement of Large-Format Objects. 2nd International Workshop on Automatic Processing of Fringe Patterns. Akademie Verlag Physical Research Series, Berlin. pp.182-187.

Sanchez, M. and Zarza, E. 1995. A Guide to Computer Programs Developed for Solar Thermal Technologies. SolarPACES technical report No. III-3/95. Available from CIEMAT-Plataforma Solar de Almeria, Apartado 22, 04200 Tabernas (Almeria), Spain.

Schubnell M (1992) Sunshape and Its Influence on the Flux Distribution in Imaging Solar Concentrators. J Sol En Eng 114: 260-266.

Seitz, T. 1995. SunFlux: A Flux Measurement System for Solar Concentrators. High Flux and Temperature Measurement Workshop March 2-3, 1995, Köln, Germany. SolarPACES Technical Report No.III-2/95, pp.47-52.

Shortis, M. R., 1993a. CRAMPA Reference Guide. Version 1.1. Department of Geomatics, University of Melbourne, Australia.

Shortis, M.R., 1993b. Department of Geomatics, University of Melbourne, Australia. Private communication.

Shortis, M.R. and Johnston, G.H.G. 1996. "Photogrammetry: An Available Surface Characterisation Tool for Solar Concentrators, Part 1: Measurements of Surfaces". J. Sol. En. Eng. vol.118. No.3. pp.146-150.

Slama, C. C. (Ed.). 1980. Manual of Photogrammetry, Fourth Edition. American Society for Photogrammetry, Falls Church, Virginia.

Solar Environment Centre, Solar Environment Laboratory. 1995 On-Line Solar-Terrestrial Data, Solar Images. Internet address: http://www.sel.noaa.gov/index.html

Starkey, D.J. and Owen, W.A. 1981. The JPL Flux mapper and the Characterisation of Point Focusing Test Bed Concentrators at JPL. Proceedings of the annual meeting of the American Section of the International Solar Energy Society. vol.4. pp.351-356.

Stein, W.B. and Diver, R.B. 1993. A Compendium of Solar Dish/Stirling Technology. Sandia National Laboratories report. SAND93-7026 UC-236.

Thomas, K. And Whelan, R.E. 1981. "Assessing Solar Flux Distribution in the Focal Region of a Paraboloidal Dish by Moonshots". Research report EP-RR-44, Department of Engineering Physics, Australian National University, Canberra, Australia. 0200.

Tugov, A.I.; Gladilin, V.I. Fundamental Features of Devices for Measuring Heat Fluxes Concentrated by the SES-5 Optical System. Geliotekhnika. Vol.21. No.5. 1985. p.37-41.

Vittitoe, C.N., Biggs, F. and Lighthill, R.E. 1977. HELIOS: A Computer Program for Modelling the Solar Thermal Test Facility - A Users Guide. Sandia National Laboratories report. SAND76-0346.

Welford, W.T. and Winston, R. 1978. The Optics of Nonimaging Concentrators, Light and Solar Energy. pp. 11-26. Academic Press, New York.

Wendelin, T.J., Jorgensen, G.J and Wood, R.L. 1991. SHOT: A Method for Characterising the Surface Figure and optical Performance of Point Focus Solar Concentrators. Solar Engineering 1991. 2nd ASME-JSES-JSME, International Solar Energy Conference, Reno, Nevada, USA. March 17-22, 1991. pp.555-560.

Yamada, T.; Noguchi, T. 1976. Digital Pyrometry in a Solar Furnace. Solar Energy. Vol.18. pp.533-539.

Yampolsky, V. 1995 "Measurements of Power Density Distribution of Solar Fluxes and Temperatures of Gas Flows Using Passable Wire Calorimeters." Proceedings of the 5th Task III Meeting within IEA SolarPACES on "Solar Technology and Applications". Paul Scherrer Institute, Villigen, Switzerland, March 8 1995. pp.177-182.

Appendix 1.1. Published and/or submitted journal articles

This appendix contains the following articles that have been published, or are in press, in the Journal of Solar Energy Engineering, together with an article submitted for publication in the Solar Energy journal.

- "Flux mapping the 400 m^2 'Big Dish' at the Australian National University." Johnston, G.H.G. 1995. J.Sol.En.Eng. vol.117. no.4. pp.290-293.

- "On the Analysis of Surface Error Distributions on Concentrating Solar Collectors." Johnston, G.H.G. 1995. J.Sol.En.Eng. vol.117, no.4. pp.294-296.

- "Photogrammetry: An Available Surface Characterisation Tool for Solar Concentrators, Part I: Measurements of Surfaces". Shortis, M.R. and Johnston, G.H.G. 1996. J. Sol. En. Eng. vol.118. No.3. pp.146-150.

- "Photogrammetry: An Available Surface Characterisation Tool for Solar Concentrators, Part II: Assessment of Surfaces". Johnston, G.H.G. and Shortis, M.R. 1997. J. Sol. En. Eng. vol. 119, No. 4. pp.286-291.

The following manuscript is in-press with the Solar Energy journal:

- "Focal Region Measurements of the 20 m^2 Tiled Dish at the Australian National University." Johnston, G.H.G. August 1998. Vol. 63. No. 2.

The articles follow.

Flux Mapping the 400 m^2 "Big Dish" at the Australian National University

G. Johnston
Energy Research Centre/Department of Engineering,
Australian National University,
Canberra, ACT, Australia 0200

Videographic flux mapping has been used to characterise the focal flux distribution of the 400 m^2 solar concentrator located at the Australian National University. Peak fluxes in the focal region of 1.13 MW m^{-2} have been recorded, which corresponds to a concentration of 1790 suns normalized to 1000 W m^{-2} insolation and 100 percent mirror reflectivity. Comparisons with ray trace predicted fluxes incorporating surface normal errors indicates that the dish surface has a mean surface error standard deviation of 6 milliradian.

1 Introduction

In April-May of 1994, the 400 m^2 paraboloidal "Big Dish" solar concentrator at the ANU was first turned onto the sun to perform an assessment of its focal region characteristics. Fig. 1 shows a picture of the dish.

The construction of the dish is a space truss structure using tubular steel struts (or members) bolted together at joining nodes in an arrangement of rigid cells, which produces a light, strong mounting framework on which to mount the reflecting mirror panels. The mirrors have a nominal reflectivity of 86 percent and are comprised of 2-mm thick back-silvered ("green") glass, bonded on to sheet metal/foam sandwich support panels. The dish has a hexagonal aperture, and its surface is comprised of 54 triangular mirror panels, each approximately 4.2 m on a side. The dish is mounted on a base frame (also of space truss construction) which provides an alt-azimuth mounting to allow two-axis tracking of the sun. Actuation is provided in both altitude and azimuth directions by a novel "walking ram" system. These work through a series of alternate extensions and retractions of appropriately mounted hydraulic rams. At the time of the reported measurements, tracking was achieved under manual control, with an approximate error of 1 to 2 milliradian. A central mounting pole supported by eight guy-wires is in place to allow the mounting of receivers in the focal region of the dish. A four legged "quadrapod" structure approximately 2 m in height is mounted at the end of the pole, upon which a support frame can be secured for the installation of receivers. The quadrapod has water cooling pipes integrated with each exposed leg to effect temperature control (and some preheating of feed water when a steam generating receiver is in use).

2 Installation of Flux Measuring Equipment

A water cooled target for the display of flux images was mounted on a suitable frame above the quadrapod support structure at the end of the receiver mounting pole. The axial position of the target in the focal region was controlled with an electric motor and gearbox.

Figure 2 shows a schematic diagram of the layout of the equipment used to carry out the flux mapping of the dish.

The target consists of two aluminium sheets separated by 20 mm "C" channel sections. The channel sections are arranged to form a series of serpentine channels for the passage of cooling water through the structure. A "HiCal"[1] foil gauge radiometer was mounted in the centre of the panel to allow direct measurement of the focal region intensity, and thermocouples were mounted on the water inlet and outlet ports of the target. The surface receiving the radiation was painted with a white, matt finish, high temperature paint. (Previous tests of a similar nature performed on a 5-m diameter dish at the ANU indicated that such a surface has an approximate reflectivity of 81 percent.) A CCD camera[2] was mounted approximately 1.8 m below the midpoint of the target travel position, at the base of the quadrapod support structure, and focused on the target. A set of high-density absorption filters was installed in front of the camera to reduce the reflected light levels impinging on its CCD element to values that fell within its operating range. (Unfortunately these filters later cracked due to the intense level of back radiation reflected from the target surface. Time restraints on the availability of the dish prohibited another test run with improved filters. However, the ensuing light leakage interfered only with the very edges of the recorded flux image, and a correction was later applied using the symmetry of the distribution.) The camera CCD response characteristics were measured and calibrated using neutral density filters to allow linearization of the images captured by the camera. Figure 3 shows the average response characteristic obtained for the camera under a range of calibrated light intensities, shown as filter transmission coefficients.

3 Collection and Analysis of Images

Images of the flux distribution viewed by the camera were recorded on a SuperVHS video cassette recorder,[3] which was later replayed, and selected images digitized using a seven-bit framegrabber card mounted in a Sun SparcStation. The images were then corrected for CCD camera nonlinearities and calibrations applied from the radiometer signal to convert the pixel levels into absolute intensity units (W m^{-2}). Figure 4 shows a mesh surface plot of the flux distribution measured at the designed focal point of 13.1 m from the dish vertex.

The anomalous peaks appearing near the skirt of the distribution shown in Fig. 4 correspond to the light leakage that occurred through the cracked filters in front of the camera lens.

Figures 5(*a*) and 5(*b*) show cross sections through the flux distributions obtained on the water cooled target at varying

Contributed by the Solar Energy Division of THE AMERICAN SOCIETY OF MECHANICAL ENGINEERS for publication in the ASME JOURNAL OF SOLAR ENERGY ENGINEERING. Manuscript received by the ASME Solar Energy Division, Feb. 1995; final revision, Aug. 1995. Associate Technical Editor: J. Davidson.

[1] HiCal calorimeter, Model C-1312-A-300-072, HiCal Engineering, 9650 Telstar Ave., El Monte, CA 91731.

[2] Sony CCD colour video camera module, Model XC-999P, 752 × 582 pixels, automatic gain turned off.

[3] Panasonic Super VHS (PAL) video cassette recorder, Model NV-FS100HQ.

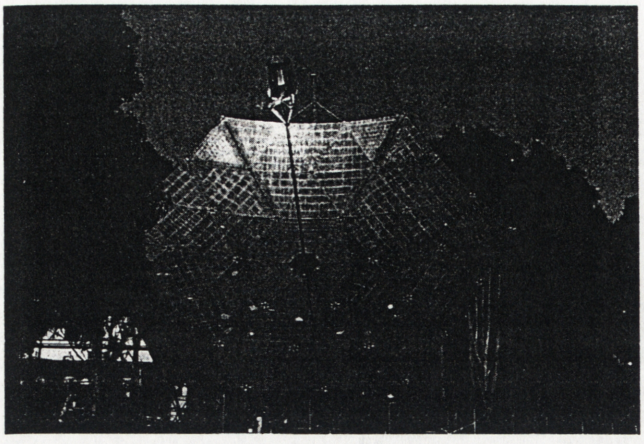

Fig. 1 The 400 m² dish at ANU

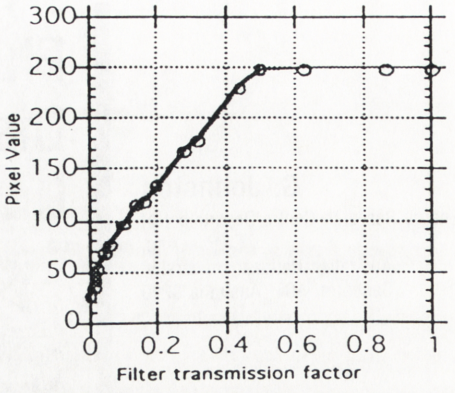

Fig. 3 CCD camera response characteristic as a function of filter transmission coefficient

positions in the focal region. Figure 6 shows a contour plot of the measured distribution at the focus.

As can be seen from Fig. 6, the flux distribution shows a high degree of symmetry. It was considered that this feature could be employed to allow an estimation of the total intercepted power under the distribution, by taking half of the distribution excluding the anomalous light leakages, and simply doubling the power contained in this half.

Figure 7 shows the resulting surface plot, together with a "filling" of the central "dropout" image of the radiometer. (It can be noted that the flat top of the 13.1 m distribution is partially due to filling of the radiometer image. However, this does not account for the full width of the flat region, and this flux flattening phenomenon appears to be a real effect which is not due to CCD saturation.)

Some investigations were made into the possible re-reflection of sunlight back onto the water cooled target by the legs of the quadrapod support structure. As noted in Section 3.1, the quadrapod legs were calculated to obstruct approximately five percent on the incoming radiation, and this is also the approximate view factor that these structures present to the light re-radiating from the target. As the quadrapod legs were shielded in stainless steel sheet having a convex outer shape, brief calculations of the view factors seen of the target by the legs indicated that much less than one percent of the re-reflected light would be redirected back to the target.

3.1 Intercepted Power. A comparison between the integrated power under the distribution shown in Fig. 4, the power calculated by cold-water calorimetry on the water-cooled target and the power calculated from the optical characteristics of the dish provides a useful cross check between these methods.

By straightforward numerical integration, the integrated power under Fig. 4 is 256 ± 25 kW. Table 1 below shows the relevant parameters measured from the water cooled target during the collection of flux images to allow a cold water calorimetry assessment.

The intercepted power is given by

$$P = \frac{\dot{m}c(T_{out} - T_{in})}{(1 - \rho_t)}$$

where c is the specific heat of water (@30°C) = 4180 kJ kg^{-1}.

From this relationship, the intercepted power is 249 ± 26 kW.

Table 2 shows the relevant parameters required to calculate the intercepted power from the dish optics.

The intercepted power is given by

$$P = I.A.\rho_r.$$

From this the intercepted power is 243 ± 18 kW.

The foregoing calculations indicate that the three methods of calculating intercepted power appear to converge to a value of

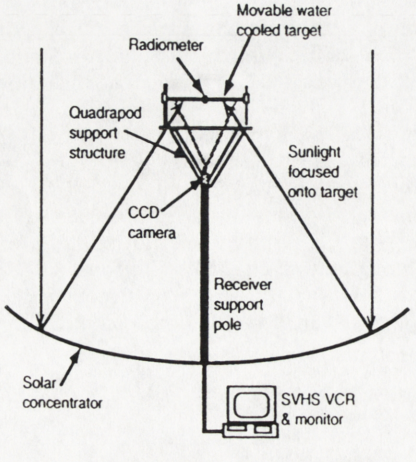

Fig. 2 Layout of flux mapping equipment

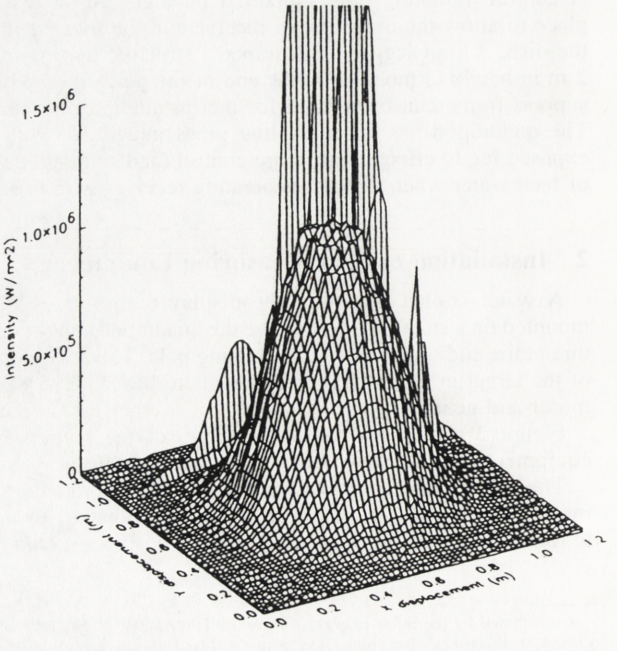

Fig. 4 Surface plot of the flux distribution measured at the 13.1 m focal point of the 400 m² dish

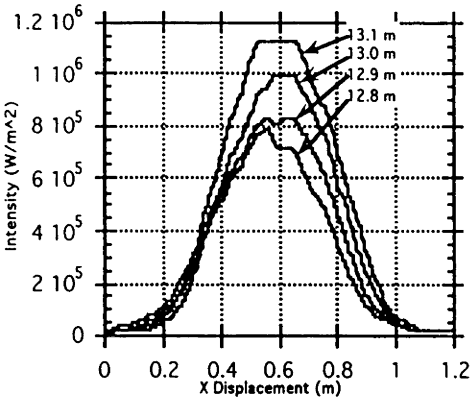

Fig. 5(*a*) Flux cross sections at positions up to the 13.1 m focal point

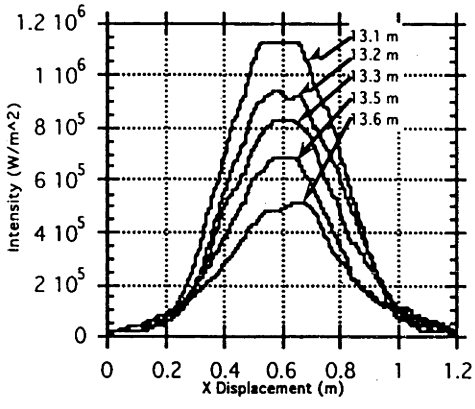

Fig. 5(*b*) Flux cross sections at positions beyond the 13.1 m focal point

approximately 250 kW (±ten percent). (Geometric calculations indicate that the quadrapod support structure intercepts approximately five percent of the incoming radiation onto the water cooled target. Convective heat losses from the water cooled target to the environment were calculated to be approximately 70 W. These were considered of negligible proportions and were not utilised in the calculations of absorbed power.)

3.2 Concentration Ratio. As shown in Figure 5(*a*), the peak flux intensity at the focal point (13.1 m) is of the order of 1.13 MW m^{-2}. This corresponds to a peak concentration ratio

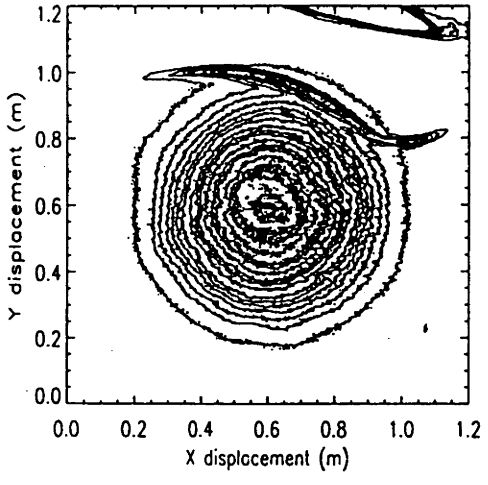

Fig. 6 Contour plot of the flux distribution at the focal position of 13.1 m

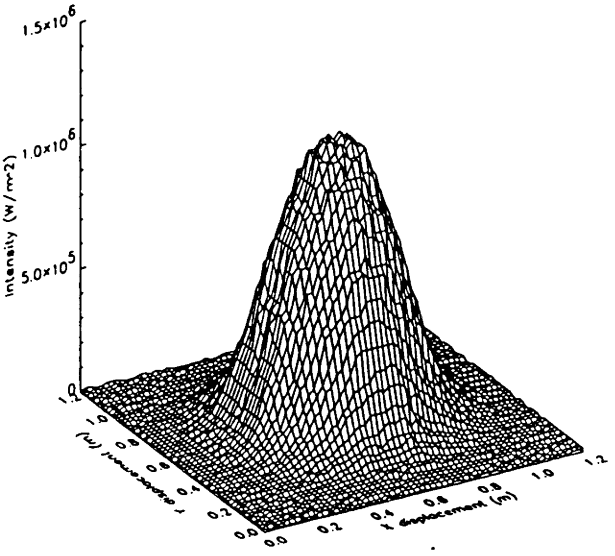

Fig. 7 Surface plot of the reconstructed flux distribution to eliminate stray light aberrations and radiometer image

of 1290 suns. The insolation level at the time of this measurement was 875 W m^{-2}, and the average dish reflectivity was measured to be 72 percent. These figures indicate that the peak concentration ratio normalised to 1000 W m^{-2} and 100 percent dish reflectivity is 1790 suns. The average concentration ratio (under this normalization) over the area encompassing 90 percent of the intercepted power (corresponding to a radius of 0.375 m from the center of the distribution) is 810. For the expected dish reflectivity of 86 percent (when cleaned) and 1000 W m^{-2} insolation, the peak concentration ratio becomes 1540 suns.

3.3 Percent Power Within Radius. Of particular interest is a measure of the proportion of the total power contained within a given radius from the centre of the distribution. Figure 8 shows a plot of the percent power contained within radius for the focal point (13.1 m) flux distribution. Also shown on the plot in Fig. 8 is the 0.34 m radius corresponding to the radius of the aperture of the cylindrical steam generating receiver designed for placement at the focal point. It is seen that approximately 85 percent of the incident radiation is intercepted by the receiver aperture. (The remaining 15 percent is captured by the 1.5 m diameter preheater skirt surrounding the receiver aperture.)

4 Comparison With Ray Trace Predicted Flux Distributions

A ray trace code dubbed COMPREC (acronym for COMPound RECeiver) has been written by the author to enable simulations to be performed for primary radiation incident on a variety of three-dimensional receiver shapes placed in the

Table 1 Parameters measured for cold water calorimetry on flux target

Parameter	Value	Comments
Water flow rate ($\dot{m}$, kg s^{-1})	0.491 ± 0.007	'Container & stop-watch' method
Inlet temperature (T_{in}, °C)	16.1 ± 0.1	Type K thermocouple
Outlet temperature (T_{out}, °C)	39.1 ± 0.1	Type K thermocouple
Target reflectivity (ρ_t, %)	81 ± 2	Previously measured using cold water calorimetry

On the Analysis of Surface Error Distributions on Concentrated Solar Collectors

G. Johnston
Energy Research Centre/Department of Engineering,
Australian National University,
Canberra, ACT, Australia 0200

The distribution of surface normal deviations from an ideal shape on concentrating solar collector surfaces is used to define the optical quality of a reflector. These distributions can be modeled by considering them to ideally follow a two-dimensional, circular Gaussian distribution. However, the measurement of these deviations in experimental systems usually defines only that component of the surface normal that deviates from the ideal surface normal direction, and ignores the rotational component of the normal vector in the plane perpendicular to the ideal direction. To compare the measured one-dimensional radial distribution with the expected two-dimensional model, we must transform the two-dimensional model into the appropriate radial distribution. The following analysis describes this transformation, and presents results gained from an application of the analysis to measured surface normal data from a mirror panel used in the reflecting surface of the 400 m^2 paraboloidal ("Big Dish") concentrator constructed at the ANU.

Introduction

Measurement of solar concentrator reflecting surface quality has been undertaken by numerous methods. These have included modified Hartmann tests using a scanning laser beam (Wendelin, Jorgensen, and Wood, 1991), measurement of reflected image deviations seen in a concentrator from geometric targets placed either at the focal point or the approximate radius of curvature (Grossman, 1994), direct contact measurement of the surface deviations from a datum or, more recently, surface measurement using photogrammetry (Shortis and Johnston, 1995). The usual information that is processed from these surface measurement techniques is that of the deviation of a surface normal vector direction at any given point (hereafter referred to as the "the surface normal") from the ideal direction. Figure 1 shows this graphically.

If we are dealing with a paraboloidal surface, then the ideal surface normal at any point will be the gradient of the surface at the point. As can be imagined in Fig. 1, however, actual surface normals can take an infinite number of positions around this direction, with their angular deviation defined by both the tangential angle, ϕ, and the radial angle, θ. It can be generally assumed that the tangential deviation (ϕ) can take any uniformly distributed random value between 0 and 2π (Hutchinson and Lai, 1991), and its effect is not as significant as the deviation of θ, its value is usually ignored and the radial angle, θ is used as a measure of the surface normal deviation. (It can be noted that some specific collector surface deformations—such as out-of-plane warping in stretched membrane dishes—do produce a nonuniform ϕ distribution.) This forms the first stage in the process of rationalizing surface errors into a manageable form.

Statistical Distribution of Deviations

The second stage arrives when it is realised that such deviations occur continuously across a surface, such that there are an infinite number of them taking an infinite range of values. This then becomes a problem of statistical distribution. The most common method of modeling this situation is to apply a Gaussian distribution of values (Romero, 1994; Taneja et al., 1992; Feurermann and Gordon, 1991) to the projection of the surface normal vector on the x-y plane. (For small deviations of the surface normal, this projected vector is suitably represented by the deviation vector shown in Fig. 1). Typically this involves using a bi-variate, circular Gaussian probability density function to describe the variation in position of the deviation vector. This function is derived from the one-dimensional Gaussian probability density function, and is given by (see Appendix A):

$$\frac{dP}{dxdy} = \frac{1}{2\pi\sigma^2} e^{-(x^2+y^2)/2\sigma^2} \tag{1}$$

where dP is the differential probability of the projection of the surface normal vector on the x-y plane falling in the elemental area, $dxdy$ (also represented by dA), and σ is the standard deviation of the distribution. This can be expressed in polar form,

$$\frac{dP}{dA} = \frac{1}{2\pi\sigma^2} e^{-r^2/2\sigma^2}. \tag{2}$$

This form gives the differential probability of a vector of length, r, and implicit tangential angle, ϕ, falling in an area, dA.

This model has been found to work satisfactorily in computer ray trace simulation studies (Romero, 1994; Taneja et al., 1992), where the probability density function is used to create devia-

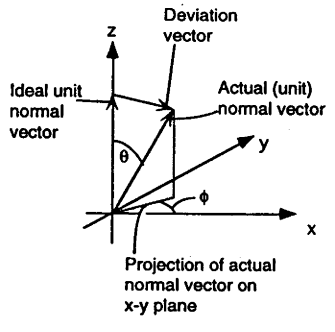

Fig. 1 Deviation between a measured surface normal vector and the ideal surface normal (arbitrary axes shown with z-coordinate aligned with ideal normal vector direction)

Contributed by the Solar Energy Division of THE AMERICAN SOCIETY OF MECHANICAL ENGINEERS for publication in the ASME JOURNAL OF SOLAR ENERGY ENGINEERING. Manuscript received by the ASME Solar Energy Division, Feb. 1995; final revision, Aug. 1995. Associate Technical Editor: J. Davidson.

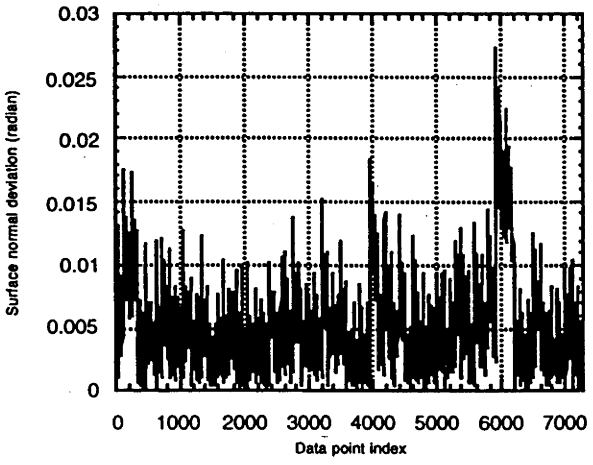

Fig. 2 Plot of surface normal errors versus data point number across the surface of a mirror panel on the 400 m² concentrator at the ANU

tions of ideal surface normals for the purposes of synthesising flux distributions on simulated target surfaces. The primary validation of the method is that a measured flux distribution can be satisfactorily recreated using a ray trace code and a suitable value of standard deviation for the Gaussian distribution of surface deviations.

Analysis of Measured Surface Normal Deviations

The foregoing probability distribution appears to be an appropriate one for the creation of surface deviation models. However, when a set of measured surface deviation data are analyzed, the Gaussian distribution discussed above does not seem to provide an immediately obvious metric by which to judge the data. This could be anticipated intuitively, as measured data are only one-dimensional, whereas the Gaussian model is a two-dimensional distribution. Figure 2 shows a graphic representation of 7200 surface normal deviations (in radian) measured using a photogrammetric analysis (Johnston and Shortis, 1995) across a mirror panel surface installed on the 400 m² "Big Dish" paraboloidal concentrator at the ANU. ("Data point index" in Fig. 2 refers to the index numbers used to define the particular data points on the reflector surface.)

Figure 3 shows these data replotted as a frequency distribution of values. (The data range of 30 milliradian is divided into 100 data bins, such that each bin has a width of 0.3 milliradian.)

As Fig. 3 clearly shows, the data do not display any symmetry or resemblance to a Gaussian distribution of data.

Bi-variate Gaussian Distributions as One-Dimensional Radial Distributions

The distribution of data shown in Fig. 3 can be reconciled with that expected from data conforming to a two-dimensional

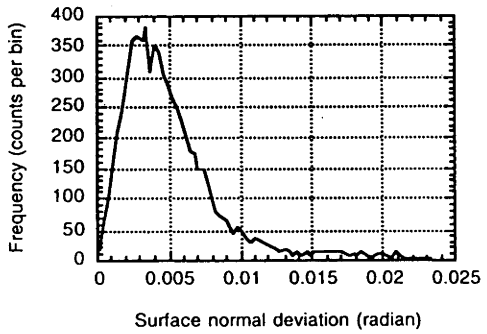

Fig. 3 Frequency distribution of the data shown in Fig. 2

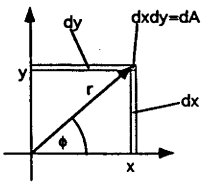

Fig. 4(a) Two-dimensional definition for the calculation of probability of a Gaussianly distributed vector having (Cartesian) coordinates x, y falling within the area, $dA = dxdy$

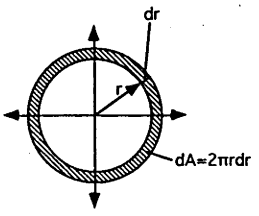

Fig. 4(b) One-dimensional definition for the calculation of probability of a Gaussian radial distribution having radius r, falling within the area, $dA = 2\pi r dr$, with equal likelihood of all tangential angles ϕ

Gaussian distribution of surface normal deviations. What is required is a conversion of the two-dimensional representation of the probability distribution into one that shows the probability distribution according to the one-dimensional radial distribution. Figures 4(a) and 4(b) show the translation that is required.

The conversion between the Cartesian and polar representations is made simply by observing that the elemental area, dA, in the polar system is given by

$$dA = 2\pi r dr. \tag{3}$$

Substituting this into the polar description of the density function (Eq. (2)),

$$\frac{dP}{2\pi r dr} = \frac{1}{2\pi\sigma^2} e^{-r^2/2\sigma^2}. \tag{4}$$

This simplifies to

$$\frac{dP}{dr} = \frac{r}{\sigma^2} e^{-r^2/2\sigma^2}. \tag{5}$$

Thus, the probability density distribution as a function of radius (rather than a function of (r, ϕ) position) is given by Eq. (5). Note that r is always positive in polar coordinates. (The distribution described by Eq. (5) is often defined as a Generalised Rayleigh or Bivariate Chi Squared distribution (Johnson and Kotz, 1972).) If the surface normal vector is made of unit length, then, for the small surface imperfections that are encountered in most concentrator surfaces, the radial distance deviations of

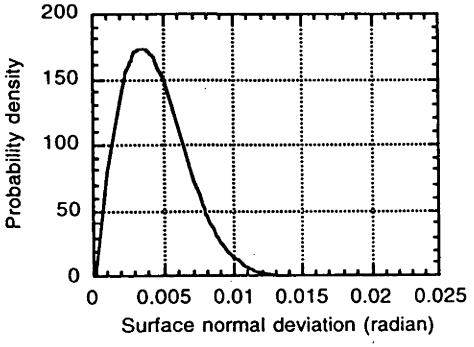

Fig. 5 Two-dimensional Gaussian probability density distribution expressed as a one-dimensional function of radius. Standard deviation (σ) = 3.5 milliradian, assuming equal likelihood of all tangential angles ϕ.

the vector are very closely approximated by the radial angular deviations (in radian). Figure 5 shows the shape expected for this distribution for a standard deviation of 3.5 milliradian.

The mode of the distribution described in Eq. (5) is found in the standard way by differentiating the equation with respect to r, and setting the result to zero and solving for r. When this is done, the outcome shows the simple result that the mode occurs when

$$r = \sigma.$$

Thus, to quantify the surface error of a surface (assuming that the errors follow a bi-variate Chi Squared distribution), one needs to measure the deviations of the surface normals, plot them as a density distribution of errors, and note the mode of the distribution. This value gives the standard deviation of the Gaussian distribution of errors directly. Thus, for the distribution of measured data shown in Fig. 3, the apparent mode, or standard deviation, is approximately 3.5 milliradian.

Figure 6 shows the density distribution from the measured data shown in Fig. 3 superimposed with the theoretical distribution of Eq. (5), with the standard deviation set to the mode of 3.5 milliradian observable in the measured data. (The value of 3.5 milliradian was also confirmed by using a least squares algorithm to fit Eq. (5) to the data of Fig. 3, with σ defined as the adjustable variable. The height of the theoretical distribution was also adjusted by a least squares fit to accommodate the difference between the probability densities arising from the (theoretical) continuous distribution and the (measured) discrete distribution.)

Discussion and Conclusions

It can be noted that while Fig. 6 shows good agreement between the measured data and the theoretical model it is expected to conform to, there is some deviation, particularly noticeable in the tail of the distribution. In this region the model would be predicting negligible probabilities for surface deviations greater than approximately 14 milliradian, while the measured data shows a significant number of values up to 25 milliradian. There are also some deviations near the mode of the distribution. These effects most likely reflect the situation that the real data is not exactly conformant with an ideal Gaussian distribution of errors. Further work is being undertaken to examine other types of possible probability distributions that could show an improved correlation with the measured data.

However, the developments presented to date show that where Gaussian distribution of surface errors is suspected, a straightforward analysis of the errors can be made by plotting the data as a probability density distribution and noting the mode of the resulting distribution. This value defines the standard deviation of the Gaussian distribution of errors. For the data available in this study, this process shows it to closely conform to a Gaussian distribution of surface deviations.

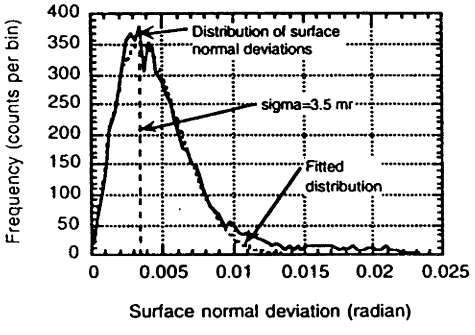

Fig. 6 Superposition of measured and theoretical values for the distribution of surface normal errors across a mirror panel of the ANU "Big Dish"

Acknowledgments

The author would like to offer his thanks to Mr. Mark Dymond for the insights and discussions that led to the analysis in this publication, and to Prof. Peter Hall for his advice and review of the concepts contained in it.

References

Feuermann, D., and Gordon, J. M., 1991, "Analysis of a Two-Stage Linear Fresnel Reflector Solar Concentrator," ASME JOURNAL OF SOLAR ENERGY ENGINEERING, Vol. 113, pp. 272–279.

Grossman, J. W., 1994, "Development of a 2f Optical Performance Measurement System," *Joint Solar Engineering Conference*, ASME, Work conducted at Sandia National Laboratories, Albuquerque, New Mexico, supported by DOE contract DE-AC04-94AL85000. pp. 25–32.

Hutchinson, T. P., and Lai, C. D., 1991, *The Engineering Statistician's Guide to Continuous Bivariate Distributions*, Rumsby Scientific Publishing. p. 280.

Johnson, N. L., and Kotz, S., 1972, *Continuous Multivariate Distributions*, (Distributions in Statistics Series), John Wiley and Sons. New York, p. 220.

Johnston, G., and Shortis, M. R., 1995, "Photogrammetry: An Available Surface Characterization Tool for Solar Concentrators—Part II: Assessment of Surfaces," *Int. J. Sol. En. Eng.*, in revision for publication.

Romero, V., 1994, "CIRCE2/DEKGEN2: A Software Package for Facilitated Optical Analysis of 3-D Distributed Solar Energy Concentrators," Theory and User Manual, Sandia Report SAND91-2238.

Shortis, M. R., and Johnston, G., 1995, "Photogrammetry: An Available Surface Characterisation Tool for Solar Concentrators—Part I: Measurement of Surfaces," submitted for publication.

Taneja, P., et al., 1992, "Concentration Characteristics of a Two Stage Solar Concentrator: Effect of Primary Mirror Surface Errors," *Int. J. Energy Research*, Vol. 16, John Wiley and Sons. pp. 203–211.

Wendelin, T. J., Jorgensen, G. J., and Wood, R. L., 1991, "SHOT: A Method for Characterizing the Surface Figure and Optical Performance of Point Focus Concentrators," *Solar Engineering*, The Second ASME-JSES-JSME International Solar Energy Conference, Reno, NV, pp. 555–560.

APPENDIX A

The Two-dimensional (Bi-variate) Gaussian Probability Density Distribution

The bi-variate Gaussian probability density function is developed from the basic one-dimensional function:

$$\frac{dP_x}{dx} = \frac{1}{\sigma\sqrt{2\pi}} e^{-x^2/2\sigma^2} \quad \text{or} \quad dP_x = \frac{1}{\sigma\sqrt{2\pi}} e^{-x^2/2\sigma^2} dx.$$

This gives the differential x-dimension probability, dP_x, of a value falling in the range, dx, at the value of x. If we consider a two-dimensional vector, having both x and y coordinates, and that the distribution of both these coordinates follows a Gaussian probability density function, then in the y-dimension the distribution will be

$$\frac{dP_y}{dy} = \frac{1}{\sigma\sqrt{2\pi}} e^{-y^2/2\sigma^2} \quad \text{or} \quad dP_y = \frac{1}{\sigma\sqrt{2\pi}} e^{-y^2/2\sigma^2} dy.$$

And by probability theory, the probability of two independent probabilities (which can be safely assumed for the x and y dimensions) occurring together is simply the product of the two probabilities

$$dP = dP_x dP_y = \frac{1}{2\pi\sigma^2} e^{(-x^2+y^2)/2\sigma^2} dxdy$$

or

$$\frac{dP}{dxdy} = \frac{dP}{dA} = \frac{1}{2\pi\sigma^2} e^{(-x^2+y^2)/2\sigma^2} = \frac{1}{2\pi\sigma^2} e^{-r^2/2\sigma^2}.$$

Photogrammetry: An Available Surface Characterization Tool for Solar Concentrators, Part I: Measurements of Surfaces

M. R. Shortis
Department of Geomatics,
University of Melbourne,
Parkville 3052
Australia

G. H. G. Johnston
Department of Engineering,
Australian National University,
Canberra, ACT 0200,
Australia

Close range photogrammetry is a sensing technique that allows the three-dimensional coordinates of selected points on a surface of almost any dimension and orientation to be assessed. Surface characterisations of paraboloidal reflecting surfaces at the ANU using photogrammetry have indicated that three-dimensional coordinate precisions approaching 1:20,000 are readily achievable using this technique. This allows surface quality assessments to be made of large solar collecting devices with a precision that is difficult to achieve with other methods.

Introduction

The development of large-scale solar concentrators, such as the 400 m^2 "Big Dish" developed at the ANU, brings accompanying problems in assessing the quality (i.e., nearness of fit to a perfect parabolic/paraboloidal shape) of their surfaces. A number of methods have been proposed and used to perform these assessments by various research efforts. These have often been accomplished by direct measurement using accurate coordinate displacement transducers connected to a probe. The probe is placed at various positions on the surface to be characterized and coordinates read off the transducers. Other systems have used a scanning laser beam reflected off the concentrator surface and sensed by a detector that can determine the spatial position of the reflected beam (usually) on a plane, and from this surface displacements can be calculated (Wendelin et al., 1991). Another technique has optically assessed the image reflected by a concentrator with a specially marked and/or colored object placed at its focus or radius of curvature (Grossman, 1994). Moiré fringe effect techniques and laser interferometry (Sainov, 1993; Kowarschik et al., 1993; Nadeborn et al., 1993) have also been investigated for surface contour measurement, and provide interesting insights into current endeavors in surface remote sensing (although to the authors' knowledge have not been implemented for large-scale solar collector analysis).

These methods are mostly applicable to smaller scale collectors (<10 m maximum dimension) and it can be difficult to ensure that both optimum and reliable precisions are achieved in the results. They are also usually system specific, in that they are constructed to assess one particular collector size or geometry, and must be modified and/or reconstructed to assess new collector designs or shapes.

Experiments at the ANU have investigated the usefulness of close range (sometimes referred to as analytical) photogrammetry in the pursuit of surface quality assessments of paraboloidal dish concentrators, with a particular view to determine the actual shape of the recently completed 400 m^2 (22.6 m effective diameter) "Big Dish," and from this data to perform a ray trace analysis to predict the flux distribution that will occur in the focal region of this concentrator.

Contributed by the Solar Energy Division of THE AMERICAN SOCIETY OF MECHANICAL ENGINEERS for publication in the ASME JOURNAL OF SOLAR ENERGY ENGINEERING. Manuscript received by the ASME Solar Energy Division, May 1995; final revision, Feb. 1996. Associate Technical Editor: J. H. Davidson.

Photogrammetry: An Overview

Photogrammetry is essentially the science of quantitative analysis of measurements from photographs. Photogrammetry predates photography, as da Vinci and Desargues developed the principles of perspective and projective geometry in the 14th and 16th centuries. The first actual applications of photogrammetry for qualitative mapping occurred with the early photographic processes, but production line mapping systems were not introduced until the 1930s (Slama, 1980).

The most familiar aspects of modern day photogrammetry are maps and charts of the Earth. Aerial photography and photogrammetric analysis are used to produce the vast majority of topographic maps, street directories, and tourist maps in use today. Most of these maps and charts can be described as medium (1:5,000 to 1:50,000) or small scale (1:100,000 and smaller). Smaller scale maps, for example those used in an atlas, are generally derived from compilations of photogrammetric products. All such maps and charts are cartographically designed, analyzed, and enhanced to aid in the presentation of spatial features, and the relationships between features, to the map user.

Photogrammetry is also in use for archaeological and architectural recording, biological measurement, industrial metrology, and engineering surveillance, to name just a few of the many "close-range" applications (Karara, 1989). In many cases a large-scale map or a chart is the result of the photogrammetric measurement, for example a line plot and sections of a building facade undergoing restoration produced for analysis and interpretation by an architect. However, for industrial and engineering applications of close-range photogrammetry, the output of the process is often only coordinates of signalized points on the object. Individual locations to be measured are marked with a target or other unambiguous signal to uniquely identify the point and enhance the accuracy of measurement. Such points may be placed to identify key dimensions of the object, or to characterize a surface at a known sampling density. The coordinate set is then subjected to post-analysis, generally by the client for whom the measurement task was undertaken.

Photogrammetry has been used specifically for the recording of various types of antennae. Microwave astronomic (Fraser 1986) and compact range radar (Fraser, 1992) antennae have been the type most frequently measured by photogrammetry particularly because of the very high accuracies required to meet the surface tolerance specifications. Photogrammetric measurement of optical reflector systems is less common, al-

Photogrammetry: An Available Surface Characterization Tool for Solar Concentrators, Part II: Assessment of Surfaces

M. Shortis
Department of Geomatics,
University of Melbourne,
Parkville 3052, Australia

G. Johnston
Department of Engineering,
Australian National University,
Canberra 0200, Australia

In a previous paper, the results of photogrammetric measurements of a number of paraboloidal reflecting surfaces were presented. These results showed that photogrammetry can provide three-dimensional surface characterisations of such solar concentrators. The present paper describes the assessment of the quality of these surfaces as a derivation of the photogrammetrically produced surface coordinates. Statistical analysis of the z-coordinate distribution of errors indicates that these generally conform to a univariate Gaussian distribution, while the numerical assessment of the surface normal vectors on these surfaces indicates that the surface normal deviations appear to follow an approximately bivariate Gaussian distribution. Ray tracing of the measured surfaces to predict the expected flux distribution at the focal point of the 400 m^2 dish show a close correlation with the videographically measured flux distribution at the focal point of the dish.

Introduction

Photogrammetry utilizes the principle of stereoscopic reconstruction of a three-dimensional surface through the use of photographs or images taken of the surface from two or more viewing positions. The three-dimensional coordinates of specific targets placed on the surface are determined through a combination of observations made on common targets in different photographs, and the application of photogrammetric processing software to provide a least-squares adjustment of resultant data arrays, which in turn produces the estimated target coordinates and associated precisions. A previous paper (Shortis and Johnston, 1995) described the application of photogrammetry to characterize the surfaces of four separate sets of reflecting surfaces.

These measured surfaces included the surface of a 5-m diameter, circular aperture paraboloidal dish solar concentrator, a 30-cm square, curved mirror tile, a 4.2-m triangular mirror panel that supports approximately 70 of these tiles, and finally the surface of the ANU 400 m^2 dish, that is covered with 54 of these 4.2-m mirror panels. In addition to these, a further seven 60-cm mirror tiles and an equal number of their associated triangular mirror panels have been measured using digital photogrammetry. This technique has provided a higher coordinate accuracy, data point density, and much reduced processing time compared to the film based technique described previously.

The seven additional mirror tiles and panels were chosen such that one tile from each panel was measured. Ideally, a total of nine panels and tiles should have been measured to accommodate all the panel types used on the dish, but due to difficulties photographing the ninth panel, it was omitted, and the fifth panel was duplicated and used at the coordinates applicable to the ninth panel. Figure 1 shows the overall layout on the 400 m^2 dish surface, also illustrating the positions of the measured panels and tiles.

Further analysis is required to assess the quality of the measured surfaces. Two measures of ideality have been used to compare the surfaces in the present study with the expected paraboloidal shape. The first looks at the deviation of the z-coordinates of the measured surfaces from the z-coordinates of a corresponding ideal paraboloid. This allows a visual inspection to be made of the surface perturbations as they exist in three-dimensional space. The second method numerically calculates the surface normal vectors of a measured surface, and then assesses the angular deviations (surface normal error) of these vectors from the normal vectors expected for an ideal paraboloid. This latter metric appears to be the more widely utilized measure of the "quality" of a solar concentrator reflecting surface, and is often referred to as "surface slope error" or simply "slope error" (Romero, 1994), (Grossman et al., 1992), (Taneja et al., 1992), (Krasilovskii et al., 1978). There will be some correlation between figures of merit based on the two quality measures. However, direct comparison is qualitative at best, as surface slope error is dependant on both the magnitude and relative spacing (spatial frequency) of the z-coordinate deviations, and the effect of both of these quantities on the surface slope error is difficult to quantify without doing a full surface normal analysis.

An approximate cross-check on the validity of the calculated normal vectors and slope errors can be performed by using a ray trace algorithm to simulate the focal flux that would be produced from the photogrammetrically measured surfaces, and to compare this distribution with the measured distribution for the concentrator. Comparisons with a simulated ideal paraboloidal surface having an assigned level of random surface error (which follows a bivariate Gaussian distribution) can also be made. Depending on the degree of closeness to a bivariate Gaussian distribution of errors in the measured surface, the two flux distributions should show a significant degree of correlation.

Assessment of Surfaces

Z-Coordinate Deviations. All surfaces should ideally fit the equation to a paraboloid, that is,

$$z = \frac{(x^2 + y^2)}{4f} = \frac{1}{f}\frac{r^2}{4}$$

where f is the focal length.

Contributed by the Solar Energy Division of THE AMERICAN SOCIETY OF MECHANICAL ENGINEERS for publication in the ASME JOURNAL OF SOLAR ENERGY ENGINEERING. Manuscript received by the ASME Solar Energy Division, June 1995; final revision, Mar. 1997. Associate Technical Editor: J. H. Davidson.

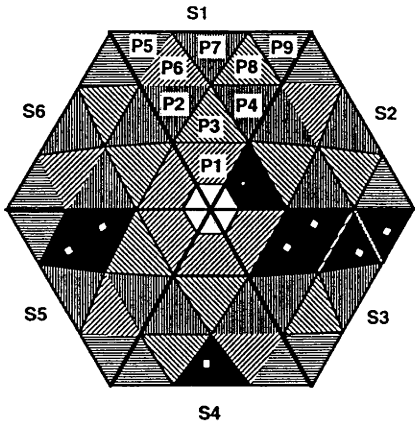

Fig. 1 Layout and nomenclature of triangular panels on the surface of the 400 m² "Big Dish" (diagram not to scale). Panels, and associated mirror tiles, measured photogrammetrically, are marked in black (tiles superimposed in white).

Plotting the z-coordinates versus $r^2/4$ should yield a straight line with a slope of $1/f$. A least-squares linear fit was performed on such plots for the 5-m dish, the eight triangular mirror panels and the 400 m² dish, the 30-cm mirror tile, and the seven 60-cm tiles. Following this, the focal lengths were used to construct ideal paraboloidal surfaces with which to compare the deviation of z-coordinates of the measured surfaces from the ideal. When plotted as a frequency distribution, the z-coordinate deviations appeared to follow an approximately Gaussian distribution of values. The standard deviations of these distributions can be used as a measure of the overall "ripple" in the surfaces. Figures 2 and 3 show the surface deviation plot and the frequency distribution of surface deviations, respectively for the 5-m dish. Similar analyses were performed for the other reflector surfaces. Table 1 summarizes the corresponding results.

Surface Normal Determinations

Development of a Surface Normal Calculation Routine. Of primary interest in solar concentrator assessment is a measure of the deviation of the surface normals away from the ideal normal direction (slope error). A numerical surface normal calculation routine, dubbed GRADFITTER, has been developed to assess surface normals for numerically defined surfaces. It utilizes a bicubic B-spline fit to the surface data points using automatic knot placement according to the value specified in a smoothing variable. This variable was adjusted such that closest approximation to local variations was obtained, while avoiding

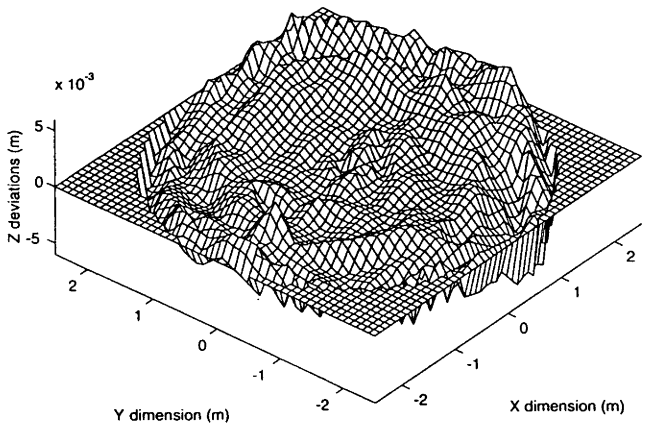

Fig. 2 Surface deviations observed between the photogrammetrically assessed 5-m dish and a 1.81-m focal length paraboloid

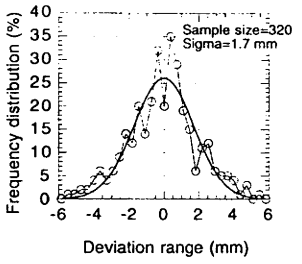

Fig. 3 Statistical frequency distribution plot of photogrammetrically determined z-coordinate (depth) deviation data for the 5-m dish

spurious oscillations and instabilities between knots (knots are anchor points placed in the fitting function through which the surface must pass).

GRADFITTER utilizes the EO2DDF and EO2DEF surface fitting algorithms in the NAG[1] library of numerical analysis routines. This routine is in turn based on the SURFIT algorithm contained in the FITPACK analysis package developed by Dierckx (1993). The robustness of fit was maintained by minimizing the z-coordinate deviations of the interpolated spline surface compared to a bilinear interpolation of the surface. (It was found that the deviations from a bilinear fit were large when the smoothing factor was large (indicating that the spline surface was smoothing the data points too severely), and when the smoothing factor was excessively small (indicating that the spline surface was "rippling" excessively between knots). The deviations were at a minimum when the spline surface most closely approximated the local variations in the data). The surface normals were calculated by taking the cross-product of interpolated elemental vectors within the fitted surface in close proximity to the actual data points. The algorithm accommodates both nonrectangular and nonregular data arrays. The assessment of surface slope errors at a particular surface coordinate was performed by calculating the ideal surface (unit) normal (finding the surface gradient of the paraboloid) and then subtracting this from the calculated surface (unit) normals determined using GRADFITTER (i.e., the radial component of the error displacements was used). The length of this difference vector was then used as the measure of the slope error at the coordinate point. This process assumes that the error distribution is circularly symmetric around the ideal normal direction (i.e., tangential error displacements are assumed uniform, and thus ignored). While this assumption is not always necessarily correct, particularly where systematic surface distortions are apparent, calculation of surface slope error is generally performed, and specified, for the radial error component.

Surface Fitting Accuracy Assessment. Determining the accuracy of fit for a general spline curve or surface to unknown data can prove a difficult exercise. Experience with spline fits shows that they can either smooth a surface excessively, or introduce unrealistic fluctuations between data points, depending on the placement of knots. Data point density also affects the accuracy of fit. The data point density chosen for the measured surfaces was initially based on a visual inspection of the mirror tiles to assess the "characteristic ripple distances" that appeared upon them. These ripple distances were characterized by measuring the distances between apparent peaks and troughs that occurred on a range of tiles in both their "x" and "y" dimensions. (The mirror tile surfaces were smoothly varying functions across both dimensions—cracked mirrors, containing sharp discontinuities, were not used for assessment.) Target point spatial frequency was chosen to ensure at least six data points per peak (or trough) in both dimensions were

[1] Numerical Algorithms Group, Jordan Hill, OX2 8DR, Oxford, UK. Email: infodesk@nag.co.uk.

Table 1 Focal length and standard deviation of surface error determinations for the 5 m dish, eight triangular mirror panels, and eight mirror tiles and 400 m² dish. (Labels for the mirror tiles are derived from their position on the dish surface; e.g., s3p2 refers to sector #3, panel #2, etc. See Fig. 1.)

Surface	Focal length (m)	Standard deviation of z-coordinate deviations (mm)	Number of data points
5 m dish	1.812 ± 0.0007	1.7	320
s2p1 mirror panel	13.23 ± 0.01	1.0	167
s3p2 mirror panel	12.89 ± 0.02	5.9	104
s3p3 mirror panel	12.92 ± 0.02	4.6	105
s5p4 mirror panel	12.98 ± 0.02	3.8	103
s3p5 mirror panel	13.16 ± 0.01	2.6	104
s3p6 mirror panel	13.09 ± 0.01	2.5	104
s4p7 mirror panel	13.16 ± 0.01	6.6	105
s5p8 mirror panel	12.98 ± 0.01	3.3	104
s2p1 30 cm tile	13.14 ± 0.04	0.16	36
s3p2 60 cm tile	13.26 ± 0.02	0.8	171
s3p3 60 cm tile	13.37 ± 0.03	1.0	171
s5p4 60 cm tile	13.04 ± 0.02	0.8	171
s3p5 60 cm tile	13.156 ± 0.007	0.5	171
s3p6 60 cm tile	13.106 ± 0.006	0.3	171
s4p7 60 cm tile	13.168 ± 0.009	0.6	171
s5p8 60 cm tile	13.22 ± 0.02	0.9	171
400 m² dish	13.086 ± 0.005	3.5	162

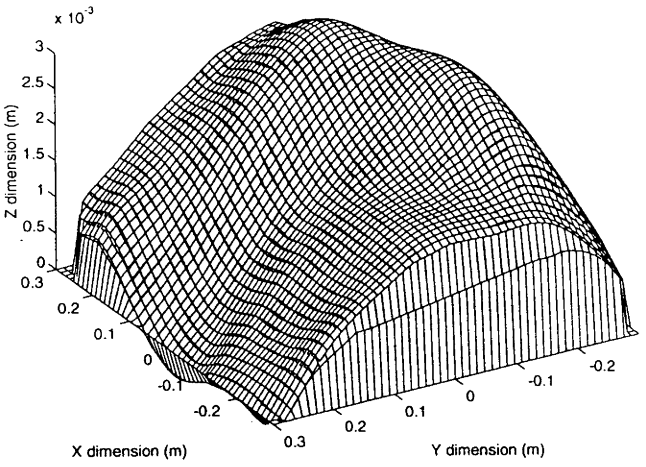

Fig. 5 Superposed surface plots of bilinear and bicubic spline fitted surfaces to a 60-cm mirror tile. Variations can be observed where double lines are apparent in some regions. (For clarity the surface is shown inverted from its normal (concave) orientation.)

achieved, and it was found that an average of one peak and/or one trough appeared in either dimension on any (60-cm) mirror tile. It was decided to create a 13 × 13 target array on the 60-cm mirror tiles, thus allowing adequate data coverage for the 1 peak/1 trough combinations that could occur.

The accuracy of fit for GRADFITTER was assessed by first constructing an artificial surface composed of a paraboloid with superimposed sinusoidal ripples whose frequency and amplitude could be varied. Average slope error of the bicubic spline fit was calculated for a range of ripple amplitudes and frequencies. Figure 4 shows the resulting plot of slope error versus ripple frequency for a family of ripple amplitudes. It can be seen that uncertainties of approximately 0.2 milliradian or less in the surface normal determinations can result if surface ripple deviations are below ±2 mm and frequencies below 2 m^{-1}. Further definition of error beyond this becomes difficult, as real surfaces will not conform to any easily defined mathematical form. For the present, assessment of the deviations of the measured tile surfaces from an ideal paraboloidal shape indicated that the worst case rippling showed deviations of ±1.5 mm, and approximate low-frequency components of 1.5–2 m^{-1}. It is thus expected that uncertainties in the surface normals calculated by GRADFITTER will be 0.2 milliradian or less.

Figure 5 shows the superposition of a bilinear fit to the measured surface data for a 60-cm tile and the corresponding bicubic spline fit generated using GRADFITTER. (The surfaces shown in Fig. 6 are inverted for clarity—the surfaces are concave in reality.) It can be seen that the differences are very minor. Calculations indicate that the rms difference between the measured and fitted surfaces shown in Fig. 5 is 26 μm.

Surface Normal Assessments Across Measured Surfaces. Slope errors were assessed across the surfaces of the 5-m dish, the triangular mirror panels, the 30-cm tile, and the seven 60-cm tiles using GRADFITTER. (The 400 m² dish coordinates were not assessed for surface normals, as the data were distributed too sparsely to provide a robust surface normal calculation.) Figure 6 shows an example of the spatial distribution of surface slope errors across the surface of one of the 60-cm mirror tiles. Similar graphical descriptions can be made for the other surfaces.

While visualisation of the spatial distribution of surface slope error has many practical uses, another useful quantity that can be developed is an estimate of the standard deviation of the distribution of slope errors. This then becomes a "figure of merit" for a surface. It can be shown (Johnston, 1995a) that if the distribution of surface normal vectors follows a circular bivariate Gaussian probability density function, then the radial distribution of errors (which are measured in the present analysis) can be expected to follow a Rayleigh distribution of the form,

$$\frac{dP}{dr} = \frac{r}{\sigma^2} e^{-r^2/2\sigma^2},$$

where dP/dr is the change in probability as a function of radial

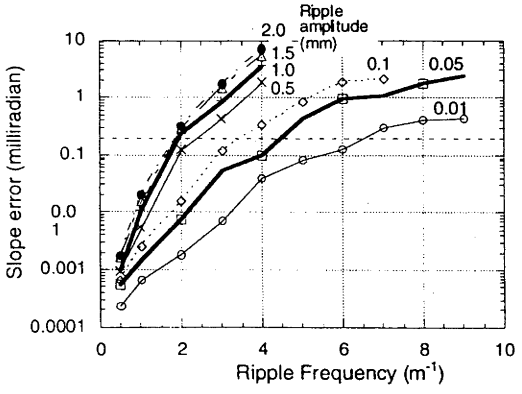

Fig. 4 Variation of surface slope error versus ripple frequency for a family of sinusoidal ripple surfaces of differing amplitudes superimposed on a paraboloidal surface assessed by the surface fitting algorithm GRADFITTER

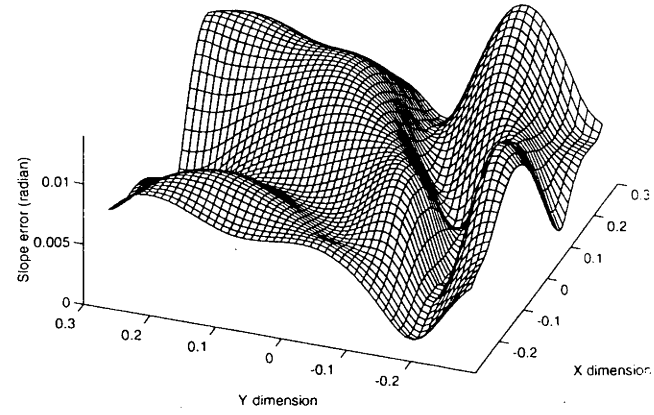

Fig. 6 Distribution of surface slope errors across a 60-cm mirror tile. (Ideally, the surface should be a flat plane through the origin.)

cameras to capture the required photogrammetric images, with subsequent processing of images using a digital computer. This technique results in orders of magnitude improvements in processing speed, with an improved accuracy capability factor two to three times better than that achieved with the analog equipment used in the film-based analysis. The additional seven mirror tiles and panels described in the present paper were measured using this advanced photogrammetric method, and, in conjunction with other test objects, have shown that relative coordinate precisions up to 1:70,000 appear to be readily achievable with this technique. The reduced operator processing time means a corresponding reduction in cost in this part of the analysis, while equipment cost reductions in the order of 50 percent over the film-based process are also an attractive feature that accompanies digital photogrammetry.

Conclusions

The results achieved with the measured reflecting surfaces indicate that quantifiable solar concentrator surface coordinates and surface slope errors can be achieved using close-range photogrammetry. This quantification is available with appropriate precisions to allow both solar collector surface quality determinations to be made, and for focal region flux distributions to be estimated based on the measured surface coordinate data.

The accomplishments to date indicate that close range photogrammetry is a viable and available tool to undertake solar collector surface analysis.

Acknowledgments

The author (GJ) would like to thank Dr. Andrew Blakers and Dr. Keith Lovegrove of the Department of Engineering, ANU, together with Prof. Stephen Kaneff, and the staff at the Energy Research Centre (ANUTECH) for their advice, discussions, and technical support. Thanks are also due to the Northern Territory Power and Water Authority, Pacific Power, New South Wales Office of Energy, the Energy Research and Development Corp., Electrical Distribution and Transmission of South Australia, Queensland Electricity Commission, and the State Electricity Commission of Victoria for their financial assistance in the purchase of photogrammetric software, and to Kayell, Sydney, for their generous loan of a Kodak DCS series digital camera for the digital photogrammetry of the seven 60 cm mirror tiles and triangular mirror panels.

References

Dierckx, P., 1993, "Curve and Surface Fitting with Splines," Oxford University Press, Oxford, UK, pp. 249–280.

Grossman, J. W., Houser, R. M., and Erdman, W. W., 1992, "Testing of the Single-Element Stretched-Membrane Dish," Sandia Report SAND91-2203.UC-237, Sandia National Laboratories, U.S. Department of Energy.

Johnston, G., 1995a, "On the Analysis of Surface Error Distributions on Concentrating Solar Collectors," ASME JOURNAL OF SOLAR ENERGY ENGINEERING, Vol. 117, pp. 294–296.

Johnston, G., 1995b, "Flux Mapping the 400 m^2 Dish at the Australian National University," ASME JOURNAL OF SOLAR ENERGY ENGINEERING, Vol. 117, pp. 290–293.

Krasiliovskii, V. I., Tarnizhevskii, B. V., and Tver'yanovich, E. V., 1978, "Facility with sectioned photoreceiver and laser radiator for determining solar radiation concentrator accuracy characteristics," *Geliotekhnika*. Vol. 14, No. 1, pp. 30–35.

Romero, V., 1994, "CIRCE2/DEKGEN2: A software package for facilitated optical analysis of 3D distributed solar energy concentrators," Sandia Report SAND91-2238.UC-236, Mar. 1994, Sandia National Laboratories, U.S. Department of Energy.

Shortis, M. R., and Johnston, G., 1996, "Photogrammetry: An Available Surface Characterisation Tool for Solar Concentrators—Part I: Measurement of Surfaces," ASME JOURNAL OF SOLAR ENERGY ENGINEERING, Vol. 118, pp. 146–150.

Taneja, P., Kandpal, T. C., and Mathur, S. S., 1992, "Concentration characteristics of a two stage solar concentrator: Effect of primary mirror surface errors," *Int. J. En. Research*, Vol. 16, pp. 203–211.

Pergamon

PII: S0038-092X(98)00041-3

Solar Energy Vol. 63, No. 2, pp. 117–124, 1998

0038-092X/98 $–See front matter.

FOCAL REGION MEASUREMENTS OF THE 20 m^2 TILED DISH AT THE AUSTRALIAN NATIONAL UNIVERSITY

GLEN JOHNSTON
Centre for Sustainable Energy Systems, Department of Engineering, Australian National University, Canberra 0200, ACT, Australia

Received 11 December 1996; revised version accepted 17 March 1998

Communicated by LORIN VANT-HULL

Abstract—Focal region characterisation of a 20 m^2 point focus dish concentrator having approximately 2300 flat, 10 cm square mirror tiles as its reflecting surface has indicated a focal flux distribution having a flat-topped peak with approximately Gaussian limbs. A peak concentration of 970 suns was evident, while a dish optical efficiency of 74% was measured, which is a direct indication of the average dish reflectivity. Total integrated power of 14.8 kW was measured under the focal flux distribution. Predicted fluxes using a ray trace algorithm (COMPREC) developed at the Australian National University (ANU) and utilising 2.0 mrad surface slope error showed a good approximation to the measured distribution. The value of 2.0 mrad also compared well with a photogrammetrically predicted value of 1.8 mrad.

1. INTRODUCTION

Measurement of flux distributions in the focal regions of solar concentrating devices using charge coupled device (CCD) imaging cameras has become a standard technique in many solar energy research institutions (Neumann, 1994; Grossman *et al.*, 1992; Schubnell, 1992; Blackmon, 1985). While Australian solar energy research has advanced in a number of fields, there has not been a great deal reported in the field of focal region characterisation of high concentration solar collectors in this country. This is generally attributable to the twin facts that (1) work using high concentration collectors has not been undertaken in Australia to a large extent, and (2) mathematical modelling of flux distributions using computer-based ray trace algorithms has been relied on almost exclusively to produce the required estimates of power distributions in focal receivers in the past (Bannister, 1991). The present work seeks to redress these imbalances by utilising a CCD camera to apply the technique of videographic flux mapping to the focal region of a 20 m^2 (5 m diameter) paraboloidal dish solar collector situated at the Australian National University. This paper presents the results of this characterisation, together with a comparison with ray-trace-predicted focal region distributions under specific conditions of measurement.

2. THE CONCENTRATOR

Fig. 1 shows the 20 m^2 concentrator in place at the ANU.

This dish is a duplicate of the 14 dishes that were built to implement the White Cliffs solar thermal power station project, which became operational in January 1982 in the town of White Cliffs, situated some 200 km north-east of Broken Hill, in western New South Wales, Australia. The reflecting surface consists of approximately 2300 flat mirror tiles made of 2 mm thick back-silvered ("green") glass and each approximately 10 cm on a side. The nominal focal length of the concentrator is 1.8 m, with an actual focal length of 1.812 ± 0.005 m (determined from a photogrammetric analysis (Shortis and Johnston, 1995) of the concentrator surface coordinates). The tiles are glued on to a fibreglass shell that was cast on a paraboloidal mould, and this composite collector is pedestal mounted on an alt-azimuth drive system, consisting of a printed circuit motor and gear box driving a pinch roller on a guide track in the azimuth direction, and a similar motor and gear box driving a lead screw in a guided arm to effect the altitude control. Sun tracking is effected through feedback from a sun sensor providing input to a discrete electronic controller mounted on a frame on the mounting pedestal. The original reflectivity of the mirror tiles was nominally 86%, some 10 years prior to the present analysis, although at the time of the present investigations a number of degraded tiles were apparent, such that overall dish reflectivity was difficult to estimate. The average dish reflectivity was calculated from the ensuing focal region flux measurements.

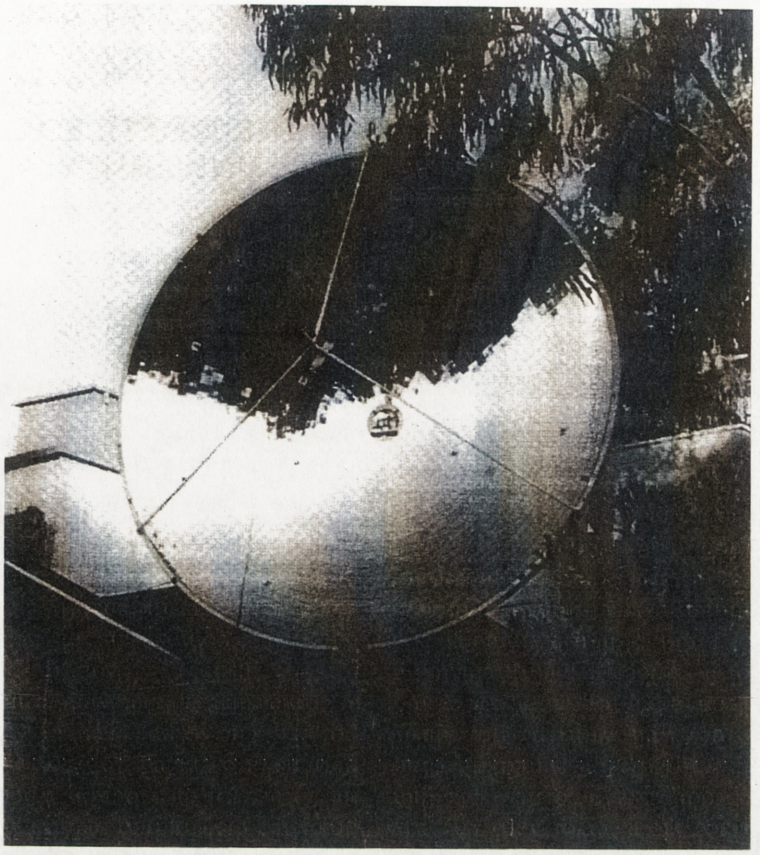

Fig. 1. The 20 m² White Cliffs concentrator used in the current assessment.

3. THE FLUX MAPPING SYSTEM

Fig. 2 shows a schematic layout of the arrangement of the CCD‡ camera and the flux imaging system on the dish.

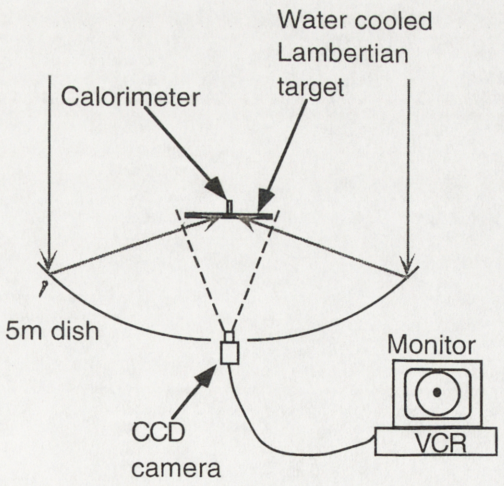

Fig. 2. Arrangement of the flux mapping equipment on the 20 m² dish.

‡Sony CCD colour video camera module. Model XC-999P; 752 × 582 pixels.

The focal spot was projected onto a water cooled, circular copper target, 0.5 m in diameter, mounted onto a movable slide that allowed motion of the target in the focal region along a direction parallel to the axis of the dish. The front surface of the target was spray painted with a white, matt finish high temperature paint to create an approximately Lambertian reflecting surface. As the measured flux distribution was to be compared with a ray-trace-predicted distribution, it was considered necessary to investigate the effect of the reflectivity response of the white painted surface of the target, such that its influence could be modelled in the ray trace algorithm if necessary. An experimental arrangement was constructed that simulated the videographic measurement conditions—that is, a camera was maintained in a constant viewing position perpendicular to a surface sample painted with the white matt paint, and a light source mounted on a goniometer was rotated to specified angles relative to the sample surface. Images were captured of the viewing surface under different angles of illumination, were corrected for CCD camera response non-linearities,

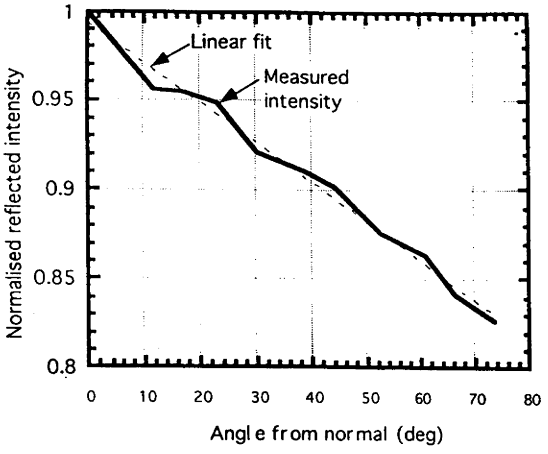

Fig. 3. Relative intensity versus viewing angle response (heavy line) for the surface paint used on the flux target in the focal region of the 20 m² dish (dashed line shows line of best fit).

and the relative intensities of the images were normalised to the peak intensity viewed by the camera when the light source was perpendicular to the sample surface. Figure 3 shows the results of these measurements.

The response shown in Fig. 3 was incorporated into the ray trace algorithm and used to model the focal flux distribution predicted for the concentrator, such that the effect on the perceived flux image of the differing angles of incidence of rays coming from different regions of the dish concentrator could be realistically assessed.

An HyCal[§] foil gauge radiometer was mounted in the centre of the target such that absolute intensity readings could be continuously monitored and used to calibrate the pixel intensities recorded by the CCD camera. The scaling was performed by choosing a narrow, annular band of pixels, some 7 to 10 pixels wide, surrounding, and adjacent to (but not including) the black radiometer image in the flux images. An average value was taken of these pixel values, and this average value was used in scaling the pixel values with the radiometer reading at the time of the measurement.

The CCD camera was mounted at the vertex of the dish, looking upwards to the focal region. A set of high density absorption filters were placed in front of the camera lens to avoid saturating the CCD array with the high light levels occurring on the imaging target. The video signals produced by the camera were

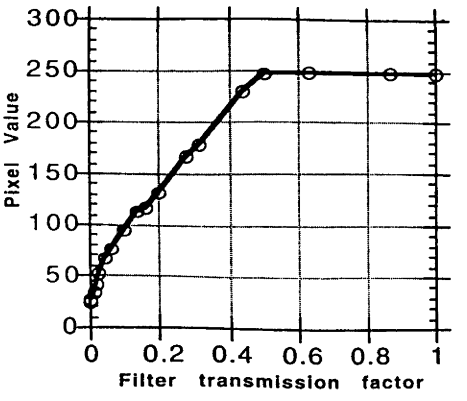

Fig. 4. CCD camera and VCR response to calibrated light levels (measured as a function of the transmission factor of neutral density filters placed in front of the camera).

recorded on a high resolution Super VHS video cassette recorder[¶] (VCR), and the appropriate images later replayed, captured and digitised using a 7-bit frame grabber card mounted in a Sun SparcStation[4] computer. While it would have been most desirable to have digitised the CCD images with an 8-bit framegrabber, such equipment was not available at the time of the measurements.

The combined response of the CCD camera and the Super VHS video recorder to light of varying levels was calibrated prior to focal region measurements by placing calibrated neutral density filters in front of the camera while it viewed a uniformly illuminated screen and recorded on to the VCR. The images were digitised from the VCR and the average pixel intensities across the field of view were plotted against the transmission factors of the corresponding neutral density filters to provide a measure of the response of the camera and VCR to varying levels of light. Figure 4 shows the results of this calibration.

The response data shown in Fig. 4 was fitted to a seventh order polynomial and used to correct the measured flux distribution, such that measured pixel values were linearised to more accurately reflect the actual intensity they are representing. Absolute intensity scaling was also applied using the output from the radiometer. An interesting property of the 7-bit framegrabber was that it output its 7-bit image digitisations in a "pseudo 8-bit" format, such that the pixel values ranged from 0 to 255, but changed value in increments of 2, such that there were

[§]HyCal calorimeter. Model C-1312-A-300-072; HyCal Engineering, 9650 Telstar Ave., El Monte, CA 91731, U.S.A.

[¶]Panasonic Super VHS (PAL) videocassette recorder. Model NV-FS100HQ.

[4]Sun "VideoPix" framegrabber card.

still only 128 levels, but they covered the "normal" 8-bit range of values. Thus Fig. 4 is seen to have an abscissa ranging up to approximately 250 while still only representing 128 levels.

An assessment was also made of the influence of the video cassette recorder on the overall quality of the captured images. A series of images of a uniformly illuminated white screen was taken under different levels of illumination, firstly using the CCD camera feeding directly into the computer-based framegrabber, and secondly, feeding into the VCR. The latter set of VCR images were then also digitised using the same framegrabber, and the mean intensities between the two sets of images were compared. This comparison indicated that the VCR images were generally some 3–6% deviant from the directly measured CCD camera images.

4. THE RESULTS

While 1.8 m was the nominal focal point for the dish, a series of flux measurements were performed for target placements at distances 1.76 to 1.88 m from the dish vertex, in 2 cm increments. These measurements showed that a distribution with highest peak flux and minimum extent occurred at 1.82 m. Later photogrammetric analysis (Shortis and Johnston, 1995; Johnston and Shortis, 1997) showed that a focal length of 1.812 ± 0.0005 m, and a standard deviation of surface slope error of 1.8 mrad could be expected for the dish. (Slope error is defined as the angular deviation (usually in mrad) of the actual surface normal vectors from their ideal directions. The figures for slope error used in this study represent a combination of both surface specularity slope error and manufacturing slope error.) Figs 5 and 6 show a cross-section and a contour plot of the flux distribution measured on the target positioned at 1.82 m from the dish vertex. (The distributions shown in Figs. 5 and 6 have had the image of the (black) radiometer removed from their central region.)

Table 1 records the salient features of the flux distribution shown in Fig. 5.

Figure 5 shows that the flux field exhibits a flat-topped, non-Gaussian type of distribution. This would be expected from the tiled nature of the dish reflecting surface. Each 10 cm square tile will reflect a uniform beam of sunlight onto a common point in the focal plane, such that a region of intense, but uniform intensity should

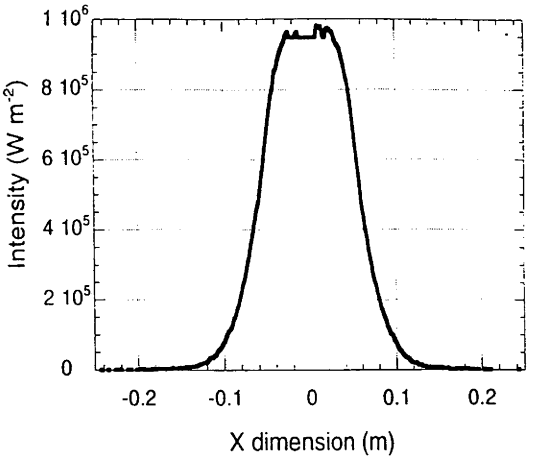

Fig. 5. Cross-section through a flux image produced by the 20 m² dish. Imaging plate at 1.82 m from dish vertex. Insolation normalised to 1000 W m².

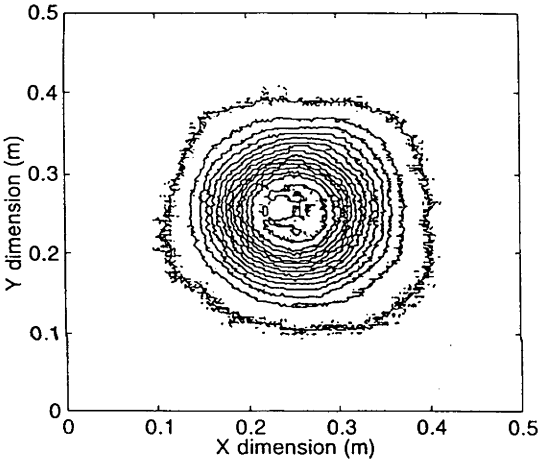

Fig. 6. Contour plot of the distribution shown in Fig. 5.

be seen where the tile beams overlap. The skirt around the central area will follow an approximately Gaussian shape, constituted from a combination of surface slope errors, variations in projected area between the tiles near the dish

Table 1. Features of the flux distribution shown in Fig. 5 (all figures normalised to 1000 W m^{-2} insolation)

Peak intensity (kW m^{-2})	$970 \pm 70^{\ddagger}$
Intercepted power† under the distribution (kW)	$14.8 \pm 1^{\ddagger}$
Collected power (in dish aperture) (kW)	$20.1 \pm 0.2^{\ddagger}$
Peak concentration ratio (CR) (suns)	$970 \pm 70^{\ddagger}$
Optical efficiency (%)	$74 \pm 6^{\ddagger}$

†Calculated by normalising the distribution to an insolation of 1000 W m^{-2} and then integrating the flux array and multiplying by the effective (target scale) pixel area.

‡Uncertainties calculated by a quadratic combination of errors of component values.

vertex and those towards its edges, together with the overlapping edges of the non-circular beam image projections on the focal plane.

5. FLUX MODELLING USING A RAY TRACE CODE

A ray trace computer algorithm was written to enable modelling of flux distributions on a given receiver configuration placed in the focal region of reflecting concentrating devices. The code was dubbed COMPREC (acronym for COMPound RECeiver) and can model the primary flux distributions expected on receivers having planar rectangular, disk or annular shapes, as well as cylindrical, conical and partial spherical geometries. Concentrator pointing errors and surface errors can also be included, and concentrators having a range of configurations (paraboloidal, spherical, trough or arbitrary shape) can be implemented in the model. The solar disk can be modelled with any desired sunshape, and Fig. 7 shows a typical sunshape cross-section, together with Kuiper's empirical sunshape model (Biggs and Vittitoe, 1979) used to represent the sunshape in the present analysis. Kuiper's distribution has the form

$$I = \frac{1+\beta\sqrt{1-\frac{r^2}{\sigma^2}}}{\pi\sigma^2\left(1+2\frac{\beta}{3}\right)}$$

where I=relative intensity, β=limb darkening parameter (controls the degree of limb darkening), r=angular displacement from the centre of the distribution (mrad) and σ=angular half-width of the solar disk=4.65 mrad.

The limb darkening parameter, β, was given a value of 1.0 in the present analysis to provide an approximation to the measured sunshape shown in Fig. 7. However, modelling studies indicated that using Kuiper's model or a simple "pillbox" sunshape (also shown in Fig. 7) did not show any discernible difference in predicted flux distributions for the 20 m² tiled dish. This arises due to the tiled nature of the dish, where the flat mirror tiles make it impossible to form an image of the solar disk, and details associated with the solar image, such as limb darkening, are "washed out" by the image smearing effects of the tiles.

Output from COMPREC compares favourably with analytic calculations of ideal flux distributions (Jeter, 1986). Figure 8 shows the results of these comparisons for ideal paraboloidal dishes having 1.0 m focal lengths and rim angles of 45° and 60°, respectively.

6. COMPARISON OF MEASURED AND PREDICTED RESULTS

Fig. 9 shows a superposition of the flux image of Fig. 5, and the flux distribution predicted by COMPREC on a 0.5 m diameter absorber placed 1.82 m from the dish vertex, using a focal length of 1.81 m and zero surface slope error.

In order to compare the spread of the two distributions, the ray traced distribution shown in Fig. 9 was scaled by a factor of 79% to match the peak intensity of the measured distribution.

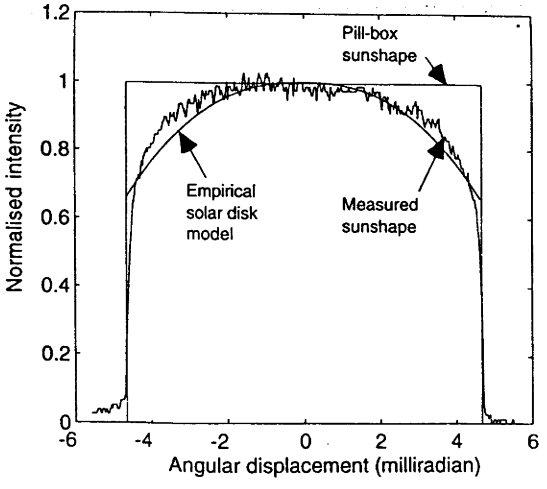

Fig. 7. Measured and empirical sunshapes (the measured sunshape was taken from an actual solar image taken on 21 December 1995 at Holloman AFB, New Mexico at 22:46 UT). Also shown is a "pillbox" sunshape, often used in ray trace modelling.

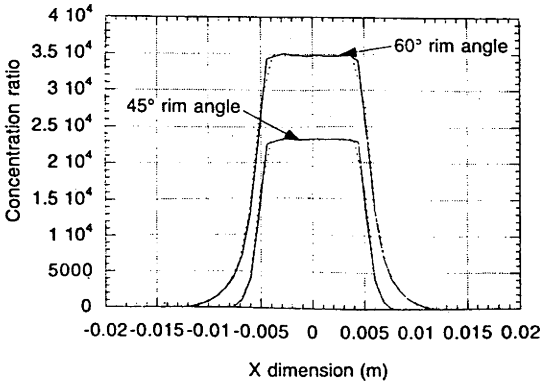

Fig. 8. Superposition of flux images predicted by COMPREC (dotted lines) and by analytical calculations (Jeter, 1986) at the 1.0 m focal point of smooth dishes having rim angles of 45° and 60°, respectively.

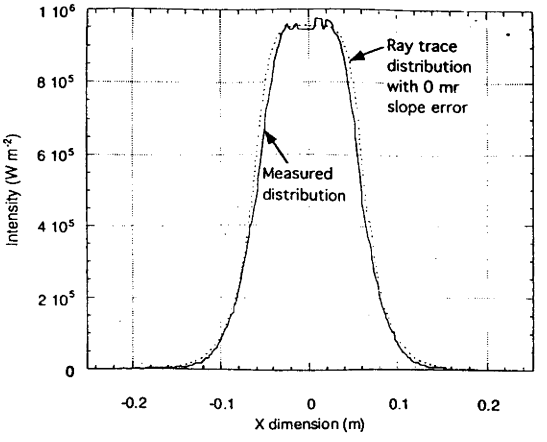

Fig. 9. Superposition of measured flux distribution (solid line) and ray traced distribution (dotted line) on a 0.5 m diameter absorber placed 1.82 m from the vertex of a 1.81 m focal length dish. The ray trace distribution assumes zero surface slope error and 100% mirror reflectivity, and has been scaled down by 79% to match the height of the measured distribution for comparison purposes.

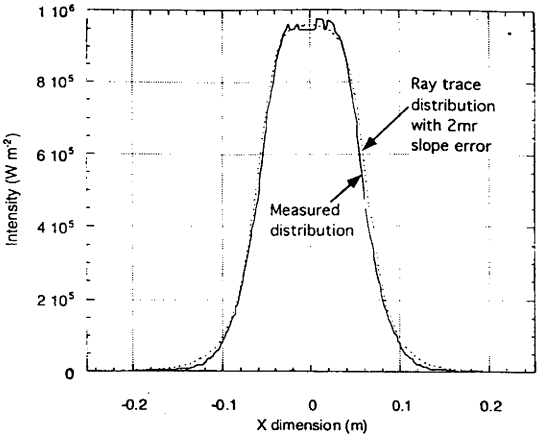

Fig. 10. Measured (solid line) and predicted (COMPREC, dotted line) focal flux having a surface slope error of 2.0 mrad.

Figure 9 shows that the measured distribution is noticeably narrower than the predicted distribution. As noted previously, a photogrammetric analysis of the dish indicated that a standard deviation of surface slope error of 1.8 mrad was apparent on the dish surface. (Slope error in this instance is defined as the standard deviation of a bivariate Gaussian distribution of surface slope errors (Johnston, 1995).) Tiled dish surfaces were modelled using a range of surface slope errors varying from 1.5 to 4.0 mrad in 0.5 mrad steps, and the focal fluxes calculated. (Slope errors were simulated on the tiled dish model by defining a random slope error value according to the bivariate Gaussian distribution model, and then applying this to all surface normals on a given tile (each tile was divided into an 11×11 array of data points and associated surface normals). This process was repeated until all tiles had been processed to have varying degrees of slope applied to their normal vectors.) Fig. 10 shows the superposition of the measured distribution with a predicted distribution arising from a tiled dish having 2.0 mrad of surface slope error. This value of slope error produced the smallest RMS error between the two distributions.

However, in reality the predicted flux array should be scaled to have the same integrated power under its distribution as the measured distribution (rather than have the same peak value). Integration of the power under the measured flux showed that it contained 74% of the power integrated under the predicted distribution (which assumed 100% mirror reflectivity). Assuming that all reflected radiation is intercepted by the target, this scaling factor is a direct measure of the average reflectivity of the dish surface.

Figure 11 shows the superposition of the two distributions when scaled to have equal integrated powers. Due to the slightly larger extent of the predicted flux, its peak value is seen to decrease by some 7%, in accordance with energy conservation principles.

Another way of assessing the distribution of energy in a flux distribution is to measure the percentage of total power intercepted by the dish as a function of radius from the centre of the flux distribution. Figure 12 shows the per cent power within radius (PIR) plots for the measured and predicted distributions shown in Fig. 11.

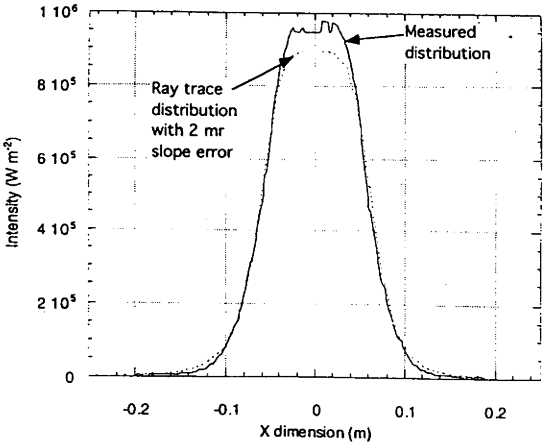

Fig. 11. Superposition of measured (solid line) and predicted (COMPREC, dotted line) flux arrays having equal power under the distributions.

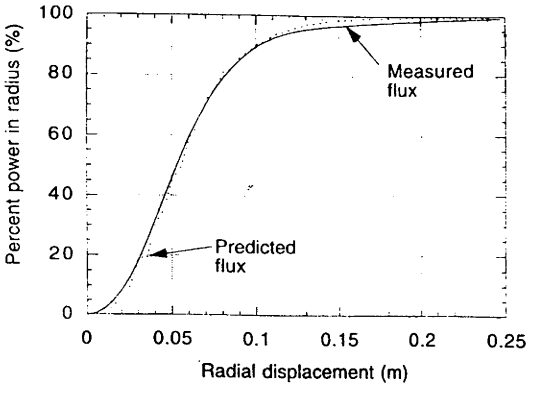

Fig. 12. Per cent power within radius for the measured (solid line) and predicted (dotted line) distributions shown in Fig. 11.

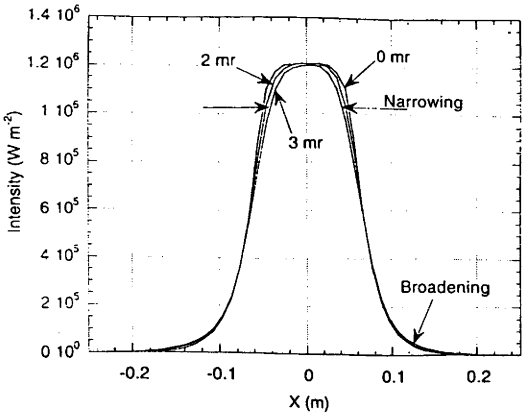

Fig. 13. Superposition of flux cross-sections using different slope errors showing the effect of central region narrowing and base region broadening.

The "jagged" appearance of the PIR plot for the predicted distribution in Fig. 12 is due to the coarser spatial quantisation grid used in the predicted flux array (50 × 50 grid) compared to the finer grid used in the measured image (412 × 412).

7. DISCUSSION

Fig. 10 shows that the introduction of 2.0 mrad of surface slope error into the ray trace algorithm produces a predicted flux that correlates closely with the measured distribution. This value lies well with the previously reported results from a photogrammetric analysis of the tiled dish surface, which predicted a slope error of 1.8 mrad. (Photogrammetry is a process that accurately extracts the three-dimensional coordinates of target points on a surface through the method of stereoscopic reconstruction of the surface from a number of different photographs of the object taken from different positions.)

The fact that the introduction of surface slope error appears to "narrow" the distribution may seem counter-intuitive, as it would be expected that the presence of slope error would cause the distribution to spread somewhat, rather than narrow it. However, this effect can be understood by considering that slope error does indeed broaden the distribution, but this broadening occurs in the skirt or tails of the distribution, and that the "higher" portion of the distribution "pulls in" accordingly to maintain the energy balance under the distribution (as broadening in the base means more energy is contained in the base regions, the corresponding amount of energy must be taken out of the central region of the distribution). This can be seen in Fig. 13 below, which shows a series of flux distribution cross-sections corresponding to different levels of surface slope error for the 20 m² dish.

As can be seen in Fig. 13, the central regions narrow while the base regions broaden for increasing slope error.

Figure 11 indicates that the peak value of the predicted distribution reduces by some 7% from the measured distribution when the two distributions are scaled to have equal integrated powers. The scaling factor of 74% can be used as a measure of the average mirror reflectivity for the dish. The drop in peak intensity is required to compensate for the increased energy contained under the slightly larger radius of the predicted distribution. A scaling factor of 79% is required to give the measured and predicted distributions equal peak intensities, and this can be used as an upper bound on the probable average dish reflectivity, with the actual value falling somewhere between 74 and 79%. An outstanding feature that becomes apparent from such measurements is the sensitivity of integrated power to the extent of a distribution, due to the square relationship between radial distance from the distribution centre and the corresponding area covered by the flux image. Apparently small differences in radial extent, as shown in Fig. 11, can cause noticeable differences in the integrated power measured for a distribution. However, the observed differences between the two distributions are within the error bounds calculated in Table 1, and can be attributable partly to normal measurement error, as well as slightly greater uncertainty in

the digital flux due to only 7 bits of digitisation being available (instead of the usual 8).

The measured average reflectivity of 74% for the dish mirrors represents a significant reduction from their nominal value of 86% when first installed, some 10 years before the present measurements were made. Inspection of the mirrors (after cleaning the dish surface in preparation for the flux measurements) showed that a number of them displayed slight discolouration, although no measurements were taken of their reflectivities. The silvering has clearly suffered degradation over time.

8. CONCLUSION

Measurements of the flux distribution produced by a 20 m^2 paraboloidal dish solar concentrator covered with 2300, approximately 10 cm square, flat mirror tiles showed an essentially flat-topped distribution with approximately Gaussian limbs. Peak fluxes of 970 kW m^{-2}, and an integrated power of 14.8 kW (both normalised to 1000 W m^{-2} insolation) were measured at the focal point. Average mirror reflectivity appears to lie between 74 and 79%. Ray trace modelling indicated that the measured distribution could be approximated using a tiled paraboloidal dish model having a surface slope error standard deviation of 2.0 mrad. This value correlates closely with the predicted value of 1.8 mrad gained from a photogrammetric analysis of the dish surface.

Points of key interest that arose from this work include:

(1) The use of a high resolution videocassette recorder to capture flux images with the introduction of comparatively small (3–6%) values of error. However, this level of quality may be specific to the brand of VCR used in the present study, and may not be representative of measurements that could be taken with other VCRs.

(2) Reporting of the flux distribution in the focal region of a tiled dish represents a rarely reported analysis, as the vast majority of dishes available today use reflective surfaces that are continuously curved to an appropriately paraboloidal shape. Clearly, the 10 cm flat tiles introduce an "error" into the surface that shows itself in the flat-topped nature of the flux distribution, and the relatively small sensitivity of the flux distribution to surface slope error.

(3) A high correlation between the measured focal region distribution and that predicted from computer-based ray tracing using surface slope data derived from photogrammetric assessments of the concentrator surfaces. The use of photogrammetry shows itself to be a valuable aid to concentrator analysis and design.

REFERENCES

Bannister P. (1991) An experimental and analytical assessment of a steam Rankine solar thermal system. Ph.D. thesis, Australian National University, Canberra 0200, Australia.

Biggs F. and Vittitoe Ch. N. (1979) The helios model for the optical behaviour of reflecting solar concentrators. Technical Report SAND76-0347, Sandia National Laboratories.

Blackmon J. B. (1985) Development and performance of a digital image radiometer for heliostat evaluation at Solar One. *J. Sol. En. Eng* **107**, 315–321.

Jeter S. M. (1986) The distribution of concentrated solar radiation in paraboloidal collectors. *J. Sol. En. Eng* **108**, 219–225.

Johnston G. (1995) On the analysis of surface error distributions on concentrating solar collectors. *J. Sol. En. Eng* **117**, 4, 294–296.

Johnston G. and Shortis M. (1997) Photogrammetry: an available surface characterization tool for solar concentrators, part II: assessment of surfaces. *J. Sol. En. Eng* **119**, 4, 286–291.

Grossman J. W., Houser R. M. and Erdman W. W. (1992) Testing of the single-element stretched-membrane dish. Sandia Report, SAND91-2203. UC-237. Sandia National Laboratories, Feb. 1992, p. 11.

Neumann A. (1994) Flußdichtemessung von konzentrierter solarstrahlung mit videokameras. 9. Internationales sonnenforum 1994, pp. 67–77. Work conducted at Deutsche Forschungsanstalt für Luft-undRaumfahrt (DLR), Köln.

Schubnell M. (1992) Sunshape and its influence on the flux distribution in imaging solar concentrators. *J. Sol. En. Eng* **114**, 260–266.

Shortis M. R. and Johnston G. (1995) Photogrammetry: an available surface characterisation tool for solar concentrators – part I: measurement of surfaces. *J. Sol. En. Eng* **118**, 3, 146–150.

Appendix 1.2. Description of the SG3 400 m^2 dish concentrator

The following descriptions have been supplied by Professor S. Kaneff, of the Energy Research Centre, ANUTECH, Canberra, Australia. 0200.

A1.1 Features of the SG3 collector

Figure A1.1 portrays the current SG3 collector.

Table A1.1 indicates the main features and parameters of the Mark 2 version of the SG3, 400 m^2 dish concentrator. The manufacturing processes produce, as standard, very accurate members for the structure such that assembly in the field requires no adjustment, and results in an optical performance to design specifications.

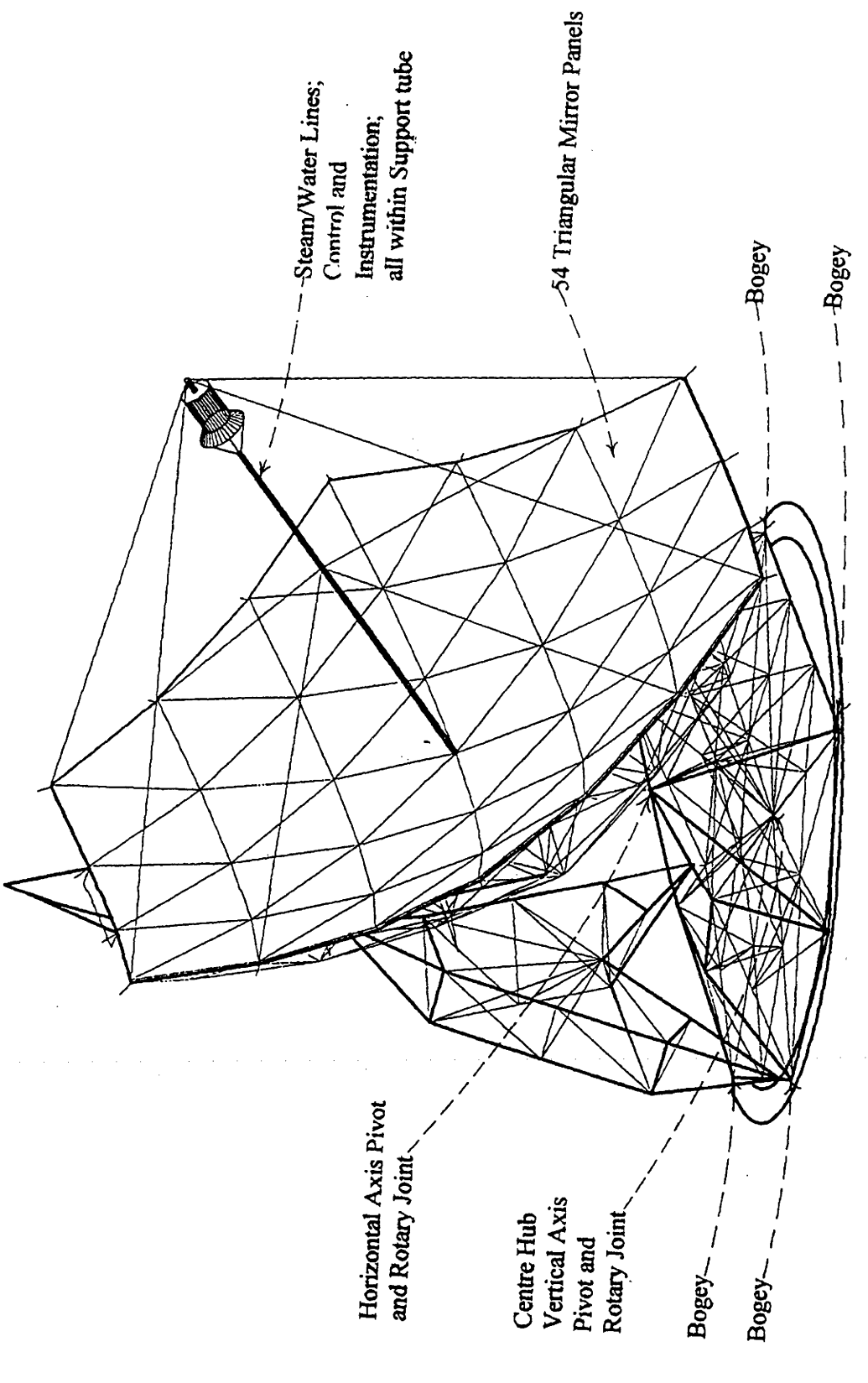

Figure A1.1. Schematic description of the SG3 400 m^2 dish solar concentrator.

Table A1.1. Specifications for the 400 m^2 dish solar concentrator

Reflecting surface	Aperture shape	Hexagonal
	Area (nett)	400 sq. metres.
	Diameter (mean)	22.6 m
	Diameter (max. span)	24.8 m
	Diameter (min. span)	21.5 m
	Focal length	13.1 m
	Rim angle	46.6°
	Number of panels	54
	Mirror reflectivity	96% with 1mm low-iron glass
Tracking envelope	Elevation	0° to 90°
	Azimuth (limited by cabling arrangements)	±270° relative to N-S axis
Position and sun tracking	Position transducers for azimuth and elevation Control and monitoring computer Sun position programme Control system for dish motion (tracking and protection) Dish pointing accuracy - sum of all pointing errors is always less than ±2 mrad.	
Fabrication	Space frames/trusses	Dish and base frames
	Reflector	Substrate supporting mirrored glass
	Track and foundation	Reinforced concrete
Weights	Dish frame	4.5 tonnes
	Mirror panels	5.4 tonnes
	Receiver and mounts	1.3 tonnes
	Base frame	5.5 tonnes
	Foundations	Concrete-25 m^3 (depends on site)
Receiver for steam generation	A range of useful combinations	200 to 700°C 1 to 160 bar, depending on materials

A1.2 Dish Description

A paraboloidal 400 m^2 aperture segmented mirrored glass shell is supported and moved to face and track the sun by two space frame/truss structures, each constructed from steel tubes accurately dimensioned and joined to form a network of nodes constituting a precise, rigid overall combination which maintains its shape irrespective of orientation or wind loading. Consequently, the dish focal region is well defined and accurate, allowing receivers to be designed to have and to maintain specified characteristics, irrespective of the sun's position.

The dish frame carrying the reflecting surface is actuated by hydraulic rams to rotate about a horizontal axis carried on a base frame which is rotated, also hydraulically, on a vertical axis which is being constrained by a centre bearing. The structures are carried on six dual-wheeled bogeys rolling on a concrete track foundation. The hydraulic actuation systems, in conjunction with an electronic controller, allow the collector to face and move in any orientation; for example to track the sun (in altitude/azimuth mode) or to perform other defined motion (including that required to protect against strong winds or overheating of the receiver), as well as to go to the start or to the survival position, or to place the reflecting surface in a position of no solar illumination.

The centre constraining bearing, apart from locating the collector in relation to the foundations, provides an anti-toppling constraint which supplements that provided by the collector weight in the presence of strong winds, as well as resisting sideways wind forces.

Because of the configurational and dimensional accuracy of the collector structure and its maintenance during all designed operating conditions, the mirrored glass segments can define a focal region having specified properties, such as particular concentration ratio or energy density profile.

Design usually provides for effective operation and tracking at wind velocities to 80 km/hr (at higher velocities the solar resources are rarely useful) and to withstand - in the vertically facing survival position - winds to 270 km/hr or more as required by each location. An ever vigilant wind monitoring system causes the collector to move to the survival position at wind speeds above 80 km/hr.

Collectors with apertures less or more than 400 m^2 can be realised.

Appendix 2.1. Calibration Relationships for Hycal Foil Gauge Radiometers

Figure A2.1.1 and Figure A2.1.2 show the calibration relationships provided by HyCal Engineering for two radiometers that were tested by that company. During some initial tests radiometer number #931285 was found to produce an intermittent output, which investigations did not resolve. It was thus decided to use radiometer #931284 for all tests on both the 20 m^2 and 400 m^2 dishes.

CERTIFICATE OF CALIBRATION ANU #7

HY-CAL Engineering
A Unit of General Signal
9650 Telstar Avenue · El Monte, CA 91731-3093

DATE 6/25/93

CUSTOMER AUSTRALIAN UNIVERSITY

P. O. NO.

INST. TYPE CALORIMETER

MODEL C-1312-A-300

ABSORPTIVITY .89

CERTIFIED RECORD OF CALIBRATION DATA ON THE INSTRUMENT DESCRIBED ABOVE. THE DATA WAS OBTAINED IN HY-CAL ENGINEERING'S THERMAL FLUX FACILITY.

REFERENCE STANDARD 149335

TESTED BY HC 5

Q. C. APPROVAL HC 12

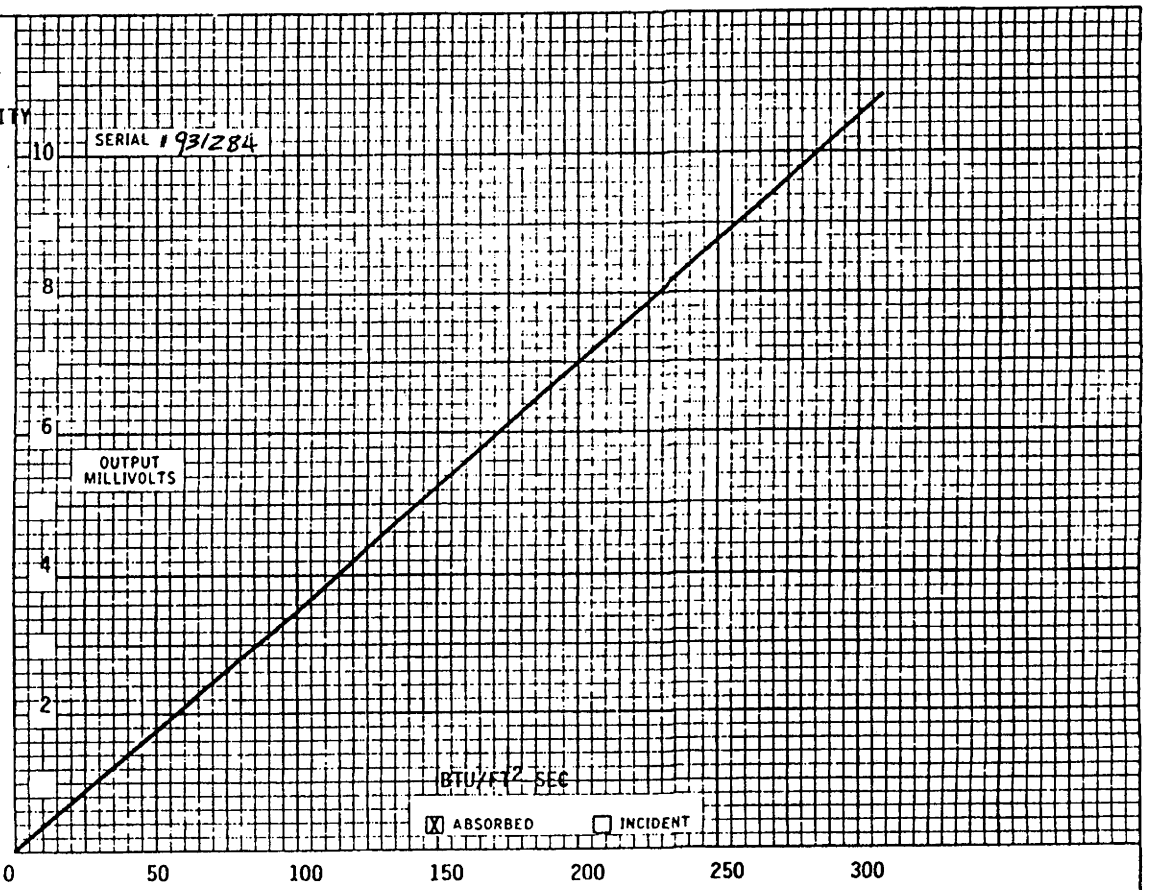

$Wm^{-2} = Btu\ ft^{-2}s^{-1} \times 11356.3$

Eqn. to curve: $Wm^{-2} = 323654 \times mV(input)$

Figure A2.1.1. Calibration curve for HyCal foil-gauge radiometer #931284.

CERTIFICATE OF CALIBRATION

AWU #9

HY-CAL Engineering
A Unit of General Signal
9650 Telstar Avenue · El Monte, CA 91731-3093

DATE 6/25/93

CUSTOMER AUSTRALIAN UNIVERSITY

P. O. NO.

INST. TYPE CALORIMETER

MODEL C-1312-A-300

ABSORPTIVITY .89

CERTIFIED RECORD OF CALIBRATION DATA ON THE INSTRUMENT DESCRIBED ABOVE. THE DATA WAS OBTAINED IN HY-CAL ENGINEERING'S THERMAL FLUX FACILITY.

REFERENCE STANDARD 149335

TESTED BY HC 5

Q. C. APPROVAL HC 12

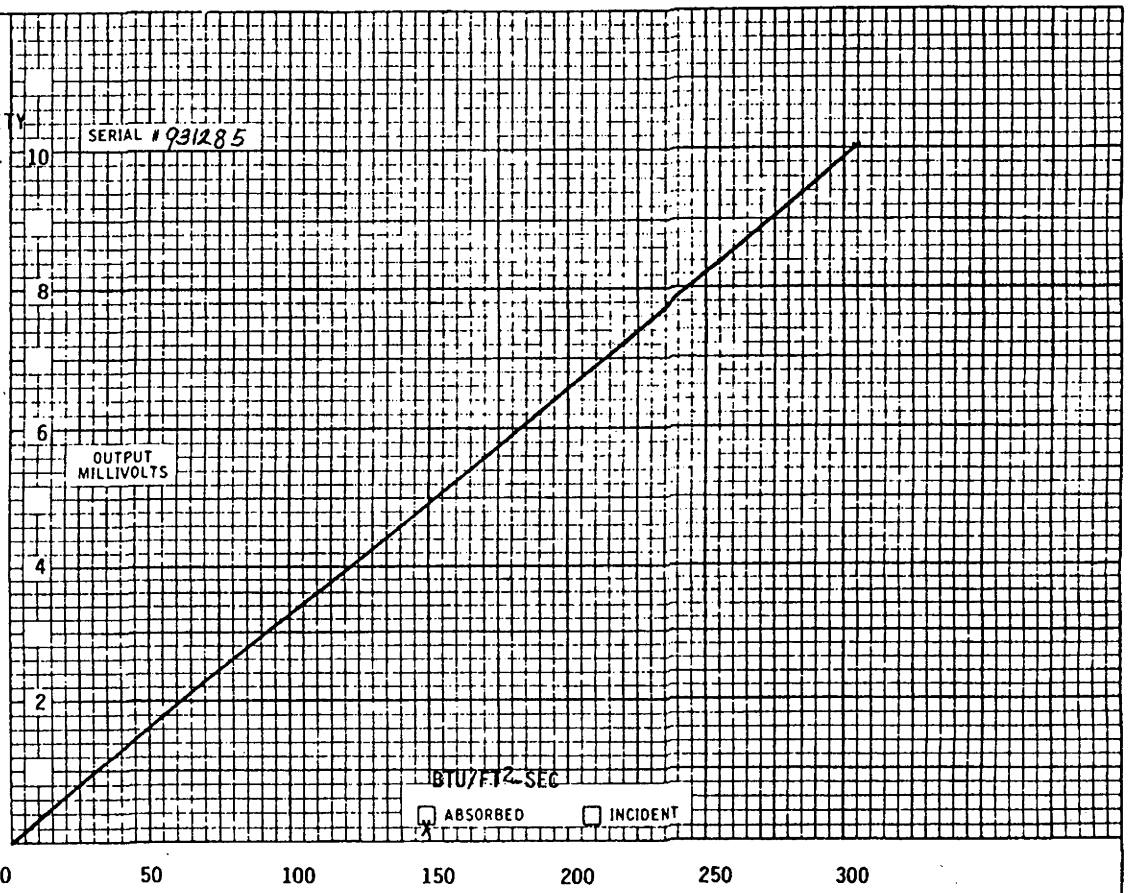

$W m^{-2} = Btu\ ft^{-2} s^{-1} \times 11356.3$

Eqn. to curve : $W m^{-2} = 344.096 \times mV(input)$

Figure A2.1.2. Calibration curve for HyCal foil-gauge radiometer #931285.

Appendix 2.2. Relationships for Calibration/Correction of CCD Camera Images.

A2.2.1 Camera Conversion Function.

Figure A2.2.1 shows the average response of the CCD camera field to varying levels of radiation, created by viewing a uniformly illuminated screen of arbitrary, but constant, intensity through a series of calibrated neutral density filters.

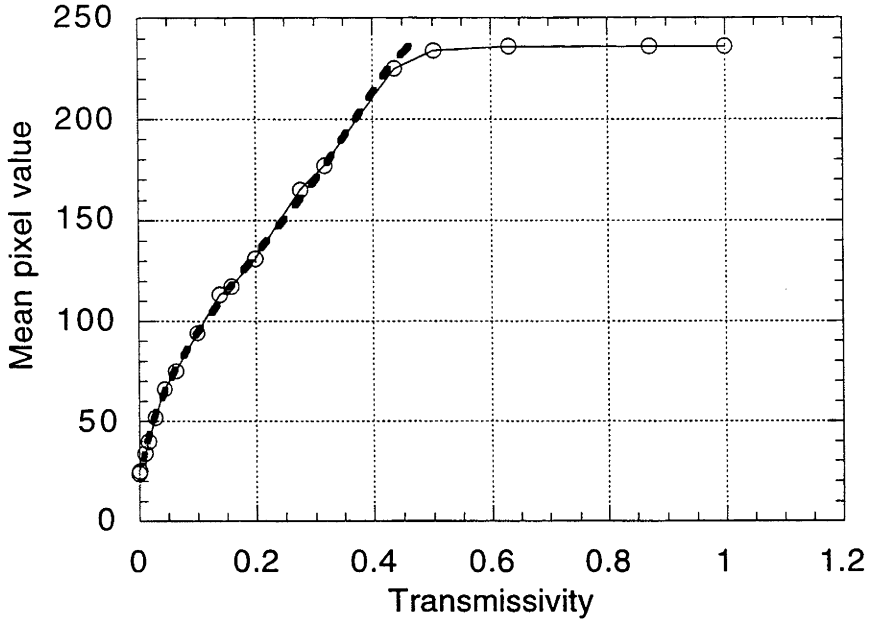

Figure A2.2.1. Average field response of Sony CCD camera to varying light levels created by calibrated neutral density filters. Graph shows average camera pixel response (full line) versus neutral density filter transmissivity. Also shown is 7th order polynomial curve fit (dashed line). Lens f-stop = f8.

The response shown in Figure A2.2.1 can be approximated by fitting the data with a 7th order polynomial curve fit. The inverse of this function allows calculation of an equivalent filter density for a given pixel value. This inverse response was calculated for each pixel in the CCD image, and can be called the inverse camera conversion functions, C^{-1}, and will be specific for each pixel.

A2.2.2 Image Correction and Calibration

Now consider that we are viewing a known intensity, I (measured with the radiometer in the flux field), through a filter, F, which has an uncalibrated density. This describes the actual flux measurement system. The intensity transmitted through the filter is I'. The camera has a pixel conversion function, C, which produces pixel intensities, P. Figure A2.2.2 shows these parameters.

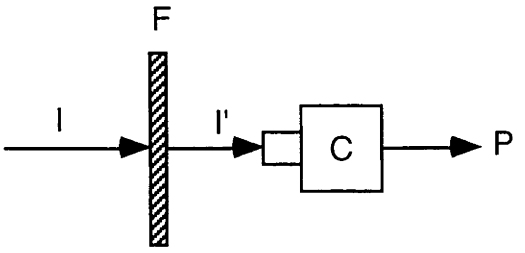

Figure A2.2.2. Relationship of filter, F, and camera conversion function, C to incident intensity, I, and resultant pixel value, P.

Using a filter transmission factor, k, we can say,

$$I' = kI$$

As the filter transmission factor is unknown, it can be found from,

$$k = \frac{I'_r}{I_r}$$

where I_r is the reference radiometer output, and I'_r is the intensity calculated from the inverse camera conversion function, C^{-1}, for a given pixel value, P_r, next to the radiometer.

As I'_r is given by,

$$I'_r = C^{-1}(P_r)$$

we can calculate the overall filter transmission factor, k, from,

$$k = \frac{C^{-1}(P_r)}{I_r}$$

Once k is known for the filter, the actual intensity at a point in the image represented by a pixel value, P, (and its associated camera conversion function) is found from,

$$I = \frac{C^{-1}(P)}{k}$$

Appendix 2.3 Assessment of CCD Camera Field Linearity

Videographic flux mapping requires measuring the spatial displacement of light across a target surface. Spatial linearity of the CCD camera array was assessed by capturing an image of a grid pattern 60x60 cm with grid lines every 2 cm as shown in Figure A2.3.1.

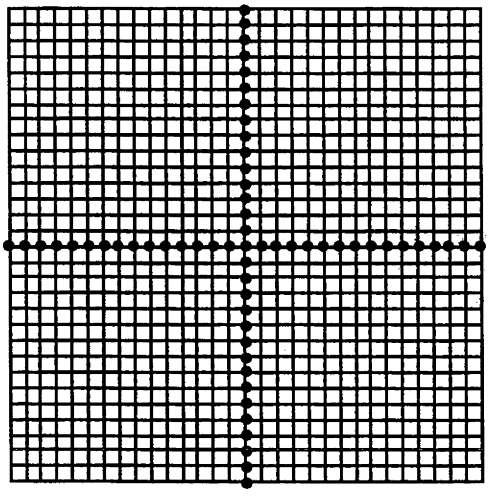

Figure A2.3.1. Linearly spaced grid pattern used to test CCD array spatial linearity.

The pixel positions of the grid lines along the two central axes (shown with dots in Figure A2.3.1) were recorded. Figure A2.3.2 shows a calibration plot of the recorded pixels positions versus the spatial position of the corresponding points on the grid.

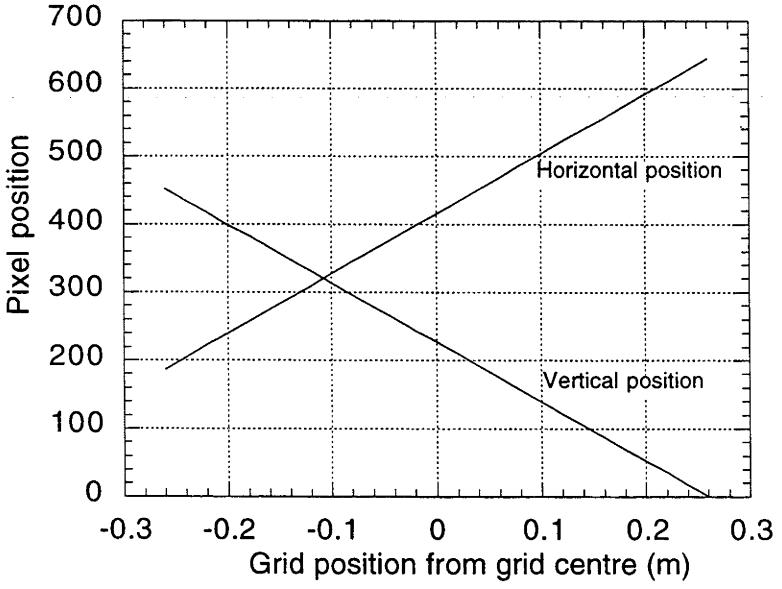

Figure A2.3.2. Calibration plot of CCD array pixel position versus spatial distance for grid points shown in Figure A2.3.1.

Inspection of Figure A2.3.2 shows a high degree of linearity. Regression analysis of the lines shown for horizontal and vertical displacement returns the following equations:

$$X = (881.4 \pm 0.5)x + (415.43 \pm 0.08) \quad (1)$$

$$Y = (-867.87 \pm 0.5)y + (226.44 \pm 0.08) \quad (2)$$

where X and Y are the pixel coordinates for the given spatial coordinates, x and y.

Figure A2.3.3 shows the measured pixel deviations from ideal linearity described by equations (1) and (2).

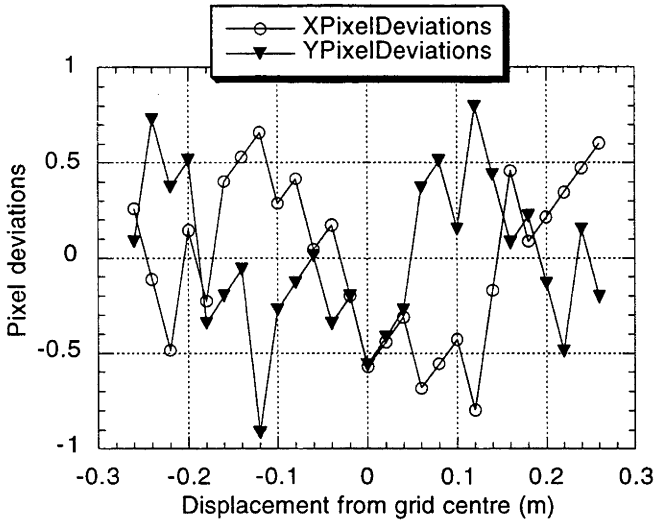

Figure A2.3.3. X and Y pixel deviations from ideal positions as a function of grid position.

Inspection of Figure A2.3.3 indicates a worst case deviation of ± 1 pixel, which over the minimum array size of 575 pixels constitutes a 0.2% error.

Appendix 3.1. Assessment of Lambertian Surface Quality of Diffuse White Painted Surface Used for Videographic Flux Imaging.

The videographic flux measurement exercises all utilised water-cooled targets coated with a flat ('matt') white, high-temperature paint. As the Lambertian nature of the paint was unknown, a test was performed to assess its angular reflectivity. Figure A3.1.1 shows the experimental set up used for this assessment.

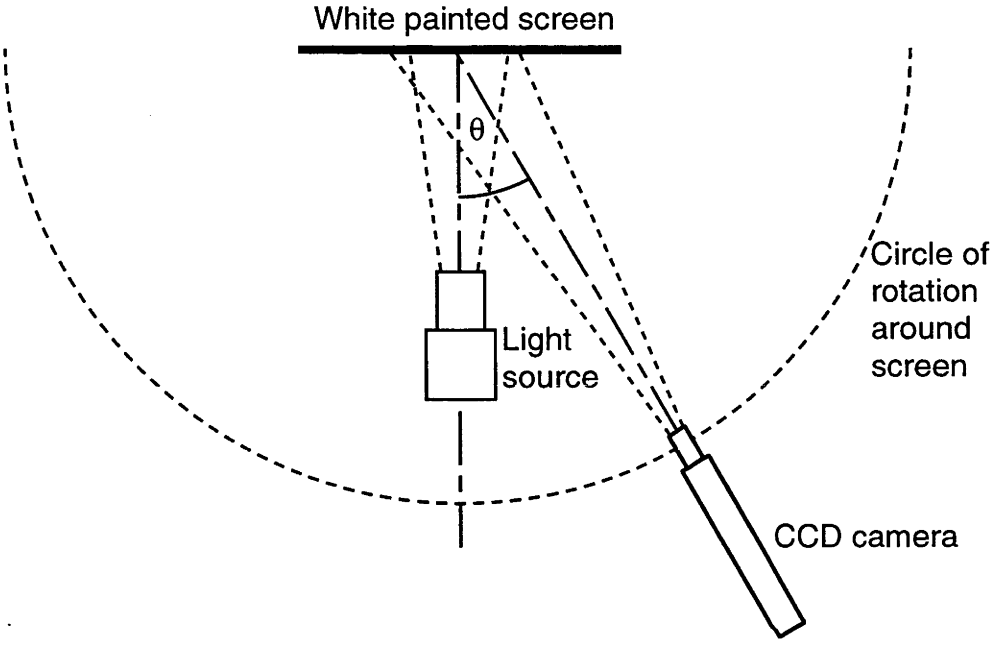

Figure A3.1.1. Experimental arrangement to assess angular reflectivity of a painted target surface.

Method

An aluminium plate 130x115 mm was painted with the matt white high temperature plate and mounted such that it could be viewed from a range of angles using a CCD camera and a light source. The lamp's collimating lens was adjusted to produce a projected light field that was uniform to 5% (measured using the CCD camera) in the central region of the plate either side of the axial line.

Two test regions, either side of the axis of rotation marked on the screen, and the average intensity in these test regions was measured for different angular orientations of the camera with respect to the screen. The average pixel levels of the two test regions for the different rotation angles were normalised by the peak average value (ie. at 0° rotation from normal) to give the proportional change in intensity for the reflective surface.

Figure A3.1.2 shows the resulting variation in reflected light intensity versus angle from normal incidence.

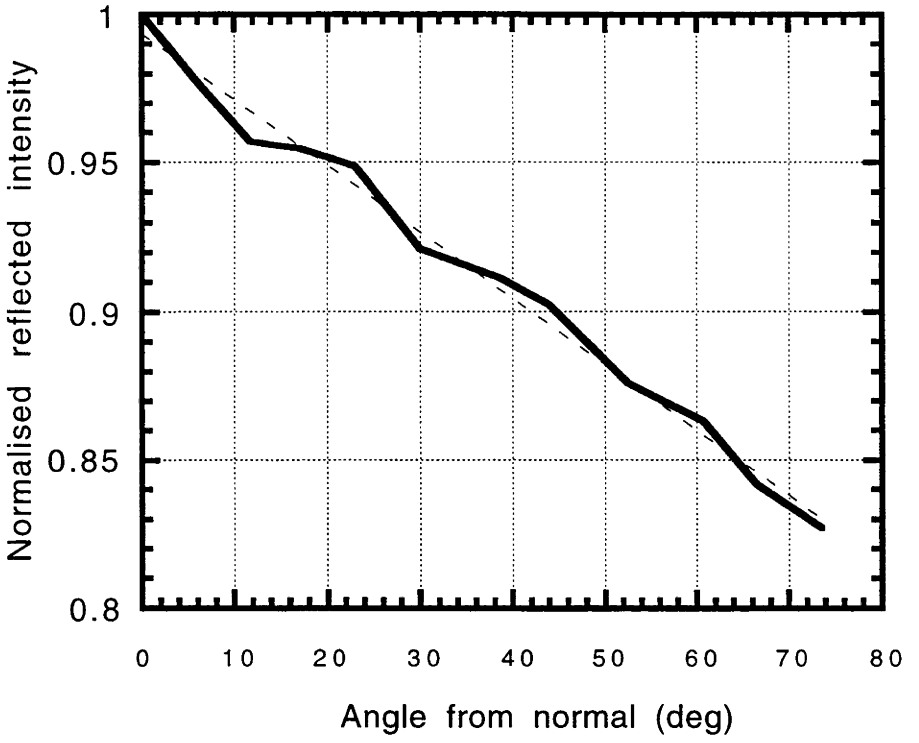

Figure A3.1.2. Variation of normalised reflected intensity versus viewing angle for light projected onto an aluminium plate coated with a matt white paint.

The dashed line in Figure A3.1.2 shows the linear regression line for the data, and has the following form:

$y = -0.0022188x+0.99329$

This equation was used when incorporating the non-Lambertian nature of the reflecting surface into the ray trace code, COMPREC.

Appendix 3.2. Calculation of Vector Intersection Points With Predefined Analytic Surfaces.

A3.2.1 Vector surface intersections

In all of the following analyses, vector variables will be referred to in **bold case**. Variables in normal case will refer to scalar quantities.

Determination of the vector intersection point, **P**, with a defined receiver surface requires the specification of a source point, **S**, from which the reflection vector, **SPu**, emanates. Position (**C**) and orientation (**N**) vectors for the receiver surface must also be known. Figure A3.2.1 illustrates the required components, using a cylindrical receiver as an example surface.

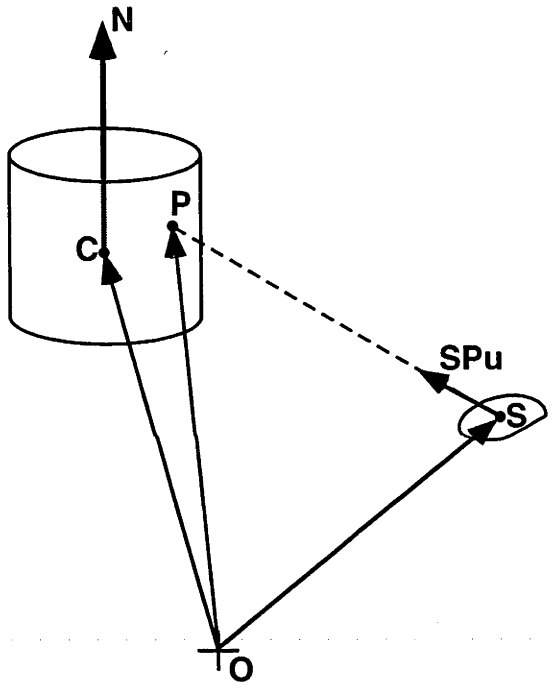

Figure A3.2.1. Illustration of vector intersection relationships to calculate the intersection point, P, of a reflection vector, SPu, from a source point, S, on the surface of a receiver.

We have an origin, **O**, (coordinates (0,0,0)), and a source point, **S**, (representing the reflection point on a dish surface) for the start of the unit reflection vector, **SPu**, which has been calculated previously. **C** defines a reference position vector for the receiver (the centre of the cylinder, in this example), while **N** defines an orientation vector.

Generally, the calculation of the intersection point requires equating the vector equations for the hit point, **P**, with the equation for the surface of the receiver.

The analyses undertaken for the intersection points with plane receivers having rectangular, annular, and circular (disk) boundaries, as well as cylindrical, partial-spherical and conical frusta receivers will be described in the following sections.

A3.2.2 Planar receiver intersections

Figure A3.2.2 illustrates the intersections being studied for this case.

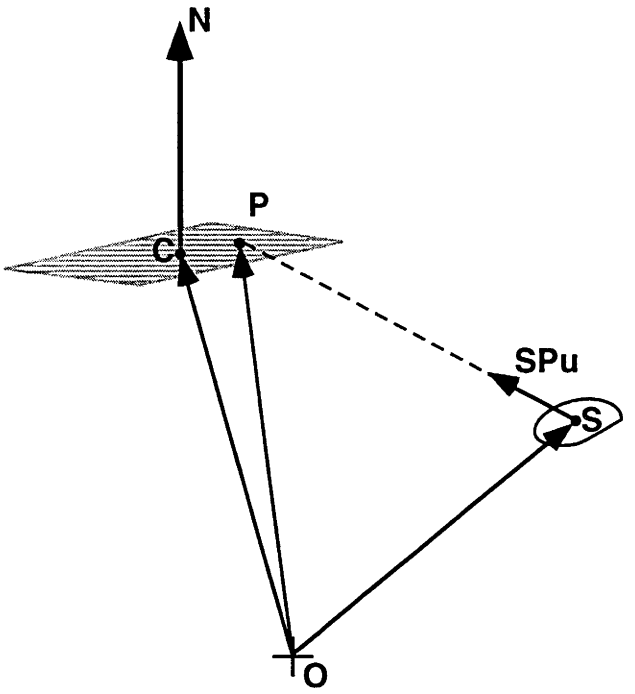

Figure A3.2.2. Vector intersection relationship for reflected vector intersection with a plane.

If we define the normal vector as having components **N**(A,B,C) and a plane point, **C**(D,E,F). The intersection point is defined as **P**. Starting from an origin, **O** (0,0,0), defining a source point, **S**, the associated equations for the intersection point, **P**, are:

$$\mathbf{OP} = \mathbf{OS} + \mathbf{SP} \qquad (4)$$

However, SP will have a length, g, along the direction of the unit vector, **SPu**:

$$\mathbf{SP} = g\,\mathbf{SPu} \qquad (5)$$

Thus,

$$\mathbf{OP} = \mathbf{OS} + g\,\mathbf{SPu} \qquad (6)$$

Using vector components,

$$\mathbf{OP} = (OS_x + g\,SPu_x, OS_y + g\,SPu_y, OS_z + g\,SPu_z) \qquad (7)$$

Now, the coordinates of the hit point, OP must obey the equation for a plane, given by,

$$Ax + By + Cz = T \qquad (8)$$

where T is given by,

$$T = AD + BE + CF = \mathbf{C} \bullet \mathbf{N} \qquad (9)$$

That is, the x,y,z components of the plane must be equal to the x,y,z components of **OP**. Substituting (5) into (4) gives,

$$A(OS_x + g\,SPu_x) + B(OS_y + g\,SPu_y) + C(OS_z + g\,SPu_z) = T \quad \textbf{(10)}$$

Expanding and simplifying for g,

$$g = \frac{(T - AOS_x - BOS_y - COS_z)}{(ASPu_x + BSPu_y + CSPu_z)} \quad \textbf{(11)}$$

OP is then found by back substituting into (3), ie.,

$$\mathbf{OP} = \mathbf{OS} + g\mathbf{SPu}$$

A plane has two sides, and the ray trace algorithm (COMPREC) can specify which side is to be regarded as the 'active' side - whether the side on the same side as the specified normal (**N**), or opposite it, or both sides of the plane. Determination of the side of intersection is accomplished through examination of the polarity of the dot product between the surface normal and the reflection vector, **SPu**. Figure A3.2.3 shows the necessary relationships.

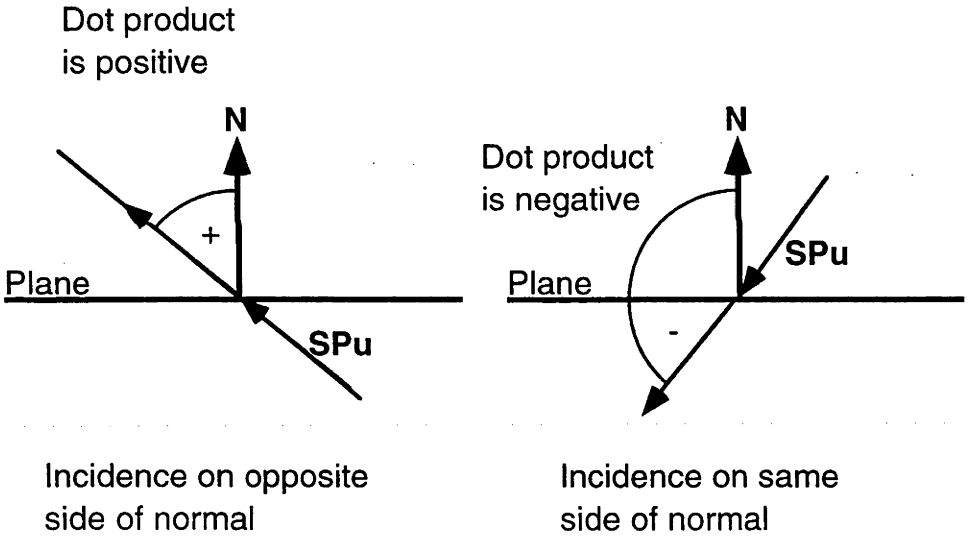

Figure A3.2.3. Relationships between the polarity of the dot product between the reflection vector, SPu, and the plane surface normal, determining the side of intersection on the plane.

As Figure A3.2.3 shows, the polarity of the dot product between the reflection vector, **SPu**, and the plane normal, **N**, determines the side of intersection on the plane. A positive polarity indicates the reflection vector hits the plane on the opposite side to the normal, while a negative polarity indicates the converse. Determination of the validity of a 'hit' on the plane must ensure correspondence between the side of intersection with that specified for the surface, and must also ensure the hit point falls within the rectangular boundaries specified for the surface.

A3.2.3 Annular and disk receiver intersections

Calculating the hit points, **P**, for annular and disk receivers uses the same equations as defined above for the case of a rectangular, planar receiver. Disks and annuli only have different boundary descriptions, which are assessed by software after the hit point has been calculated.

A3.2.4 Cylindrical receiver intersections

Reference to Figure A3.2.1 illustrates the intersections being studied for this case. For expediency, it was considered that the majority of applications using cylindrical receivers would be for devices aligned with the z-axis. This both simplified the analysis and allowed for faster execution times (due to the much reduced calculational complexity) when programmed into an algorithm. In this case the equation for a cylinder simply becomes,

$$x^2 + y^2 = r^2 \qquad \textbf{(12)}$$

where r is the radius of the cylinder.

Considering the vector intersections, we have,

$$\mathbf{OP} = \mathbf{OC} + \mathbf{CP} \qquad \textbf{(13)}$$

and $$\mathbf{OP} = \mathbf{OS} + \mathbf{SP} \qquad \textbf{(14)}$$

Thus,

$$\mathbf{CP} = \mathbf{OS} + \mathbf{SP} - \mathbf{OC} \qquad \textbf{(15)}$$

However, the vector **CP** will be defined by the equation for a cylinder (equation (9)). The x,y dimensions referred to in (9) correspond to the x and y components of CP, ie.,

$$x = CP_x, \qquad y = CP_y \qquad \textbf{(16)}$$

Substituting in (9) yields,

$$CP_x^2 + CP_y^2 = r^2 \qquad \textbf{(17)}$$

Substituting in (12),

$$(OS_x + SP_x - OC_x)^2 + (OS_y + SP_y - OC_y)^2 = r^2 \qquad \textbf{(18)}$$

Now, the unknown vector, SP will be given by,

$$\mathbf{SP} = g\,\mathbf{SPu} \qquad \textbf{(19)}$$

Substituting in (15), we have,

$$(OS_x + g\,SPu_x - OC_x)^2 + (OS_y + g\,SPu_y - OC_y)^2 = r^2 \qquad \textbf{(20)}$$

This quadratic can be solved for g. Simplifying, and using expressions (Exp) to put the solution into a more compact form for programming

$$g = \frac{\pm\sqrt{Exp_1} - Exp_3}{2\,Exp_2} \tag{21}$$

where,

$$Exp_1 = Exp_3^2 - 4(Exp_4 - r^2)Exp_2 \tag{22}$$

$$Exp_2 = SPu_y^2 + SPu_x^2 \tag{23}$$

$$Exp_3 = 2((OS_x - OC_x)SPu_x + (OS_y - OC_y)SPu_y) \tag{24}$$

$$Exp_4 = (OC_x - OS_x)^2 + (OC_y - OS_y)^2 \tag{25}$$

OP is then found from,

$$\mathbf{OP} = \mathbf{OS} + g\,\mathbf{SPu}$$

If Exp_1 is negative, then there is no real solution to the equations. This case applies when the reflection vector, **SPu**, does not intersect the defined cylinder. When the reflection vector is parallel to the z-axis, Exp_1 is zero. The solution to the quadratic clearly indicates two possible real hit points on the cylinder surface, and accommodates the case when the line of the reflection vector can pass through the cylinder at two points. In this case, g should first be tested for polarity, and if both a positive and negative solutions exist, then the positive value should be used, as the negative value indicates that **S** is inside the cylinder radius, and two hit points can occur, one in the direction of **SPu** (the desired hit point), and the other in the direction opposite to **SPu** (undesired). If g has two positive values, then their conformance with the specified inside or outside interception criteria should be tested. Surface interception criteria are assessed in a similar manner as described for the planar intersections - that is the sign of the dot product between the receiver surface normal at the hit point and the reflection vector **(SPu)** is assessed. The dot product should be negative for the intersection of **SPu** with the **outside** of the cylinder, and should be **positive** for intersection with the **inside** of the cylinder, as illustrated in Figure A3.2.4 below:

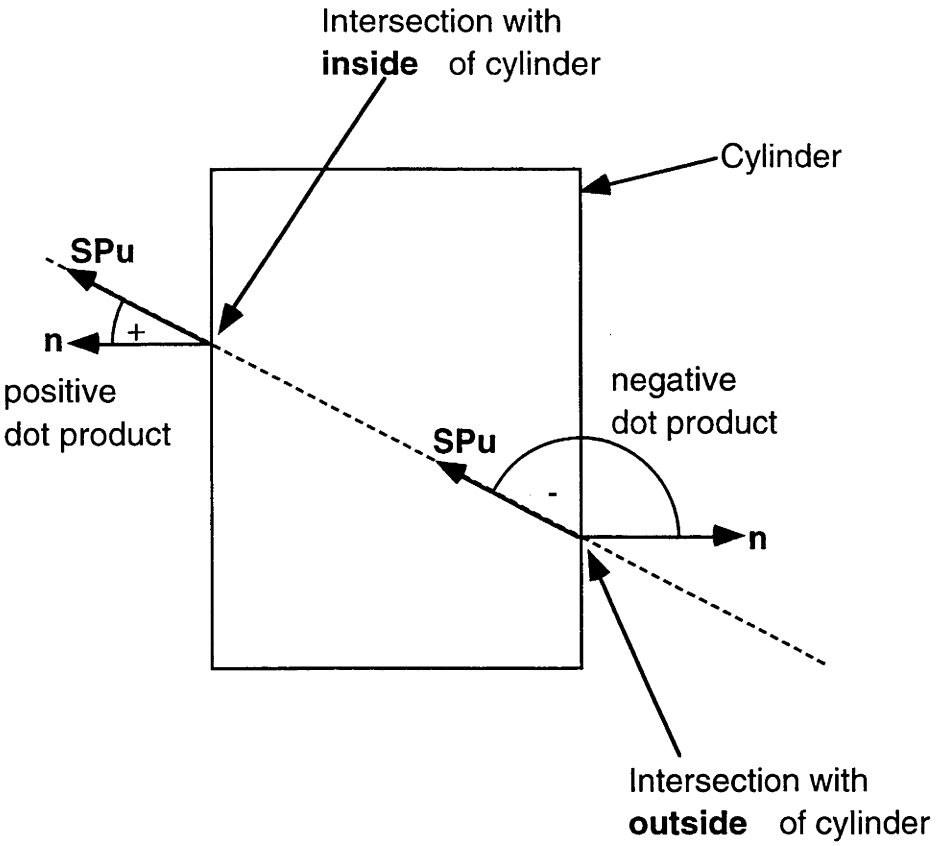

Figure A3.2.4. Illustration of the inside/outside intersection criterion for the reflection vector, SPu, with a cylinder.

Finally, checking for the containment of the hit point within the specified boundaries of the cylinder should be performed. In summary, a successful hit point should then fulfil the following criteria:

(i) length of **SP** must be positive;
(ii) the dot product of **SPu** and the cylinder surface normal must satisfy the inside/outside specification for the intersection point;
(iii) the hit point must fall within the specified boundaries of the cylinder.

A3.2.5 Partial spherical receiver intersections

Partial spherical surfaces can be modelled utilising the lower portion of a sphere (pointing downwards, aligned with the z-axis).

Calculation of the intersection point, **P**, on the surface of a sphere proceeds in a similar manner to that described above for the cylindrical case, except that the equation to the sphere,

$$x^2 + y^2 + z^2 = R^2 \qquad \textbf{(26)}$$

will be used to constrain the vector intersection equations.

Using analysis similar to that described above for the cylindrical case, the length, g, of the vector **SP** can be shown to be,

$$g = \pm\sqrt{(\mathbf{CS} \bullet \mathbf{SPu}) + \left(R^2 - |CS|^2\right)} - \mathbf{CS} \bullet \mathbf{SPu}, \qquad \textbf{(27)}$$

with the hit point on the surface of the sphere fulfilling similar criteria described for the cylindrical case above, that is,

(i) length of **SP** must be positive,
(ii) the dot product of **SPu** and the spherical surface normal must satisfy the inside/outside specification for the intersection point;
(iii) the hit point must fall within the specified boundaries of the sphere.

A3.2.6 Conical frusta receiver intersection

Figure A3.2.5 shows the vector intersection diagram applicable to this analysis.

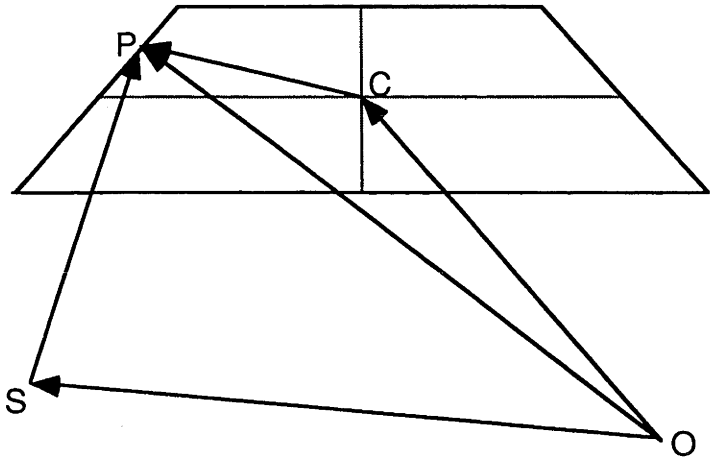

Figure A3.2.5. Vector intersection diagram for the intersection of reflection vector, SP, with the surface of a conical frusta.

The equation to a frusta is described most simply in cylindrical coordinates:

$$z = mr + c \qquad \textbf{(28)}$$

where,

m=slope of the walls of the frusta
c=intercept of the frusta walls on the z-axis.

Using the fact that,

$$r = \sqrt{x^2 + y^2} \qquad \textbf{(29)}$$

and substituting in (25) gives,

$$x^2 + y^2 = \left(\frac{z - c}{m}\right)^2 \qquad \textbf{(30)}$$

This then become the surface equation which constrains the vector intersection equations. Analysis similar to that performed in the previous sections allows calculation of the length, g, of the reflection vector, **SP**, as,

$$g = \frac{\pm\sqrt{Exp_1} - Exp_3}{Exp_2} \qquad \textbf{(31)}$$

where,

$$Exp_1 = Exp_3^2 - Exp_4\, Exp_2$$
$$Exp_2 = \left(SPu_x^2 + SPu_y^2\right)m^2 - SPu_z^2$$
$$Exp_3 = \left(CS_x\, SPu_x + CS_y\, SPu_y\right)m^2 - \left(c - CS_z\right)SPu_z$$
$$Exp_4 = \left(CS_x^2 + CS_y^2\right)m^2 - \left(c - CS_z\right)^2$$

If Exp_1 is zero, then the reflection vector, **SPu**, is parallel to the sides of the frusta, whereas if it is negative, then the length, g, is unreal and no intersection with the frusta occurs. As with previous surfaces, the following criteria must be satisfied to register a 'hit' with the specified receiver:

(i) length of **SP** must be positive,
(ii) the dot product of **SPu** and the frusta surface normal must satisfy the inside/outside specification for the intersection point;
(iii) the hit point must fall within the specified boundaries of the frusta.

Appendix 3.3. Example of input file 'RecDishIn.dat' for data input to ray trace program COMPREC

It was decided to use a data input file for feeding specifications to COMPREC, primarily because it provides a record for later reference after the program is completed. Interactive data entry for each program run is also a time consuming and tedious process, particularly for simulations that are very similar to each other, with minimal changes in data values between runs. 'RecDishIn.dat' is a static file that can be accessed with any text processor, and the modifications made and saved with minimal effort.

The header in the file explains the structure of the data variables, and should be fairly self explanatory. Under the header are sections for the definition of some sun parameters followed by the reflector surface parameters. Then follow the receiver surface definitions. Generally these conform to the pattern of:

1. Specify the number of surfaces of specified type (eg. cylinders, disks, etc.);
2. Specify the spatial dimensions of the target surface (Xmin, Xmax, etc);
3. Specify the position coordinates (3 component vector) for locating the surface wrt to the origin (dish vertex);
4. Specify the surface normal, or alignment vector (3 component vector) for the target surface (omitted for cylinder, sphere and conical frusta target surfaces);
5. Specify the 'sensitive side' of the target surface (eg, inside, outside, or both)
6. Specify the output filename desired for storing the output flux array

An example 'RecDishIn.dat' file follows. Annotations for the benefit of the reader are in *italics* and contained in braces: *{.Annotation...}*, but are not present in the normal 'RecDishIn.dat file.

10
Header: The line above indicates the total lines of text in this header.
The data format is as follows:
The 1st line of each record below is the surface name of each surface type.
Below the name is the number of surfaces of that type (except for SunData and
DishData). If a surface is not used, then assign it a value of zero.
The subsequent lines in each record firstly show the parameter name list,
followed by the values for each parameter (separated by spaces) on the
next line.
Where multiple surfaces of the same type are used, then just keep adding
the lines of data for each surface below the appropriate parameter name list.

SunData: *{This is a heading for this data section}*
Intensity (W/m^2) NumberOfSunPoints *{These are (2) prompts for the data on the next line}*
1000 2000 *{These are actual data values used by COMPREC}*

DishData: *{This is a heading for this data section}*
DishDataFileName *{This is a prompt for the data (name) on the next line}*
5mDish_1.81f_9x9GridTiles_1.8mrerr *{This is an actual file name used by COMPREC}*
ApertureArea(m^2) DishSlopeError(mrad) DishPointingError(deg) DishReflectance *{prompts}*
19.6350 0.0 0.0 1.0 *{Data values}*

Planes: *{This is a prompt for the data on the next line}*
0 *{This specifies the number of planes to be analysed}*
Xmin(m) Xmax(m) Ymin(m) Ymax(m) Reflectance Absorbtivity *{prompts}*
-0.05 0.05 -1.2 1.2 0 1 *{Data values}*
PlanePoint(3xm) *{This is a prompt for the data on the next line}*
0 0 0.726 *{Data-3 vector components for the position of the plane centre}*
PlaneNorm(3xm) *{This is a prompt for data on the next line}*
0 0 1 *{Data - 3 vector components that specify the orientation of the plane}*
PlaneSurface - on same side as normal, opposite or both? *{Prompt for data on the next line}*
opposite *{Data used by COMPREC}*
OutPut File Name(s) *{Prompt for data on the next line}*
pvtFlux_0.2wx2.2L_Abs@0.726f *{Data value (filename) used by COMPREC}*

Disks:
1
DiskRadius(m) Reflectance Absorbance
0.25 0 1
PlanePoint(3xm)
0 0 1.81
PlaneNorm(3xm)
0 0 1
Disk Surface - on the same side as surface normal, opposite or both?
opposite
OutPut File Name(s)
5mDishFlux_0.5Abs@1.81f_1.8mrerr_9x9Tiles

Annuli:
0
InnerRad(m) OuterRad(m) Reflectance Absorbance
0.35 0.75 0 1
PlanePoint(3xm)
0 0 12.8
PlaneNorm(3xm)
0 0 1
Annulus surface - on the same side as the surface normal, opposite or both?
opposite

OutPut File Name(s)
BigDishFlux_Annulus0.35irx0.75or@12.8m_7x7SphGridTiles

Cylinders:
0

CylRad(m)	CylTop(m)	CylBot(m)	Reflectance	Absorbance
0.32	14.33	13.0	0	1

CylCentre(3xm)
0 0 0
Cylinder surface - inner, outer or both surfaces?
inner
Output File Name(s)
BigHexDish_Cyl_1.33hx0.32r@13.0m6mrerr

Spheres:
0

SphereRad(m)	Xmin(m)	Xmax(m)	Ymin(m)	Ymax(m)	Reflectance	Absorbance
0.1	-0.2	0.2	-0.2	0.2	0	1

SphereCentre(3xm)
0 0 1.8
Use inner, outer or both surfaces?:
outer
Output File Name(s):
SphereTest2

Frustra:
0

TopRadius(m)	BottomRadius(m)	FrustTop(m)	FrustBottom(m)	Reflectance	Absorbance
0.32	0.75	13.0	12.8	0	1

FrustCentre(3xm)
0 0 0
Use inner, outer or both surfaces?:
inner
OutPut File Name(s):
BigHexDish_Frust0.32TopRx0.75BotRx0.2h@12.8m6mrerr

Appendix 4.1. Flux distributions for the 20 m^2 tiled dish.

Figure A4.1.1 to Figure A4.1.6 show flux distribution cross sections for a 0.5 m diameter target placed at positions 1.78, 1.80, 1.82, 1.84, 1.86 and 1.88 m from the dish vertex. A reflectivity of 0.72, and a surface slope error of 2.0 milliradian has been used to produce all ray trace predictions.

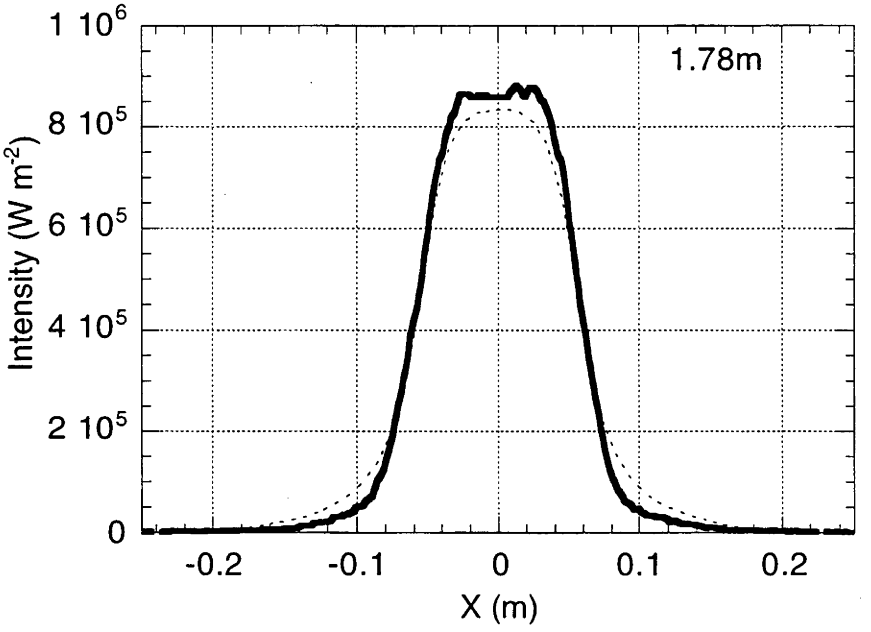

Figure A4.1.1. Superposed measured (heavy line) and predicted (dashed line) fluxes for target position 1.78 m from the dish vertex.

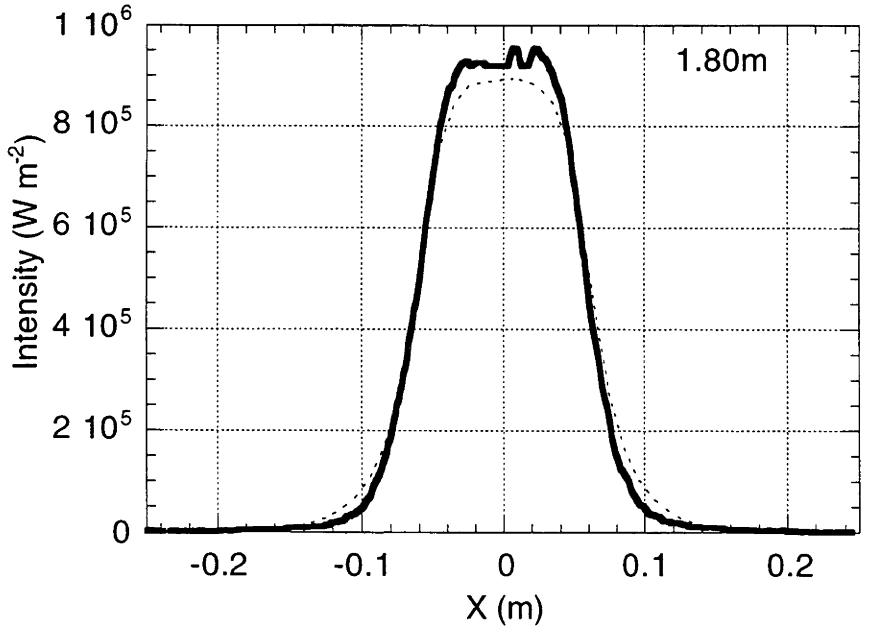

Figure A4.1.2. Superposed measured (heavy line) and predicted (dashed line) fluxes for target position 1.80 m from the dish vertex.

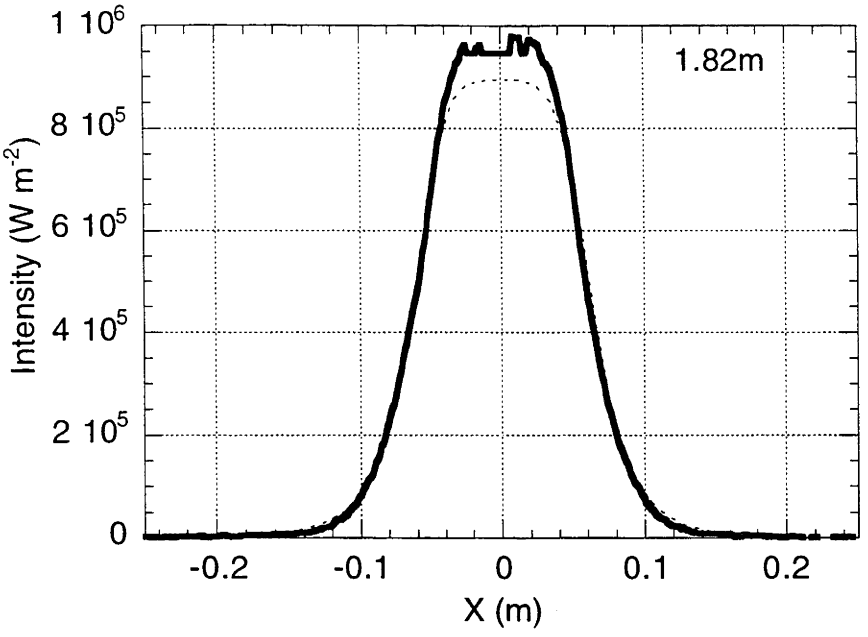

Figure A4.1.3. Superposed measured (heavy line) and predicted (dashed line) fluxes for target position 1.82 m from the dish vertex.

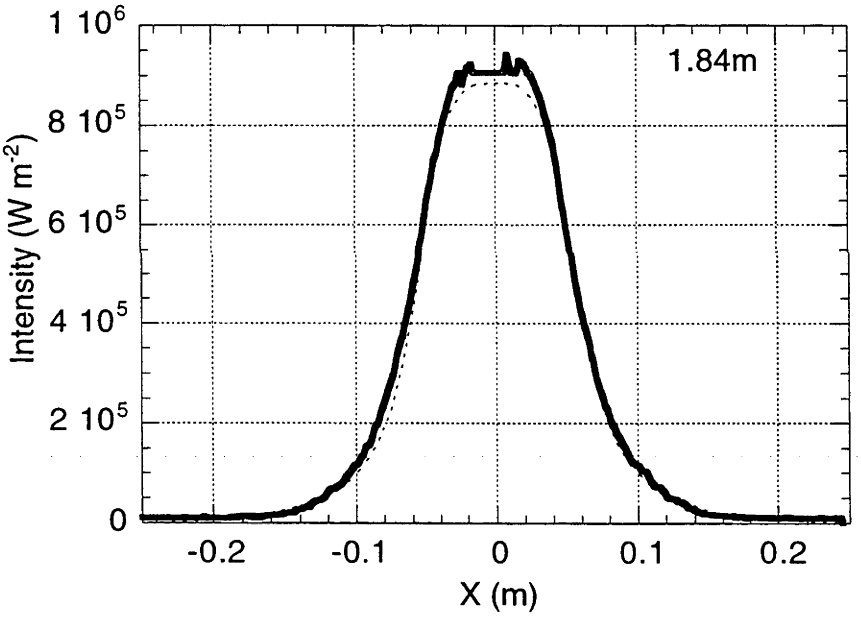

Figure A4.1.4. Superposed measured (heavy line) and predicted (dashed line) fluxes for target position 1.84 m from the dish vertex.

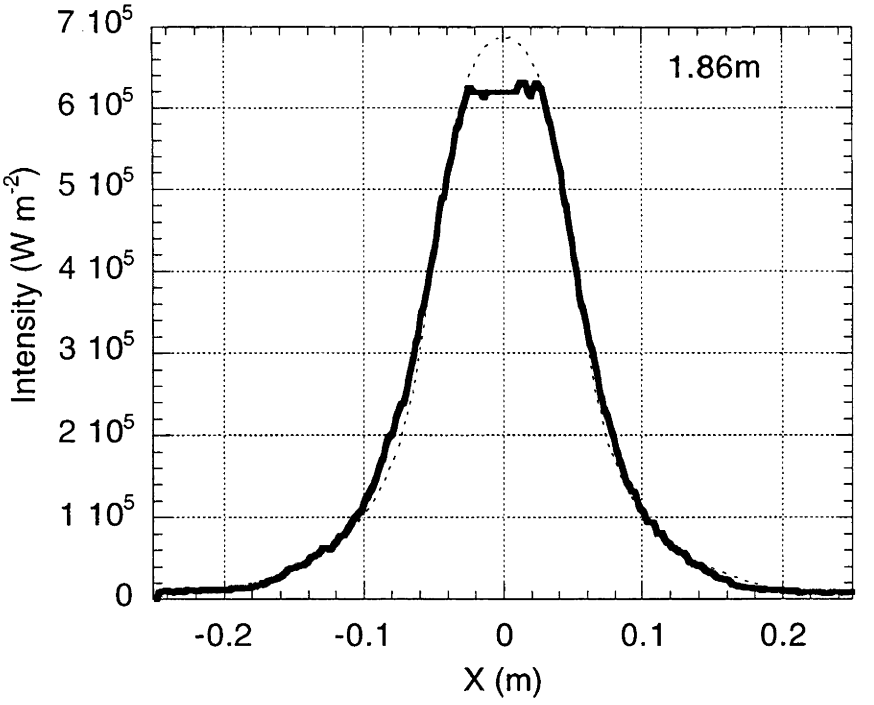

Figure A4.1.5. Superposed measured (heavy line) and predicted (dashed line) fluxes for target position 1.86 m from the dish vertex.

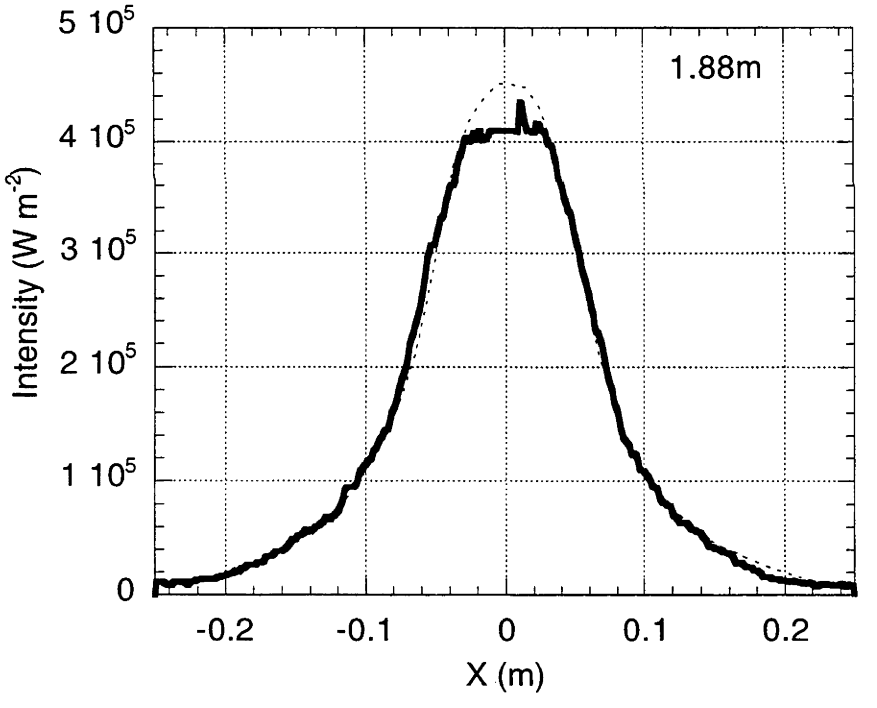

Figure A4.1.6. Superposed measured (heavy line) and predicted (dashed line) fluxes for target position 1.88 m from the dish vertex.

Appendix 5.1. Development of a novel laser scanning surface measurement system.

The method presents a novel laser scanning technique which can provide a numerical characterisation of the paraboloidal dish surface, giving both dimensional coordinates and surface normal information. The system was developed as a possible characterisation method for the 25 m diameter (13.1 m focal length) paraboloidal dish being constructed at the Australian National University. Unfortunately, the method appeared to be too inaccurate to characterise the surface of such a large dish, but the design is reported here as a technique open to possible development for smaller dishes. The basic schematic of the laser scanning/detection system is illustrated in Figure A5.1.1 below.

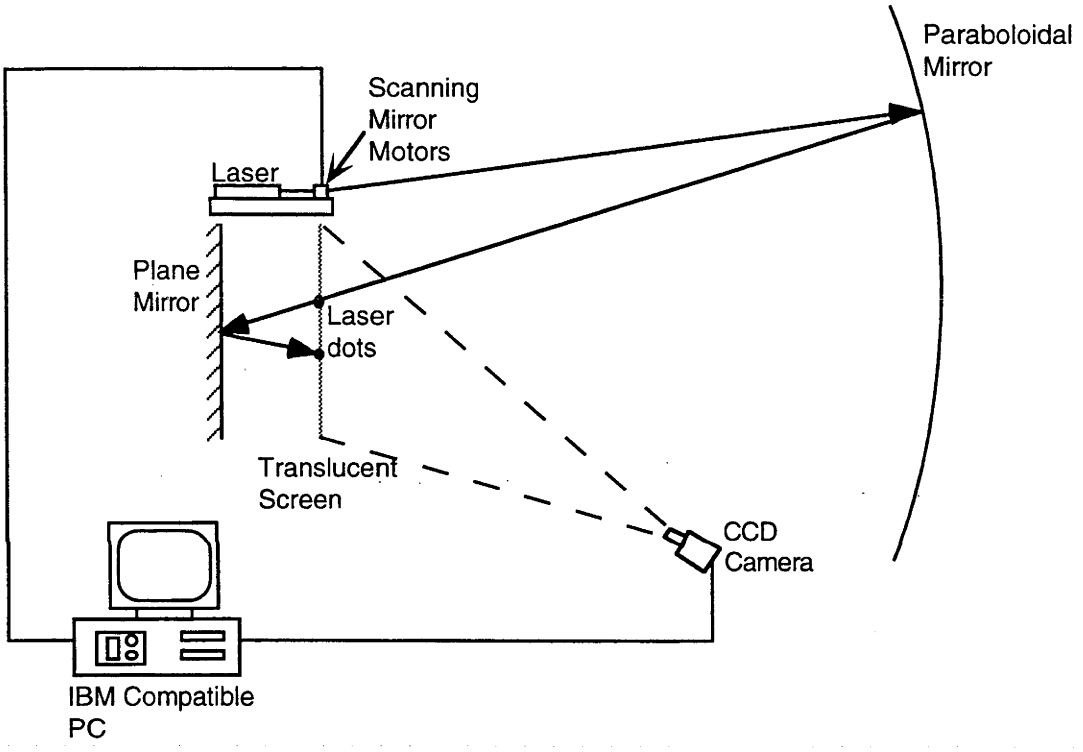

Figure A5.1.1. Schematic layout of the laser scanning surface characterisation system.

Operation

The principles of its design are as follows:

Two orthogonally mounted electromagnetic mirror deflection motors[12] were used to deflect a laser beam to any desired position on the paraboloidal dish whose surface was to be characterised. (Using angular deflection avoided the problems of linear scanning across the dish surface.) The reflected beam from the dish passes through a translucent detection screen mounted near the laser scanner, forming a detectable dot of light on the screen. The scanner and detection screen were placed near the approximate radius of curvature of the mirror, such that rays leaving the scanner were brought back to form a localised image that can be accommodated by the dimensions of the detection screen. A plane mirror was mounted behind the detection screen, such that the laser beam, which had already passed through the screen once, was reflected back to intercept the screen

[12]Series G, open loop optical scanner. General Scanning, Inc. 500 Arsenal Street, Watertown, MA. USA. 02172.

a second time, thus forming a second detectable dot of light. A CCD camera[13] was mounted to allow video frames to be taken of the detection screen, and an image framegrabber[14] was used to 'snatch' and digitise the image of the two laser dots on the detection screen. This allowed rapid quantification of the X and Y coordinates of the dots on the detection screen. The determination of the numerical coordinates of the paraboloidal surface at the point of laser beam reflection can be found by reference to Figure A5.1.2 below:

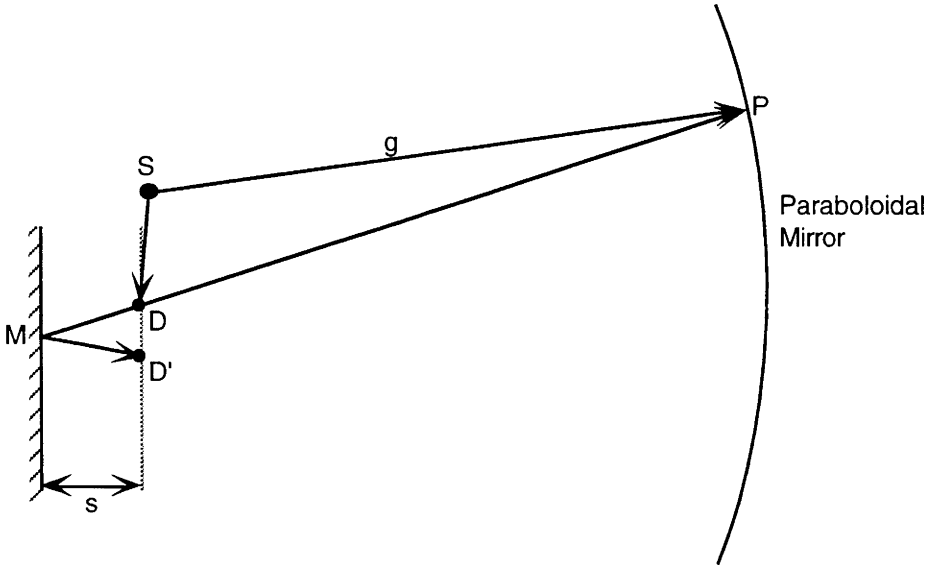

Figure A5.1.2. Definition of parameters used to analyse the laser scanning surface characterisation system.

The laser beam leaves at the source point, S, and intercepts the paraboloid at point P. The beam reflects off the dish and intercepts the detection screen at point D. The beam makes a light spot on the screen and continues through to the plane mirror mounted behind, and parallel to the translucent screen. Further reflection occurs at the reflection point, M, on the plane mirror, to produce the second interception with the detection screen at point D'. The direction cosines (ie. unit vector) of SP are known (by directing the mirror motors under computer control to point the beam in a specified direction), while the detection screen and plane mirror combination allow the determination of the direction cosines of the vector DP. The vector SD is known by measurement (through digitisation of the dots on the detection screen, and the known distance from S to the detection screen).

Vector analysis (see Appendix) allows the distance, g, from S to P to be formulated as follows:

$$g = \frac{|SD|}{SDu \bullet SPu - \dfrac{SDu \bullet DPu\sqrt{1-(SDu \bullet SPu)^2}}{\sqrt{1-(SDu \bullet DPu)^2}}}$$

[13]Pulnix TM6-CN CCD camera. Obtained through Hadland Photonics Pty. Ltd. 19A Hampshire Rd. Glen Waverley, Victoria, Australia. 3150.
[14]"QuickCapture" frame grabber board. Data Translation, Inc. 100 Locke Drive, Marlboro, MA, 01752-1192. USA.

where DPu is given by

$$DPu = \frac{MD}{|MD|}$$

and

$$MD = \frac{s(SD \otimes SD') \otimes (SD'\text{-}SD)}{|(SD \otimes SD') \otimes (SD'\text{-}SD)|} - \frac{(SD'\text{-}SD)}{2}$$

SDu, SPu and DPu are the unit vectors in the directions of SD, SP and DP, respectively.

The unit surface normal of the paraboloid at the point of intersection, Nu, is given by:

$$Nu = \frac{SDu + DPu}{|SDu + DPu|}$$

System Uncertainties

The uncertainties in g will be dependant on the uncertainties in the detected laser dot positions, SD and SD', and the projected beam vector, SPu. The absolute uncertainty in g, Δg, can be found simply through the sum of the squares of the differential errors due to SD, SD' and SPu, as given in the equation below:

$$(\Delta g)^2 = \left(\frac{\partial g}{\partial SD_x}\Delta SD_x\right)^2 + \left(\frac{\partial g}{\partial SD_y}\Delta SD_y\right)^2 + \left(\frac{\partial g}{\partial SD'_x}\Delta SD'_x\right)^2 + \left(\frac{\partial g}{\partial SD'_y}\Delta SD'_y\right)^2 + \left(\frac{\partial g}{\partial \theta}\Delta\theta\right)^2 + \left(\frac{\partial g}{\partial \phi}\Delta\phi\right)^2$$

where θ and ϕ are the altitude and azimuth spherical coordinate angles of SPu, and no uncertainty is assumed in the z-components of SD and SD'. 'Δ' indicates the uncertainty of measurement in the respective variables.

Values were developed to simulate the reflected rays that would occur for a 14 m focal length dish with a laser source and detection screen placed at the approximate radius of curvature of the dish (~28 m from the dish vertex). Values for g were calculated for given values of SD, SD' and SPu, together with the uncertainties in g for given uncertainties in SD, SD' and SPu.

It was estimated that the centroids of the dots of laser light on the translucent screen could be determined by image processing techniques to within 0.5 mm of their true positions, and this value was taken for the uncertainties ΔSD_x, ΔSD_y, $\Delta SD'_x$, $\Delta SD'_y$. Commonly available mirror deflection motors[4] have angular precisions of the order of 100 μrad. This value was used for the angular uncertainties $\Delta\theta$ and $\Delta\phi$.

---

[4] Model G138DT Optical Scanner. General Scanning Inc. 500 Arsenal Street, Watertown, MA, 02172. USA

Using these values in the foregoing equations for g yielded worst-case uncertainties in g of approximately 50 mm. Such a large uncertainty arises because of the close proximity of the laser source and detection screen (~1 m), effectively creating a large triangulation base to height ratio. This error could be reduced by separating the source and detector by a larger distance, but then most reflected rays from the dish would miss the detector, due to coma spreading of the off-axis image rays.

Methods and Equipment

To provide a qualitative test of the validity of the beam detector (translucent screen/plane mirror) concept, a prototype system was constructed using 'General Scanning' mirror motors which had no temperature stabilisation, no positional feedback control and which allowed maximum beam deflections of approximately ±15°. The motors were driven by current controlled linear amplifiers, which in turn were driven by the analog outputs of a dual channel digital-to-analog converter mounted in an IBM compatible personal computer. The translucent detection screen was constructed by first stretching a 0.05 mm thick Mylar sheet onto a 1 m x 1m light aluminium frame. A dilute (10:1) solution of white high-gloss paint in paint thinners was then poured onto, and distributed evenly across the (horizontal) Mylar sheet, and then left for several hours while the solvent evaporated. This left a fine, white, translucent film of paint on the Mylar sheet, which was found to easily show the interception of a laser beam, while at the same time producing negligible distortion or scattering of the beam as it passed through the film. This film was then mounted parallel to, and 0.5 m from a 1 m x 1m plane mirror. The laser scanner was then mounted on the top side of this screen/mirror combination and the laser beam directed to scan across a 0.5 m diameter model paraboloidal reflector. The CCD video camera was fitted with a 25 mm focal length lens, and was mounted on a boom at an approximate distance of 5 m from the screen, such that the 1 m x 1m screen could be captured in a single frame. Software was written to move the laser beam to a specified angular deflection, and then framegrab the resultant laser dot images appearing on the detection screen.

Results

The beam detector and video imaging system proved capable of detecting the reflected laser beam. Apart from the difficulties associated with improving the precision discussed in the theoretical analysis, it was observed that multiple spurious reflections and images created by the plane mirror were detected by the CCD camera. These would have to be eliminated by image processing algorithms to enable the extraction of the positions of the two desired dots of light on the translucent screen. This could best be accomplished by using a wide CCD camera lens aperture and focussing on the translucent screen such that spurious images are defocused. Image processing could then be applied to detect the sharper (desired) images and reject those that are defocused. Another difficulty arises when the two detected dots of laser light overlap each other, although this is a classical problem for which there are standard image processing techniques that can be used to extract the centroids of the overlapping images.

Conclusion

A qualitative test of a novel laser scanning dish characterisation technique indicated that conceptually the method could be developed into a working characterisation system, although in its present form it would produce large errors in the data generated, especially when applied to a large (~25 m diameter) paraboloidal dish. However, these errors could be significantly reduced if the system was applied to smaller dishes, and if

the base distance between the laser source and the associated reflected beam detector could be made larger.

The author presents the technique as one open to further development.

Appendix

The determination of the length of the vector from the laser source, S, to the interception point on the paraboloid, P, is a problem in three-dimensional triangulation, as described in the diagram below:

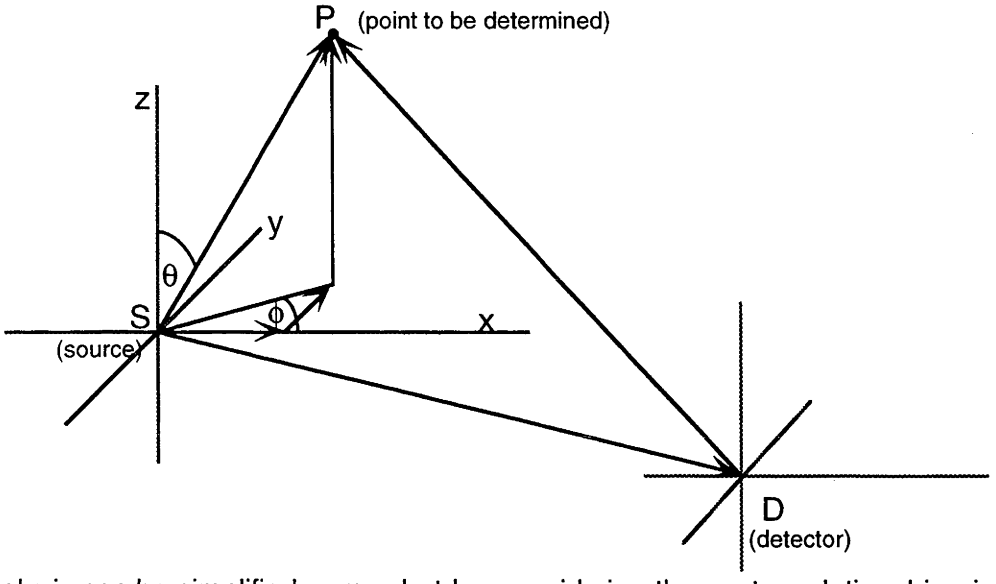

The analysis can be simplified somewhat by considering the vector relationships in the plane SDP, as shown below:

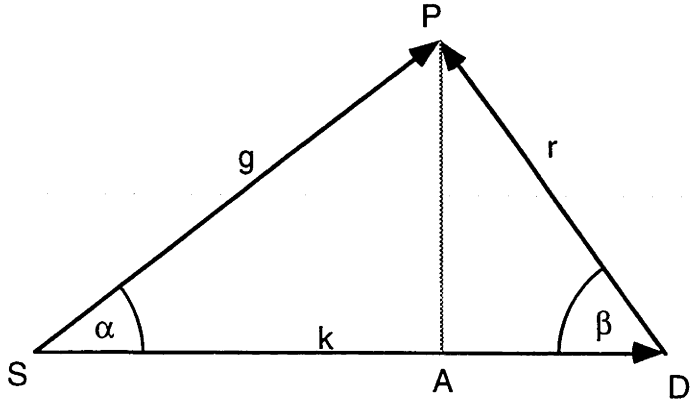

It is desired to find the length of SP (ie. the distance, d).

$$k = |SD| = g\cos(\alpha) + r\cos(\beta)$$

r can be eliminated by developing an alternative expression from the fact that

$$g\sin(\alpha) = r\sin(\beta)$$

or

$$g^2\sin^2(\alpha) = r^2\sin^2(\beta)$$

giving,

$$r = g\sqrt{\frac{1-\cos^2(\alpha)}{1-\cos^2(\alpha)}}$$

The cosines can be replaced by

$$\cos(\alpha) = SPu \bullet SDu; \qquad \cos(\beta) = -DPu \bullet SDu$$

where SPu, SDu and DPu are the unit vectors in the directions of SP, SD and DP, respectively. Combining (1) and (2), substituting for the cosines and rearranging gives

$$g = \frac{|SD|}{SDu \bullet SPu - \dfrac{SDu \bullet DPu\sqrt{1-(SDu \bullet SPu)^2}}{\sqrt{1-(SDu \bullet DPu)^2}}}$$

Surface normal determination

To calculate the surface normal at the reflecting surface, we consider the typical situation for reflection:

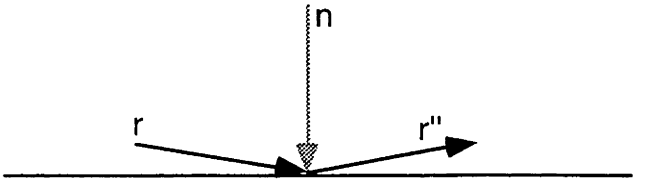

Adding the vectors, we have,

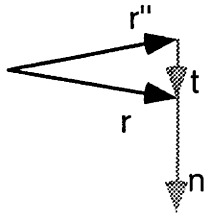

From this we can say,

$r''+t=r \Rightarrow t=r-r''$

and,

$$n = \frac{t}{|t|}$$

Substituting for t,

$$n = \frac{r-r''}{|r-r''|}$$

In the present analysis,

$r = SPu,\ r'' = -DPu$

Substituting for r and r'',

$$n = \frac{DPu + SPu}{|DPu + SPu|}$$

Appendix 5.2. Photogrammetric Analysis Procedures - Use of CRAMPA

A5.2.1 Introduction

The processing of images into final object space coordinates proceeds through a series of stages using different software packages, known collectively as the CRAMPA (Close Range Analytical Multistation Photogrammetric Adjustment) suite of programs (Shortis, 1993a). The following descriptions will move through the software and its respective input and output requirements, and assumes images have been taken using a Kodak DCS 200 or 420 still digital camera (CCD pixel array of 1524x1012 pixels, pixel size of 9x9 μm), using a lens of 28 mm focal length.

A5.2.2 DISKVIEW

Processing digital images first utilises DISKVIEW, which loads and displays the digital image on the monitor of an IBM PC or compatible computer. The program is invoked with the command line,

diskview h=1524 v=1012 x=9.0 y=9.0 Test

where,

- diskview invokes the program,
- h and v refer to the horizontal and vertical pixel ranges of the digital image,
- x and y refer to the physical size of the CCD pixels in the digital camera (units: micron)
- 'Test' is the name of the project file that will be used to define the image coordinate files that will be created by DISKVIEW.

Once in DISKVIEW, the internal operating parameters can be set by calling up menu windows and defining the relevant values. For most digitisation, the following parameters and values were found most functional:

- set thresholding algorithm to 'b', for Burner's algorithm,
- the number of bytes, N, contained in the TIFF image header file was found to be variable function of the program that was used to download the digital images from the camera into a TIFF format. Using 'NIH Image' generally produced TIFF headers 768 bytes in length,
- windows size, w, was dependent on the size of the target images, although 20x20 pixels was generally found suitable for most (small) target images,
- background threshold level, 't', and gray range value, 'g', were found to vary greatly, depending on the relative contrast between the background level and the peak intensity registered for the targets. Satisfactory operation was often found using a 't' value of 30, and a 'g' value of 150.

Once having set these parameters, an image can be loaded into memory and displayed on the screen. A mouse is used to simply point and click on the target images, and centroiding software in DISKVIEW identifies the target boundaries and calculates the target centroid. The image space coordinates of the centroid are stored sequentially in a text file, and the program is available to measure the next target image. If the target layout has been arranged to be in a regularly spaced rectangular grid pattern, then clicking on the first two target images in a linear sequence then allows the program to identify the spacing and direction of the remaining targets in the sequence, and

automatically searches for and identifies targets in the sequence until the edge of the grid pattern has been reached. The process is repeated on the next line of target images. This feature allows for great speed in target digitisation to be attained.

Once all the targets have been identified, the sequences of image space coordinates are written to file and closed. The next digital image of the object being analysed can then be read in and the targets sequentially digitised. Maintenance of identical target identification and digitisation sequencing is absolutely essential, otherwise a solution using later photogrammetric software will be almost impossible.

The image space coordinate files for the different photographs will usually be automatically labelled with the photo number and a '.pre' extension, such that the files for a four photo sequence will be saved under,

Test1.pre
Test2.pre
Test3.pre
Test4.pre

Another file is created called the print (.prn) file, which contains a record of all the parameters that were defined and adjusted during the course of using DISKVIEW.

A5.2.3 PRESORT

PRESORT is used to sort the sequences of image coordinates for all the photographs digitised using DISKVIEW, according to photo number and data point index numbers. It is invoked with command line,

presort Test Test1.pre Test2.pre Test3.pre Test4.pre ... etc.

where,

- presort invokes the program,
- 'Test' again identifies the project name to be used to label any output files,
- Test1.pre, Test2.pre, etc identify the image coordinate files to be sorted

The sorted coordinates are saved in a single file called,

Test.obs

which is now called the observations file for the data set.

Another print (.prn) file is also created that overwrites any previous .prn file(s), and contains a record of all the parameters that were defined and read by PRESORT, along with any error messages that may have arisen during the processing.

A5.2.4 PRE_CRAMPA

In addition to the observations file, a series of new files must now also be defined for use with PRE_CRAMPA and CRAMPA. These are,

1. A camera station file - 'Test.stn'
2. A lens calibration file - 'Test.cal'
3. A target (control point) coordinate file - 'Test.tar'

1. Camera station file

A typical camera station (.stn) file is shown below:

!Camera station coordinates for Test.

!Photo#	X	Y	Z	Phi	Omega	Kappa
1	1.5	-2.6	1.8	0.0	0.0	0.0
2	-1.5	-2.6	1.8	0.0	0.0	90
3	-1.5	-2.6	-1.8	0.0	0.0	180
4	1.5	-2.6	-1.8	0.0	0.0	270

where,

- lines starting with exclamation marks (!) are comment lines,
- the first data column defines the photo number of the station coordinates being defined,
- the 2nd data column defines the X coordinates of the camera station in object space coordinates (see below)
- the 3rd data column defines the Y coordinates of the camera station in object space coordinates (see below)
- the 4th data column defines the Z coordinates of the camera station in object space coordinates (see below)
- the 5th data column defines the Phi angle orientation of the camera at the time of the photograph (no need to define anything other than 0.0 - the software iteratively solves for the correct values later)
- the 6th data column defines the Omega angle orientation of the camera at the time of the photograph (no need to define anything other than 0.0 - the software iteratively solves for the correct values later)
- the 7th data column defines the Kappa angle orientation of the camera at the time of the photograph, and defines the rotation of the camera about the lens axis, and it is usual to input the rough orientation (in degrees) here.

The X,Y,Z coordinate system for the file is defined as follows:

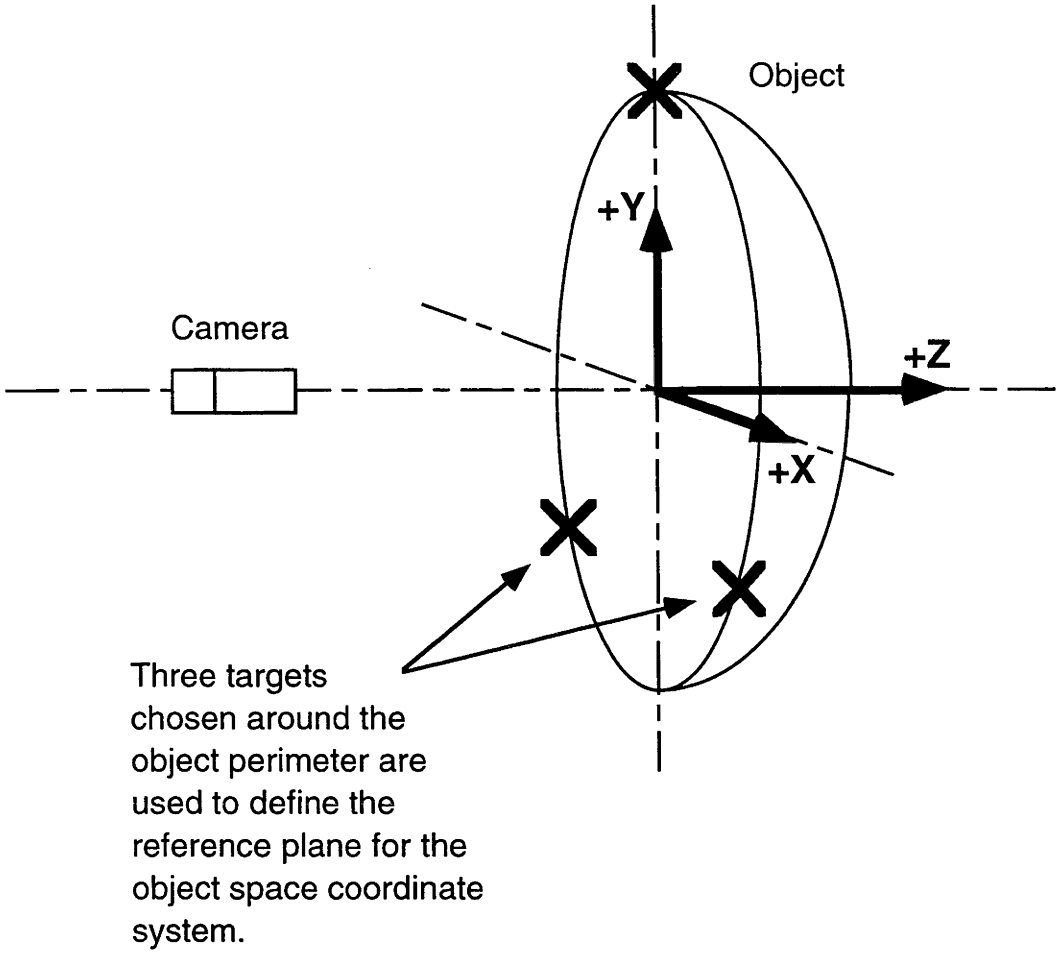

Figure A5.2.1. Coordinate system used by the CRAMPA photogrammetric processing software.

All of the coordinates given in the file are used as initial estimates only for 'kick starting' the software, and are iteratively refined to find their most probable actual values as the processing progresses.

2. Lens calibration file

A typical lens calibration (.cal) file is shown below.

!Lens calibration parameters for DCS420 28 mm lens

!Parameter	Value	Precision
1	0.008	1.000
2	-0.064	1.000
3	28.815	1.000
4	-1.6232e-004	7.569e-007
5	3.8255e-007	1.553e-008
6	0.0000e+000	0.000e+000
7	-1.2335e-005	1.093e-006
8	-2.1925e-005	1.039e-006

The 8 parameters defined above are the 'basic set' of lens calibration parameters. Using a polynomially defined set can introduce up to 23 parameters.

- Column 1 defines the calibration parameter identification number;
- Column 2 defines the most probable initial estimate of the parameter;
- Column 3 defines the degree of precision with which the parameter is known: 0 describes a parameter that is known exactly, 1.0 defines a parameter that is only roughly estimated.

- Parameter 1 defines the x-coordinate (mm) of the principle point (the point where the axis of the lens intersects the film plane). Ideally this should be zero, but the actual principle point is usually offset from the centre of the film plane;
- Parameter 2 defines the y-coordinate (mm) of the principle point;
- Parameter 3 defines the focal length of the lens;
- Parameters 4, 5 and 6 define the radial lens distortion (parameter 6 can usually be set to zero, with zero precision)
- Parameters 7 and 8 define the lens decentring distortion

When setting up starting values for an unknown lens, usually parameters 1 and 2 can be set to zero, with a precision of 1.0. Parameter 3 should be set to the nominal focal length of the lens, while the remaining parameters can be set to 0.0 with precisions of 1.0.

3. Target (control point) file

The table below shows a typical target (.tar) file:

!Control point coordinates for project Test

!Target#	X	Y	Z	Index	sX	sY	sZ
25	0.0	0.0	1.5	7	1.0	1.0	1.0
88	1.5	0.0	-1.5	7	1.0	1.0	1.0
129	-1.5	0.0	-1.5	7	1.0	1.0	1.0

- Column 1 defines the target number in the sequence of digitised targets on the surface that identifies a control point;
- Columns 2, 3 and 4 define the x, y and z-coordinates (m), respectively (referenced to the defined coordinate system, Figure A5.2.1) of the control point;
- Column 5 defines the coordinate index. This parameter identifies the number of coordinates that are known for the control point - 7 says that all X,Y,Z,sX,sY and sZ coordinates are known;
- Columns 6, 7 and 8 define the absolute precision with which the coordinates are known (mm).

These values must be fairly accurate and have a well known precision.

Using PRE_CRAMPA

PRE_CRAMPA is invoked with the (example) command line,

```
pre_cram e=0.3 Test
```

- pre_cram invokes the program for execution;
- e=?? defines the expected error (μm) that exists in the image space coordinates that have been determined in the DISKVIEW processing of the target image coordinates. This is usually set to a number between 0.3 and 3 microns. This number later

becomes the subject of a manual iteration and refinement process that must be undertaken between PRE_CRAMPA and CRAMPA.
- 'Test' defines the generic project name that will be used to look for the respective auxiliary files, Test.obs, Test.stn, Test.cal and Test.tar.

PRE_CRAMPA outputs a specifications (.spe) file and a data (.dat) file, as well as a .prn file that contains a record of all the final output values of the initial input parameters, such as camera stations, lens calibrations and control points, as well as information on numerous other parameters that were calculated by the program.

If a target resection or camera station intersection errors occur, it may be due to:

1. Mis-identification of targets in the image digitisation process. This can be very difficult to identify, but can be looked for in the .prn file. In this case, the residual errors of some camera station positions and/or some target coordinates can provide an indication of which photographs and/or targets may be causing the problem. Sometimes removing ('commenting-out') some camera stations (ie. photographs) from the .stn file and rerunning PRE_CRAMPA can help identify which photographs may be causing problems.
2. Camera station starting coordinates that are too far from their actual values. This can require adjusting the coordinates in the .stn file until a solution is found, or simply increasing the number of iterations (from 6 to a maximum of 20) used by PRE_CRAMPA to find a solution.

Once a solution has been obtained using CRAMPA, the specifications (.spe) file can be entered (using any text processor) and, if required, on the last two lines of the file, targets in specific photographs can be defined as 'Image Observation Deletions', such that they are not used in further processing (CRAMPA), and/or known straight-line distances between specified targets can be input to aid CRAMPA in correct scaling of the final out put coordinates of the complete data set.

A5.2.5 CRAMPA

CRAMPA is invoked with,

```
crampa i=20 -l -u Test
```

- crampa invokes the program;
- i=20 defines the number of iterations that the program must complete before terminating;
- -l is a switch that turns on the calculation and output (into the .prn file) of limited correlation coefficients between the various lens calibration parameters;
- -u is a switch that updates the specifications (.spe) file with the most recently calculated values of the camera station coordinates and the lens calibration parameters.
- Test identifies the project name, so that CRAMPA can access the relevant data input files (Test.spe and Test.dat);

What must be observed while CRAMPA is processing the data, is, that

1. the process converges to a solution of its own accord, before stopping at the predefined number of iterations (i=??), and without an error occuring that forces termination;

2. the value of 'sigma zero' which is calculated as a final parameter at the end of processing is as close to 1.0 as possible. If it is different from 1.0, then the value of 'e' used in PRE_CRAMPA must be multiplied by the value of sigma zero, and the new value used in PRE_CRAMPA to rerun the processing sequence again. This observation of sigma zero and adjustment of 'e' must be undertaken several times until sigma zero equals 1.0. This process ensures that the residual errors (and the uncertainties in the final output target coordinates) calculated by CRAMPA are close to the most probable values as possible.

However, it is usually found that running CRAMPA several times with the -u switch on (such that better and better refinements of the camera station and lens calibration parameters obtained in previous runs are obtained and used in the next run) will bring the sigma zero value down by several percent. This refinement should be undertaken until sigma doesn't change between CRAMPA runs, before taking the sigma zero value and adjusting the 'e' value in PRE_CRAMPA.

CRAMPA outputs a file of x,y and z coordinates, with estimated uncertainties in each coordinate, for all of the measured targets. It also outputs a print (.prn) files that contains information on all of the adjustment parameters that were calculated during the iterative refinements.

Observation should be made of the cross correlation coefficients in the final print (.prn) file. A typical array of coefficients is shown below:

*** Additional Parameter Correlation Factors ***

1	1.00						
2	-0.06	1.00					
3	-0.02	0.06	1.00				
4	-0.04	-0.00	-0.09	1.00			
5	-0.06	0.01	-0.07	-0.22	1.00		
7	0.12	0.03	0.01	0.00	0.00	1.00	
8	0.03	0.05	0.01	-0.00	-0.00	0.02	1.00

This array is larger when more additional parameters are specified, such as with a polynomially defined lens calibration set.

The array specifies the proportion of correlation (between 0.0 - no correlation - and 1.0 - complete correlation) between the listed lens calibration parameters. For example, the number in row 3, column 1 is the correlation between lens parameter 3 (focal length) and lens parameter 1 (the x-principle distance). Ideally, all values should be as close to zero as possible. However, values up to approximately 0.5 can be tolerated, while 0.5 to 0.8 is a cause for concern, and greater than 0.8 is unacceptable.

Generally, if high correlations are observed between some parameters, the .prn file should be investigated and the corrections shown against the various lens calibration parameters observed. Those parameters with the smallest corrections should be 'commented-out' of the .cal file, and the sequences of PRE_CRAMPA and CRAMPA run again.

Appendix 5.3. Z-coordinate deviations for mirror panels on the 400 m^2 dish.

Figure A5.3.1 to Figure A5.3.16 show the z-coordinate deviations for the eight mirror panels measured photogrammetrically on the surface of the 400 m^2 dish. The deviations were calculated by first orienting the three vertex alignment targets on the panels to assume an ideal paraboloidal orientation.

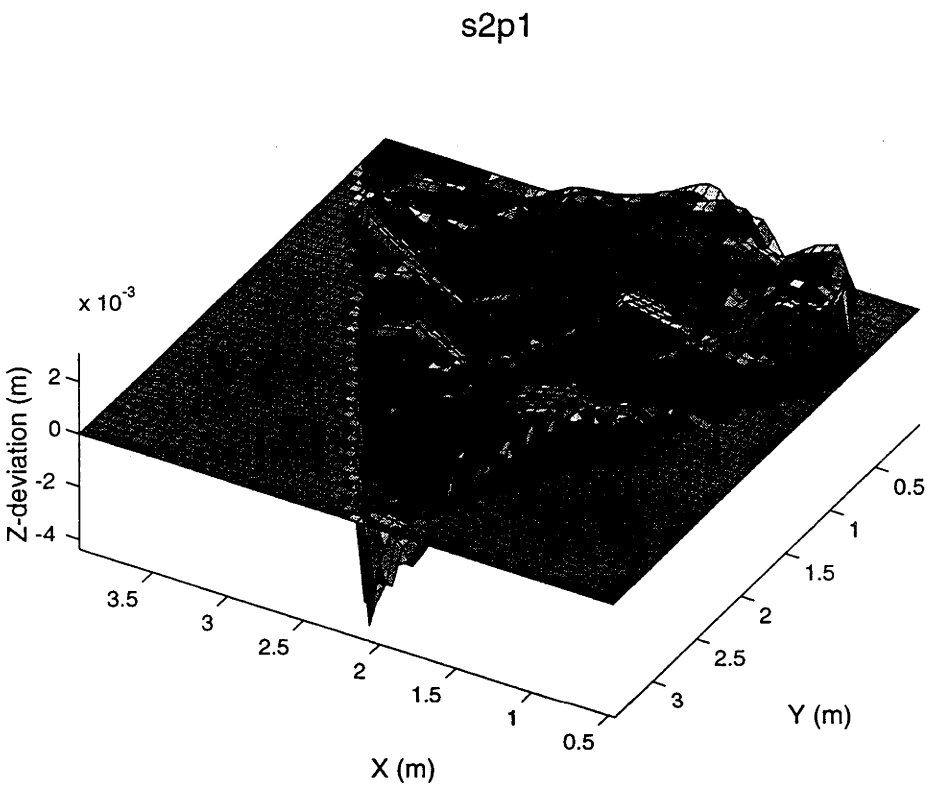

Figure A5.3.1. Z-coordinate deviations across the s2p1 mirror panel, linearly interpolated to a 50x50 grid. Note that z-deviations are calculated as (ideal-measured).

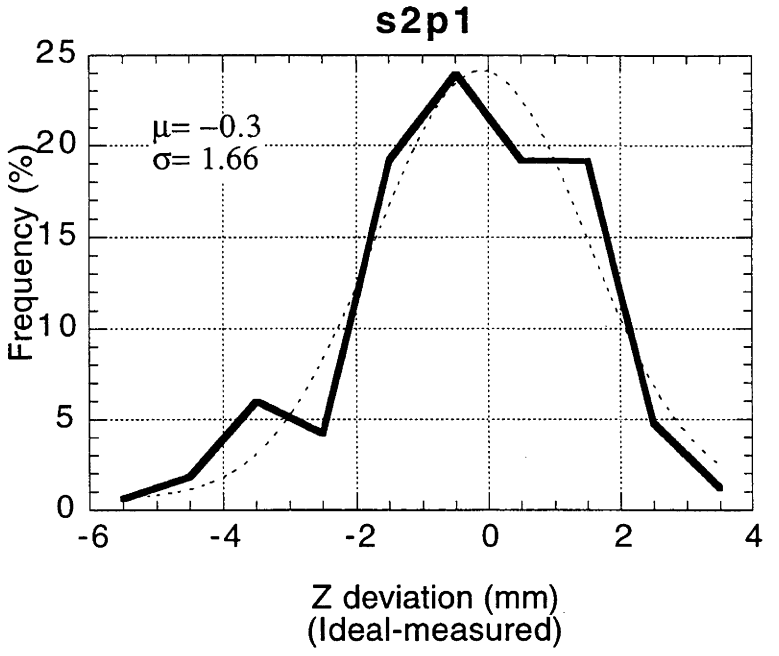

Figure A5.3.2. Frequency distribution of z-deviations for the s2p1 panel shown in Figure A5.3.1.

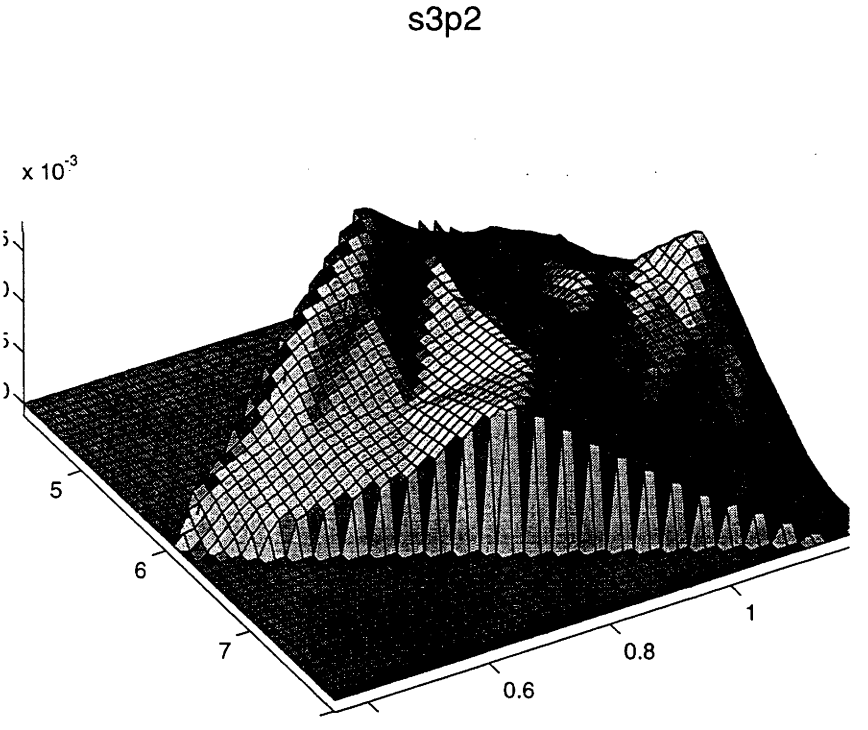

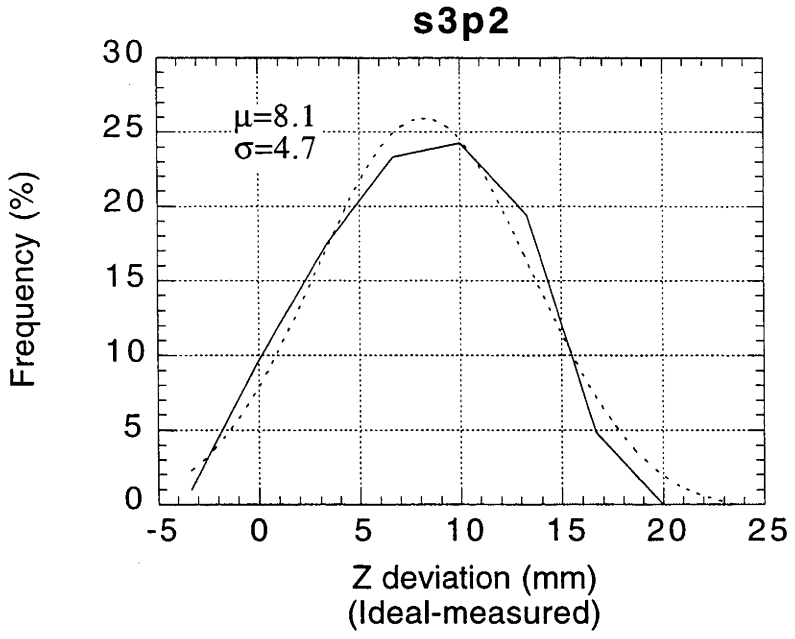

Figure A5.3.4. Frequency distribution of z-deviations for the s3p2 panel shown in Figure A5.3.3.

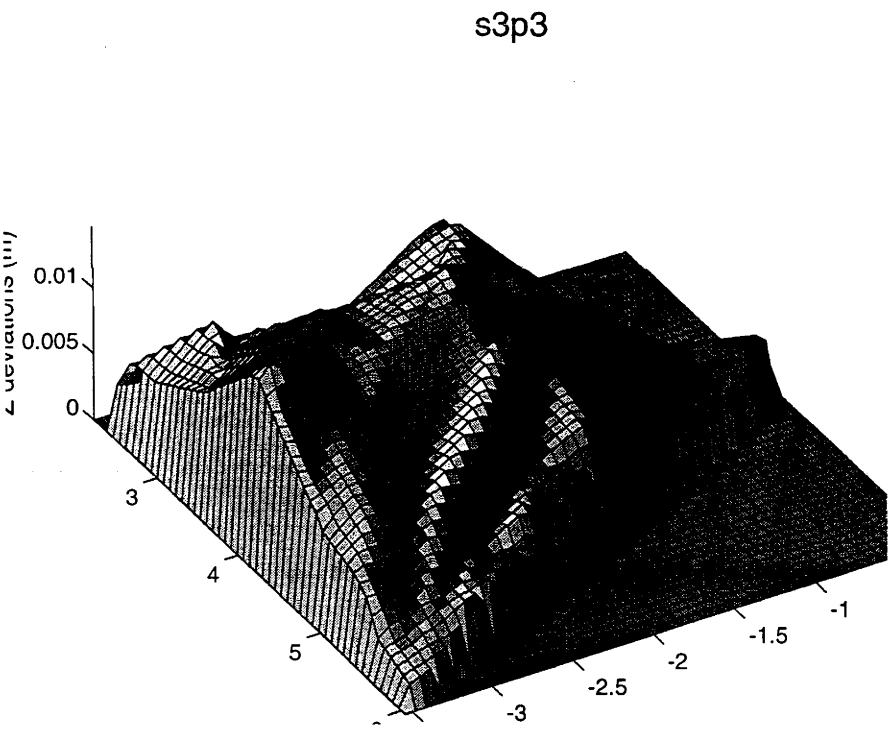

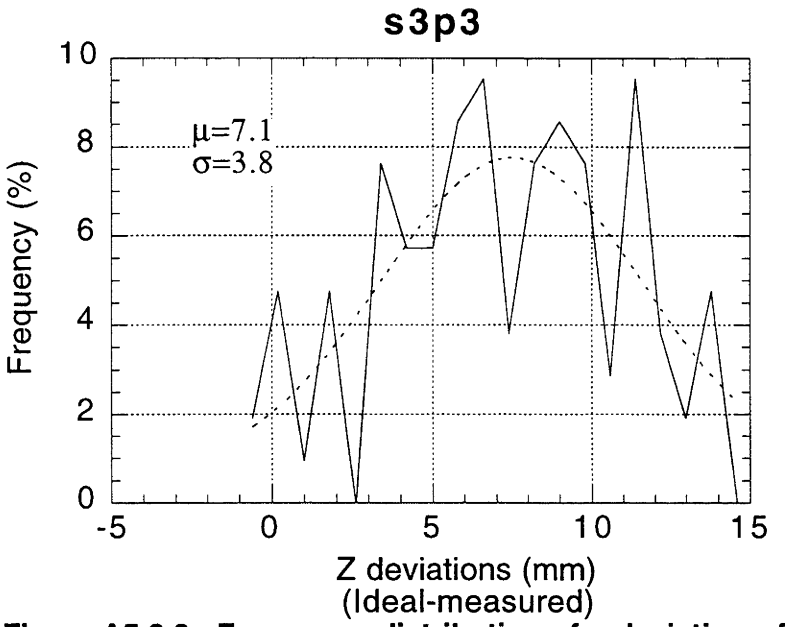

Figure A5.3.6. Frequency distribution of z-deviations for the s3p3 panel shown in Figure A5.3.5.

s5p4

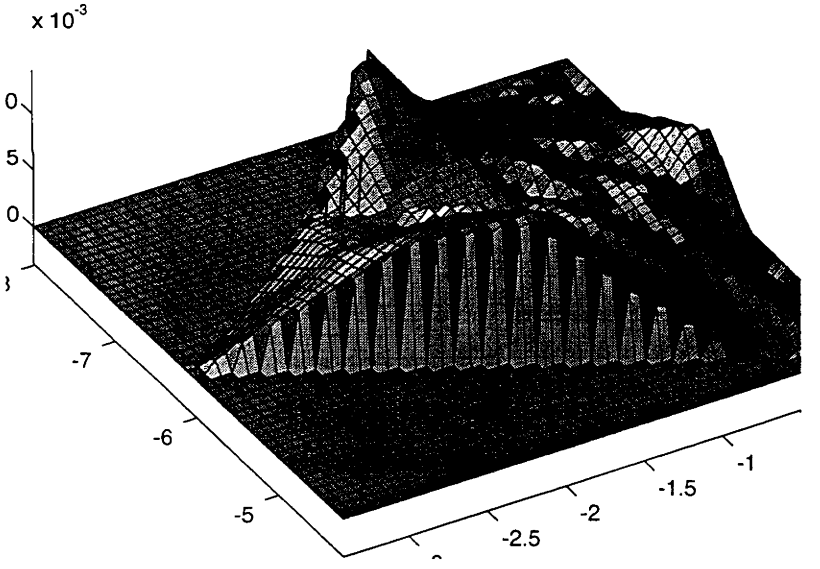

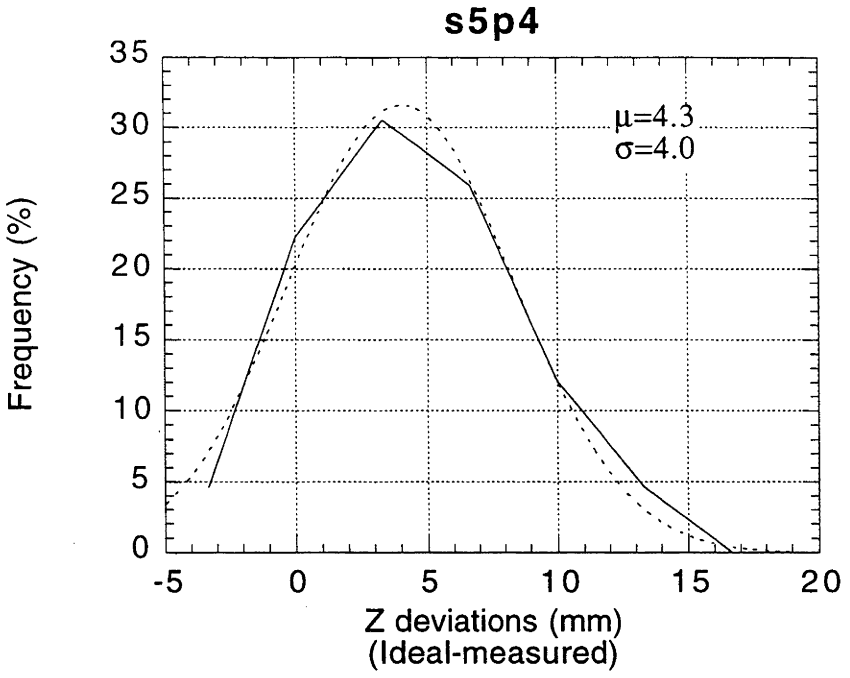

Figure A5.3.8. Frequency distribution of z-deviations for the s5p4 panel shown in Figure A5.3.7.

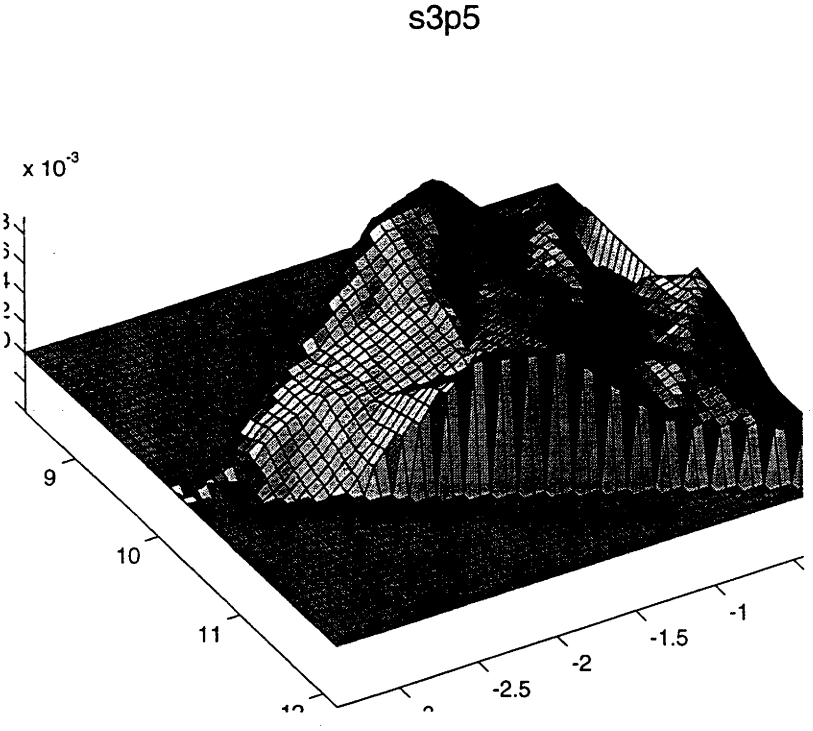

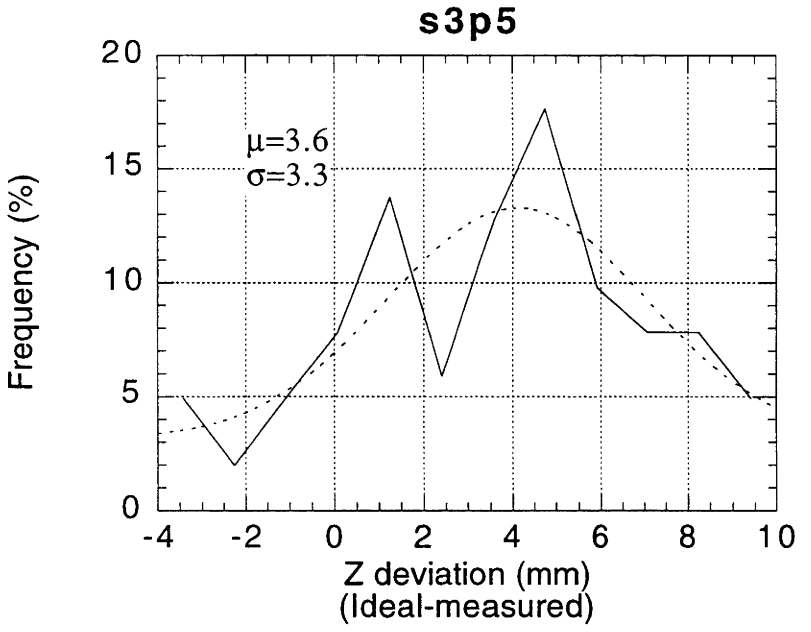

Figure A5.3.10. Frequency distribution of z-deviations for the s3p5 panel shown in Figure A5.3.9.

s3p6

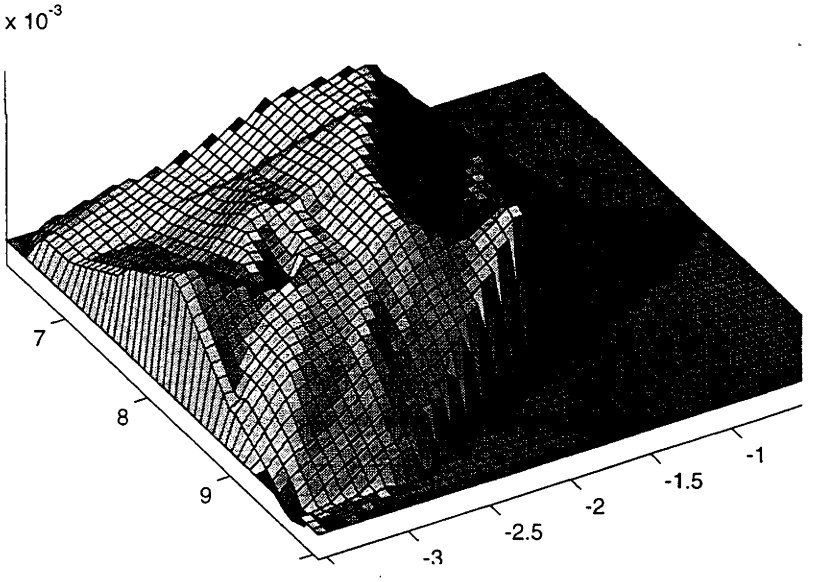

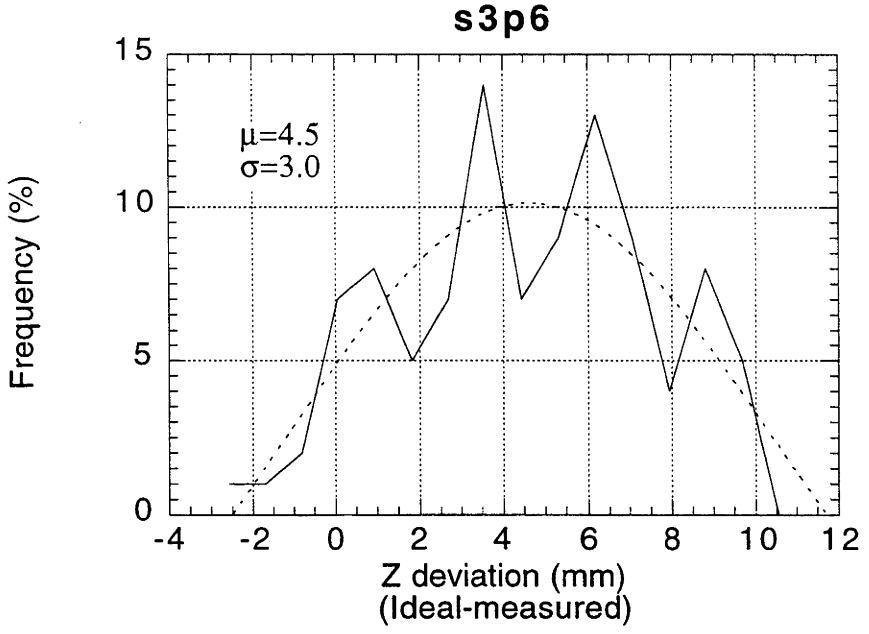

Figure A5.3.12. Frequency distribution of z-deviations for the s3p6 panel shown in Figure A5.3.11.

s4p7

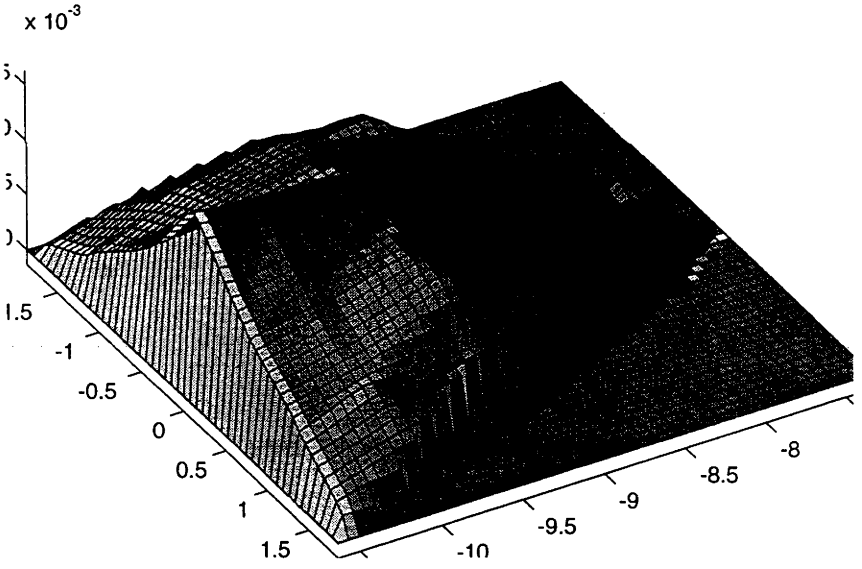

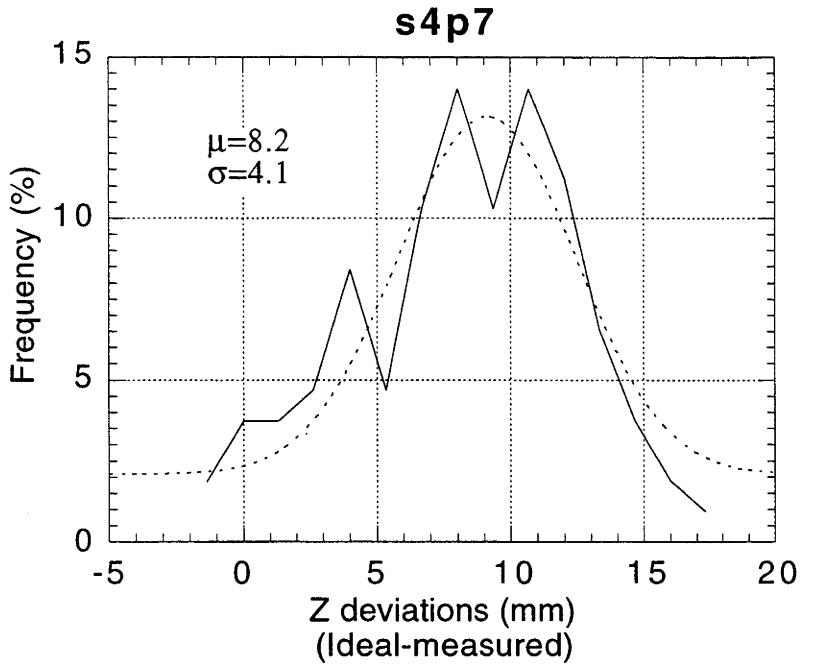

Figure A5.3.14. Frequency distribution of z-deviations for the s3p6 panel shown in Figure A5.3.13.

s5p8

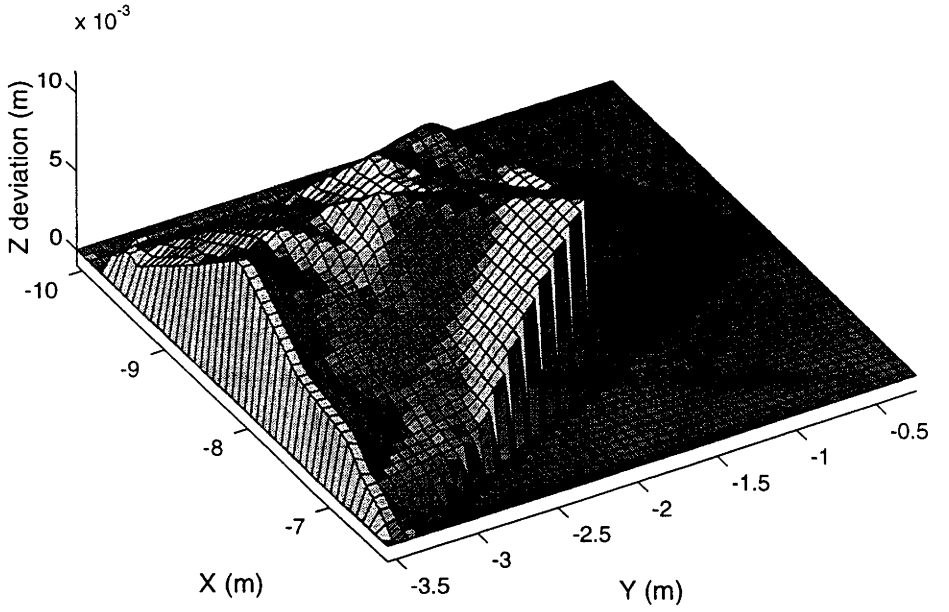

Figure A5.3.15. Z-coordinate deviations across the s5p8 mirror panel, linearly interpolated to a 50x50 grid. Z-deviations are calculated as (ideal-measured).

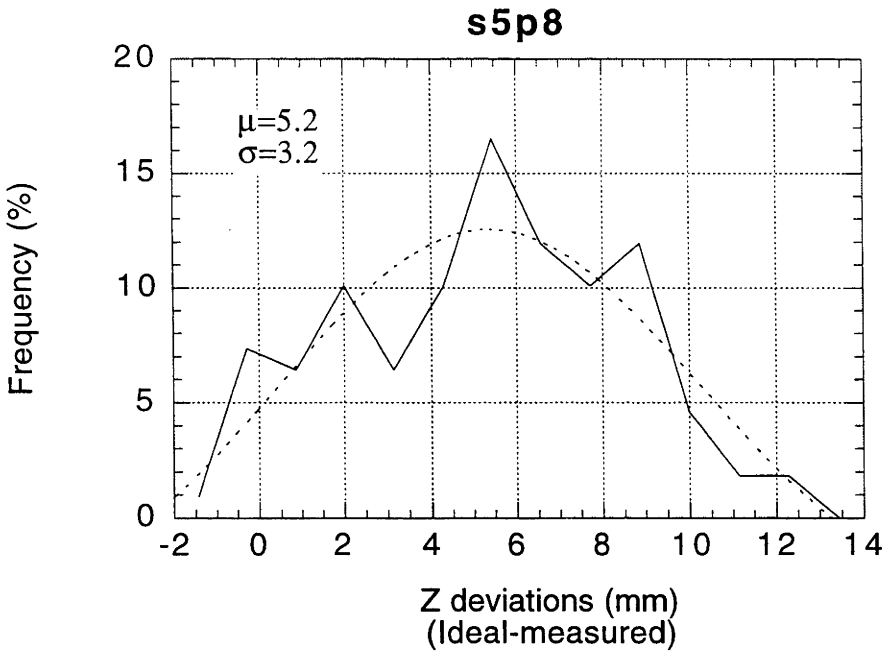

Figure A5.3.16. Frequency distribution of z-deviations for the s3p6 panel shown in Figure A5.3.15.

Appendix 5.4. Z-coordinate deviation plots and frequency distributions for the 400 m^2 dish mirror tiles.

Z-coordinate deviations were calculated for the mirror tiles using the following procedure:

1. Ideal paraboloidal coordinates were calculated for three vertex points on each mirror tile, according to each tile's respective position on the dish surface (and using a dish focal length of 13.075 m);
2. The tiles were reoriented to these calculated paraboloidal positions;
3. The reoriented x and y coordinates of all data points across the surface of a tile were used to calculate ideal z-coordinates for these points;
4. The ideal z-coordinates of the reoriented tile data points were subtracted from the measured (reoriented) z-coordinates, that is,

$$dz = z_{measured} - z_{ideal}$$

The deviation surface was visualised by interpolating the dz values to a 50x50 grid and plotting using graphics display packages (IDL and MATLAB). Frequency distribution plots were created by 'binning' the dz values into appropriate ranges, and plotting the percentage of points falling in different bins versus the central bin values. Best fit Gaussian distributions were calculated for the frequency distributions, and are displayed as dashed curves on the following graphs. However, the mean (μ) and standard deviation (s) values shown in the frequency distribution plots have been calculated using the standard statistical formula for μ and s, and have not been calculated from the best-fit Gaussian curve.

Figure A5.4.1 to Figure A5.4.16 show the spatial and frequency distributions of the z-coordinate deviations across the measured mirror tiles from the 400 m2 dish.

s2p1t

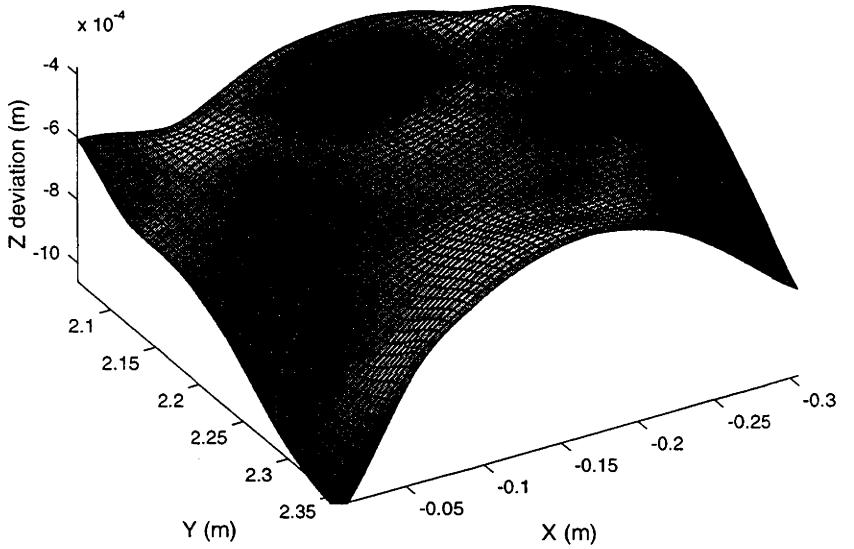

Figure A5.4.1. Z-coordinate deviation surface for s2p1t (30 cm) mirror tile. Deviations calculated as (measured-ideal).

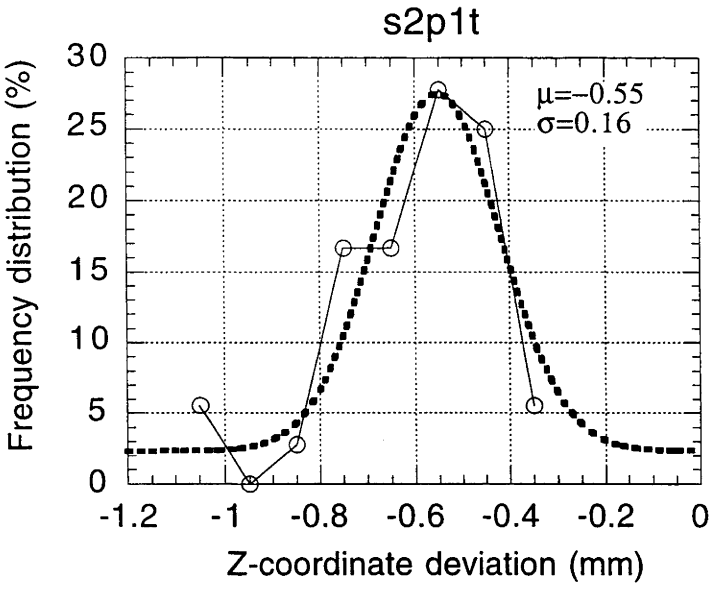

Figure A5.4.2. Frequency distribution of z-coordinate deviations for the s2p1t (30 cm) mirror tile shown in Figure A5.4.1.

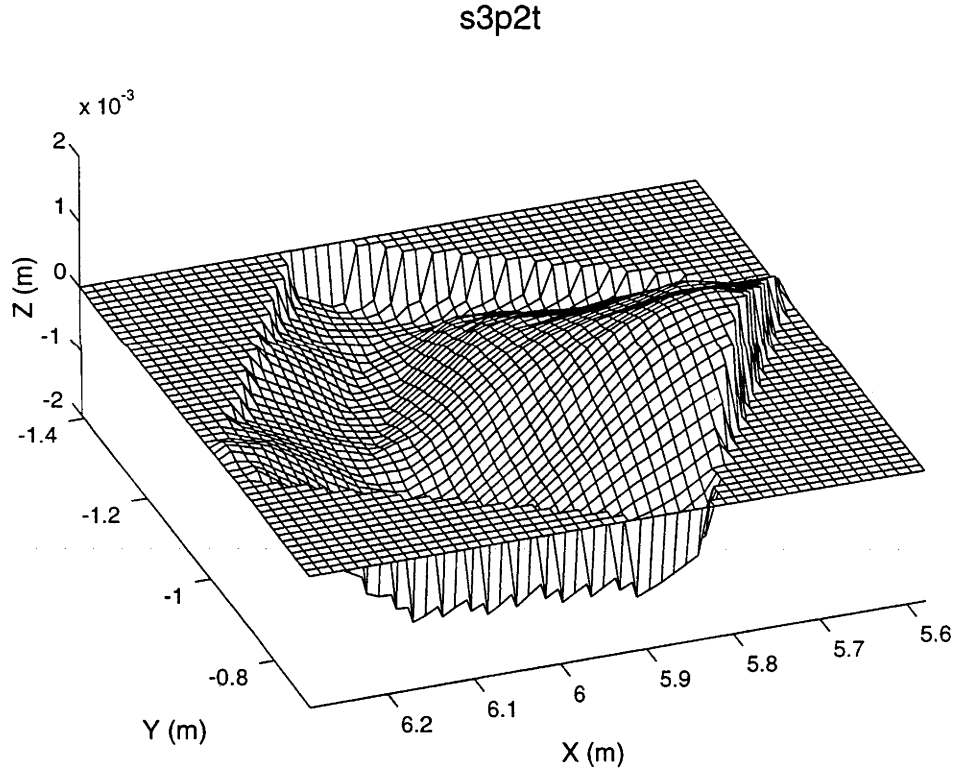

Figure A5.4.3. Z-coordinate deviation surface for s3p2t (60 cm) mirror tile. Deviations calculated as (measured-ideal).

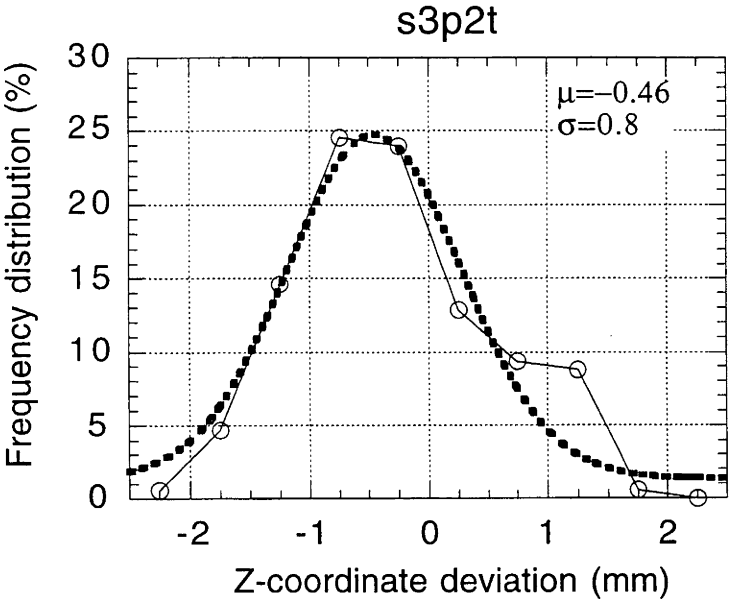

Figure A5.4.4. Frequency distribution of z-coordinate deviations for the s3p2t (60 cm) mirror tile shown in Figure A5.4.3.

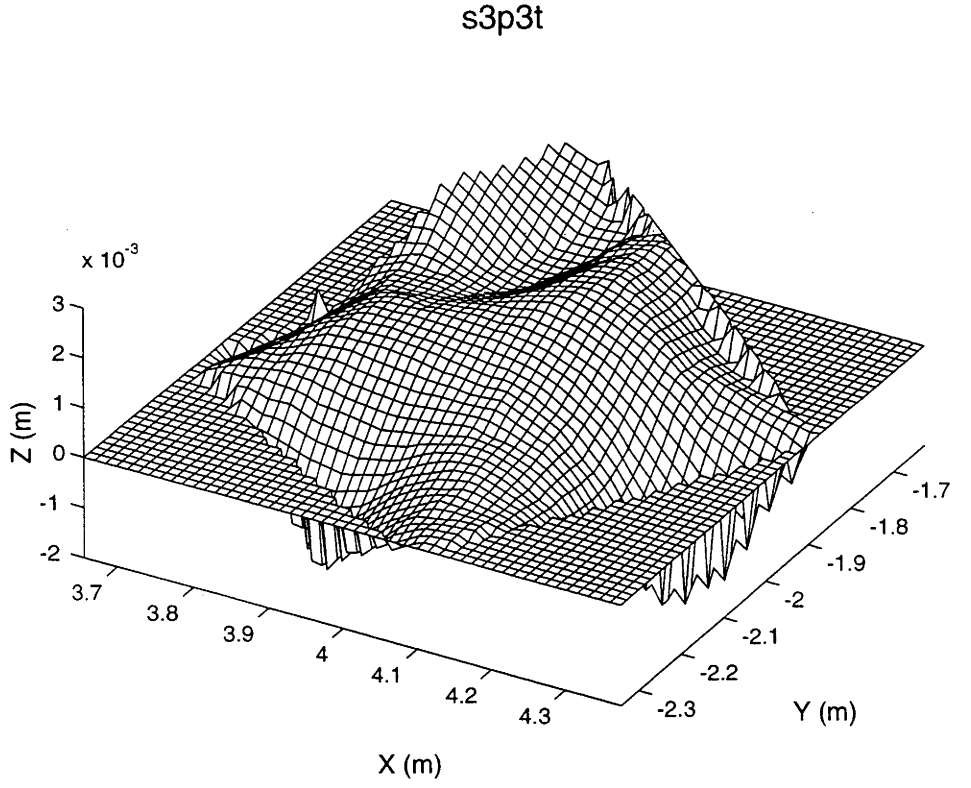

Figure A5.4.5. Z-coordinate deviation surface for s3p3t (60 cm) mirror tile. Deviations calculated as (measured-ideal).

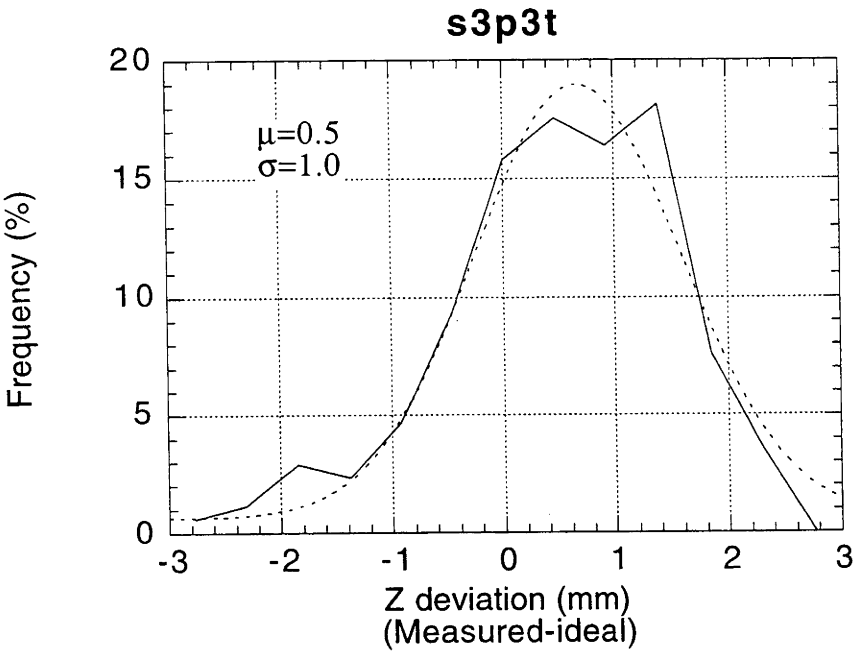

Figure A5.4.6. Frequency distribution of z-coordinate deviations for the s3p3t (60 cm) mirror tile shown in Figure A5.4.5.

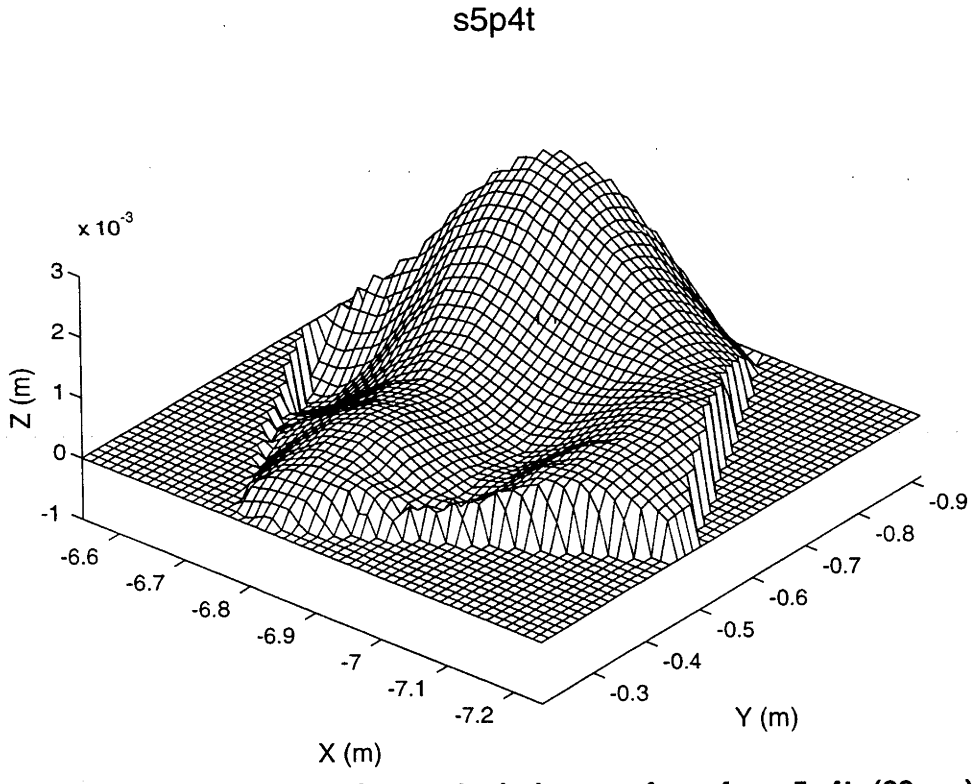

Figure A5.4.7. Z-coordinate deviation surface for s5p4t (60 cm) mirror tile. Deviations calculated as (measured-ideal).

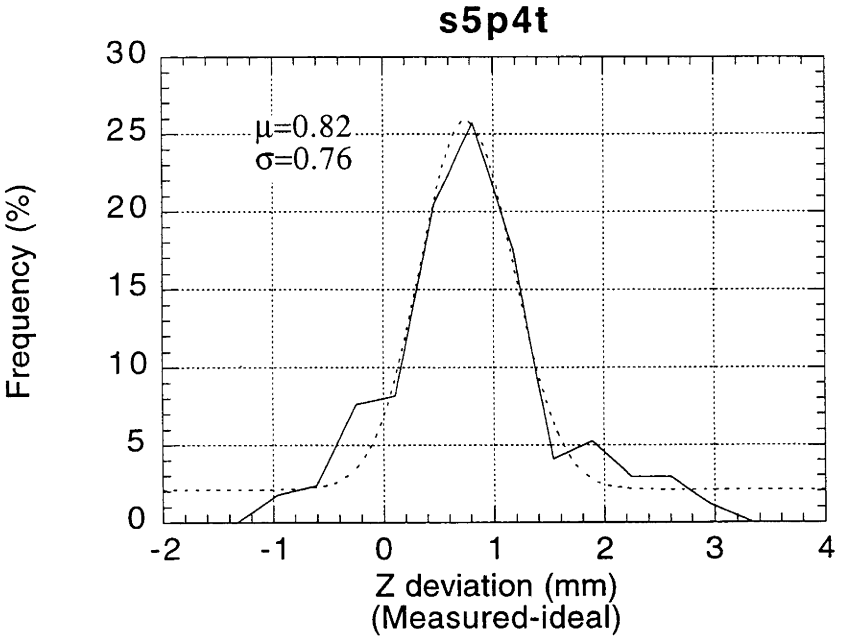

Figure A5.4.8. Frequency distribution of z-coordinate deviations for the s5p4t (60 cm) mirror tile shown in Figure A5.4.7.

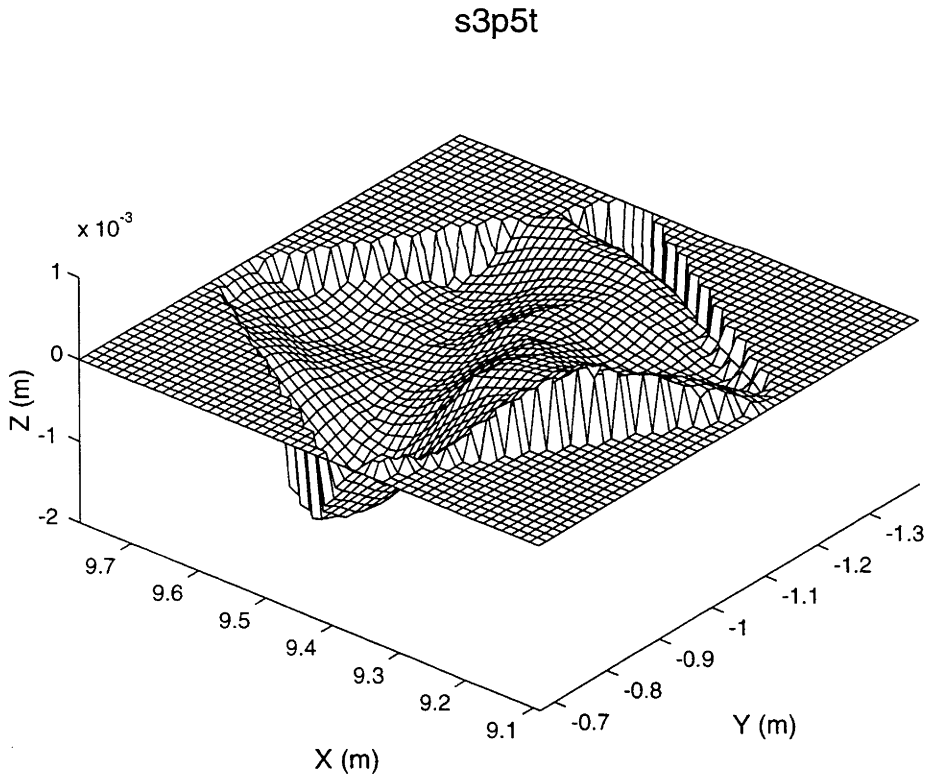

Figure A5.4.9. Z-coordinate deviation surface for s3p5t (60 cm) mirror tile. Deviations calculated as (measured-ideal).

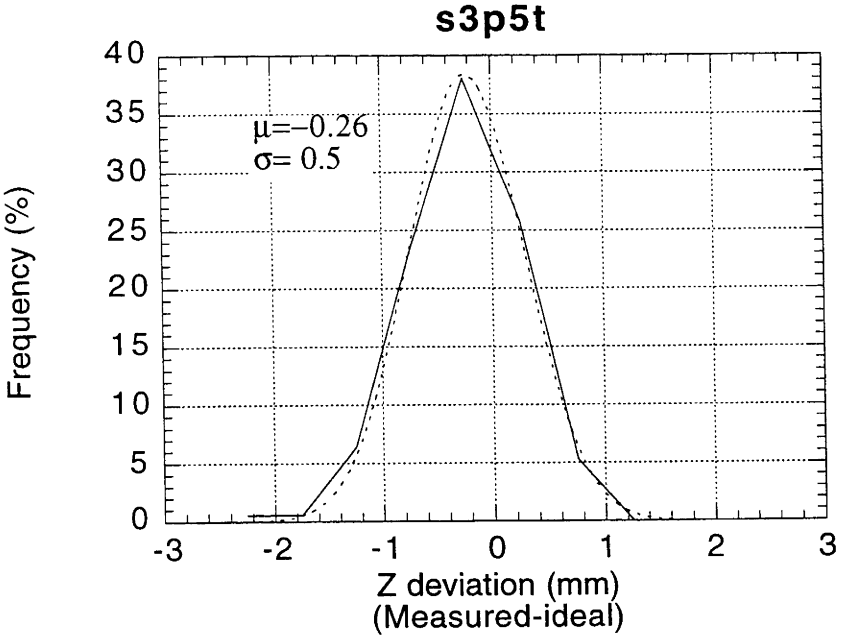

Figure A5.4.10. Frequency distribution of z-coordinate deviations for the s3p5t (60 cm) mirror tile shown in Figure A5.4.9.

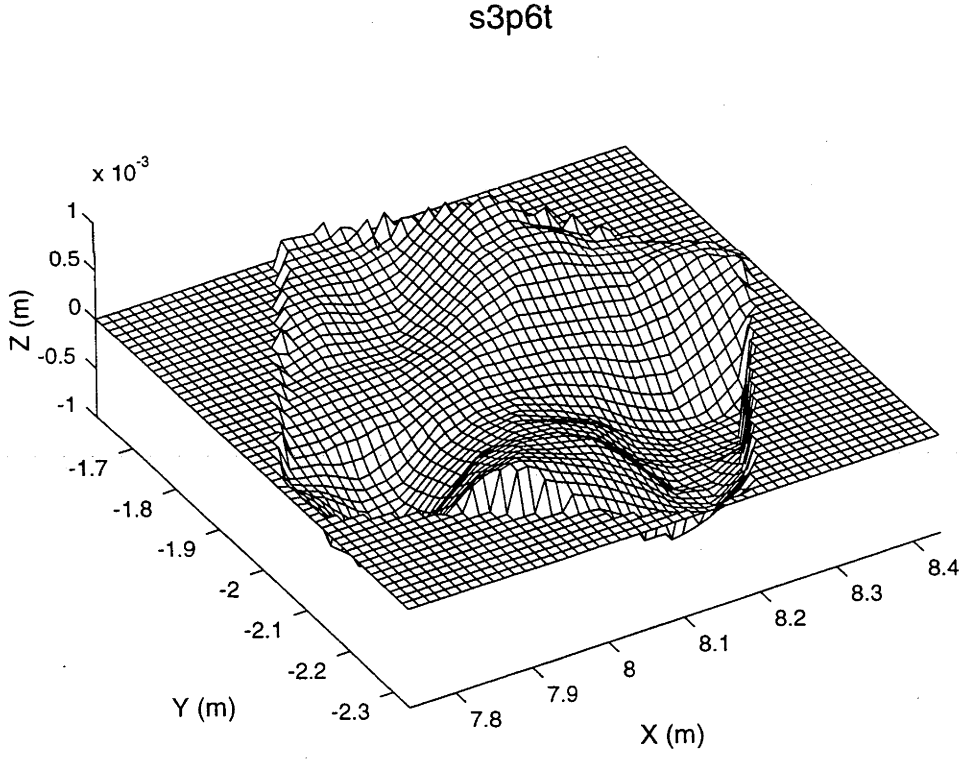

Figure A5.4.11. Z-coordinate deviation surface for s3p6t (60 cm) mirror tile. Deviations calculated as (measured-ideal).

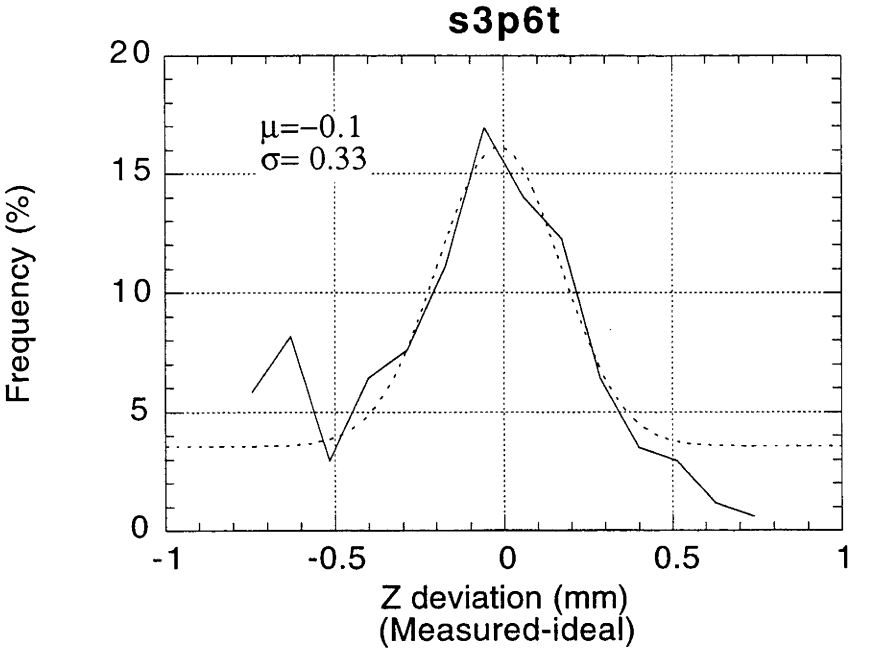

Figure A5.4.12. Frequency distribution of z-coordinate deviations for the s3p6t (60 cm) mirror tile shown in Figure A5.4.11.

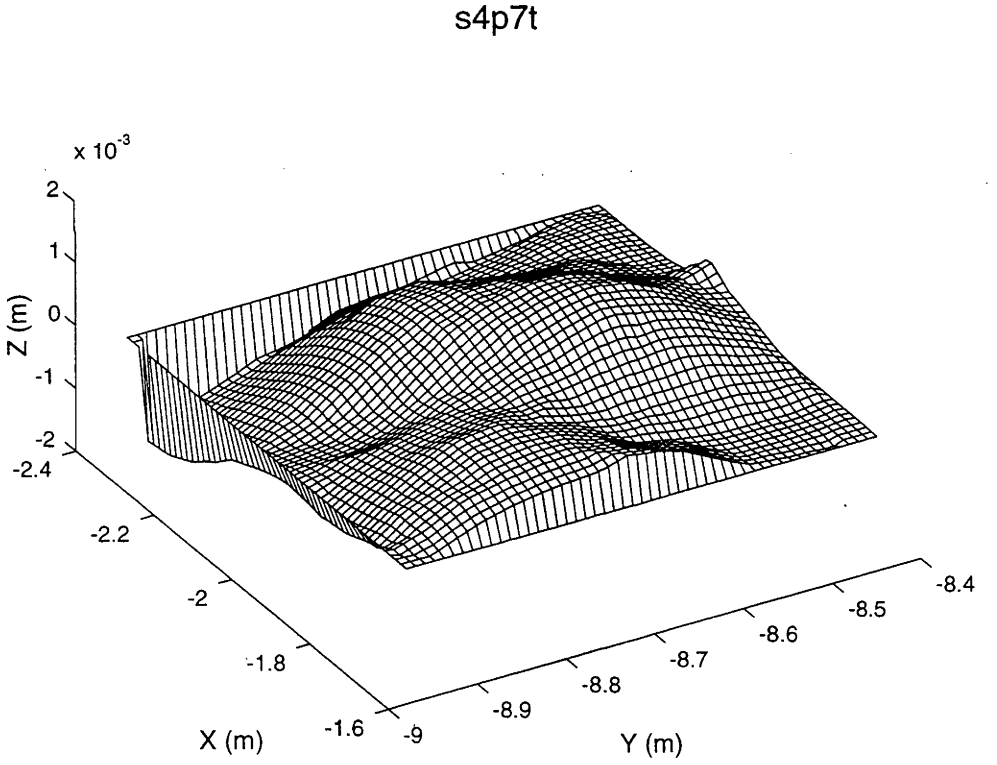

Figure A5.4.13. Z-coordinate deviation surface for s4p7t (60 cm) mirror tile. Deviations calculated as (measured-ideal).

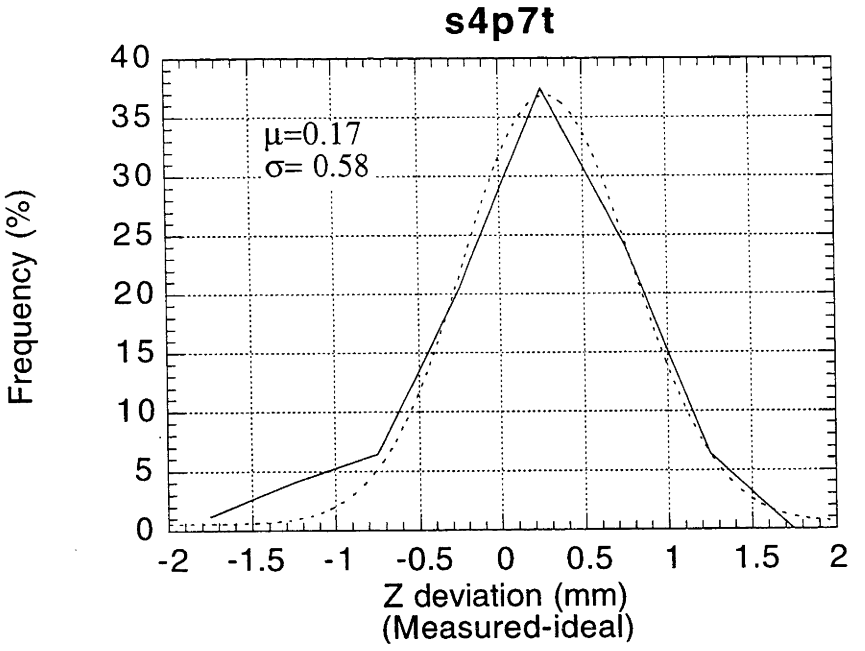

Figure A5.4.14. Frequency distribution of z-coordinate deviations for the s4p7t (60 cm) mirror tile shown in Figure A5.4.13.

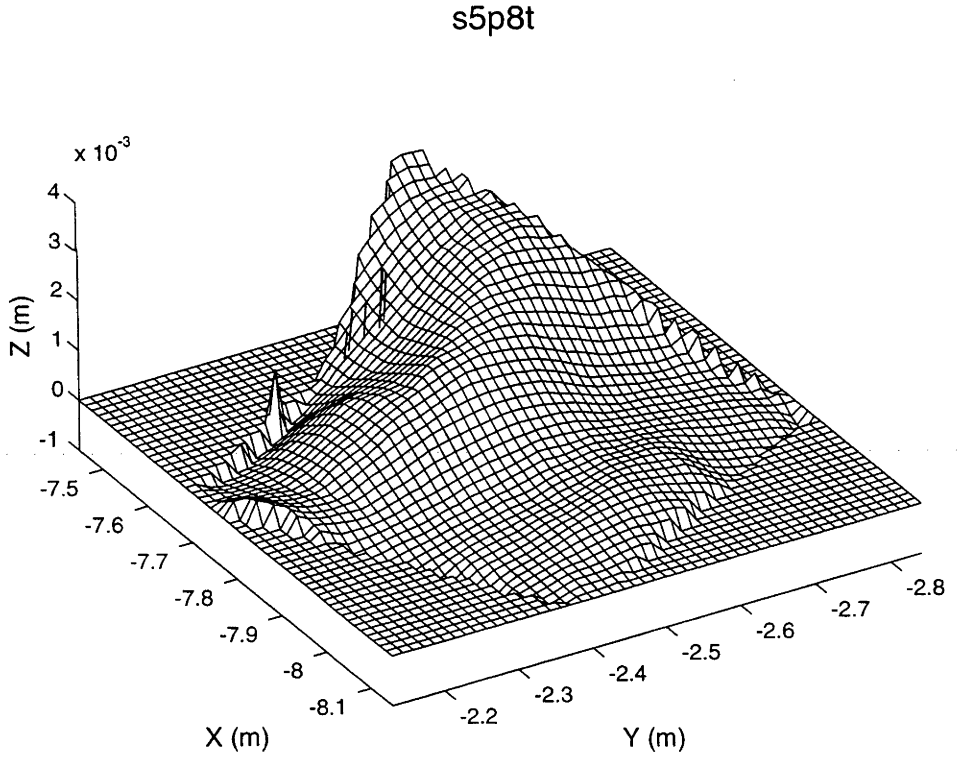

Figure A5.4.15. Z-coordinate deviation surface for s5p8t (60 cm) mirror tile. Deviations calculated as (measured-ideal).

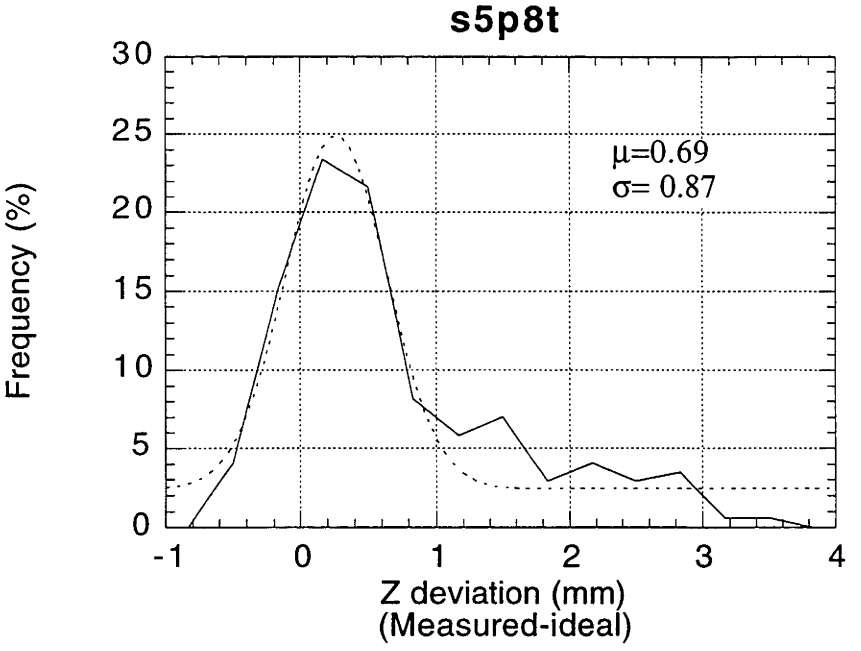

Figure A5.4.16. Frequency distribution of z-coordinate deviations for the s5p8t (60 cm) mirror tile shown in Figure A5.4.15.

Appendix 6.1. Fourier spectra for mirror tile z-coordinate deviations

Figure A6.1.1 to Figure A6.1.8 show the x and y spatial spectral components of the z-coordinate deviations measured on the 400 m^2 dish mirror tiles. These were obtained by performing a 2-dimensional fast Fourier transform (FFT) on the z-coordinate deviations of the mirror tiles. The FFT produces an amplitude versus frequency surface, but it was found that the dominant components of the spectra occurred along the two dimensional axes of the plots, and it is these components that have been plotted against frequency in the following figures. The figures also contain a 0.2 milliradian error cut-off curve, which defines the points where the expected uncertainty in slope errors calculated by GRADFITTER will exceed 0.2 milliradian. These points are evident in most of the plots at spatial frequencies of approximately 5.5 m^{-1}.

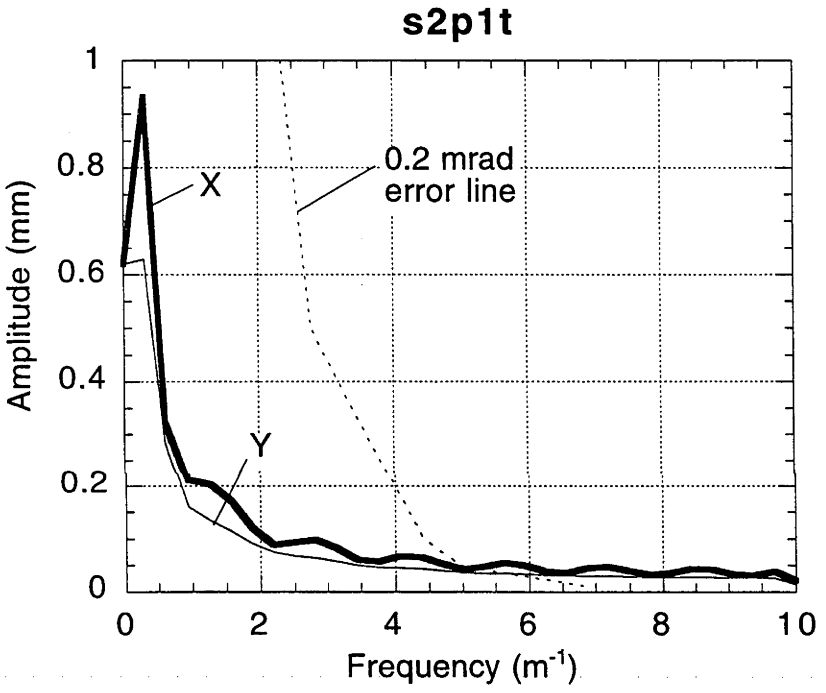

Figure A6.1.1. Fourier spectrum plot of the x and y frequency amplitudes for the z-coordinate deviations of the s2p1t (30 cm) mirror tile.

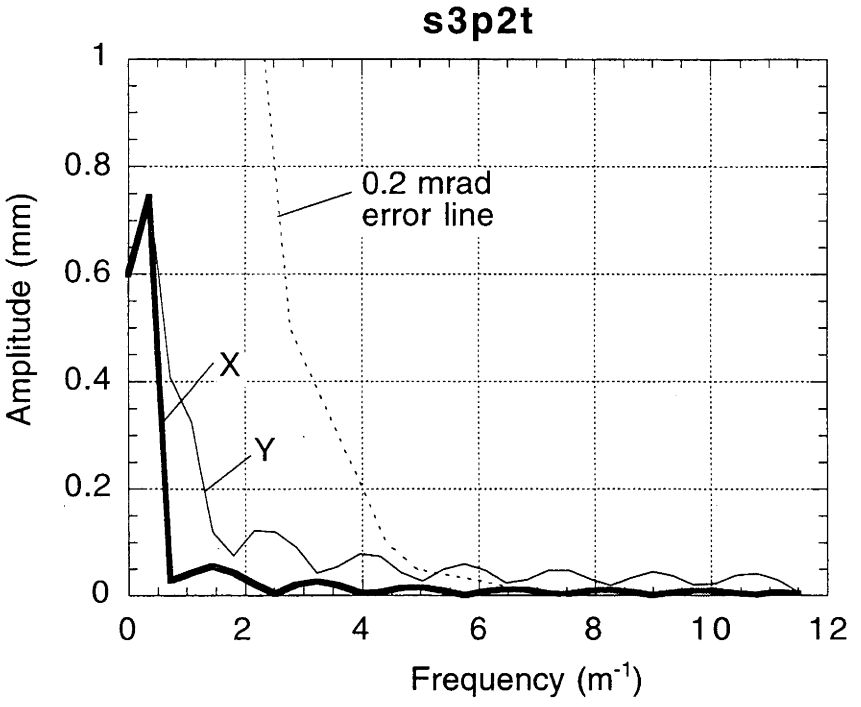

Figure A6.1.2. Fourier spectrum plot of the x and y frequency amplitudes for the z-coordinate deviations of the s3p2t (60 cm) mirror tile.

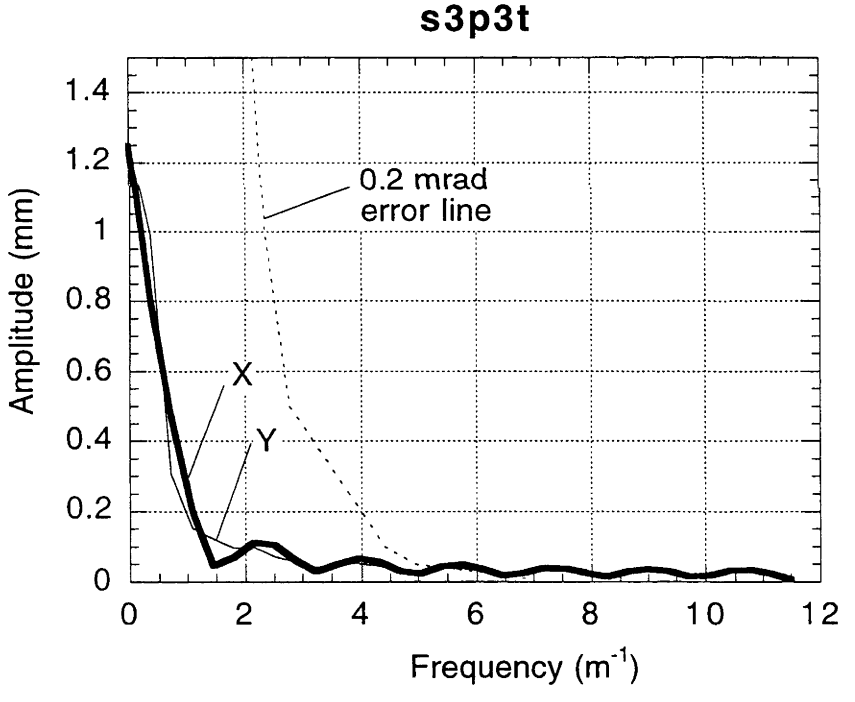

Figure A6.1.3. Fourier spectrum plot of the x and y frequency amplitudes for the z-coordinate deviations of the s3p3t (60 cm) mirror tile.

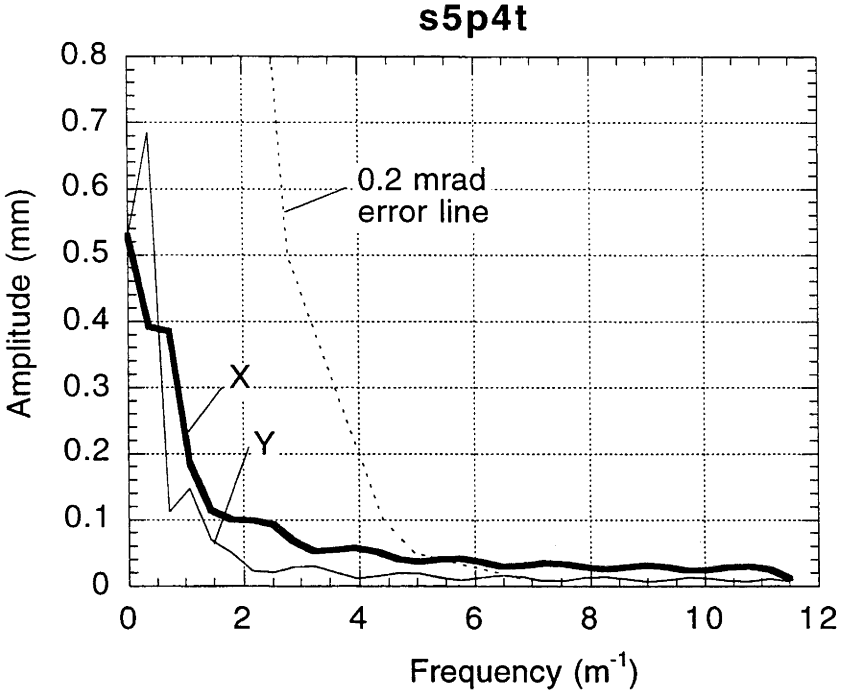

Figure A6.1.4. Fourier spectrum plot of the x and y frequency amplitudes for the z-coordinate deviations of the s5p4t (60 cm) mirror tile.

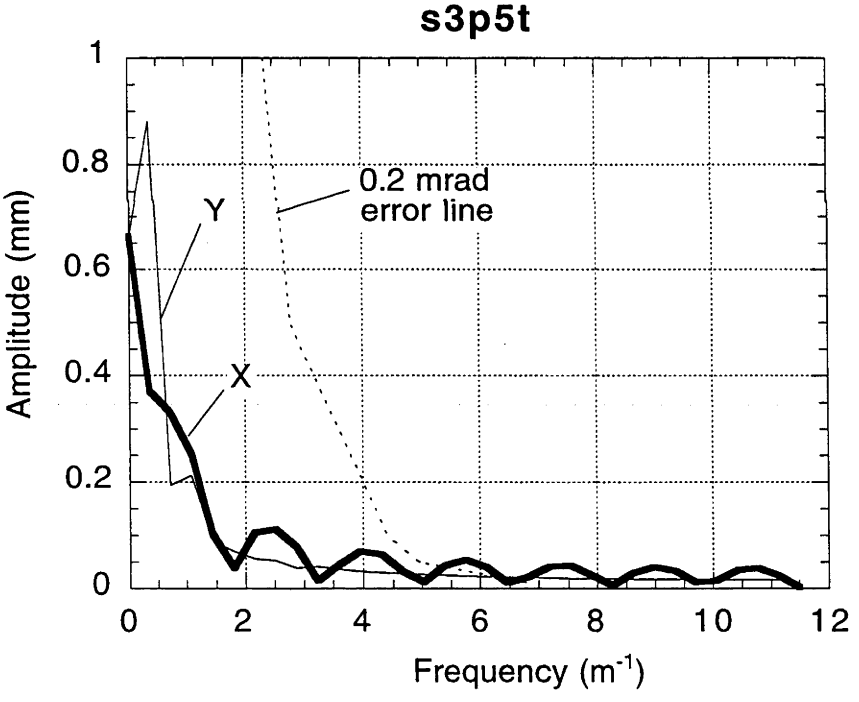

Figure A6.1.5. Fourier spectrum plot of the x and y frequency amplitudes for the z-coordinate deviations of the s3p5t (60 cm) mirror tile.

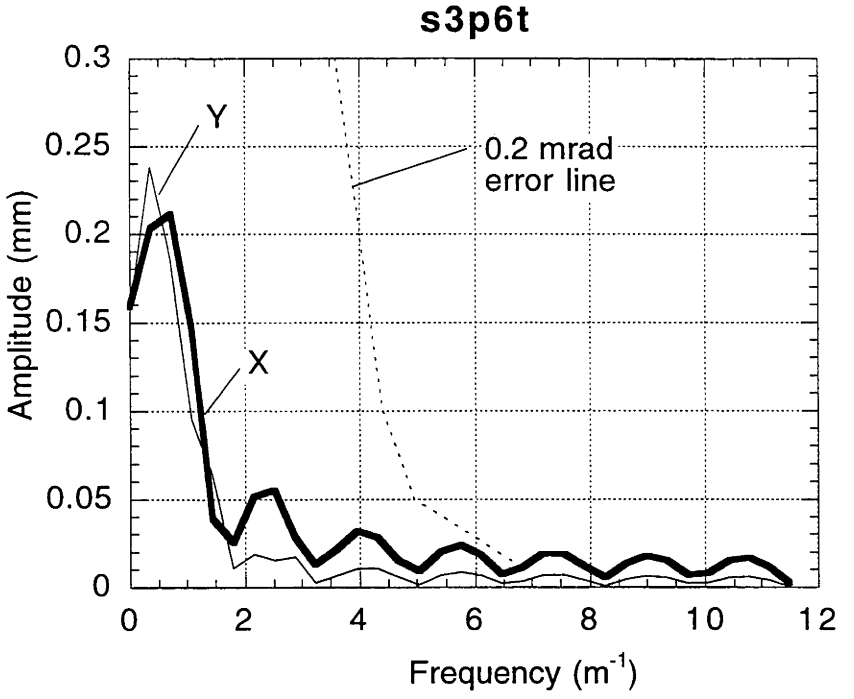

Figure A6.1.6. Fourier spectrum plot of the x and y frequency amplitudes for the z-coordinate deviations of the s3p6t (60 cm) mirror tile.

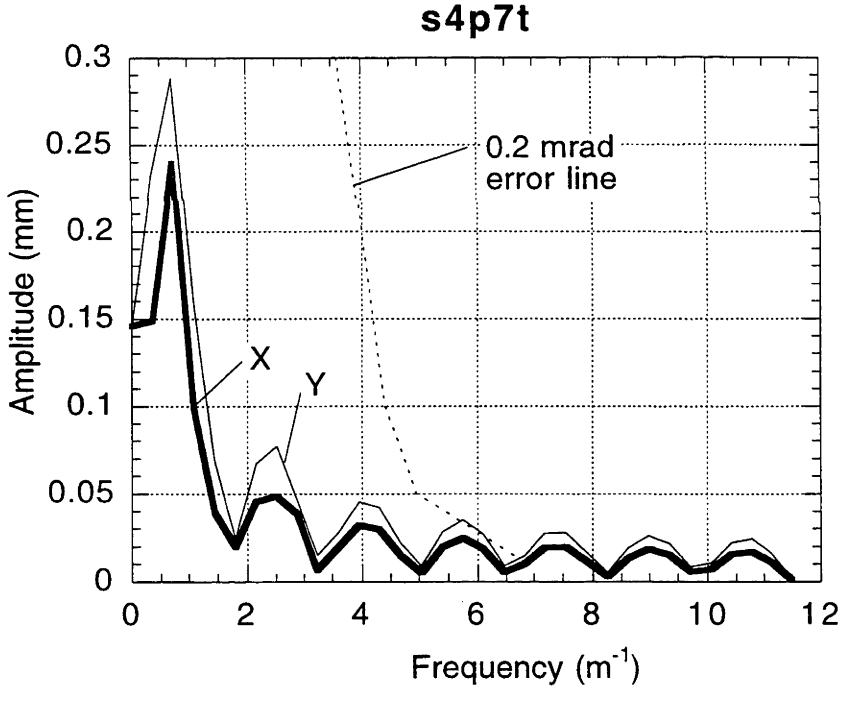

Figure A6.1.7. Fourier spectrum plot of the x and y frequency amplitudes for the z-coordinate deviations of the s4p7t (60 cm) mirror tile.

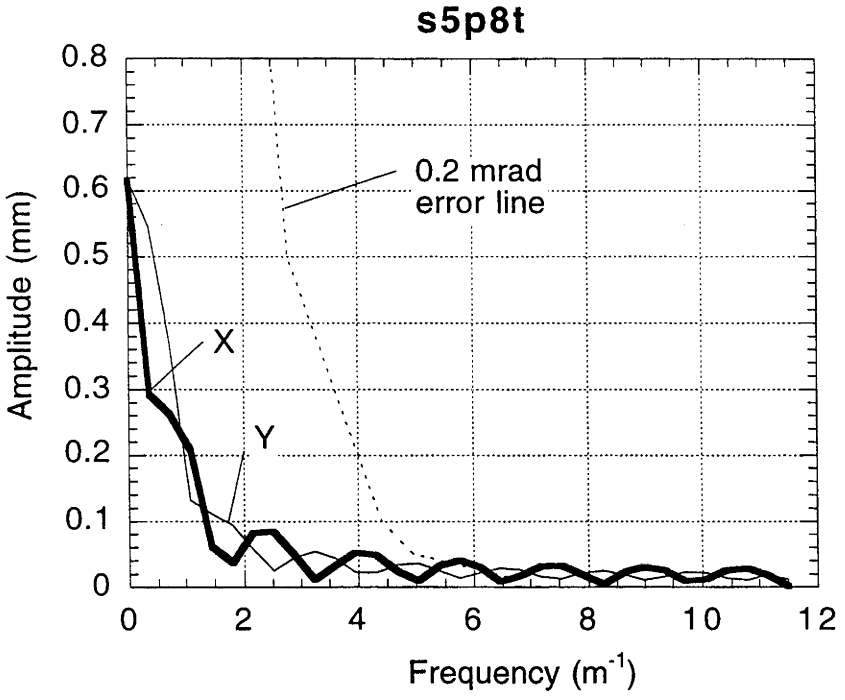

Figure A6.1.8. Fourier spectrum plot of the x and y frequency amplitudes for the z-coordinate deviations of the s5p8t (60 cm) mirror tile.

Appendix 6.2. Spatial distribution of surface slope errors across the surface of the 400 m^2 dish mirror tiles.

Figure A6.2.1 to Figure A6.2.8 show the spatial distribution of surface slope errors across the surfaces of the mirror tiles measured photogrammetrically on the 400 m^2 dish surface. Surface slope error is measured as the magnitude of the deviation vector between the ideal (paraboloidal) surface normal and the numerically calculated surface normal for the measured surface. The ideal normal is calculated for a paraboloidal surface having a 13.075 m focal length.

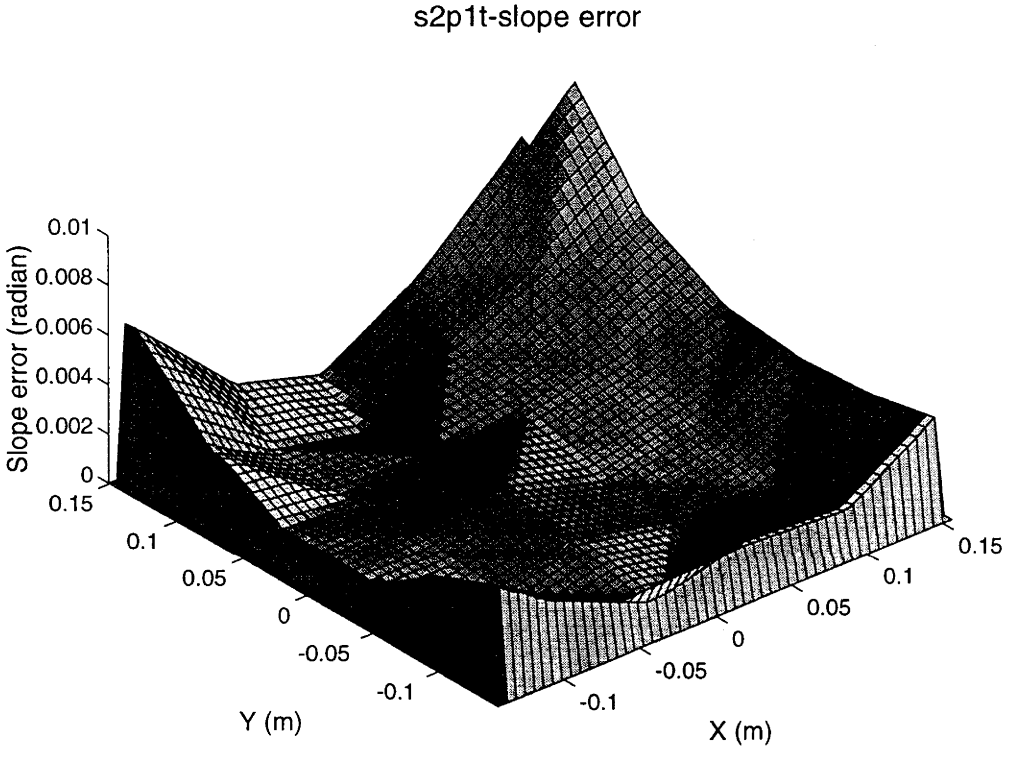

Figure A6.2.1. Distribution of slope errors across the s2p1t (30 cm) tile.

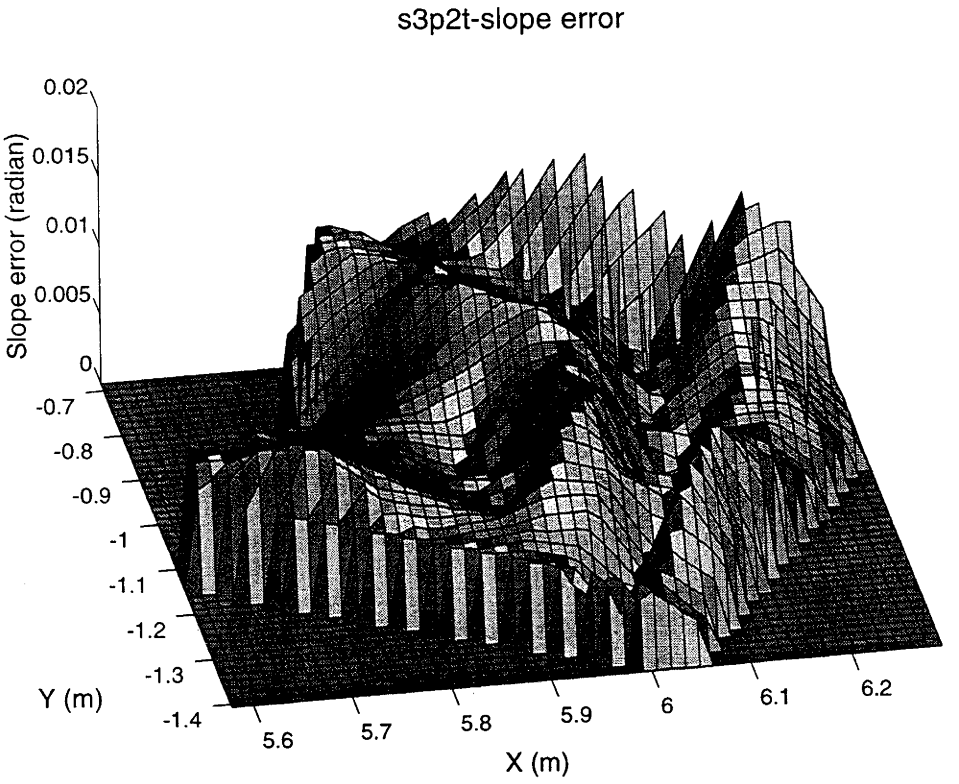

Figure A6.2.2. Distribution of slope errors across the s3p2t (60 cm) tile.

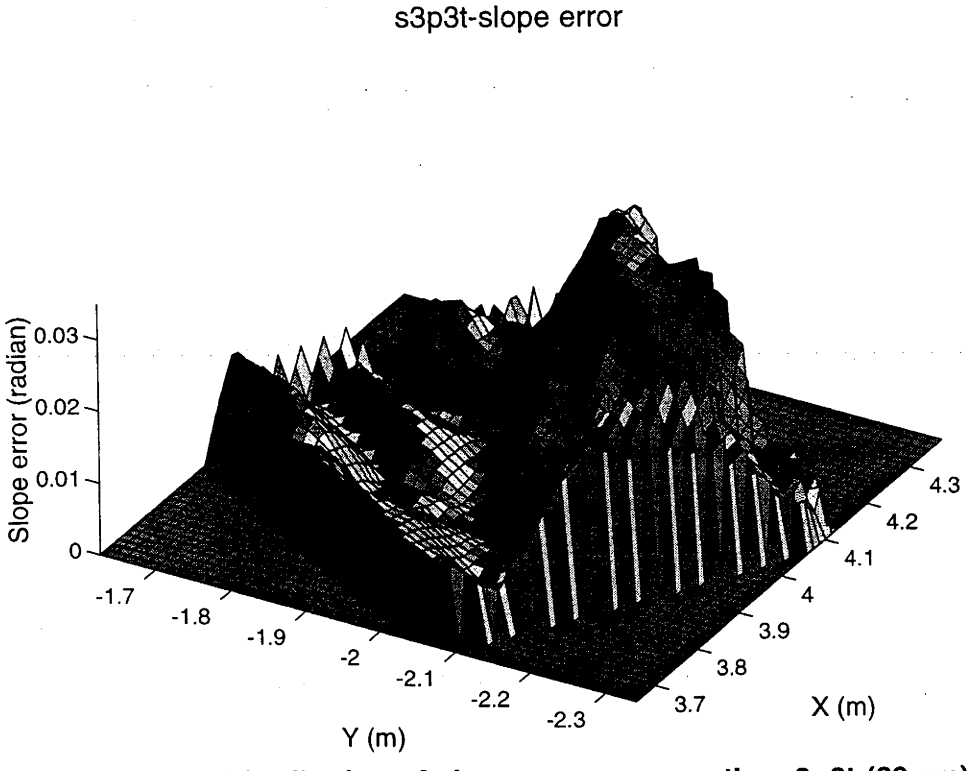

Figure A6.2.3. Distribution of slope errors across the s3p3t (60 cm) tile.

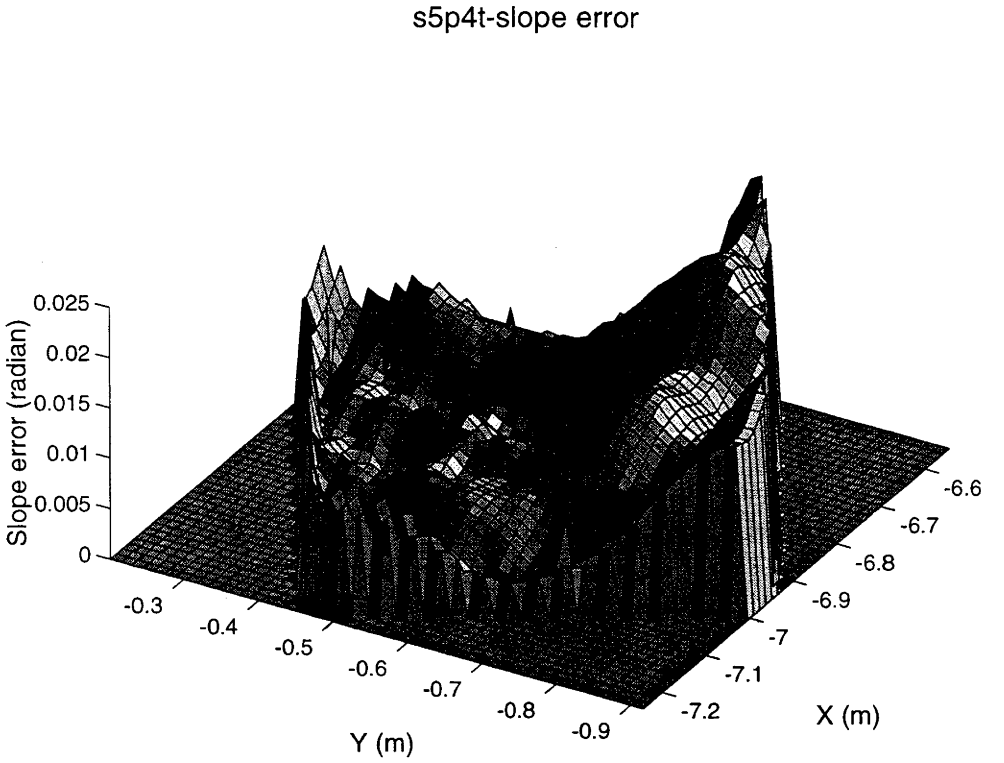

Figure A6.2.4. Distribution of slope errors across the s5p4t (60 cm) tile.

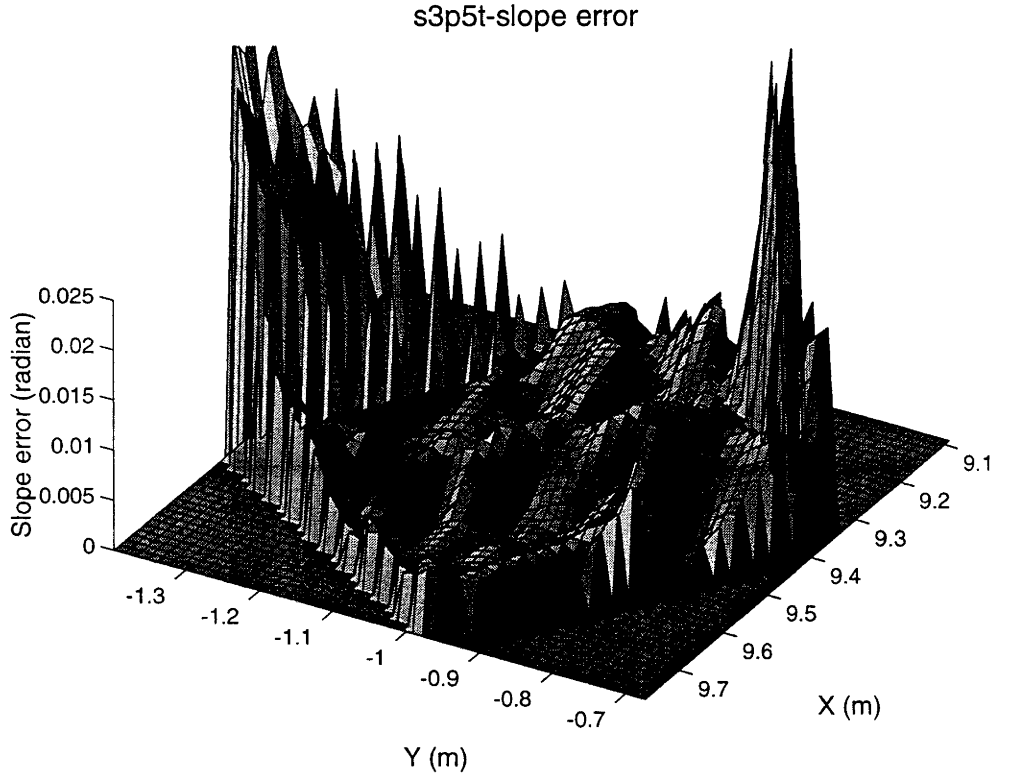

Figure A6.2.5. Distribution of slope errors across the s3p5t (60 cm) tile.

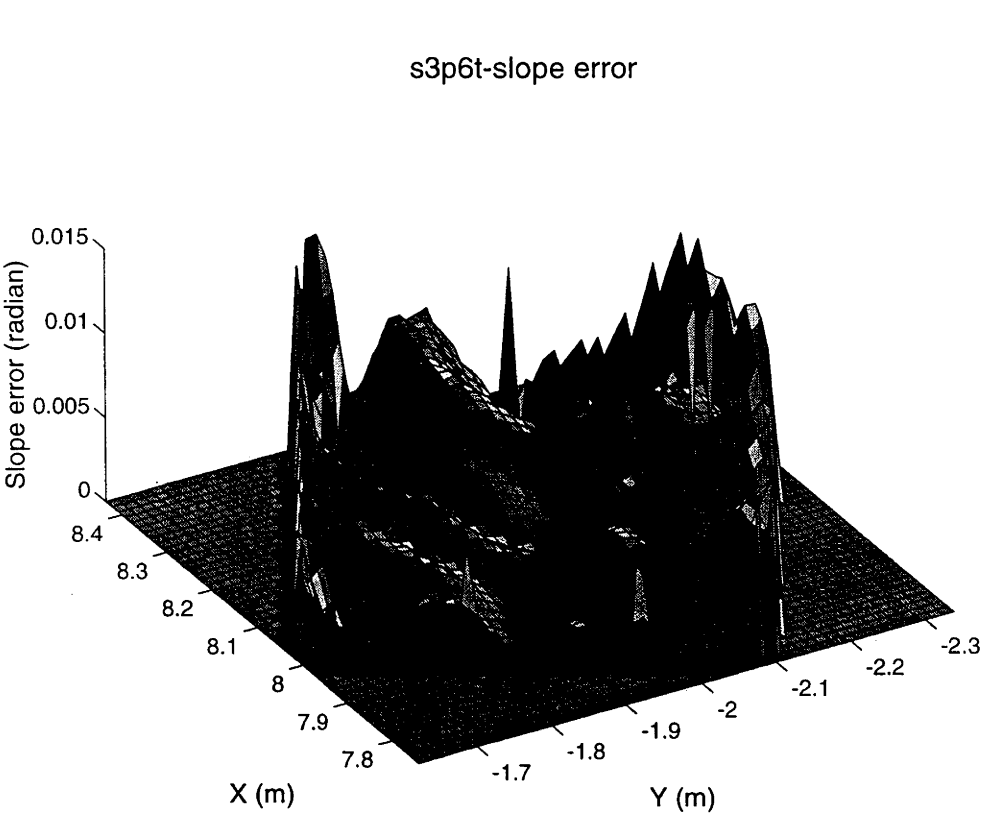

Figure A6.2.6. Distribution of slope errors across the s3p6t (60 cm) tile.

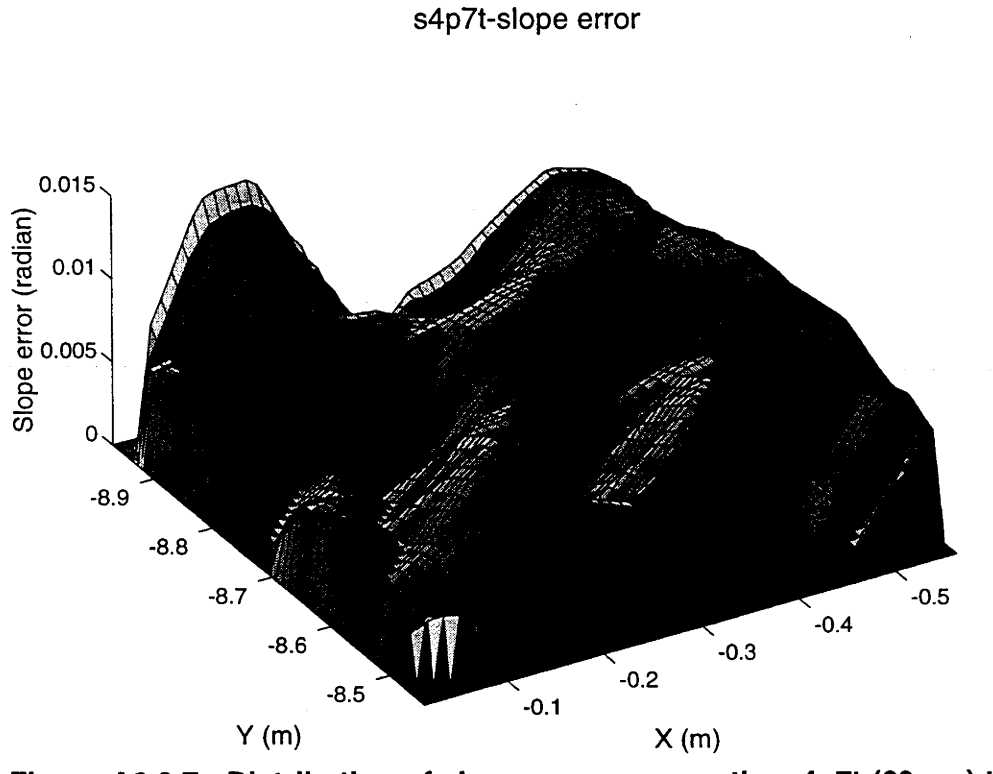

Figure A6.2.7. Distribution of slope errors across the s4p7t (60 cm) tile.

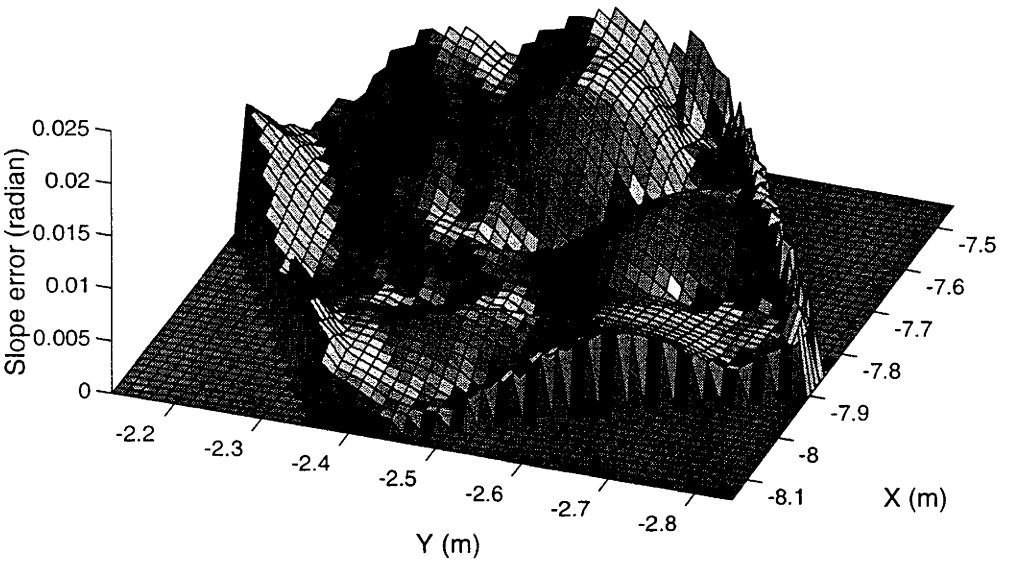

Figure A6.2.8. Distribution of slope errors across the s5p8t (60 cm) tile.

It can be seen that the slope errors for most tiles have a greater magnitude around the tile perimeters. This can be an artifact of the numerical fitting process, and will be prone to some inaccuracy in these regions. However, these 'edge errors' constitute a relatively small component of the overall surface slope error, and will not have a dominant influence on the standard deviation of the bivariate Gaussian distribution of errors that can be assumed to exist for the distribution of surface slope errors.

Appendix 6.3. Surface slope error distributions for mirror tiles on the 400 m^2 dish

Figure A6.3.1 to Figure A6.3.8 show the frequency distribution plots for the eight measured mirror tiles on the surface of the 400 m^2 dish. These plots show the distribution of errors for the tiles oriented to ideal paraboloidal coordinates. As such they show the errors due to the tile surfaces only, without additional errors that would be introduced if the tiles were oriented to the measured coordinates on their respective mirror panels.

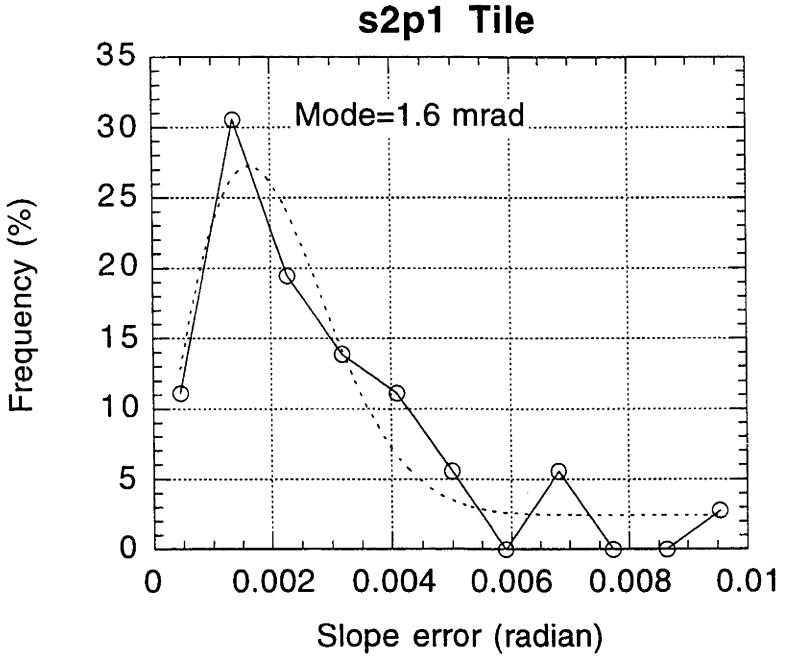

Figure A6.3.1. Frequency distribution of surface slope errors on the s2p1t (30 cm) mirror tile.

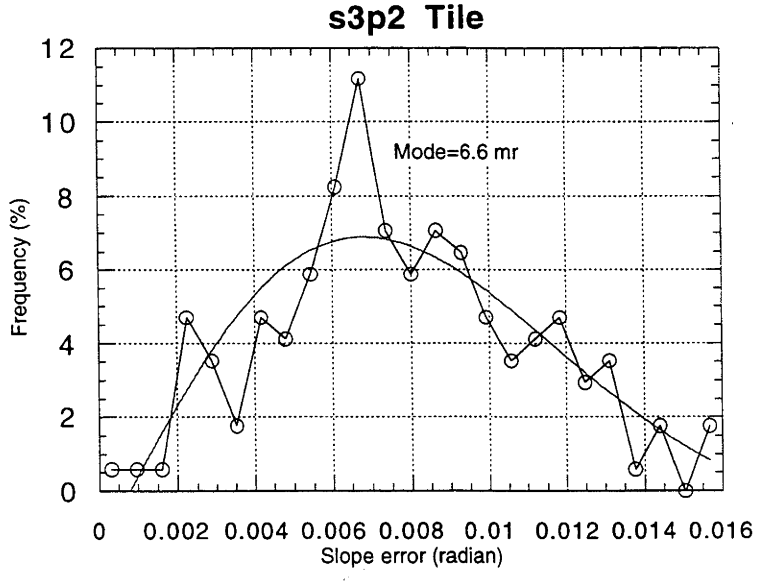

Figure A6.3.2. Frequency distribution of surface slope errors on the s3p2t (60 cm) mirror tile.

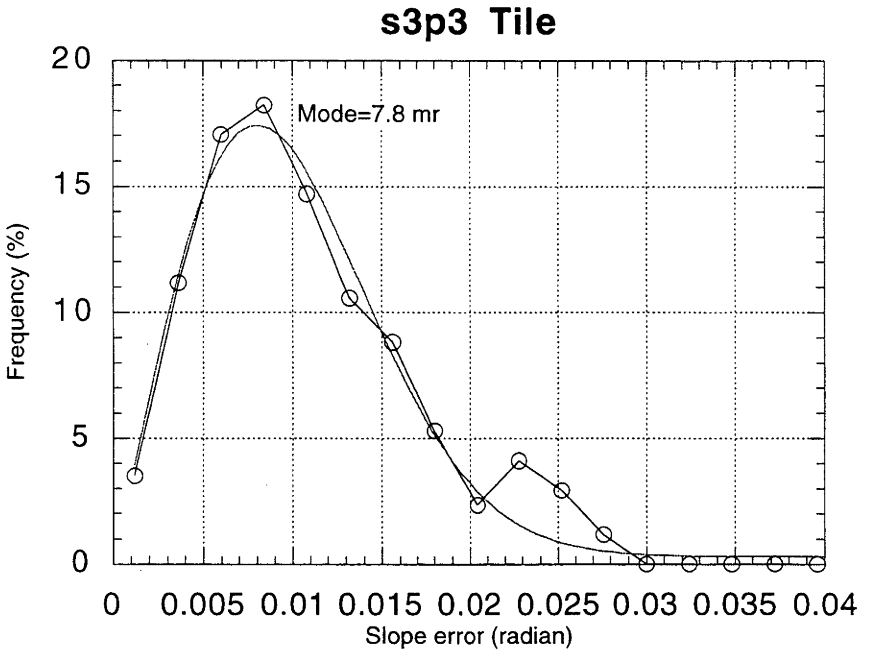

Figure A6.3.3. Frequency distribution of surface slope errors on the s3p3t (60 cm) mirror tile.

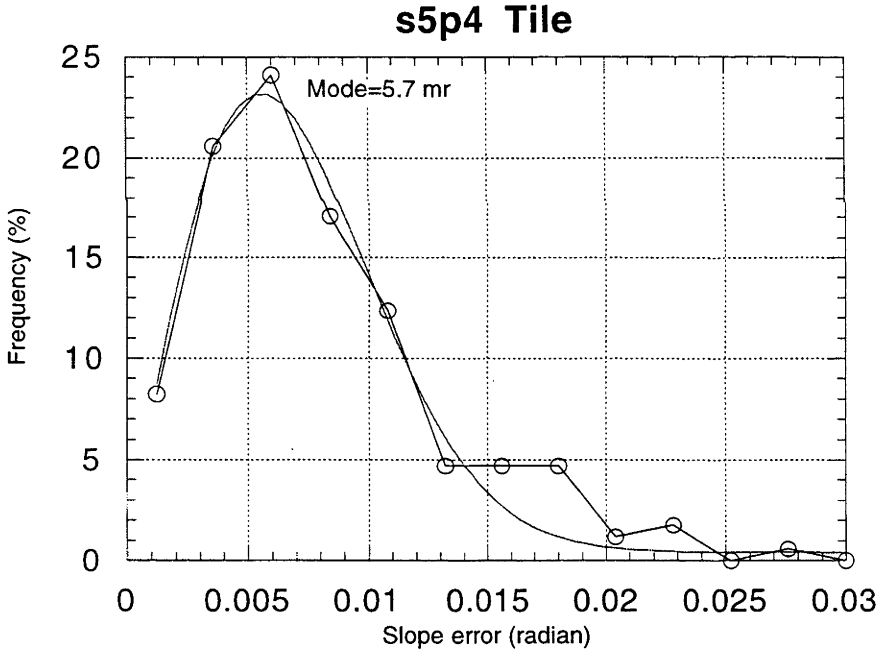

Figure A6.3. 4. Frequency distribution of surface slope errors on the s5p4t (60 cm) mirror tile.

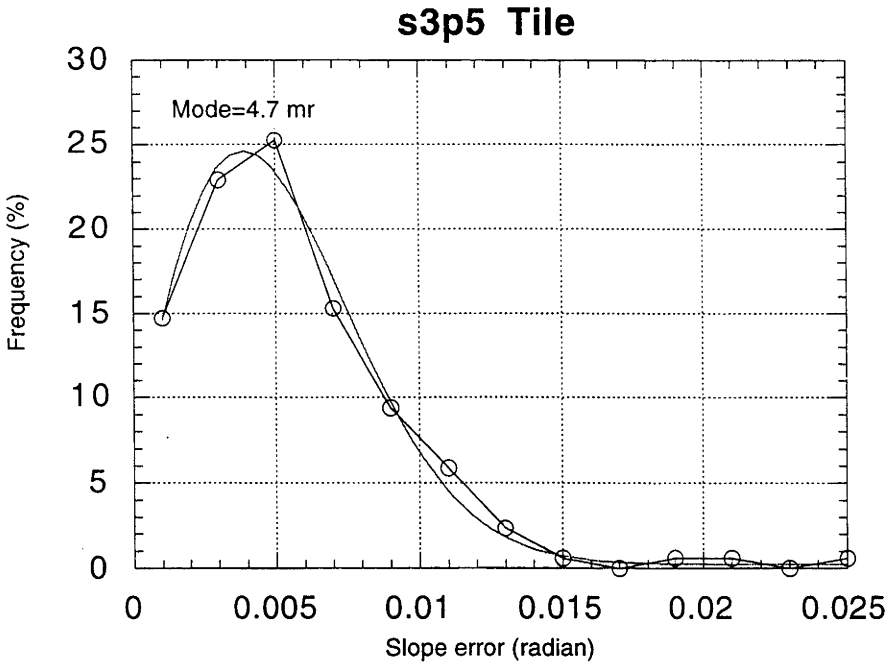

Figure A6.3.5. Frequency distribution of surface slope errors on the s3p5t (60 cm) mirror tile.

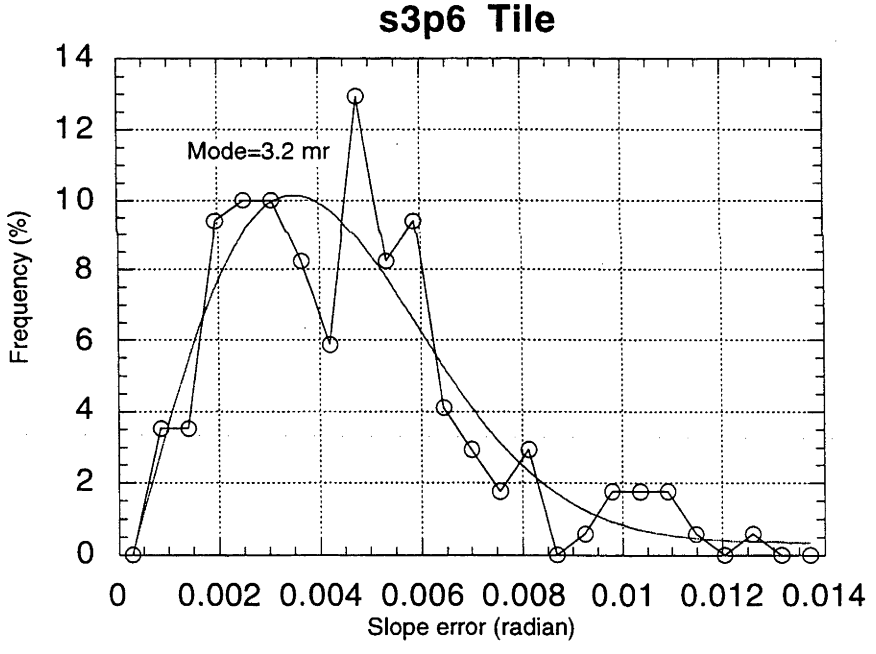

Figure A6.3.6. Frequency distribution of surface slope errors on the s3p6t (60 cm) mirror tile.

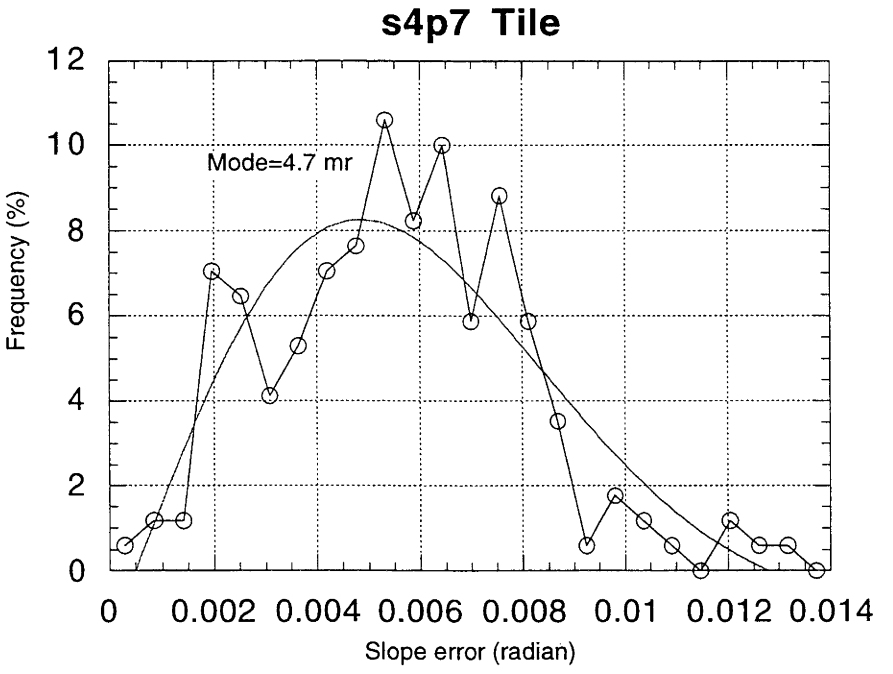

Figure A6.3.7. Frequency distribution of surface slope errors on the s4p7t (60 cm) mirror tile.

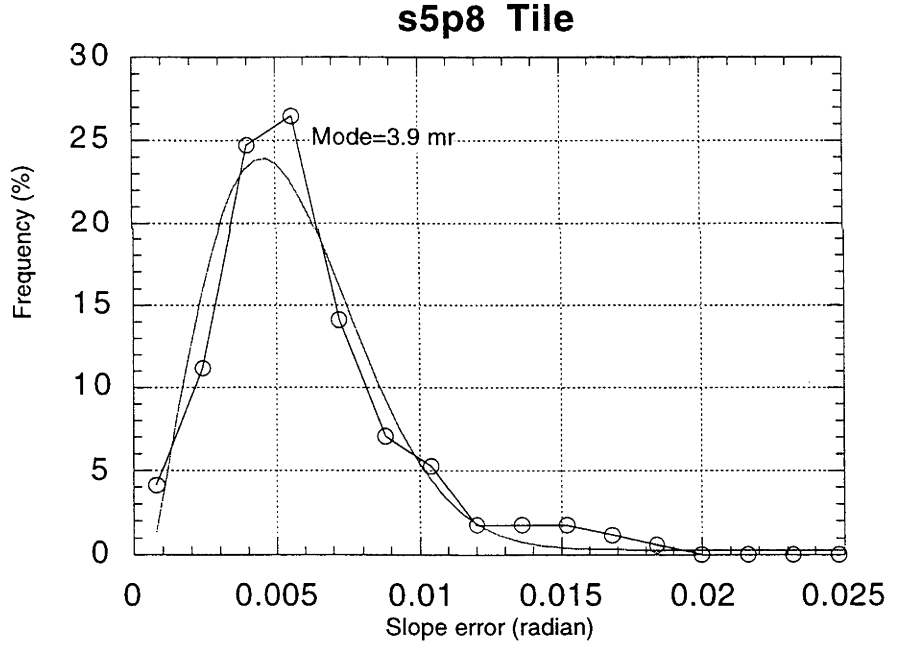

Figure A6.3.8. Frequency distribution of surface slope errors on the s5p8t (60 cm) mirror tile.

Appendix 6.4. Frequency distribution of surface slope errors for mirror panels (s2p1 to s5p8) sans mirror tiles.

Figure A6.4.1 to Figure A6.4.8 show the frequency distributions of surface slope errors calculated for the s2p1 to s5p8 mirror panels, without mirror tiles on their surfaces. The panels were oriented into the measured vertex positions on the 400 m^2 dish surface, and the surface slope errors calculated for these positions. As noted in the text, it can be seen that the panels exhibit relatively high slope error standard deviations, which is attributable to the poor data point regularity and frequency of the surfaces. This fact could also be the most likely cause of some distributions displaying poor approximations to the expected Rayleigh distribution, although it should not be discounted that these surfaces could indeed contain error distributions that do not conform to a circular, bivariate Gaussian distribution of slope errors.

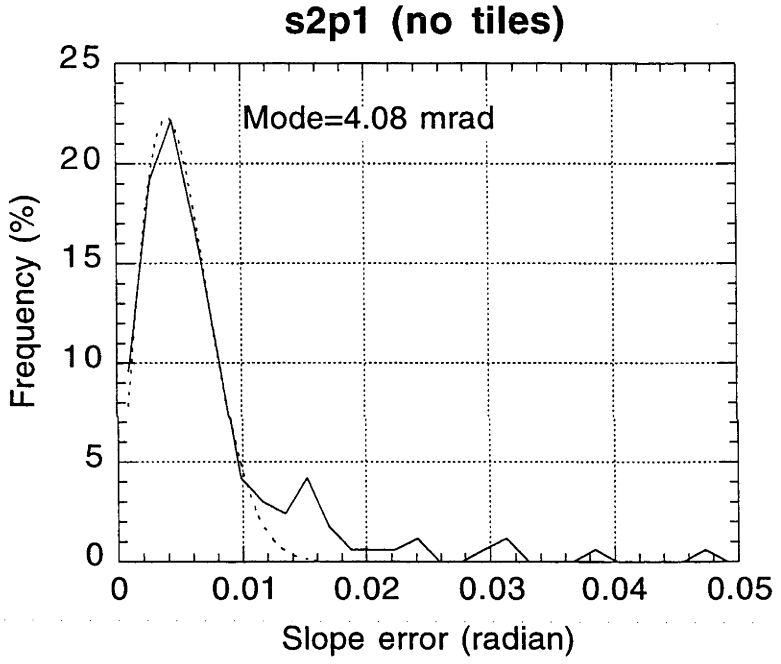

Figure A6.4.1. Frequency distribution of surface slope errors across the s2p1 mirror panel sans mirror tiles. Dashed line shows the bets-fit Rayleigh distribution to the data, with the mode calculated from this best-fit function.

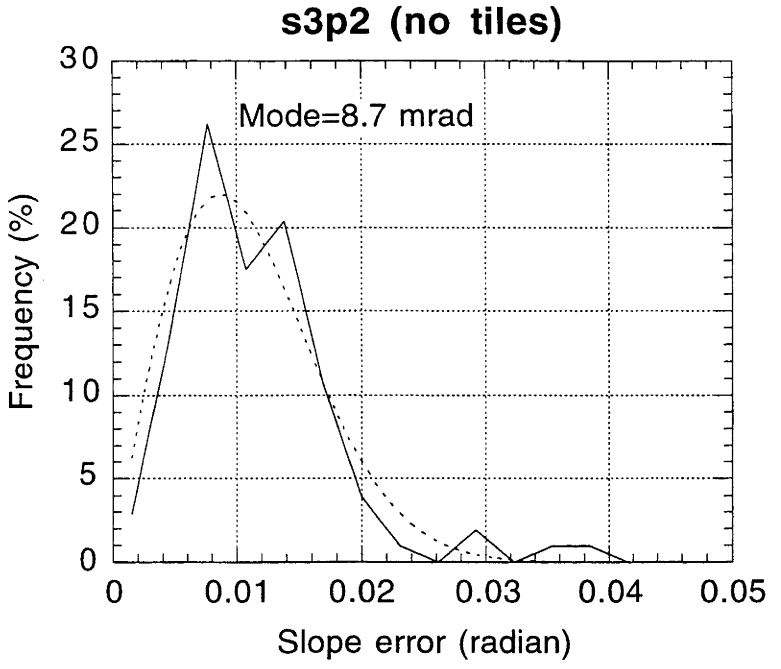

Figure A6.4.2. Frequency distribution of surface slope errors across the s3p2 mirror panel sans mirror tiles. Dashed line shows the bets-fit Rayleigh distribution to the data, with the mode calculated from this best-fit function.

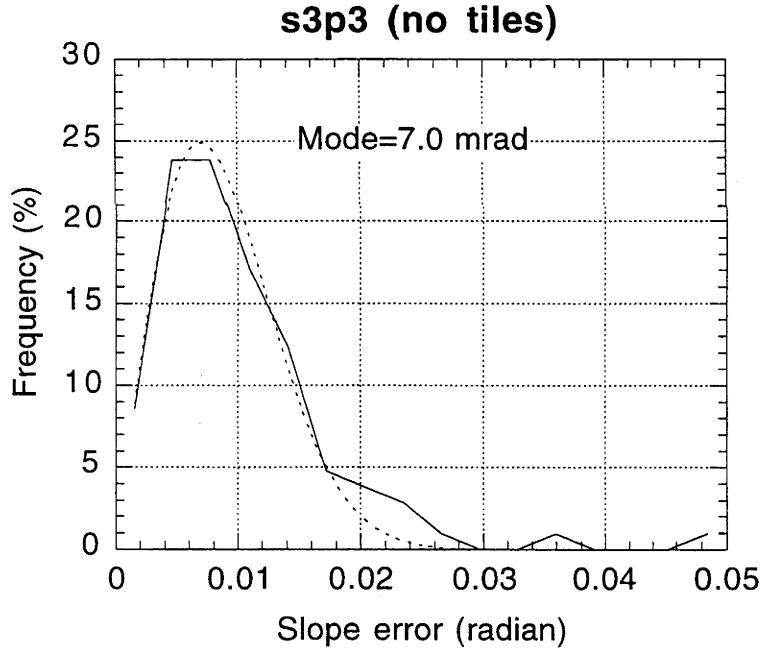

Figure A6.4.3. Frequency distribution of surface slope errors across the s3p3 mirror panel sans mirror tiles. Dashed line shows the bets-fit Rayleigh distribution to the data, with the mode calculated from this best-fit function.

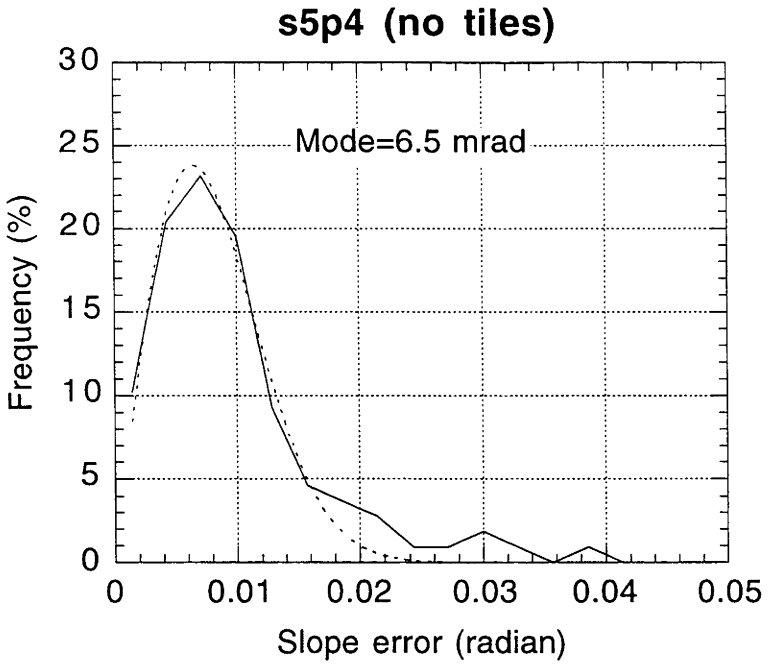

Figure A6.4.4. Frequency distribution of surface slope errors across the s5p4 mirror panel sans mirror tiles. Dashed line shows the bets-fit Rayleigh distribution to the data, with the mode calculated from this best-fit function.

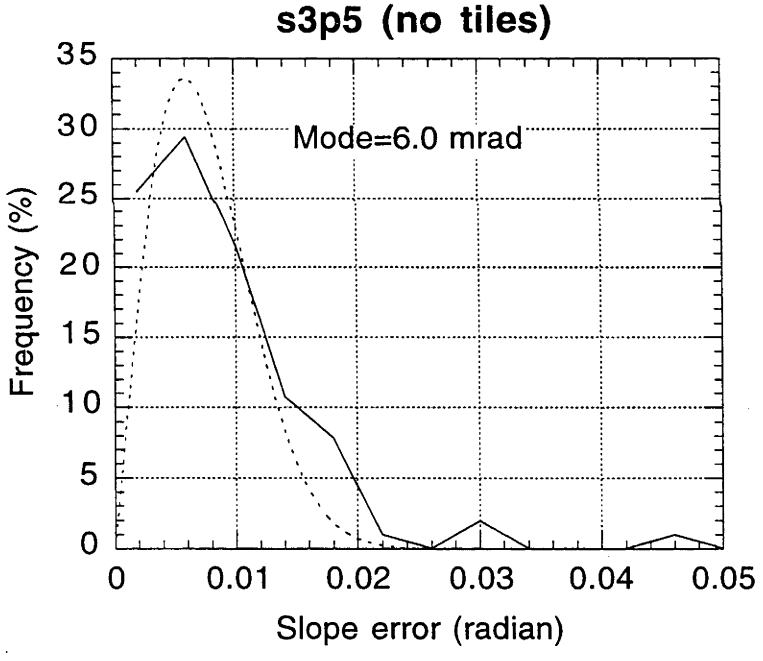

Figure A6.4.5. Frequency distribution of surface slope errors across the s3p5 mirror panel sans mirror tiles. Dashed line shows the bets-fit Rayleigh distribution to the data, with the mode calculated from this best-fit function.

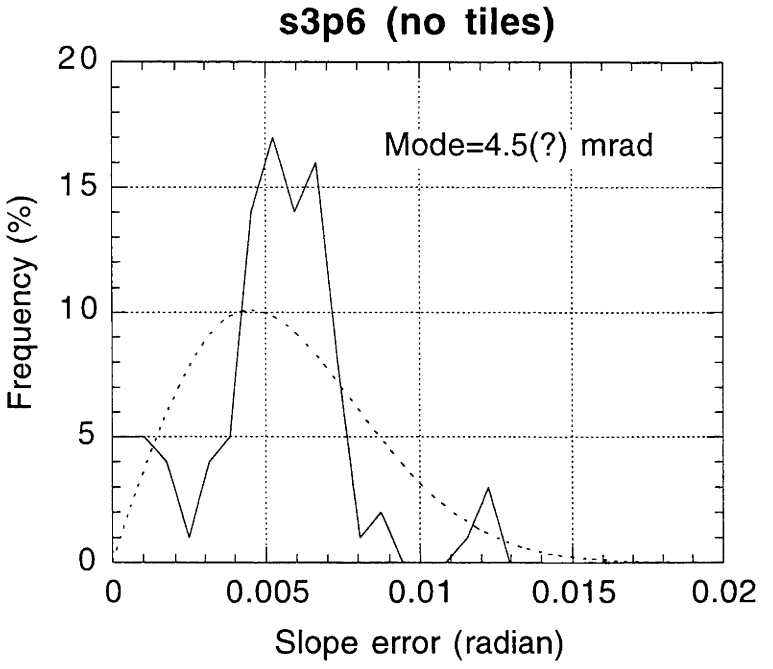

Figure A6.4.6. Frequency distribution of surface slope errors across the s3p6 mirror panel sans mirror tiles. Dashed line shows the bets-fit Rayleigh distribution to the data, with the mode calculated from this best-fit function.

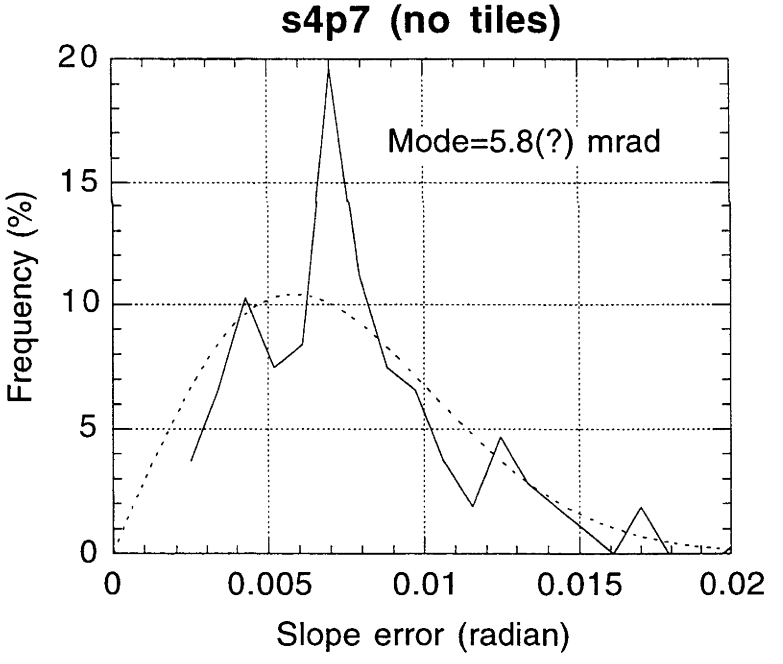

Figure A6.4.7. Frequency distribution of surface slope errors across the s4p7 mirror panel sans mirror tiles. Dashed line shows the bets-fit Rayleigh distribution to the data, with the mode calculated from this best-fit function.

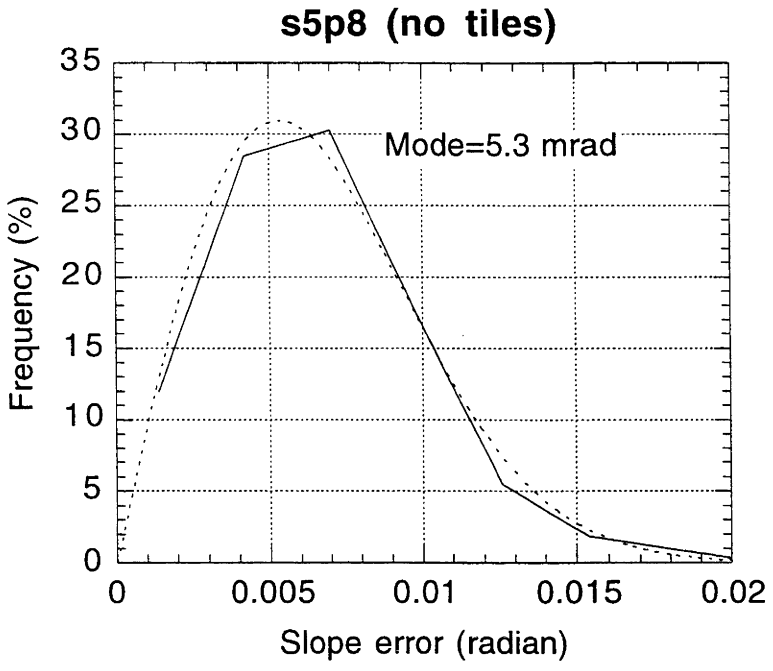

Figure A6.4.8. Frequency distribution of surface slope errors across the s5p8 mirror panel sans mirror tiles. Dashed line shows the best-fit Rayleigh distribution to the data, with the mode calculated from this best-fit function.

Appendix 6.5. Frequency distributions for surface slope errors on mirror covered with their respective mirror tiles.

Figure A6.5.1 to Figure A6.5.9 show the surface slope error frequency distributions for mirror panels s1p1 to s1p9 covered with mirror tiles. The 'assembly' of the panels was undertaken by first duplicating the mirror tile appropriate for that panel type (for example, s3p2t tiles would be duplicated across the s3p2 panel), and then reorienting the array of tiles on the panel into the measured coordinates of the panel's respective position on the dish surface.

Figure A6.5.9 shows the frequency distribution for the s1p9 mirror panel. As noted in the caption, the p9 panels were derived by reorienting the p5 type panels and tiles into the measured p9 coordinates on the dish surface. This was done because the p9 panel type was not measured photogrammetrically, and, by symmetry, the p5 panel type represents the closest approximation to the p9 panel type. Thus the p5 type was duplicated and used in the p9 positions to accommodate the missing data set.

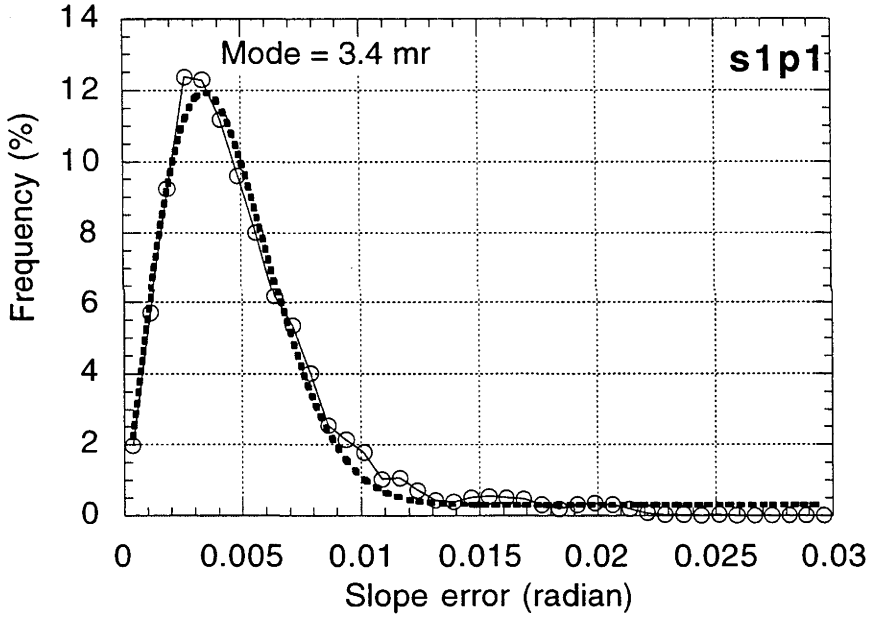

Figure A6.5.1. Frequency distribution of surface slope errors calculated for s2p1t mirror tiles (with normals) duplicated across the surface of the s2p1 mirror panel, with the panel oriented into the measured vertex coordinates for the s1p1 mirror panel on the surface of the dish.

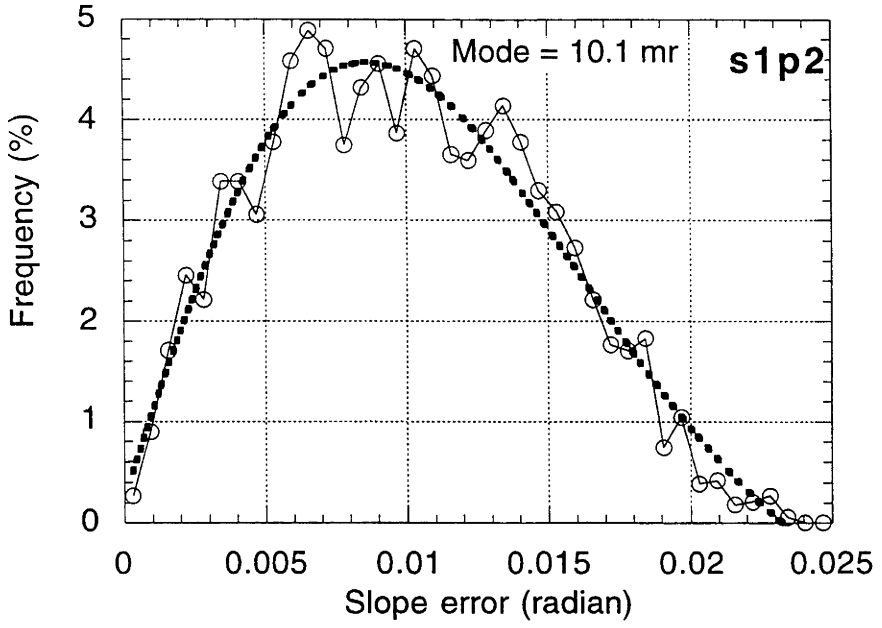

Figure A6.5.2. Frequency distribution of surface slope errors calculated for s3p2t mirror tiles (with normals) duplicated across the surface of the s3p2 mirror panel, with the panel oriented into the measured vertex coordinates for the s1p2 mirror panel on the surface of the dish.

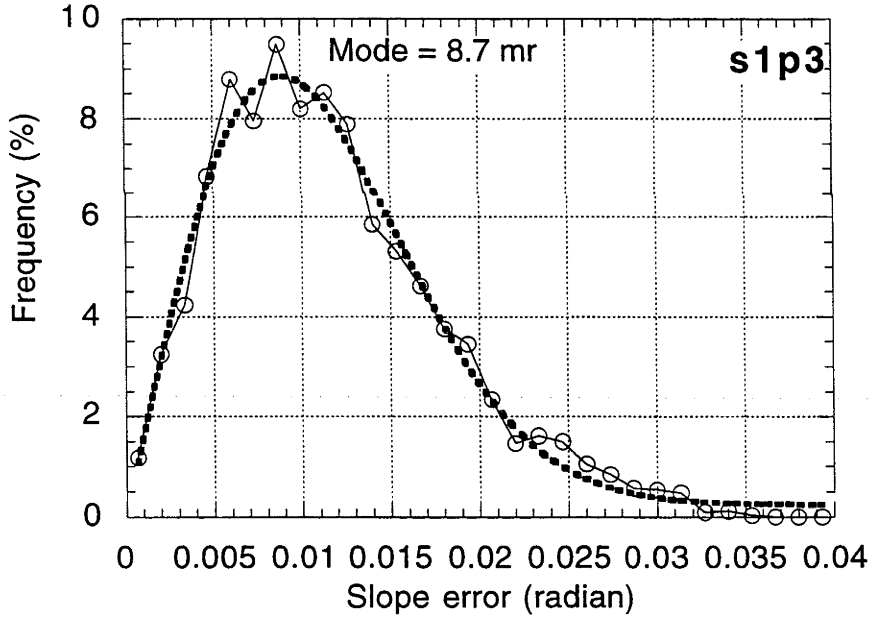

Figure A6.5.3. Frequency distribution of surface slope errors calculated for s3p3t mirror tiles (with normals) duplicated across the surface of the s3p3 mirror panel, with the panel oriented into the measured vertex coordinates for the s1p3 mirror panel on the surface of the dish.

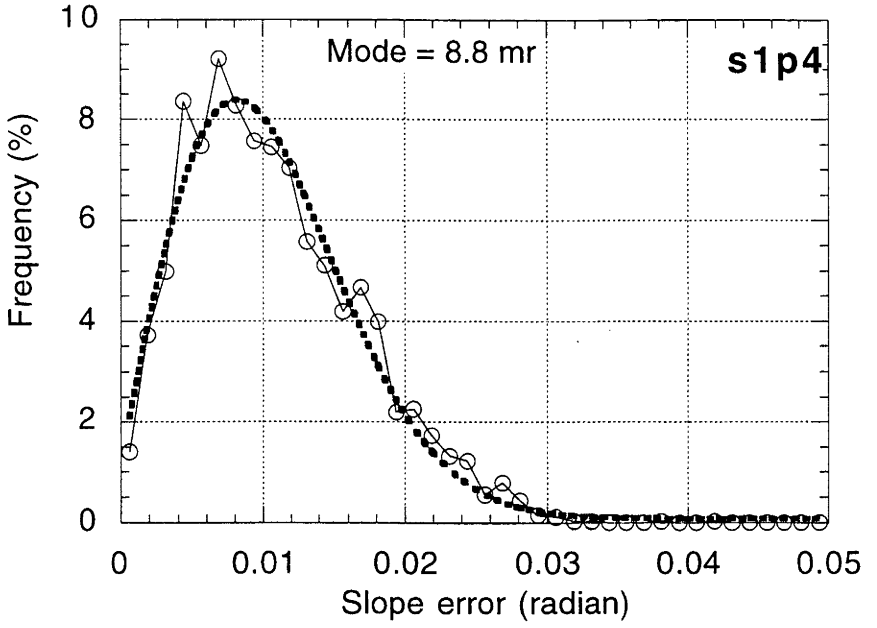

Figure A6.5.4. Frequency distribution of surface slope errors calculated for s5p4t mirror tiles (with normals) duplicated across the surface of the s5p4 mirror panel, with the panel oriented into the measured vertex coordinates for the s1p4 mirror panel on the surface of the dish.

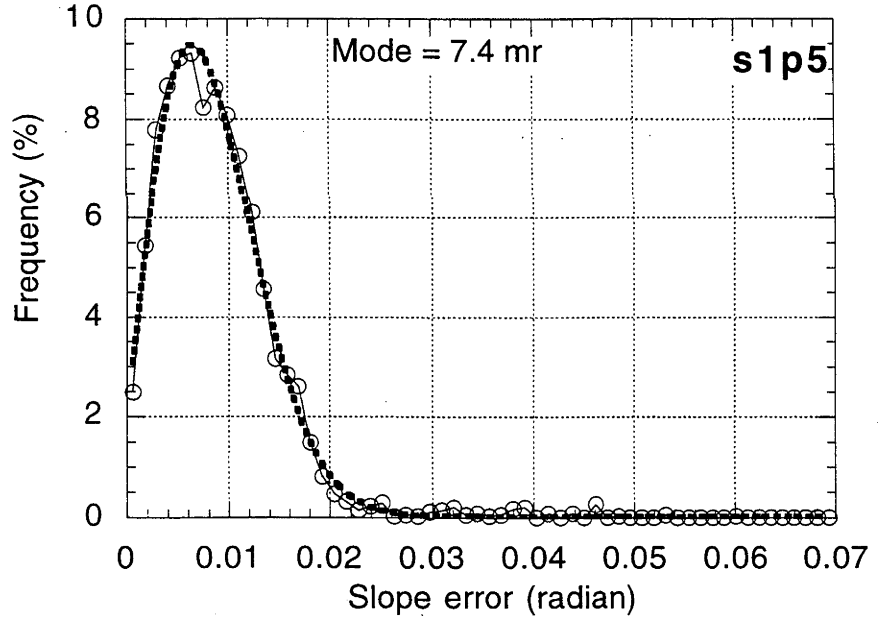

Figure A6.5.5. Frequency distribution of surface slope errors calculated for s3p5t mirror tiles (with normals) duplicated across the surface of the s3p5 mirror panel, with the panel oriented into the measured vertex coordinates for the s1p5 mirror panel on the surface of the dish.

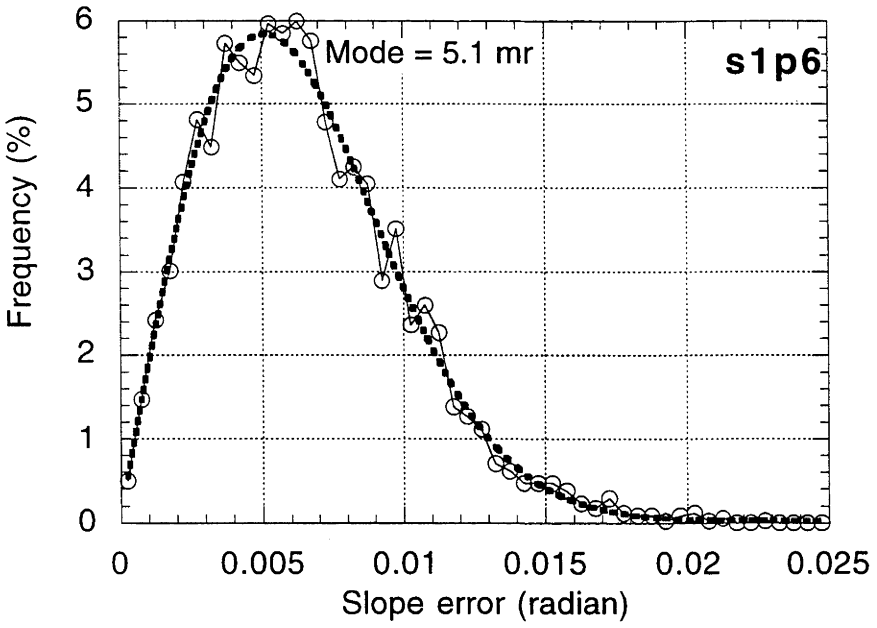

Figure A6.5.6. Frequency distribution of surface slope errors calculated for s3p6t mirror tiles (with normals) duplicated across the surface of the s3p6 mirror panel, with the panel oriented into the measured vertex coordinates for the s1p6 mirror panel on the surface of the dish.

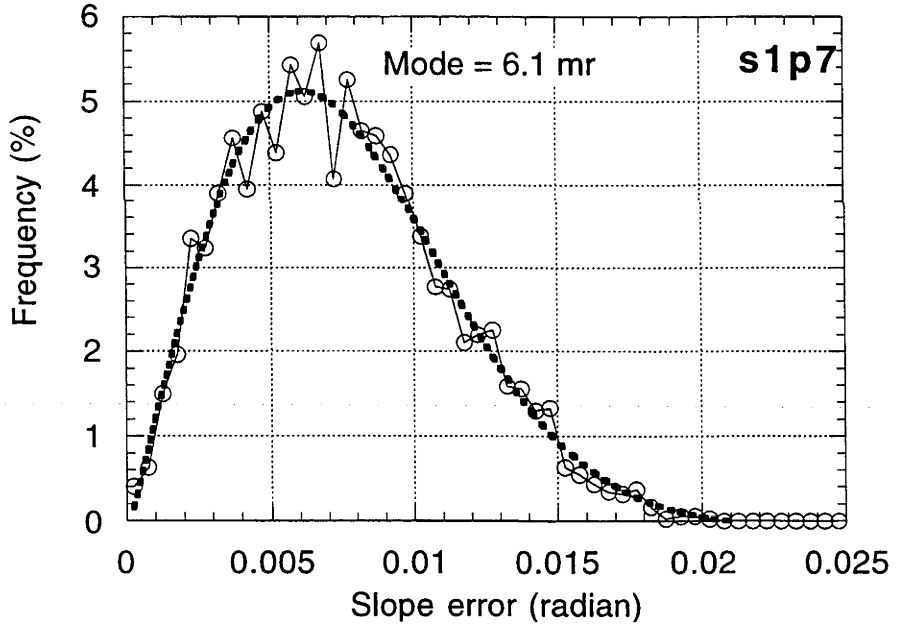

Figure A6.5.7. Frequency distribution of surface slope errors calculated for s4p7t mirror tiles (with normals) duplicated across the surface of the s4p7 mirror panel, with the panel oriented into the measured vertex coordinates for the s1p7 mirror panel on the surface of the dish.

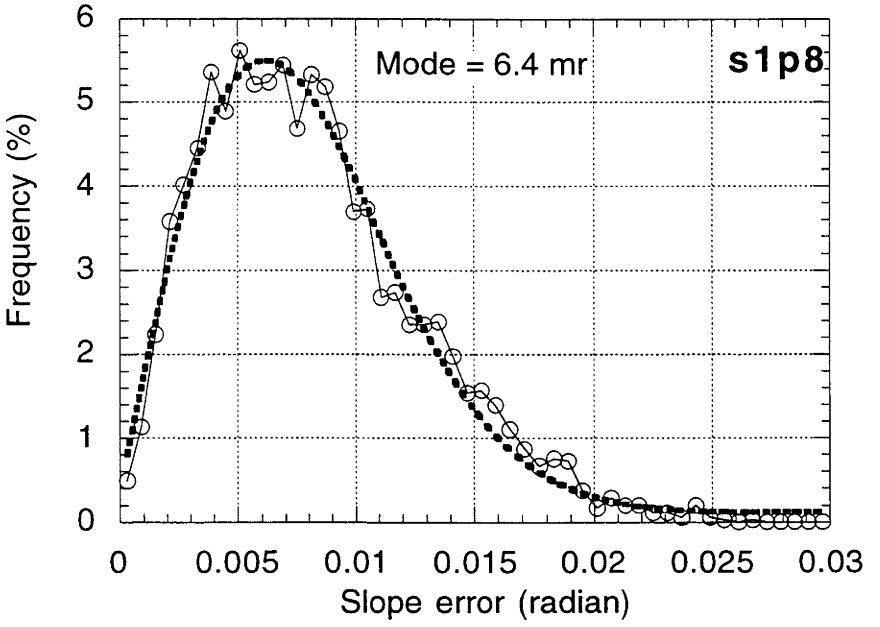

Figure A6.5.8. Frequency distribution of surface slope errors calculated for s5p8t mirror tiles (with normals) duplicated across the surface of the s5p8 mirror panel, with the panel oriented into the measured vertex coordinates for the s1p8 mirror panel on the surface of the dish.

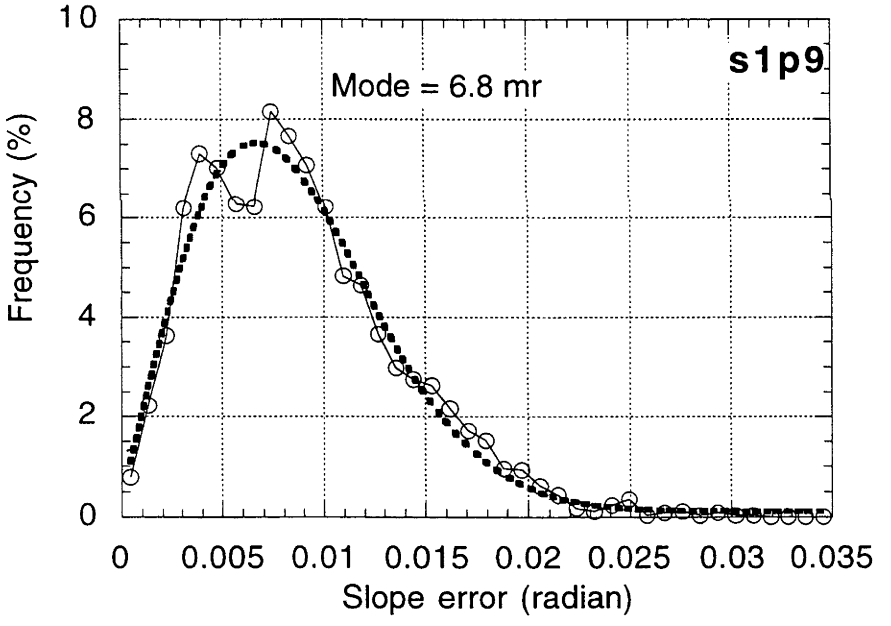

Figure A6.5.9. Frequency distribution of surface slope errors calculated for s3p5t mirror tiles (with normals) duplicated across the surface of the s3p5 mirror panel, with the panel oriented into the measured vertex coordinates for the s1p9 mirror panel on the surface of the dish.

Appendix 6.6. Frequency distributions for surface slope errors on the six sectors of the 400 m^2 dish.

Figure A6.6.1 to Figure A6.6.6 show the surface slope error frequency distributions for the 400 m^2 dish sectors, consisting of complete sets of mirror panels covered with mirror tiles, all oriented into their respective measured coordinates on the dish surface.

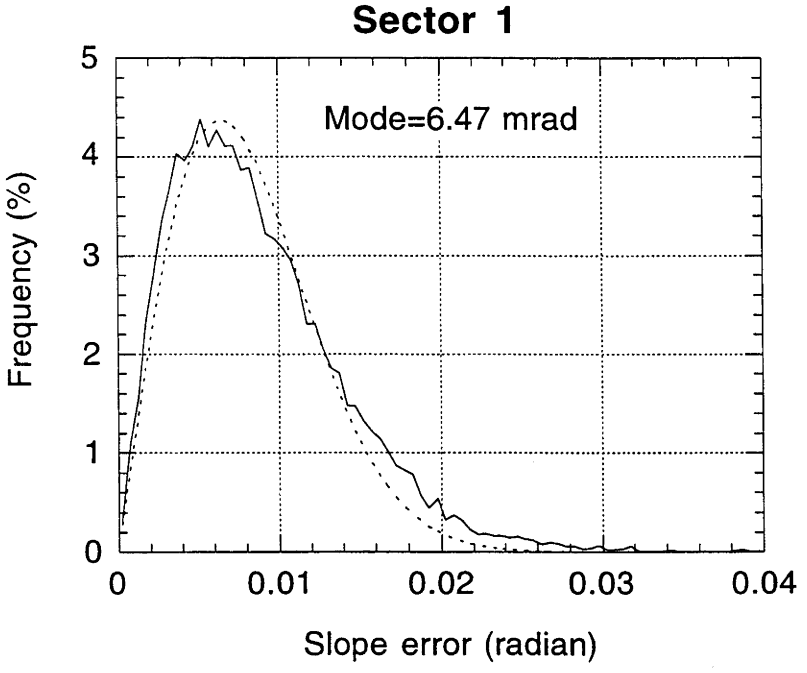

Figure A6.6.1. Frequency distribution of surface slope errors across sector 1 of the 400 m^2 dish. Dashed curve shows best-fit Rayleigh distribution to the data, with the mode calculated from this best-fit function.

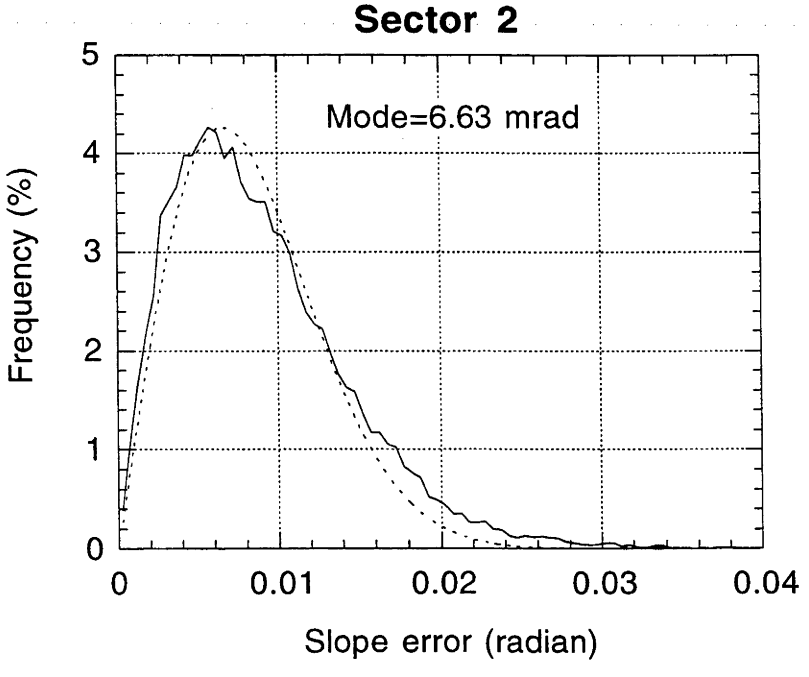

Figure A6.6.2. Frequency distribution of surface slope errors across sector 2 of the 400 m^2 dish. Dashed curve shows best-fit Rayleigh distribution to the data, with the mode calculated from this best-fit function.

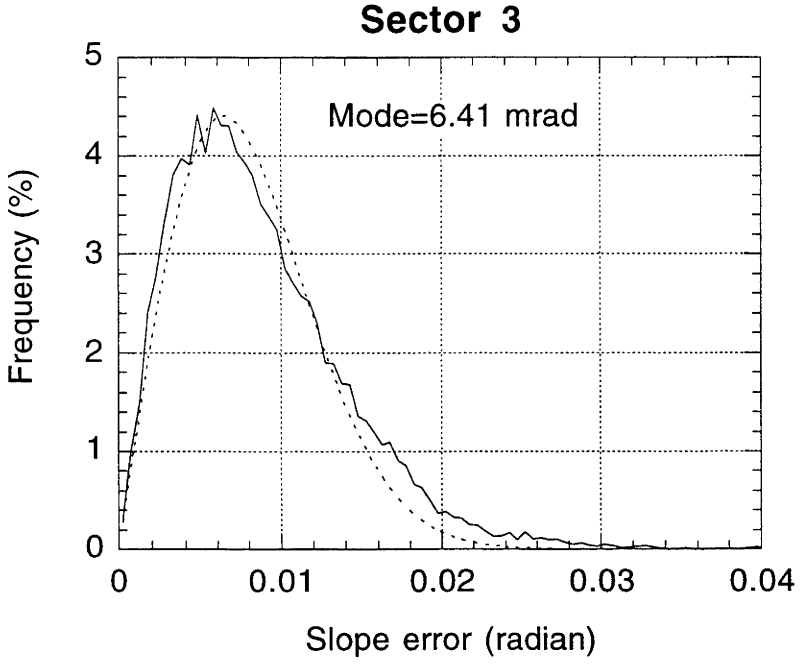

Figure A6.6.3. Frequency distribution of surface slope errors across sector 3 of the 400 m^2 dish. Dashed curve shows best-fit Rayleigh distribution to the data, with the mode calculated from this best-fit function.

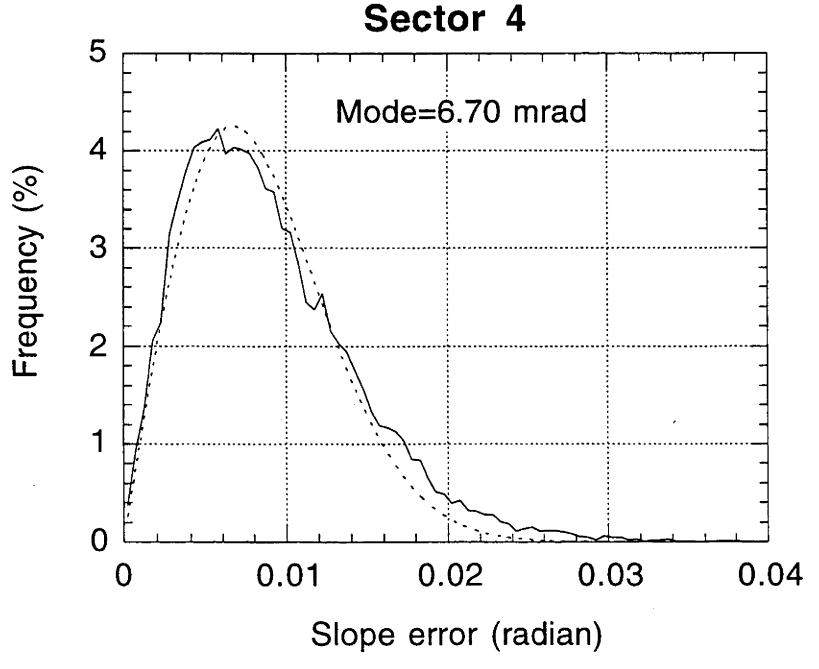

Figure A6.6.4. Frequency distribution of surface slope errors across sector 4 of the 400 m^2 dish. Dashed curve shows best-fit Rayleigh distribution to the data, with the mode calculated from this best-fit function.

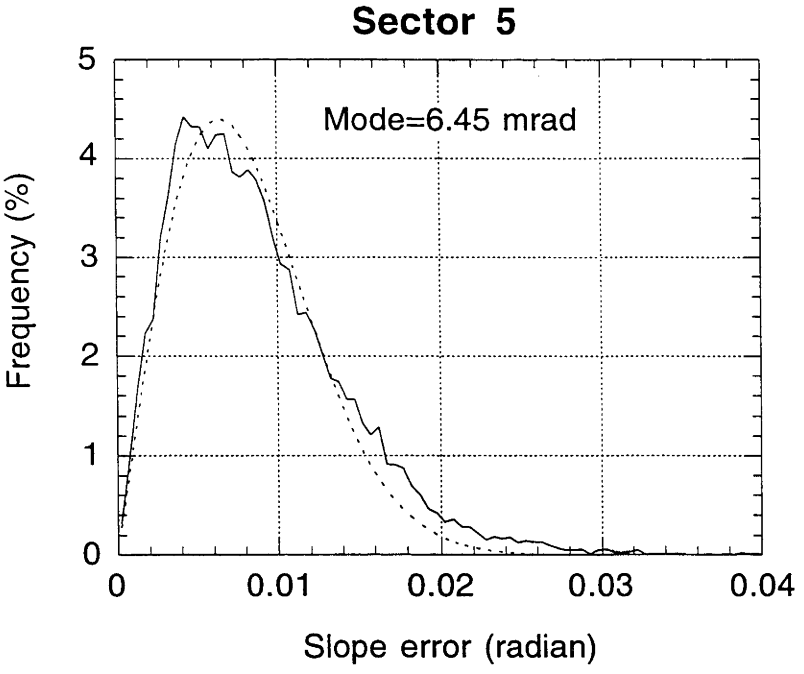

Figure A6.6.5. Frequency distribution of surface slope errors across sector 5 of the 400 m^2 dish. Dashed curve shows best-fit Rayleigh distribution to the data, with the mode calculated from this best-fit function.

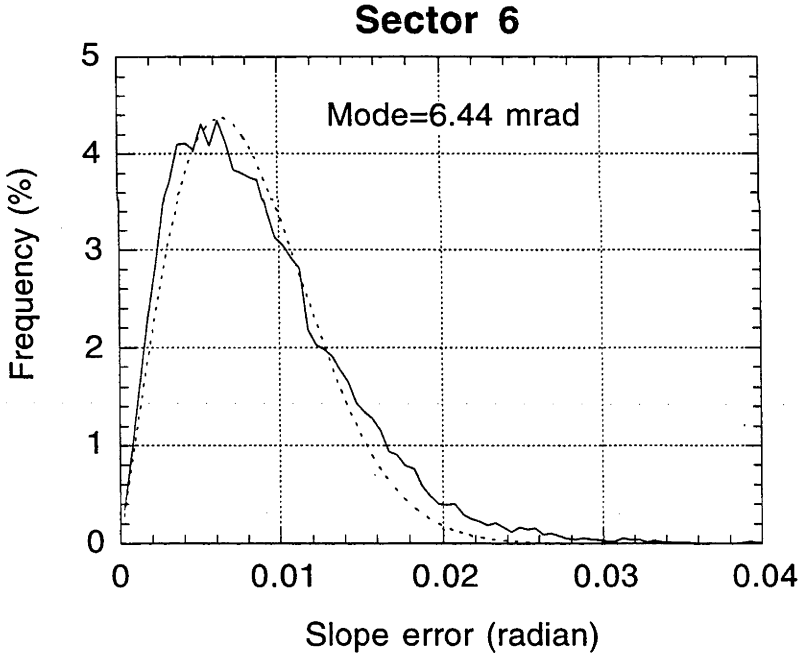

Figure A6.6.6. Frequency distribution of surface slope errors across sector 6 of the 400 m^2 dish. Dashed curve shows best-fit Rayleigh distribution to the data, with the mode calculated from this best-fit function.

Appendix 7.1. Predicted flux distributions from photogrammetrically measured panel surfaces on the 400 m^2 dish.

Figure A7.1.1 to Figure A7.1.2 show the predicted flux distributions expected on a 1.2 m square absorber placed at a nominal focal position of 13.1 m (13.06 m actual position), for the s1p1 to s1p9 mirror panels. The distributions are based on ray tracing performed on photogrammetrically derived data for the panels.

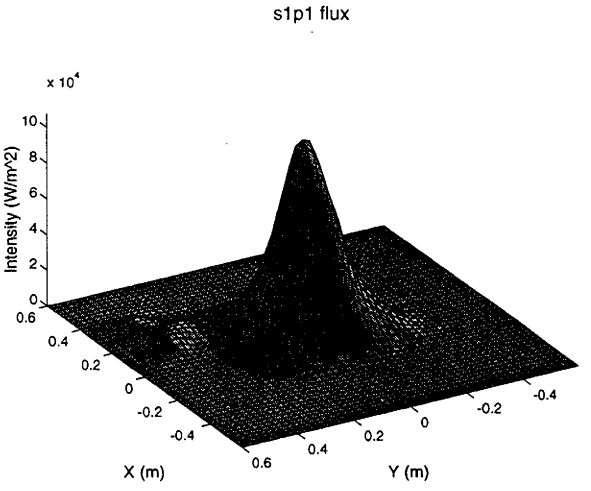

Figure A7.1.1. Surface plot of flux predicted from the s1p1 panel.

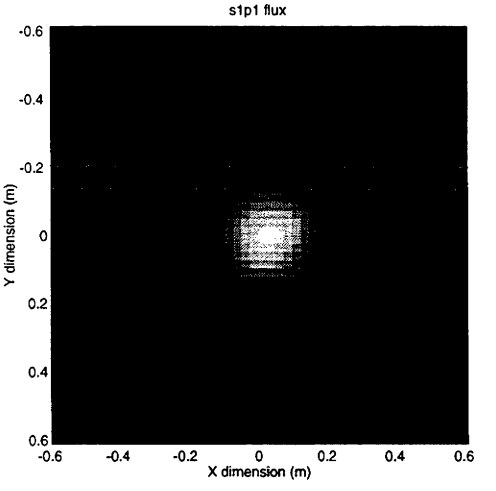

Figure A7.1.2. Flux image of the flux plot shown in Figure A7.1.1.

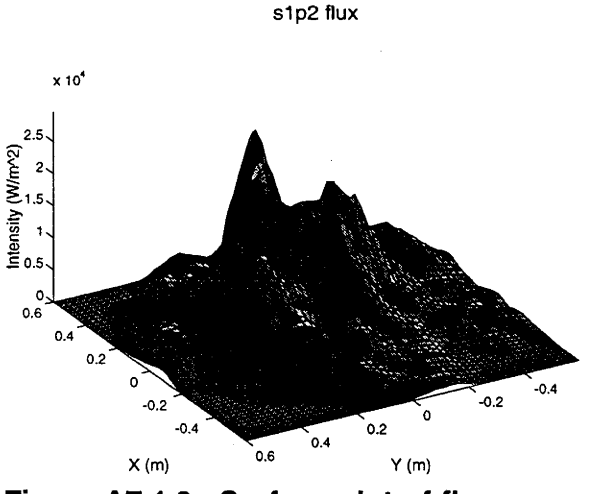

Figure A7.1.3. Surface plot of flux predicted from the s1p2 panel.

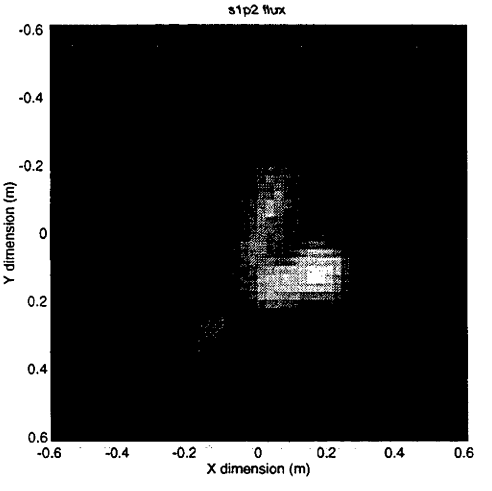

Figure A7.1.4. Flux image of the flux plot shown in Figure A7.1.3.

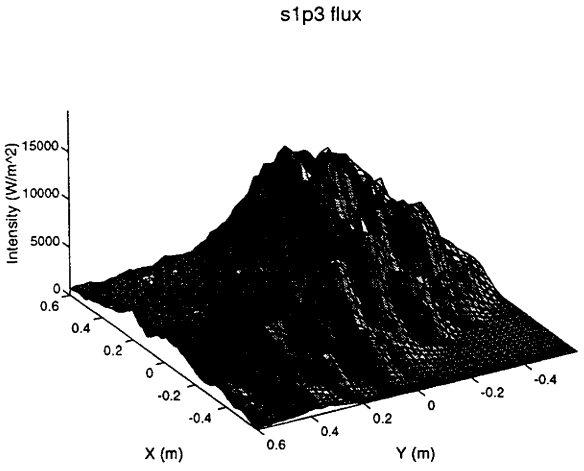

Figure A7.1.5. Surface plot of flux predicted from the s1p3 panel.

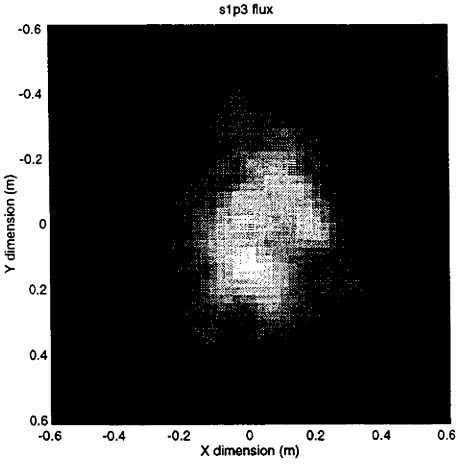

Figure A7.1.6. Flux image of the flux plot shown in Figure A7.1.5.

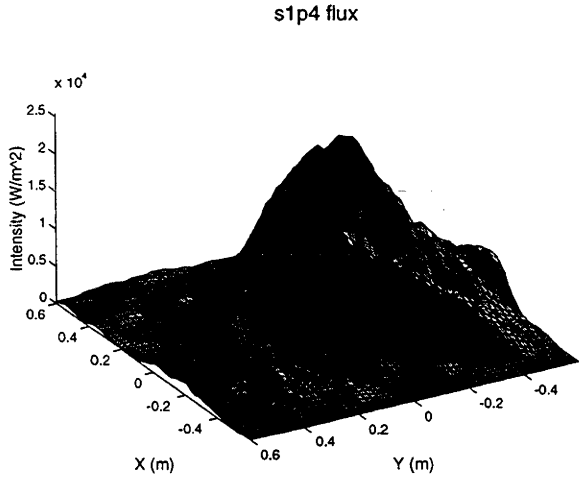

Figure A7.1.7. Surface plot of flux predicted from the s1p4 panel.

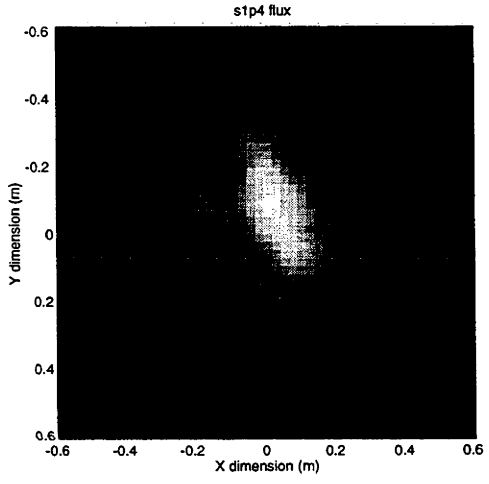

Figure A7.1.8. Flux image of the flux plot shown in Figure A7.1.7.

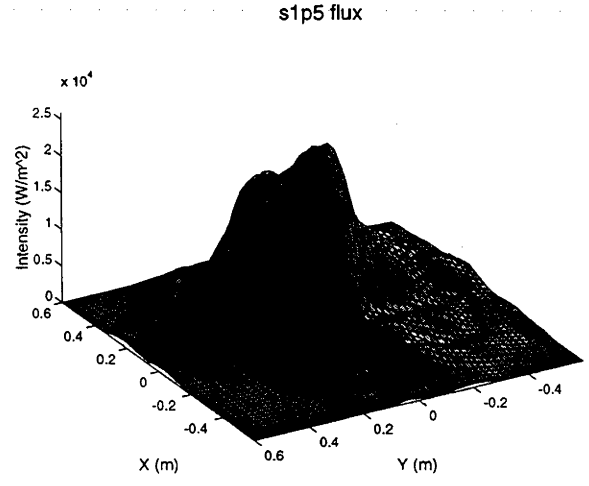

Figure A7.1.9. Surface plot of flux predicted from the s1p5 panel.

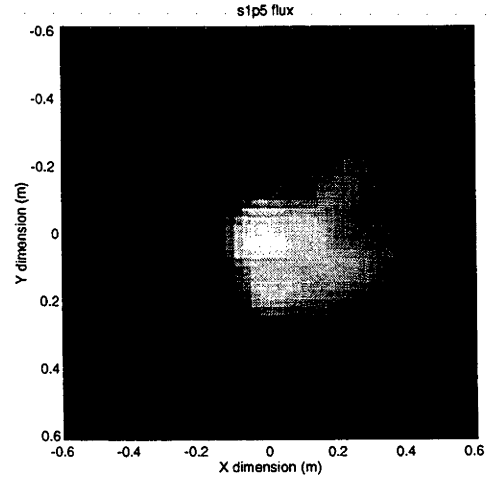

Figure A7.1.10. Flux image of the flux plot shown in Figure A7.1.9.

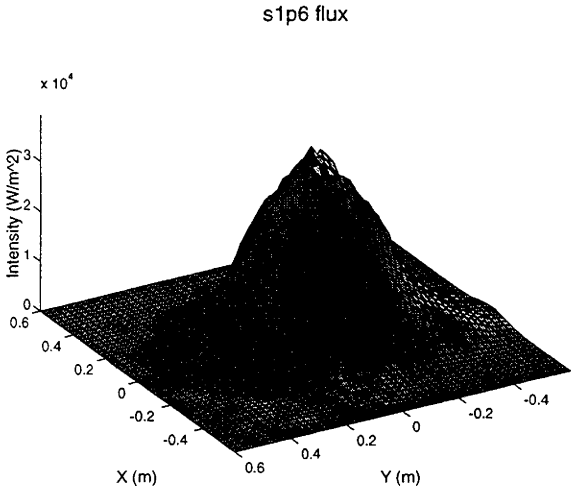

Figure A7.1.11. Surface plot of flux predicted from the s1p6 panel.

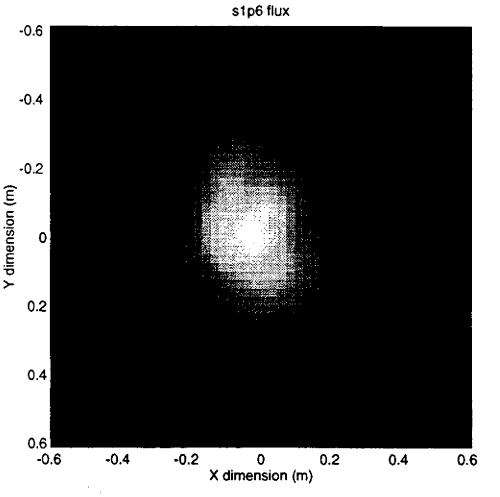

Figure A7.1.12. Flux image of the flux plot shown in Figure A7.1.11.

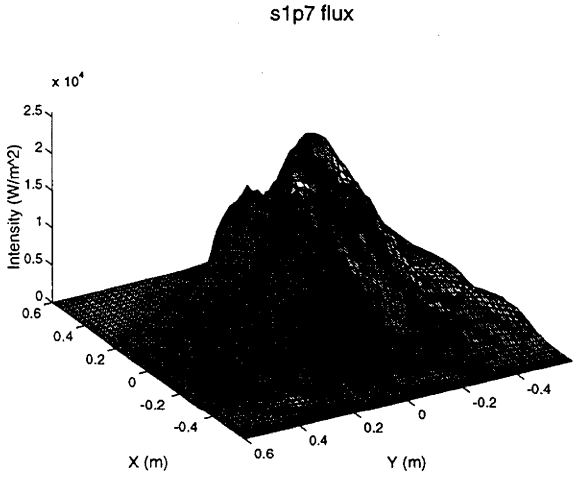

Figure A7.1.13. Surface plot of flux predicted from the s1p7 panel.

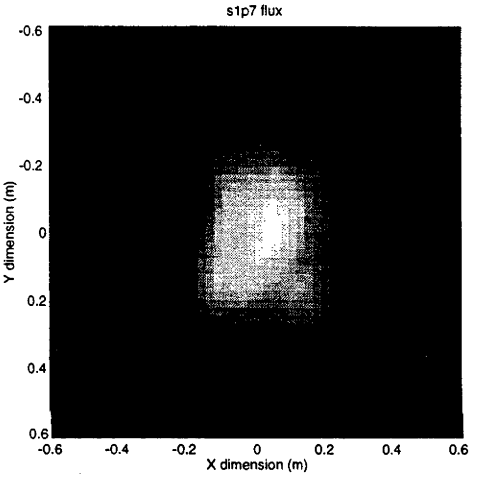

Figure A7.1.14. Flux image of the flux plot shown in Figure A7.1.13.

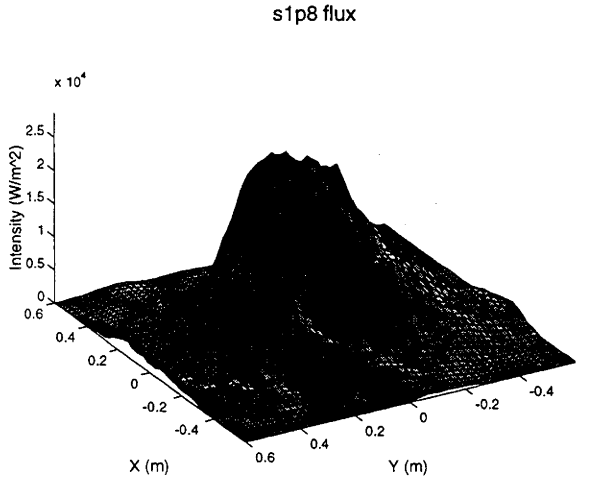

Figure A7.1.15. Surface plot of flux predicted from the s1p8 panel.

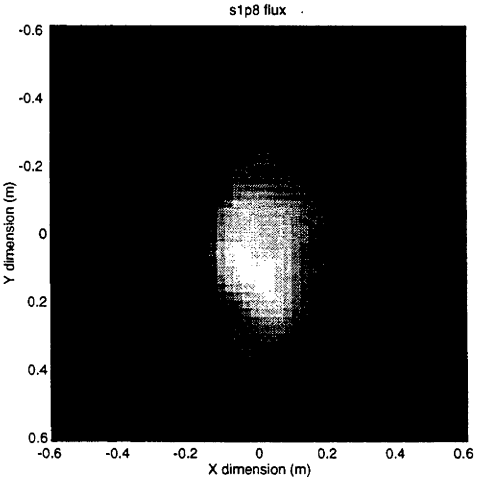

Figure A7.1.16. Flux image of the flux plot shown in Figure A7.1.15.

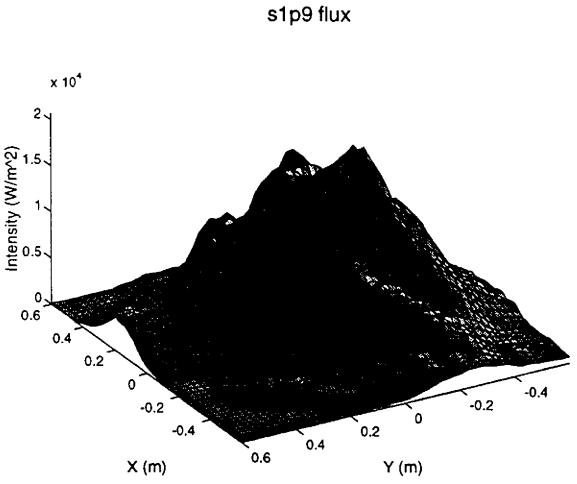

Figure A7.1.17. Surface plot of flux predicted from the s1p9 panel.

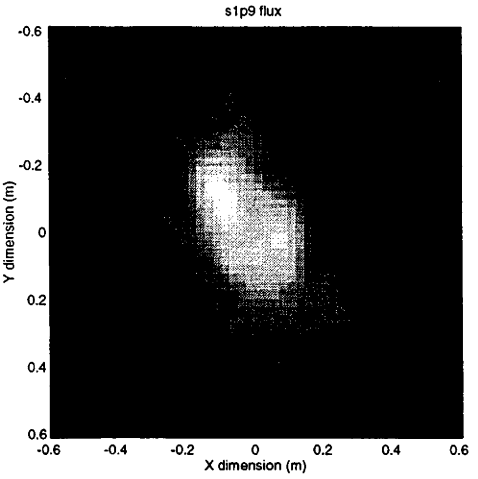

Figure A7.1.18. Flux image of the flux plot shown in Figure A7.1.17.